



UNIVERSITI PUTRA MALAYSIA

**SYNTHESIS AND THERMAL PROPERTIES INVESTIGATION OF COLLOIDAL
NANOPARTICLES AND THEIR APPLICATIONS**

MONIR NOROOZI

FS 2013 31



**SYNTHESIS AND THERMAL PROPERTIES INVESTIGATION OF
COLLOIDAL NANOPARTICLES AND THEIR APPLICATIONS**

By

MONIR NOROOZI

**Thesis submitted to the School of Graduates Studies, Universiti Putra Malaysia,
in Fulfillment of the Requirement for the Degree of Doctor of Philosophy**

May 2013

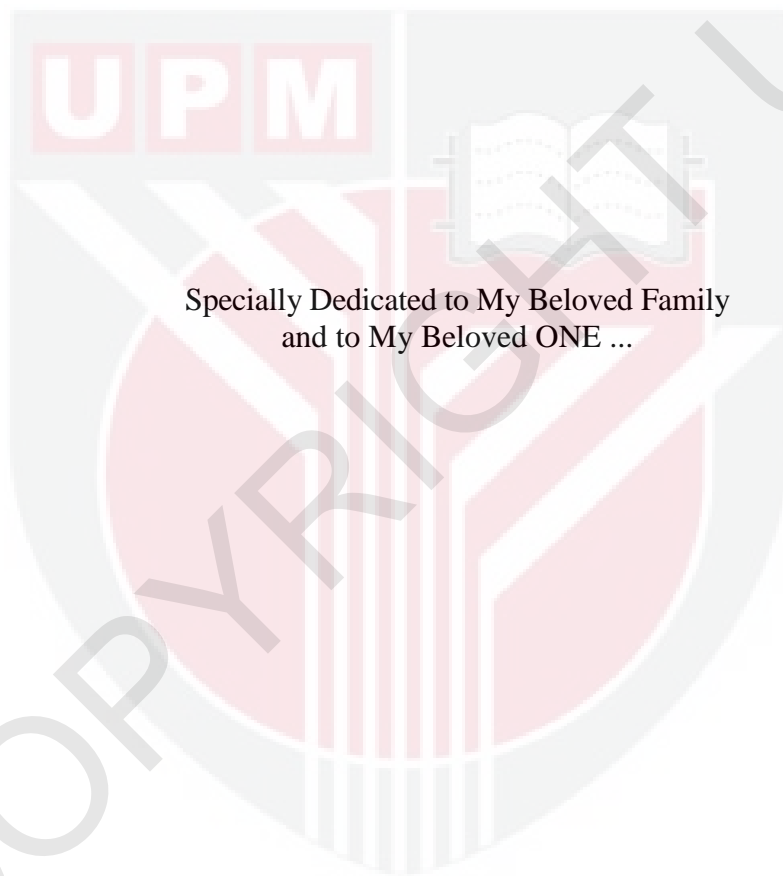
COPYRIGHT

All material contained within the thesis, including without limitation text, logos, icons, photographs, and all other artwork, is copyright material of Universiti Putra Malaysia unless otherwise stated. Use may be made of any material contained within the thesis for non-commercial purposes from the copyright holder. Commercial use of material may only be made with the express, prior, written permission of Universiti Putra Malaysia.

Copyright© Universiti Putra Malaysia



DEDICATION



Specially Dedicated to My Beloved Family
and to My Beloved ONE ...

Abstract of thesis presented to the Senate of Universiti Putra Malaysia in
Fulfilment of the requirement for the degree of Doctor of Philosophy

**SYNTHESIS AND THERMAL PROPERTIES INVESTIGATION OF
COLLOIDAL NANOPARTICLES AND THEIR APPLICATIONS**

By

MONIR NOROOZI

May 2013

Chairman: Professor Azmi Zakaria, PhD

Faculty: Science

Colloidal nanoparticles (NPs) have unique thermal, optical, electronic, and chemical properties that are extremely different from bulk materials due to their size. The central concerns in their preparation are the control of particle size, shape and the prevention of NPs agglomeration. In this relation, the objectives of the study are firstly, to green synthesize of silver nanoparticles (Ag NPs) in narrow distribution using green solvent and microwave (MW) irradiation as a cheap and fast method; secondly, to investigate the thermal diffusivity and the thermal effusivity of nanofluids by using PE technique; and thirdly, to increase the PE signal in optical fiber-thermal wave cavity (OF-TWC) technique by using Ag NPs film due to its strong optical absorption. In the first study, the fabrications of Ag NPs in water and ethylene-glycol as solvents at various MW reaction times were carried out. In the second study, a mathematical model of the multilayer samples by using thermal wave (TW) interferometry approach was developed and both Back- and Front-PE configurations were derived from it as special cases, the thermal diffusivity and thermal effusivity of nanofluids and the PE sensor were evaluated. In the third

study, the optical fiber tip was coated by Ag NPs to increase the PE signal in OF-TWC technique.

By increasing the MW irradiation time from 20 to 90 s the concentration of Ag NPs slightly increased and the NPs size increased from 7 to 12 nm. The Ag NPs prepared in ethylene glycol were more dispersed, more concentrated and more stable than those prepared in water. The observed difference may be ascribed to the high boiling points, molecular weight and dielectric loss of the ethylene glycol. The thermal diffusivity of nanofluids was investigated by using the Back-PE configuration in OF-TWC set-up. The linear increase in thermal diffusivity with Ag NPs volume fractions in nanofluids from 0 to 0.5 vol% has been observed, the highest value was $1.571 \times 10^{-3} \text{ cm}^2/\text{s}$. However, the highest value of thermal diffusivity reduced to $1.456 \times 10^{-3} \text{ cm}^2/\text{s}$ after 3 h time of leave, due to the NPs agglomeration in solution. The higher thermal diffusivity of Al_2O_3 nanofluid prepared by probe sonication than by bath sonication is due to higher dispersion of NPs in water. The fragmentation by laser irradiation at low concentration reduced the agglomerated size of NPs and increased the thermal diffusivity values, e.g., from 1.444×10^{-3} to $1.498 \times 10^{-3} \text{ cm}^2/\text{s}$ for Al_2O_3 and from 1.477×10^{-3} to $1.537 \times 10^{-3} \text{ cm}^2/\text{s}$ for CuO nanofluid from 0 to 90 min irradiation. The Front-PE configuration was designed by using a PVDF film sensor to measure thermal effusivity of the sensor itself in Thermally Thick regime, and of the nanofluids for both Thermally Thick and Thermally Very Thick regimes. The thermal effusivities of the sensor obtained from the normalized amplitude, $464.5 \text{ W s}^{1/2} \text{ m}^{-2} \text{ K}^{-1}$, and phase $479.1 \text{ W s}^{1/2} \text{ m}^{-2} \text{ K}^{-1}$ are close to each other, and the experimental error is less than 0.3 % and differs by less than 4 % to literature. The thermal effusivity of the solvents such as deionized water, ethylene glycol and olive

oil obtained from the methods showed good agreement with literatures but reduced in the presence of NPs. The TW generator comprised of Ag NPs-coated onto an optical fiber end surface, showed a significant enhancement of PE signal in OF-TWC setup owing to surface Plasmon resonance and to strong optical absorption in Ag NPs. Laser irradiation to the surface melts the NPs and connects them together to form a continuous smooth Ag film on the optical fiber end surface.



Abstrak tesis yang dikemukakan kepada Senat Universiti Putra Malaysia
sebagai memenuhi keperluan untuk ijazah Doktor Falsafah

**SINTESIS DAN KAJIAN CIRI-CIRI TERMA KOLOID NANOZARAH DAN
APLIKASINYA**

Oleh

MONIR NOROOZI

Mei 2013

Pengerusi: Professor Azmi Zakaria, PhD

Fakulti: Sains

Nanozarah (NP) koloid mempunyai ciri-ciri unik terma, optik, elektronik dan kimia yang sangat berbeza daripada bahan pukal disebabkan oleh saiz mereka. Fokus utama dalam penyediaannya adalah kawalan saiz zarah, bentuk dan pencegahan aglomerasi NP. Dalam kaitan ini, objektif kajian adalah pertamanya, untuk melakukan sintesis hijau keatas nanozarah perak (Ag NPs) dalam taburan sempit menggunakan pelarut hijau dan penyinaran mikro-gelombang (MW) sebagai kaedah murah dan cepat; keduanya, untuk menyelidik keresapan terma dan efusiviti terma nanobendalir menggunakan teknik PE; dan ketiganya, untuk menambahkan signal PE dalam kaedah Serabut Optik-Rongga Gelombang Terma (OF-TWC) dengan menggunakan sapat Ag NPs bersabit dari penyerapan optik tingginya. Dalam kajian pertama, fabrikasi Ag NPs dalam air dan etilena glikol sebagai pelarut pada pelbagai masa tindakan MW telah dilakukan. Dalam kajian kedua, model matematik dari

sampel multi-lapisan menggunakan pendekatan interferometri gelombang terma (TW) telah dibangunkan dan kedua-dua konfigurasi “PE-Belakang” dan “-Depan” telah diterbitkan daripadanya sebagai kes-kes khusus, keresapan terma dan effusiviti terma nanobendalir dan sensor PE telah diukur. Dalam kajian ketiga, hujung serabut optik telah disalut dengan Ag NPs untuk meninggikan signal PE dalam teknik OF-TWC.

Dengan meninggikan masa iradiasi MW dari 20 ke 90 s, kepekatan Ag NPs bertambah sedikit dan saiz NPs bertambah dari 7 ke 12 nm. Ag NPs disediakan dalam etilena glikol adalah lebih terserak, lebih pekat dan lebih stabil berbanding yang disediakan dalam air. Perbezaan pemerhatian boleh disabitkan dengan takat didih, berat molekul dan kehilangan dielektrik tinggi dari etilena glikol. Keresapan terma nanobendalir telah dikaji dengan menggunakan konfigurasi PE-Belakang dalam setup OF-TWC. Pertambahan linear dalam keresapan terma dengan pecahan-pecahan isipadu Ag NPs dalam nanobendalir daripada 0 to 0.5 vol% telah diperhatikan, nilai tertinggi adalah $1.571 \times 10^{-3} \text{ cm}^2/\text{s}$. Walau bagaimana pun, nilai tertinggi keresapan terma menurun ke $1.456 \times 10^{-3} \text{ cm}^2/\text{s}$ setelah 3 j dibiarkan, disebabkan oleh aglomerasi NPs dalam larutan. Keresapan terma lebih tinggi bendalir Al₂O₃ disediakan secara pensonifikasi prob berbanding oleh pensonifikasi mandian adalah disebabkan oleh serakan lebih tinggi NPs dalam air. Fragmentasi oleh iradiasi laser pada kepekatan rendah merendahkan saiz aglomerasi NPs dan menambahkan nilai-nilai keresapan terma, e.g. 1.444×10^{-3} ke $1.498 \times 10^{-3} \text{ cm}^2/\text{s}$ untuk bendalir Al₂O₃ dan 1.477×10^{-3} ke $1.537 \times 10^{-3} \text{ cm}^2/\text{s}$ untuk bendalir CuO pada iradiasi 90 min. Konfigurasi PE-Depan telah direka-bentuk dengan menggunakan sensor filem PVDF untuk mengukur keresapan terma dari sensor itu sendiri dalam

kawasan TEBAL secara-terma, dan dari nanobendalir untuk kedua-dua kawasan TEBAL secara-terma dan AMAT TEBAL secara-terma. Efusiviti-efusiviti terma sensor didapatkan daripada amplitud ternormal, $464.5 \text{ W s}^{1/2} \text{ m}^{-2} \text{ K}^{-1}$, dan fasa $479.1 \text{ W s}^{1/2} \text{ m}^{-2} \text{ K}^{-1}$ adalah rapat diantara satu sama lain, dan ketidakpastian eksperimen adalah kurang dari 0.3% dan berbeza kurang dari 4% berbanding literatur. Efusiviti terma pelarut-pelarut seperti air ternyah-ion, etilena glikol dan minyak zaitun didapatkan dari kaedah ini menunjukkan persetujuan baik dengan literatur tetapi berkurangan dengan adanya NPs. Generator TW terdiri dari Ag NPs-tersalut diatas permukaan hujung serabut optik menunjukkan peningkatan signifikan signal PE dalam setup OF-TWC disebabkan resonans Plasmon permukaan dan penyerapan optik tinggi dalam Ag NPs. Iradiasi laser kepermukaan meleburkan NPs dan menghubungkan mereka bersama untuk membentuk filem Ag licin selanjur diatas permukaan hujung serabut optik.

ACKNOWLEDGEMENTS

First and foremost, I would like to extend my praise to Allah s.w.t. that gives me the patience, strength, determination, and courage to produce this thesis.

It is a great pleasure to acknowledge my supervisor, Prof. Dr. Azmi Zakaria for his guidance, suggestion, assistance, patient, tremendous support and invaluable advice throughout the duration of this project. I would also like to extend my sincere appreciation to my co-supervisors Prof. Dr. Mohd Maarof Moxsin and Assoc. Prof. Dr. Zaidan Abdul Wahab for their advice and helpful discussion during this period of study.

I would like to thank the staff in Department of Physics and the Institute of Bioscience UPM for their co-operation throughout my work. I would also like to give my gratitude to Mohd Shahril Husin and my dear friends Sepideh Soltaninejad and Aiza Masyati Masut for all their personal and professional help. My sincere thanks to all my friends, and to my lab-mates in the Photoacoustic Laboratory who have directly or indirectly contributed towards the success of this study. In fact, all the students in the faculty of science were friendly and helpful, thank you for making my study a memorable and enjoyable one.

Especially, I dedicate this humble effort to my affectionate father (late), Houshang Noroozi, and my beloved mother, Kobra Motalebbi, who inspired me to higher ideals of life. Finally, I am greatly pleased to acknowledge all the supports and encouragements of my beloved family; my husband, Mohammad Golestan, my sons, AliReza, Mehrdad, Adib, and my siblings throughout my studies.

I certify that a Thesis Examination Committee has met on 28 May 2013 to conduct the final examination of Monir Noroozi on her thesis entitled "Synthesis and Thermal Properties Investigation of Colloidal Nanoparticles and Their Applications" in accordance with the Universities and University Colleges Act 1971 and the Constitution of the Universiti Putra Malaysia [P.U.(A) 106] 15 March 1998. The Committee recommends that the student be awarded the Doctor of Philosophy.

Members of the Thesis Examination Committee were as follows:

Elias bin Saion, PhD

Professor
Faculty of Science
Universiti Putra Malaysia
(Chairman)

Wan Mahmood Mat Yunus, PhD

Professor
Faculty of Science
Universiti Putra Malaysia
(Internal Examiner)

Abdul Halim bin Shaari, PhD

Professor
Faculty of Science
Universiti Putra Malaysia
(Internal Examiner)

K. P. Vijayakumar, PhD

Professor
Universiti Cochin
India
(External Examiner)



NORITAH OMAR, PhD
Assoc. Professor and Deputy Dean
School of Graduate Studies
Universiti Putra Malaysia

Date: 2 August 2013

This thesis was submitted to the Senate of Universiti Putra Malaysia and has been accepted as partial fulfilment of the requirement for the degree of Doctor of Philosophy. The members of the Supervisory Committee were follows:

Azmi Zakaria, PhD

Professor
Faculty of Science
Universiti Putra Malaysia
(Chairman)

Mohd Maarof Moksini, PhD

Professor
Faculty of Science
Universiti Putra Malaysia
(Member)

Zaidan Abdul Wahab, PhD

Associate Professor
Faculty of Science
Universiti Putra Malaysia
(Member)

BUJANG BIN KIM HUAT, PhD

Professor and Dean
School of Graduate Studies
Universiti Putra Malaysia

Date: 2 AUGUST 2013

DECLARATION

I declare that the thesis is my original work except for quotations and citations which have been duly acknowledged. I also declare that it has not been previously, and is not concurrently, submitted for any other degree at Universiti Putra Malaysia or other institutions.

MONIR NOROOZI

Date: 28 May 2013

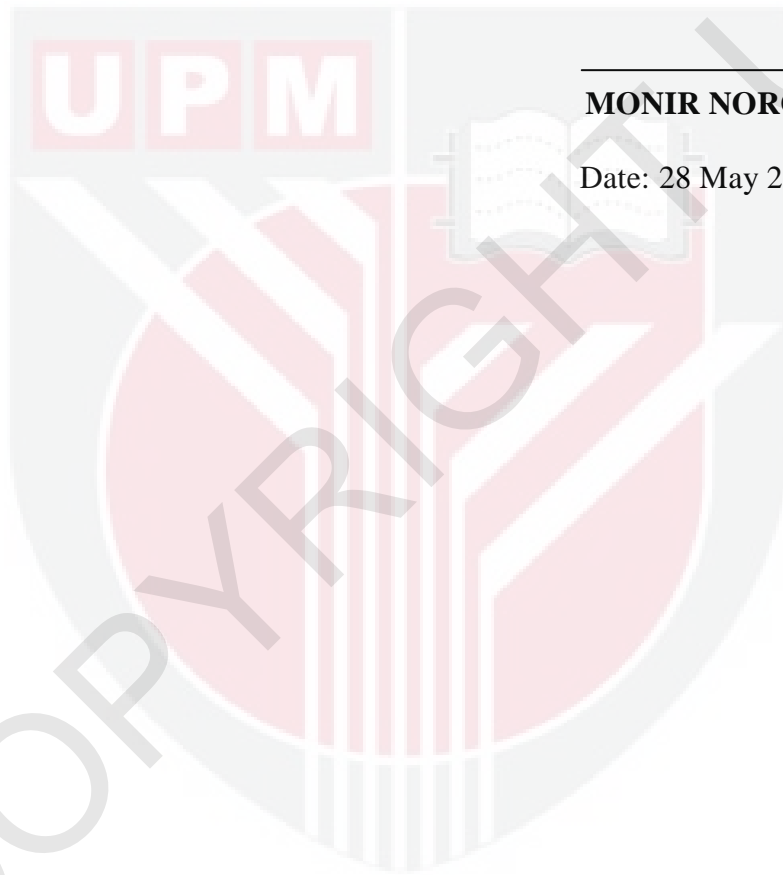


TABLE OF CONTENTS

ABSTRACT	Page
	ii
ABSTRAK	v
ACKNOWLEDGEMENTS	ix
APPROVAL	x
DECLARATION	xii
LIST OF TABLES	xvii
LIST OF FIGURES	xix
LIST OF ABBREVIATIONS	xxvii

CHAPTER

1	INTRODUCTION	
1.1	Introduction	1
1.2	Photothermal Effect	3
1.3	Pyroelectric Thermal Wave Technique	4
1.3.1	Back -Pyroelectric Configuration	4
1.3.2	Front-Pyroelectric Configuration	5
1.4	Thermal Properties of Materials	6
1.5	Nanofluids and Heat Transfer	7
1.6	Nanoparticle Material and bulk Material	8
1.7	Surface Plasmon Resonance of Metallic Nanoparticles	9
1.8	Green Synthesis of the Metallic Colloidal Ag NPs using Microwave Technology	9
1.9	Metal Nanoparticles and Photothermal Effect and its Application	11
1.10	Problem Statement	12
1.11	Objective of Research	13
1.12	Organization of the Dissertation	15
2	LITERATURE REVIEW	
2.1	Introduction	16
2.2	Nanoparticles Material	16
2.3	Synthesis of Metallic Nanoparticles using Microwave Method	17
2.4	Surface Enhanced Plasmon of Metal Nanoparticles	17
2.5	Photothermal Effect of Metal Nanoparticles	18
2.6	Potential Application of Metal Nanoparticles (NP) as Thermal Generator	19
2.7	Suspension of Nanoparticles (Nanofluids)	21

2.7.1	Potential Applications of Nanofluids as Heat Transfer Fluids	23
2.7.2	Nanofluids Thermal Properties	24
2.7.3	Synthesis and Stability of Nanofluids	24
2.8	Pyroelectric Detection Technique	26
2.8.1	Back- Pyroelectric Technique	27
2.8.2	Front- Pyroelectric Technique	29
2.9	Application of Thermal Wave Interferometry in Pyroelectric Technique	30
2.10	Thermal Properties of Nanofluids using Other Method	31
3	THEORY AND BACKGROUND	
3.1	Detection of Thermal-Wave Pyroelectric	33
3.2	Three-Dimensional Thermal Wave Field	34
3.2.1	The Comparison of Temperature Filed In 1-D and 3-D	37
3.3	Application of Thermal Wave Interferometry for PE System in 1-D	38
3.3.1	Pyroelectric Effect in a Multilayer Sample	38
3.3.2	Temperature Distribution in PVDF Film in Multilayer Samples	44
3.4	Monitoring of Back and Front Configuration as Special Cases	48
3.4.1	Back-PE Configuration (TWC technique) Theory	48
3.4.2	Front-PE Configuration	53
3.4.3	Thermal Effusivity of the Amplitude in Thermally Very Thick Regime	56
4	METHODOLOGY	
4.1	Introduction	59
4.2	Green Synthesis of Ag Nanoparticles by using Microwave Irradiation	59
4.2.1	Synthesis of Ag NPs/ DW or Ag NPs/EG Nanofluid	60
4.2.2	Comparison between Microwave and Conventional Heating	61
4.2.3	Ag NPs in Olive Oil	61
4.3	Ag-NPs in Clay Suspension by Chemical Method	62
4.4	Preparation of Metal Oxide Nanofluids	62
4.5	Methods of Stability of Nanofluids, Dispersion/Aggregation State	63
4.5.1	Ultrasonication Dispersion Process	64
4.5.2	Laser Fragmentation Process	65
4.6	Sample Characterizations	67
4.7	Pyroelectric Methods Experimental Set Up	67
4.7.1	Back- PE Configuration (Optical Fiber - TWC Setup)	68

	and Experimental Conditions	
4.7.2	Front Pyroelectric Configuration	77
4.7.3	Experimental Setup for Front-PE Configuration in Thermally Very Thick Regime	82
4.8	Designing the Ag NPs-Coated Optical Fiber as TW Generator	84
4.8.1	Synthesis of Colloidal Ag NPs	85
4.8.2	Modification of Optical Fiber (Thermal Wave Generator)	85
4.8.3	Experimental Setup with Ag NPs-Coated Optical Fiber	86
5	RESULTS AND DISCUSSION	
5.1	Introduction	89
5.2	Green Synthesis of Ag Nanoparticles without Reducing Agent at Different Microwave Irradiation Time	90
5.2.1	Dendritic Nanostructures of Ag Nanoparticles	93
5.2.2	Formation of Ag NPs under Conventional Heating	96
5.3	Synthesis of Ag NPs in Ethylene-Glycol at Different MW Irradiation Time	98
5.3.1	Self-Assembling of Ag NPs	103
5.3.2	Comparison between Ag NPs in Water and Ethylene-Glycol as a Solvent	104
5.4	Back Pyroelectric Configuration Technique and its Applications	106
5.4.1	Preliminary Work (Optimization and Calibration of System)	106
5.4.2	Thermal Diffusivity and Conductivity Determination of Clay Containing Ag-NPs; Volume Fractions Effect	111
5.4.3	Agglomeration Effect on Thermal Diffusivity of Ag/Clay	120
5.4.4	Dispersion and Fragmentation Effect on Thermal Diffusivity of Nanofluids	122
5.4.5	Effect of Ultrasonication on Thermal Diffusivity of Al ₂ O ₃ Nanofluids	123
5.4.6	Effect of Laser Irradiation on Thermal Diffusivity of Al ₂ O ₃ and CuO Nanofluids	129
5.5	Front Pyroelectric Configuration Technique by Using PVDF as a Sensor	148
5.5.1	Thermal Effusivity Measurements of Pyroelectric Sensor and Sample	148
5.5.2	Thermal Effusivity of Nanofluids Containing Al ₂ O ₃ and CuO Nanoparticles in Different Base Fluid	153

5.5.3	Thermal Effusivity Measurement Using Combined the Amplitude and Phase	158
5.6	Thermal Effusivity of Ag NPs in Different Solvent Using Front-PE in Thermally Very Thick Regime	162
5.6.1	A Comparison between Combining the Amplitude and Phase Signal and Front-PE in Thermally Very Thick Regime Method	165
5.7	Application of Ag NPs-Coated Optical Fiber to Enhance Thermal-Wave Generation in OF-TWC Technique	167
5.7.1	Surface Plasmon Resonance of Ag Nanoparticles	167
5.7.2	The Effect of Laser Irradiation on Morphology of Ag NPs Film	171
5.7.3	Ag NPs-Coated Optical Fiber to Enhancement PE Signal	174
5.7.4	Thermal Diffusivity Measurement of Air Using Ag NPs-Coated Optical Fiber	178
6	CONCLUSION AND FUTURE DIRECTION	
	Introduction	182
	Conclusion	182
	Suggestions for Future Work	188
	REFERENCES	190
	BIODATA OF STUDENT	206
	LIST OF PUBLICATIONS	207

LIST OF TABLES

Table		Page
4.1	Sources of nanopowders and their properties provided by the manufacturer	63
5.1	The thermal diffusivity values of water measured in the present work	110
5.2	Results of calibration with water and clay suspension	114
5.3	Summarized results for thermal properties of Ag NPs/ clay nanofluids at different AgNPs volume fraction.	118
5.4	Summarized results for thermal properties of Ag NPs/ clay nanofluids at different different time of leave (0, 1, 2, and 3 hours)	122
5.5	Summarized results of thermal diffusivity of Al ₂ O ₃ nanofluids in the treatment by bath (B) and probe (P) Sonication	129
5.6	Summarized results for thermal properties of Al ₂ O ₃ and CuO nanofluids at different laser irradiation time.	145
5.7	Thermophysical parameters of the PE cell components used for the calculation with water as the liquid sample	150
5.8	Thermal effusivity of some liquid samples, obtained from the phase of the PE signal, with PVDF sensor (52μm)	152
5.9	Experimental thermal effusivity for solvents with Al ₂ O ₃ and CuO nanoparticles (NPs) and thermal effusivity values of pure solvents from the literature	157
5.10	Experimental thermal diffusivity and thermal effusivity of PVDF sensor and its literature values	159
5.11	Experimental thermal effusivity of the Ag NPs dispersed in water (DW) or ethylene-glycol (EG) at different microwave irradiation time, 20, 40, 60 and 90 s	160

- 5.12 The corresponding asymptotic values, N , for the normalized PE signal for Ag/w1 and Ag/EG1 nanofluids and their thermal effusivities 164
- 5.13 Thermal diffusivity and the comparison between two methods for respective samples 166
- 5.14 Average value of Thermal diffusivity of air obtained from amplitude and phase of signal, with Ag NPs and Ag paint film as TW generator and comparison with literature values 180



LIST OF FIGURES

Figure		Page
1.1	The energy levels of noble metal NPs by a quantum size effect (Naoki, 2008)	8
2.1	Thermal conductivity of the materials (solids and liquids) at room temperature (Murshed, et al. 2008)	22
3.1	Schematic diagram of Optical Fiber- TWC, Gaussian laser beam was transmitted through the inlet of single core polymer fiber (of spot size w) and was converted into TW at the other metalized end	35
3.2	The plot of temperature field in 3-D and 1-D, with respect to scanning distance radius in water at different thickness, z , from 0 to 0.02 cm using laser spot size $w=0.05$ cm and TW generator radii, $R=0.15$ cm	37
3.3	The cross-section of a multilayer samples	40
3.4	Schematic geometry of the surface N-1, N and P, respectively, of the multilayer samples	41
3.5	TW after travelling through a distance in PVDF film partially transmitted into substrate and partially reflected into PVDF	44
3.6	1-D geometry of the TWC, (back-PE), for a cell structure (s/m/p/b)	49
3.7	The first transmitted and the reflected thermal wave in the PE cell	49
3.8	1-D geometry of the Front-PE configuration, for a cell structure (g/p/s)	53
3.9	1-D geometry of the Front-PE configuration, for a cell structure (s/p/g)	56
4.1	Schematic diagram of the process of laser fragmentation of nanofluids	66
4.2	PE signal generation chamber in the Back-PE technique	69
4.3	(a) Schematic diagram of OF-TWC technique and (b) the optical fiber and PE cell	70

4.4	Microscopic image of end of fiber after remove the jacket, the clean removing (left) and the damage fiber after remove the jacket (right)	72
4.5	The frequency behavior of the amplitude of signal obtained from distilled water	73
4.6	Typical results of the (a) amplitude and (b) phase vs relative cavity length for water, the thermal diffusivity can be obtained from the slope fitting parameter $A=(\pi f / \alpha_2)^{1/2}$	75
4.7	Typical results of the (a) In-phase and (b) quadrature of signal vs relative cavity length for distilled water. The thermal diffusivity from (a) In-phase and (b) quadrature using Equations. 3.25a-b	77
4.8	Schematic view of experimental setup of Front -PE configuration	78
4.9	Frequency behaviour of the normalized (a) amplitude and (b) phase measured for the PVDF sensor with water as substrate. Solid lines are the best fit of amplitude to Equation 3-31 and phase to Equation 3-30, respectively.	80
4.10	Schematic diagram of Front-PE configuration in thermally very thick regime	83
4.11	Schematic diagram of OF-TWC technique, the tip of optical fiber was coated by Ag NPs film as the TW generator	87
5.1	Synthesis Ag nanoparticles dispersed in water by using MW irradiation at 20 s, 40 s, 60 s and 90s, left to right respectively	90
5.2	Synthesis Ag nanoparticles dispersed in DW by using MW irradiation	91
5.3	TEM images and their particle size distributions of Ag nanofluids at the different MW-irradiation time: 20.s (A, B), 40.s (C, D), 60.s (E, F), and 90.s (G, H)	92
5.4	(a) TEM micrographs (b) FESEM of the dendritic nanostructures to the formation of Ag trees	94
5.5	(a) UV adsorption during the formation of Ag+PVP nanofluids (W0 , W1 , W2 , W3 and W4 at before and after 20, 40, 60 and 90s MW irradiation times) was on the traces. (b) UV adsorption of sample W3, fresh and after six months storage	95

5.6	UV-vis spectra of Ag-NPs prepared with MW irradiation and thermal method at the same temperature, the concentration of silver nitrate and PVP are the same, while the temperatures reach to 60.°C	97
5.7	The TEM images of Ag-NPs synthesized by conventional heating method	98
5.8	Synthesis Ag NPs dispersed in EG by using MW irradiation at 20 s, 40 s, 60 s and 90s, left to right respectively	99
5.9	UV adsorption spectra during the formation of Ag nanofluids at the various MW irradiation times, the irradiation times was shown on the traces	100
5.10	TEM images and their corresponding particle size distributions of Ag nanofluids at the different MW-irradiation time: 20 (A, B), 40 (C, D), 60 (E, F), and 90 s (G, H)	102
5.11	TEM images of the individual spherical nanostructure self-assembled of Ag colloids in EG solution	103
5.12	Simulated IP of signal and the first overtone resonances as a function of cavity length with (a) $f=5$ Hz, (b) $f=100$ Hz , water thermal diffusivity ($\alpha_w=0.00145$ cm ² .s ⁻¹)	107
5.13	Simulated IP of signal and first overtone resonances as a function of modulated frequency with (a) $L=0.005$ cm, (b) $L=0.015$ cm, water thermal diffusivity ($\alpha_w=0.00145$ cm ² .s ⁻¹)	108
5.14	The plots of logarithmic amplitude and phase versus the cavity length , and (c-d) shows the real (in-phase) and imaginary (quadrature) of signal versus the cavity length in water	109
5.15	PVDF signals recorded vs. time for distilled water, the baseline for distilled water, is a steady-state signal various the times	111
5.16	TEM images and the corresponding particle size distributions of prepared Ag NPs in clay suspension at different volume fractions [(a) 0.1, (b) 0.2, and(c) 0.5 vol%]	113
5.17	Typical (a) logarithmic amplitude and (b) phase as a function of the relative cavity length of Ag/clay nanofluids at different Ag NPs volume fractions [0, 0.1, 0.2, and 0.5 vol%]	115

5.18	Comparison of six cavity lengths (0-0.025 cm) of the (a) logarithmic amplitude and (b) phase of water and Ag/clay nanofluids at different Ag NPs volume fractions [0, 0.1, 0.2, and 0.5 vol%]	116
5.19	Thermal diffusivity ratio of Ag/clay nanofluid at different Ag NPs volume fractions [0, 0.1, 0.2 and 0.5 vol%]	119
5.20	Thermal conductivity of Ag/clay nanofluid at different Ag NPs volume fractions [0, 0.1, 0.2 and 0.5 vol%] and the comparison of experimental result with HC model	119
5.21	phase of signal for measuring thermal diffusivity of Ag/clay nanofluid in 0.5% vol in various time (0, 1, 2, 3 h) after dispersion, the slope gradient of phase of the signal will be change in nanofluid of different time of leave	121
5.22	(a) Thermal diffusivity (b) and Thermal diffusivity ratio of Ag/clay nanofluid at different time of leave (0, 1, 2, and 3 h)	121
5.23	PSD of alumina suspensions in the treatment by bath (sample B) and probe (sample P) sonication	124
5.24	Distribution density function of sample P, in the treatment by probe sonication, measured with Nanophox Machine	123
5.25	UV-Vis absorption spectra of the Al ₂ O ₃ nanofluids, in the treatment by bath (sample B) and probe (sample P) sonication, respectively	126
5.26	TEM images of alumina nanoparticles (a) bath (b) probe sonication at 30 min of sonication	127
5.27	Typical (a) logarithmic amplitude and (b) phase as a function of relative cavity length of Al ₂ O ₃ nanofluids in the treatment by bath (sample B) and probe (sample P) Sonication, respectively	128
5.28	The TEM images of the Al ₂ O ₃ -NPs (a) before and after (b) 20 and (c) 90 min of laser irradiation at an excitation wavelength of 532 nm	131
5.29	The hydrodynamic diameters of Al ₂ O ₃ nanofluids measured 3 times before irradiation, after 20 min and after 90 min irradiation	132
5.30	The distribution density and the cumulative distribution of Al ₂ O ₃ NPs suspension (a) before (b) after 20 min and (c) after 90 min irradiation. The center of gravity of the density curve gives the mean sphere diameter.	133

5.31	Hydrodynamic diameter distribution of Al ₂ O ₃ NPs from Nanofluid before irradiation of 87.7±14.59 nm, after 20 min of 90.97±9.21 nm, and after 90 min irradiation of 91.57±2.61 nm	134
5.32	ln(σ/σ_0) vs laser irradiation time of Al ₂ O ₃ nanofluid	135
5.33	Optical absorption spectra of the Al ₂ O ₃ nanoparticles prepared in DW at various irradiation times	136
5.34	TEM images and the relative size histograms of the CuO-NPs before and after 20 and 90 min of laser irradiation (a): 0 min (47.45±26.15 nm), (b): 20 min (47.15±20.71 nm) and (c): 90 min (45.65±17.4 nm), respectively. Clearly (b) and (c) shows some small particles resulting from the fragmentation process and the breakup of these aggregations	137
5.35	The hydrodynamic diameters of CuO nanofluids measured 3 times for before, after 20 min and after 90 min laser irradiations	138
5.36	The distribution density and the cumulative distribution of CuO nanoparticle suspension in the (a) before (b) after 20 min and (c) 90 min irradiation. The center of gravity of the density curve gives the mean sphere diameter.	139
5.37	Average CuO particle size of TEM result and Nanophox results (Hydrodynamic diameter distribution) of particles before irradiation and after 20 and 90 min irradiation.	140
5.38	ln(σ/σ_0) vs laser irradiation time of CuO nanofluid	141
5.39	Optical absorption spectra of the Al ₂ O ₃ NPs prepared in DW at various irradiation times	142
5.40	The nanoparticles after laser irradiation into smaller fragments; the mechanism of fragmentation	143
5.41	ln(σ/σ_0) vs laser irradiation time of Al ₂ O ₃ and CuO nanofluid	144
5.42	Typical Ln(Amplitude) (a) and phase (b) as a function of the relative cavity length of Al ₂ O ₃ nanofluids at different irradiation times (0, 20 and 90 min)	146
5.43	The thermal diffusivity values for Al ₂ O ₃ and CuO nanofluid at different irradiation times.	147

5.44	Simulated frequency dependence of the normalized PE signal: (a) amplitude and (b) phase according to Equations 3.31 and 3.30, respectively, for PVDF sensors (52 μm and 28 μm), LiTaO_3 ; (300 μm) and PZT (200 μm); water as liquid sample	149
5.45	Frequency behavior of the normalized (a) amplitude and (b) phase obtained for the PVDF sensor with water as the substrate. Solid lines are the best fit of amplitude to Equation 3.31 and phase to Equation 3.30	150
5.46	Frequency behavior of the normalized phase of the PE signal for the different substrates: water, glycerol, soya oil, and olive oil	152
5.47	TEM images and their size distributions of (a) CuO particles and (b) alumina particles	155
5.48	The PE normalized phase of Al_2O_3 + olive oil (a) and CuO + olive oil; (b) as a function of the light modulation frequency, and the solid line is the best fit to Equation 3.30.	156
5.49	Comparison of the thermal effusivity of Al_2O_3 and CuO nanofluids with (DW, EG and olive oil) and the pure solvents	157
5.50	The behaviour of ϕ vs the square frequency, the thermal diffusivity of PE sensor was obtained from the gradient of curve	159
5.51	The thermal effusivity of Ag/DW and Ag/EG in 20, 40, 60 and 90 s MW irradiation times, respectively	161
5.52	The horizontal line represents the corresponding asymptotic values, N, for the normalized PE signal as a function of the modulation frequency from 50 to 100 Hz, in steps of 1 Hz, for Ag/W1 and Ag/EG1 nanofluids.	163
5.53	The thermal effusivity of (a) Ag NPs/DW and (b) Ag NPs/EG in 20, 40, 60 and 90 s irradiation microwave time, respectively	165
5.54	The corresponding UV-vis spectra of the Ag NPs colloid, initial fresh; the optical absorption of AgNPs is very high in spatial wavelength, and storage over approximately 6 months; absorption peak was red-shifted and broadened	168
5.55	The corresponding UV-vis spectra of the Ag NPs colloid were dropped onto two 1 cm \times 1 cm glass slides with different amount of Ag NPs coating, low coverage film (20 μL) and high coverage film (50 μL) densities of Ag NPs, and dried at room temperature	169

5.56	(a) TEM image of silver nanoparticles and (b) histogram distribution of the particle size	171
5.57	(a) low and (b) high magnification FESEM images of Ag NPs coated on tip of optical fiber (Ag NPs-coated optical fiber):	172
5.58	The concept of the fabrication processes of Ag NPs film; the effect of laser irradiation on the morphology of Ag NPs	172
5.59	FESEM images of sample 1, Ag NPs-coated optical fiber (low density film) a) before and b) after 10 min laser irradiation in 10 min at range of frequency 7-50 Hz (at the condition of experiment	173
5.60	FESEM image of sample 2, Ag NPs-coated optical fiber (high density film) after laser irradiation at range of frequency 5-50 Hz (the condition of PT experiment)	174
5.61	(a) Amplitude as a function of the modulation frequency, and linear (b) ln (amplitude) and (c) phase as a function of square root of frequency, responses of the coated optical fiber (Ag NPs and Ag paint films)	176
5.62	(a) Amplitude as a function of modulation frequency, and linear (b) phase as a function of square root of frequency, responses of the Ag NPs-coated optical fiber (Ag NPs thin and thick films)	177
5.63	Amplitude and phase vs. square root of frequency for air sample with TW generator: (a) Ag paint (b) Ag NPs 1(low density) (c) Ag NPs 2(high density), respectively	179

LIST OF ABBREVIATIONS

AAS	Atomic Absorption Spectroscopy
Ag	Silver
Al ₂ O ₃	Aluminum Oxide
Back-PE	Back Pyroelectric
CuO	Copper Oxide
CW	Continues Wave
DW	Deionized Water
DPSS	Diode Pumped Solid State Laser
EG	Ethylene glycol
EM	Electromagnetic
FESEM	Field Emission Scanning Electron Microscopy
Front-PE	Front Pyroelectric
FWHM	Full width at half maximum
MMT	, Montmorillonite
MW	Microwave
NPs	Nano Particles
OF-TWC	Optical Fiber- Thermal Wave Cavity
PE	Pyroelectric
PSD	Particle size distribution
PT	Photothermal
PVDF	polyvinylidene difluoride
S/N	Signal to noise ratio
TEM	Transmission electron microscopy

TW	Thermal wave
1-D	one-dimensional
3-D	three-dimensional



CHAPTER 1

INTRODUCTION

1.1 Introduction

In recent years, nanotechnology has become one of the dominant technologies; nano-materials possess unique thermal, optical, electronic, and chemical properties that are significantly different from individual atoms or their bulk materials (Petrayeva *et al.*, 2011). The general optical properties, experimentally, Surface Plasmon resonances (SPR), of nanoparticles (NPs) are significantly different from those observed in bulk material. These novel phenomena enable some unique applications in a wide area of nanotechnology. Size distribution of the particles causes narrowing or broadening of SPR, which is among the various techniques that exist for synthesis of NPs using microwave (MW) irradiated synthesis that show promise (Sreeram *et al.*, 2008).

Colloidal suspensions of NPs (known as nanofluids) can be the next generation of the technique of transfer of heat in fluid samples, offering the possibility of enhancing thermal conductivity compared to the base fluids themselves (Wang and Mujumdar, 2007). Nanofluids preparation is the first important step in the investigation of heat transfer performance in nanofluids, since the size of the NPs, as well as Particle size distribution (PSD) in nanofluids critically affects their thermal properties. However, in particular, NPs show a much stronger aggregation tendency, due to different surface structures and surface interactions of NPs. In nano-powders there are many uncontrolled parameters including variability in the morphology, which depends on

the details of synthesis and processing. Particle fragmentation processes, due to laser irradiation of nanofluids, and ultrasonic agitation, due to physical dispersion of powders in the liquid, either in a bath or probe agitation may lead to more stability, and can be employed to enhance the thermal properties of nanofluids. While the investigation of the thermal conductivity of nanofluid has attracted a lot of attention in the last few years, a little work was done on the determination of the thermal diffusivity and thermal effusivity of nanofluids that are suitable thermal parameters of materials. (Murshed *et al.*, 2008).

During the past two decades, pyroelectric (PE) technique has attracted considerable attention, as a useful method in high resolution to measure thermal properties of materials in many aspects of science and technology. The thermal properties resulted directly from PE measurements are usually the “fundamental” ones: the thermal diffusivity and effusivity (Dadarlat and Neamtu, 2009). In recent years, the two PE techniques Back- and Front- configurations have been applied to investigate the thermal diffusivity and thermal effusivity, respectively. The Back-PE technique, which was designed to measure thermal properties of liquid and gas, and named the thermal-wave cavity (TWC), has been introduced in 1995 (Kwan *et al.*, 2007). Front- PE technique was widely used to measure thermal effusivity of gases and liquid samples by using the amplitude or the phase of PE signal. However, the signal phase is not dependent on power of incident light. For the Front-PE two main sensor schemes have previously been proposed, PVDF sensor as a thermally thin and LiTaO₃ crystal slabs sensor as a thermally thick (Dadarlat and Neamtu, 2006).

Based on the above, in this thesis, the research results of synthesis, characterization,

thermal properties and applications of nanostructured materials has been included. One major subject is the synthesis of silver (Ag) NPs by using MW heating technique, their thermal and structural properties, as well as their characterization and also the development of the optical fiber tip TW generator by coating it with Ag NPs. The other subject is the study on the determination of the most suitable conditions to stabilize and the measure the variation in thermal properties of nanoparticle colloids or nanofluids containing Ag, Al₂O₃ and CuO NPs as a function of base fluid, particles size, and particle volume fraction. The modeling is derived based on the PE technique of TW's that are induced by TW interferometry.

1.2 Photothermal Effect

In recent years there has increased interest in optical excitation thermal processes, called photothermal effects, which use laser as an optical heat source (Chirtoc *et al.*, 1989). The photothermal effect in a material is a consequence of the deposition of heat in the sample following absorption of a laser beam and subsequent thermal deexcitations, which result in the indirect heating of the sample. Photoacoustics, photothermal deflection, thermal lens, photothermal radiometry and PE methods are some of the commonly used and powerful techniques for the thermal and optical characterization of materials using lasers (George *et al.*, 2001). The PE technique involves measurement of the thermal waves in the sample due to absorption of optical radiation, by placing a PE detector in thermal contact with the sample.

1.3 Pyroelectric Thermal wave Technique

There are two PE thermal wave techniques, Back- or Front- configurations to investigate the thermal diffusivity and thermal effusivity, respectively. This technique is the only method based on the direct detection of photothermal heating, and therefore has a number of advantages over other detection schemes involving secondary mechanisms (like photoacoustic technique). The TW in the sample can be detected with a polyvinylidene difluoride (PVDF) thin-film. In this way, the PE technique has become a powerful tool for high resolution measurement of thermal properties of materials, solid, liquid and also highly diffusing gas. In this work the results of the systematic investigation of the variations in the thermal diffusivity and effusivity of nanofluids contain Ag, Al₂O₃ and CuO NPs in selected systems employing both Back- and Front- PE techniques were presented.

1.3.1 Back -Pyroelectric Configuration

The Back-PE configuration, mostly used to measure the thermal diffusivity of sample, requires an optically opaque sensor a thermally thick sensor and sample. In this technique the light modulation impinges on the front surface of a sample and the PE detector, located in good thermal contact with the sample's back side (Dadarlat and Neamtu, 2006) so the PE signal can be measured by performing either a frequency or a cavity length scan (Balderas-Lopez and Mandelis, 2003).

Recently, the Back-PE configuration, which was designed to measure thermal properties of liquid and gas, called “thermal-wave cavity (TWC) technique” has been

introduced in 1995 (Shen and Mandelis, 1995). It has been demonstrated that, the phase and the amplitude of the PE signal with a cavity length scan or a frequency scan methods were used to measure thermal diffusivity of sample.

The applications of the TWC techniques have all taken a one-dimensional (1-D) approach of the plane TW theory to describe the signal measurement. Although this assumption greatly simplified model, this approach may not be sufficient to describe the experimental results, if the spot size w of the Gaussian laser beam is sufficiently small compared to the cavity length, or the cavity diameter is large compared to the thermal diffusion length (Kwan *et al.*, 2007). The first attempt to design the TWC technique in order to resolve the dimensional issue has been done recently, named the optical fiber - thermal-wave cavity (OF-TWC) (Azmi *et al.*, 2008). In that study, the metalized optical fiber was used as light transfer and also as TW generator, and the set up was used to measure thermal diffusivity of liquids in a small volume by using cavity length scanning. Attention has been paid to the boundary conditions of the theoretical 3-D approach in cylindrical coordinates. The other advantage of this simplification is the arrangement of TW generator and PE sensor which need not necessarily be in a vertical position as the optical beam always guided in the fiber and illuminates the metalized surface at the end of optical fiber tip.

1.3.2 Front-Pyroelectric Configuration

A modification to the classical configuration is the Front-PE configuration (Dadarlat *et al.*, 1996). The thermal effusivity was generally obtained, by using the amplitude or phase of PE signal. It is very useful to measuring the phase of signal, because the

phase represents only a time delay of the signal, and it is not dependent on the power fluctuations of the incident light (as in amplitude case), (Dadarlat and Neamtu, 2009, 2006; Longuemart *et al.*, 2003, 2002). Front-PE configuration was applied to pure liquid and liquid mixtures. In this technique, the light impinges on the front surface of the detector, and the sample, which is in good thermal contact with its back side. Two major measurement schemes were proposed previously: (i) with a thermally thin PVDF sensor (only 9 μm thick) (Dadarlat *et al.*, 1996), and (ii) with a thermally thick LiTaO₃ crystal slabs sensor (Longuemart *et al.*, 2002). In all mentioned cases, the sample must be thermally thick (Dadarlat and Neamtu, 2006). However, this configuration presents some technical disadvantages as this very thick sensors (usually LiTaO₃), typically 300 μm (Dadarlat *et al.*, 1996) or 500 μm (Dadarlat *et al.*, 2009), has to be coated with gold and will allow only a fraction of light energy to be absorbed, another drawback is that one has to use a very low chopping frequency and thus needs a low chopping facility.

1.4 Thermal Properties of Materials

The thermal parameters such as thermal diffusivity and thermal effusivity can be easily measured. The relationship between thermal diffusivity and thermal conductivity is given by,

$$\alpha = \frac{k}{c_p \rho} \quad (1.1)$$

where k , c_p and ρ are the thermal conductivity, specific heat and the density, respectively. This is indicated that the thermal effusivity result behaves in opposition

to the results of the thermal diffusivity, which is due to both the thermal diffusivity and thermal effusivity are inversely proportional (Jiménez-Pérez *et al.*, 2009).

$$e = k/\sqrt{\alpha} \quad (1.2)$$

1.5 Nanofluids and Heat Transfer

Modern nanotechnology provides new opportunities to manufacture colloidal suspensions of NPs, known as nanofluids. Nanofluids containing metal such as, Cu, Fe, Au, and Ag and metal oxide, such as Al₂O₃, CuO, and TiO₂ can be considered to be in the next-generation of the heat transfer fluids, as they have shown an increase in the effective thermal conductivity of them compared with their base fluid. This notion was founded on the knowledge that the metal material particles have thermal conductivity that is typically higher than those of liquids by 1-3 orders of magnitude. There are endless cases where increasing the heat transfer efficiency can be useful for the quality, amount, and/or the cost of a product or process. In many of these cases, nanofluids are good suitable for achieving the enhancement in thermal transfer (Wang *et al.*, 2007). Nanofluid coolants also has potential application in the main processing industry, such as the material, chemistry, biomedicine industry, food and drink, oil and gas, paper and printing, and textiles (Wang *et al.*, 2007). However, due to the increase in the ratio of surface area to volume in NPs, they have the tendency of aggregation in nanofluids.

The agglomeration of NPs results in not only the size of the cluster and particles but also the decrease of thermal conductivity as well as the thermal diffusivity of

nanofluids. So, the investigation of the stability is necessary to study and also analyze influential factors to the dispersion stability of nanofluids. In designing the stable nanofluids, demand for their precise thermal properties values, especially their thermal conductivity or thermal diffusivity, has been increasing. However, there are only few previous studies on the thermal diffusivity or effusivity of nanofluids.

1.6 Nanoparticle Material and Bulk Material

NPs are significantly different from their individual atoms or bulk materials. A bulk material should have constant physical properties regardless of its size, but in the NPs the properties are often dependent on their size. NPs exhibit many unique properties, for which they are being intensely studied in a number of research fields. For example, the general optical properties, SPR, of NPs differ significantly from those that are observed in bulk material. Although bulk metal has a band structure, the electronic energy levels of metal NPs with size of a few nanometers are rather separated as shown in Figure 1.1. This may have an advantage as a catalyst.

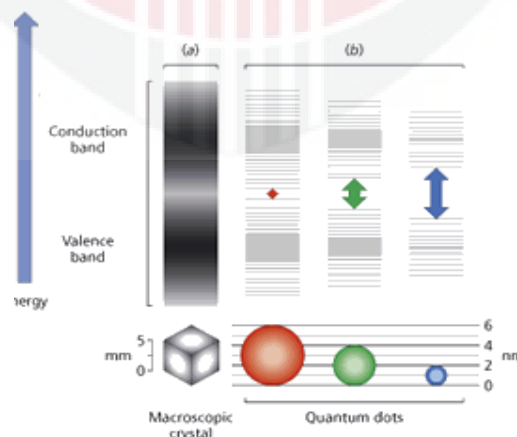


Figure 1.1. The energy levels of noble metal NPs by a quantum size effect (Naoki *et al.*, 2008)

1.7 Surface Plasmon Resonance of Metallic Nanoparticles

Metallic NPs have dimensions that put them in the quantum size regime that is responsible for increased absorption and scattering cross sections, as well as strongly increased EM fields in the vicinity of the NP surface (Petryayeva & Krull, 2011). These novel phenomena enable some unique applications in biology, integrated circuits, electronics, optics and other fields of materials science. Common materials used for NP production are noble metals such as Au and Ag, that due to the display SPR in the visible range of the wavelengths. However, Ag exhibits the sharpest and strongest bands among all metals. Recently, other relevant optical/thermal properties of metal NPs have also attracted much interest. The photothermal effect is especially strong for metal NPs, as the thermal generation becomes strongly enhanced under Plasmon resonance of the metal NPs (Govorov *et al.*, 2007). PSD leads to the different SPR the narrowing or broadening of Plasmon bands.

The central concerns in the preparation of NPs are control of the particle size, shape and prevention it from agglomeration. Among the several methods that exist for synthesizing of NPs, the use of MW assisted synthesis has shown promise. The target of the study is improving the control of particle size and stability of produced NP by this technique.

1.8 Green Synthesis of the Metallic Colloidal Ag NPs using Microwave Technology

Integration of “green synthesis” principles into nanotechnology and nanoscience has attracted much attention over the past decade. Meanwhile, the synthesis of noble metal nanomaterials by biomolecules such as silver NPs has drawn a lot of interest.

In the past, silver nanoparticles have been produced, either from the viewpoints of environmental or biological aspects. Therefore, it is necessary to develop environmentally sustainable (“green synthesis”) processes for the preparation of silver nanoparticles, especially in small particle size. Colloidal dispersions needed in many areas of science and technology must meet very strict requirements of particle size, uniform shape, and narrow size distribution. The formation of such monodisperse metal colloids from homogeneous solutions usually depend not only on the fabrication of NPs and but also requires the presence of a protective agent. In general, MW technique, as a cheap and green heating, is becoming an alternate power source strong enough to perform chemical changes in minutes, instead of conventional methods with hours heating. The use of MW irradiation as an efficient, environmentally friendly, and economically viable heating method for the production of NPs has great potential and it is clean, rapid, and simple to use and a viable avenue for the greener synthesis of nano-materials and metallic NPs. Fast nucleation during the reaction leads to formation of high concentration and more uniform size distributions.

In short, the dispersion and properties of particles are mainly depending on the interaction between solid and solution, the solvent playing an important role in the reaction process (Yin *et al.*, 2004). The polarity of a solvent plays a significant role, as the higher the polarity value of the solvent, the more efficiently a solvent couples with the MW energy. Due to this, heat is subsequently generated and may affect the morphology and size of the particles.

1.9 Metal Nanoparticles and Photothermal Effect and its Application

Recently heat generation of NPs under optical illumination has also attracted much interest in wide areas of research such as optics, electronics, biomedicine, analytical chemistry, and photo-chemistry. The phenomena of photothermal effect of that the NPs are illuminated by optical beam emitting in the specific wavelength which makes the NPs to generate SPR effect to convert the optical energy into thermal energy (Cheng *et al.*, 2011). Crystalline metal NPs such as Ag can efficiently increase thermal energy under optical excitation. Optical properties of noble metallic NPs provide efficient conversion of optical energy into thermal energy ones at nanoscale for the development of new generation nano devices (Kamat, 2002). For example, in the photothermal application of heated NPs in nanomedicine, the NPs become attached to tumor cells by selective biomolecular linkers. Then heat generated by optically stimulated NPs destroys the tumor cells (Govorov & Richardson, 2007).

The heat generation process involves not only absorption of incident photon, but also thermal conductivity of NPs, due to heat transfer from NPs to the surrounding base fluid. Therefore, the researchers investigated a wide variety of Photothermal effects of metal NPs phenomena although we are interested mainly in Photothermal application of heated NPs and its associated NPs absorption to use in heat generation devices. Such OF-TWC technique can be employed only in a narrow range of the frequency due to reduction of the signal to noise ratio. However, the design of the OF-TWC technique fabricated for the present studies allows one to enhance the PE signal. In order to achieve this goal the advantage of the SPR properties of noble

metal NPs was utilized and the colloidal Ag NPs synthesis was used to coat the optical fibers to develop OF-TWC method and to produce a better flexible Photothermal devices.

1.10 Problem Statement

The central concerns in the preparation of NPs are control of the size, shape and prevention of agglomeration of NPs. Among the several methods that exist for synthesizing of NPs the use of MW assisted synthesis has shown promise (Sreeram *et al.*, 2008). These researches aim at the design of environmentally benign nanomaterials. The target of the study is improving the control of particle size and stability of produced NPs by this technique.

Moreover, the knowledge of thermal properties of nano-materials is helpful for their appropriate applications. In particular, NPs show a much stronger aggregation tendency. Stability of the suspensions is a crucial issue for both scientific research and practical applications (Yu and Xie, 2012). Therefore, clear understanding of the aggregation structure in nanofluids is necessary in order to accomplish the research on thermal and heat transfer properties of nanofluids. Therefore, the effect of concentration, dispersion/aggregation state and particle size and the methods of stability, such as ultrasonic dispersion or laser fragmentation process and their effect on thermal properties of nanofluid prepared is an essential assay step for particle validation.

This study tried to clarify some of the unknown aspects of the nanofluid research

area, such as their thermal properties and their application. The unique features of the Back- and Front-PE techniques to measure the thermal diffusivity and the thermal effusivity of nanofluids in high resolution are not possible with other existing techniques. Moreover, the study aims to simplify the front-PE technique; modifications can be introduced to make it feasible for the signal employing PVDF in a thermally thick regime.

However, PE measurements suffer from poor S/N ratio due to the small quantities of PE signal (Heimlich *et al.*, 1995). The simple developed mechanism of Photothermal applications of heated Ag NPs is based on the TW generated by modulated laser beam which diffuses away from the nanocrystal and is transmitted to the detector. SPR in Ag NPs film can be useful to increase the PE signal in the TW generator to provide intrinsic amplification of the PE system (Heimlich *et al.*, 1995).

1.11 Research Objectives

In this thesis, an environmentally benign process was used for the “green” synthesis of narrow distribution silver nanoparticles via a microwave technique in green aqueous system. The effects of base fluid on nucleation, size distribution and growth mechanisms were investigated, and the characterization and applications of Ag NPs have been included.

The other subject is the study on the dispersion/aggregation state of NPs, to determine of the most suitable conditions to stabilize of nanofluids and measurements of the variation in thermal properties of nanofluids (containing Ag,

Al₂O₃ and CuO NPs) as a function of base fluid, particles size, and particle volume fraction. The photothermal or specifically PE technique was selected to measure their thermal properties at various conditions, such as volume fraction and NP size. The Back- and Front-PE configurations in “thermally thick” and “thermally very thick” conditions were implemented in measuring these thermal properties. Finally, the application of Ag NPs under light modulation was explored for heat generator or thermal wave generator in PE-cell.

More specifically the study pursues the following objectives:

- (i) To synthesize a homogenous Ag NPs with MW irradiation technique and to apply it in the TW generation for the PE signal enhancement.
- (ii) To develop a mathematical model of PE signal of the multilayer sample using TW interferometry approach and apply it for the Back- and Front- PE configurations as the special cases.
- (iii) To determine the effect of volume fractions, and aggregation of NPs on the thermal diffusivity of nanofluids using the Back-PE configuration and to measure the thermal effusivity of the sensor and nanofluids in different base fluids using the Front-PE configuration.

1.12 Organization of the Dissertation

The dissertation is structured in six chapters. The current chapter presents the background of the study, statement of the problem, objectives and scope of the study, definition of key concepts, and organization of the dissertation. Chapter Two reviews

historically previous work on preparation of NPs using MW, and surveys the relevant research on thermal diffusivity and thermal effusivity of nanofluids and also the research in the application of photothermal effect of metallic NPs. Chapter Three presents the theoretical TW interferometry concepts exploited during this study approach. Chapter Four is devoted to description of the experimental methods that have been used for fabrication and thermal diffusivity and thermal effusivity characterization of metal NPs such as Ag NPs and metal oxide NPs such as Al₂O₃ and CuO NPs. Moreover, various characterization techniques that were applied to analyze prepared NPs are described. Chapter Five presents the obtained results regarding the preparation and characterization of nanofluids and thermal properties of them. Finally, chapter six concludes the research finding.

CHAPTER 2

LITERATURE REVIEW

2.1 Introduction

In this chapter we present a brief review on previous works related to optical and thermal properties of NPs and preparation of NPs by using MW irradiation has been presented. A review of PE technique has been also presented for measuring thermal properties of fluids containing NPs.

2.2 Nanoparticles Material

Recently, NPs material have attracted much interest as materials for functional nano-devices, because of their unique optical, thermal, chemical, and physical properties which could not be observed in bulk materials. Size dependent property noted that the quantum effect of semiconductor particles, SPR of noble metal particles and heat enhancement and thermal properties of some nanofluids. This opens up the possibility of controlling the properties of NPs by controlling their synthesis process. Modern manufacturing technology provides excellent opportunity for procedure materials on nanometer scales. NPs materials exhibit new or different properties that cannot be exhibited in the bulk materials (Cheng *et al.*, 2011). Many techniques have been developed to synthesize NPs, including chemical reduction, electrochemical reduction, thermolysis method and MW irradiation method (Darroudi *et al.*, 2011; Dadgostar *et al.*, 2010; Bilecka *et al.*, 2009).

2.3 Synthesis of Metallic Nanoparticles Using Microwave Method

The interaction of the dielectric of liquids or solids material with high frequency electromagnetic waves causes the high, rapid and uniform heating in MW method in comparison with conventional heating (Ryu *et al.*, 2006). Using of MW irradiation increased the kinetic energy and rapid initial heating, which leads to increase the reaction rates. The MW heating method also provides the efficiency energy, in clean reaction that reduces the response time from hours to minutes or second of comparison with the conventional techniques (Kharade *et al.*, 2012; Kappe and Dallinger, 2009; 2004).

By judiciously choosing the solvents, and reactants, the precursors can be selectively heated preferentially with regard to the solvent to produce specific nanostructures. As a result, using MW irradiation as an effective, environmentally friendly, and economically feasible technique in the production of NPs has increased significantly. Even household MW ovens have been used to form NPs, (Murugan *et al.*, 2001; Rogach *et al.*, 2000; Zhu *et al.*, 2000) although the crystallinity and optical properties of the resulting materials appear to be lower in these systems.

2.4 Surface Enhanced Plasmon of Metal Nanoparticles

SPR is an optical phenomenon of metal NPs which produced by light when it interacts with NPs that are smaller than the incident light wavelength (Petryayeva *et al.*, 2011). Metal NPs are more precious than bulk metal, due to, SPR of noble metal NPs and its enhancement of the radiative and non-radiative properties of different

shapes of NPs. The metal materials such as Ag (Luo *et al.*, 2005) and Au (Lapotko *et al.*, 2009) exhibit SPR in the visible range of the wavelength, although, Ag has the strongest and the sharpest of all metals.

2.5 Photothermal Effect of Metal Nanoparticles

The photothermal effect is the phenomenon of the NPs that are illuminated by the optical excitation in the specific wavelength and convert light to heat energy by metal NPs. (Cheng *et al.*, 2011). SPR properties of the metal NPs provide efficient conversion of optical energy into the heat at nanoscale, for the development of new generating nano-devices. In the visible range of spectrum that makes the NPs generate the SPR effect to convert light into heat energy. SPR properties of metal NPs provide efficient conversion of optical energy into thermal one at nanoscale for the development of new generation nano-devices (Lapotko, 2009). The absorption of optical radiation by a sample results in the promotion of an excited state. This photon emission is through nonradiative de-excitation, which also can produce local heating modulated excitation process and induce TW in the sample material. The photothermal effect is especially strong for noble metal NPs such as Ag and Au since they have many mobile electrons and becomes strongly increased when the optical beam hits the collective SPR of a NP. The heat generation process includes not only absorb the incident light, but also thermal conductive from the NP to the base fluid in nanofluid suspension (Govorov & Richardson, 2007).

2.6 Potential of Application of Metal Nanoparticles as Thermal Generator

The photothermal effect of noble metal NPs is especially strong since they have high thermal properties. Recently, the photothermal effect of NPs and their heat generation under optical excitation is also attracting great interest in broad field of research such as optics, electronics, biomedicine, analytical. Metal NPs have great potential for chemical and biological sensor application due to their sensitive spectral and ease for monitoring the light due to their strange scattering and absorption. In biomedical science their strongly resonant light-absorbing and light-scattering properties, of metal NPs can be helpful with contrast agents in the diagnosis of tumors. (Hashimoto *et al.*, 2012) In the photothermal application of heated NPs in nanomedicine, the NPs become attached to tumor cells. Thus heat generated by optically stimulated NPs destroys the tumor cells (Govorov & Richardson, 2007)

Yi-Ting *et al.*, in (2009) developed the annealing process of thin film of gold NPs in the low temperature. They used the heat generation of Au NPs thin film to locally anneal rather than thermal annealing, of the absorption specific wavelength of light and then generate the thermal energy. Owing to SPR, of Au NPs that has a strong optical absorption at 520 nm the Ar laser Continuous laser was irradiated locally to Au NPs thin film (Cheng *et al.*, 2009). They used photothermal effect for fabrication of micro-electric components in low temperature melting and flexible system (Cheng *et al.*, 2009).

Nedyalkov *et al.*, 2011 presented the experimental and theoretical results of the heating process of nanosecond laser pulses on the metal NPs. The ability of the

heating of NPs has been estimated by running experiments on surface modified in a polycarbonate substrate which the particles are deposited. The photothermal effect was also applied in *in-vitro* photothermal therapy of human cancer cells by using the NPs in the range of 40 and 100 nm.

The capability of various metals used in optical fibre-based SPR sensing was studied theoretically by Sharma *et al.*, in 2012. They used four metallic NPs material, Al₂O₃, Cu, Au and Ag and the performance of the optical fibre-based SPR sensor with these different NPs was obtained numerically and was analyzed and compared in terms of sensitivity, signal-to-noise (SNR) ratio and quality parameter. It was concluded that the performance of the optical fibre-based SPR sensor with Au and Ag NPs were better than that of Cu and Al NPs-based SPR sensors.

Ag NPs was used and important in substance of conductive inks, pastes and adhesives for various electronic devices (Park *et al.*, 2008), due to the photothermal effect of Ag NPs in nano-electric technology. Silver nanoparticle embedded in a dielectric matrix was investigated for its potential as broadband absorbing optical detector material by Wei and Eilers in 2009. This contribution is focused on electric properties of Ag NPs at different morphology states. The signal current through thin-films, composed of Ag NPs, was described as a function of the thickness.

Yi-Ting *et al.*, in 2011 reported that, using photothermal effect of Ag NPs can provided different benefits for applications for flexible electronic devices with laser direct patterning of Ag NPs conductive patterns on a polyimide substrate. After laser beam irradiation on the Ag NPs thin film, the Ag NPs aggregate into larger

performing grain and improving the adhesion of Ag NPs and the polyimide material substrate at the same time. By this technique, they have shown a broad Ag NPs conductivity line and soft borders.

The simple developed mechanism of photothermal applications of heated NPs based on the TW generated by modulated laser beam, diffuses away from the nanocrystal and it is transmitted to the detector. The photothermal effect is that the nanoparticle is illuminated by laser-emitting in a specific spectrum, making NPs generate SPR effect to convert optical energy into heat energy. SPR of metal NPs can be useful to increase the heat in thin film, thus, the interaction of lasers with SPR of NPs gives rise to heating of the particle. The most important parameter in this process is the TW generated of metal NPs which becomes especially strong in the SPR at the surface of the NPs.

2.7 Suspension of Nanoparticles (Nanofluids)

Water, ethylene glycol and oil are universally used for transfer heating, but unfortunately these fluids have extremely poor thermal conductivity, smaller and lighter heat exchanges could be reduced leading to reduced power and the size of required heat transfer. As can be seen in Figure 2.1, copper thermal conductivity is about 700 times more than the water and about 3000 times more than the engine oil

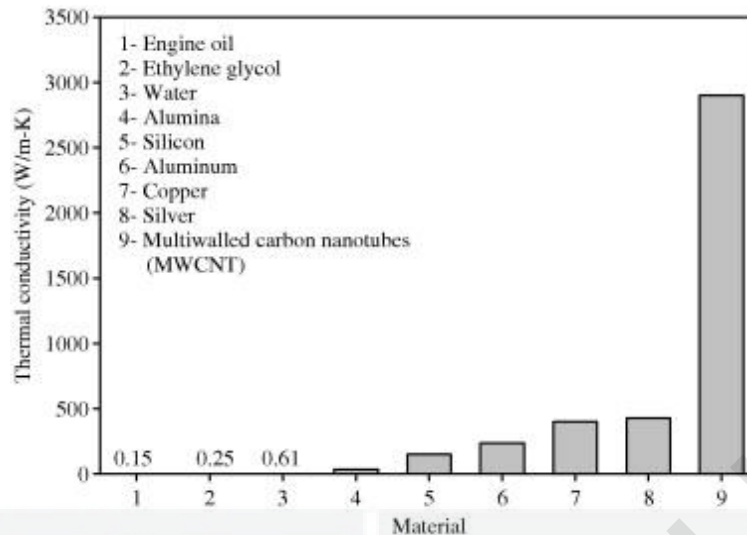


Figure 2.1. Thermal conductivity of the materials (solids and liquids) at room temperature (Murshed *et al.*, 2008)

The study of heat transport in solid-liquid dispersions (colloids) began as early as the 1970's. The major problem of the use of such suspensions is the quick settlement of particles, and increased the NPs agglomeration and size of particles and drop in the fluid. The first thermal conductivity enhancement of NPs appears to have been reported by Masuda et al (1993). NPs also are suited for using in the microsystems due to the size of NPs. They have shown that the thermal conductivity of ultrafine suspension of metal oxides in water increased by up to 30% for the NPs volume fractions of 4.3%. The term “nanofluid” was coined by Choi (1995) when he reported a class of engineered fluids consisting of nano-sized particles dispersed in ethylene glycol which resulted in a thermal conductivity almost a factor of 2 greater than the base fluid.

However, such dispersions of fairly large sized particles and with concentrations in the order of 10% (by volume) are not considered to be very helpful as the thermal conductivity enhancement method. The major drawback of such colloids stems of

the particle size, which tend to pose significant corrosion, erosion, and blockage issues in engineering systems. Furthermore, problems of rheology (e.g. high viscosity requiring high pumping power) and stability (rapidly settling out of the particles) has precluded their extensive use specifically for heat transfer.

The important factors affect in thermal conductivity of nanofluids are the shape, size and dispersion/aggregation state of NPs in base fluids (Evans *et al.*, 2008). The dispersion behavior of suspension is defined by the balance between the attractive and the repulsive forces that particles experience as they approach each other. If the attractive component is dominant over the repulsive one, particles aggregate easily, making the resulting nanofluid unstable. The Van der Waals force is responsible for the coagulation of NPs in the nanofluids (Xie and Chen, 2011).

The distribution of NPs in the nanofluids can improve the thermal conductivity and are stable. Because thermal conductivity takes effect on the NPs surface, it is advisable to using NPs of large surface area. The relatively large surface area of nanoparticle in comparison to micro size particles, provide greatly enhanced thermal conductivity capability.

2.7.1 Potential Applications of Nanofluids as Heat Transfer Fluids

Nanofluids can be used to the wide variety in the industry, medicine applications, in the engineering applications, in cooling/ heating system and in micromechanical system, due to enhance thermal management of the nanofluids. Nanofluids could improve heat transfer and would allow for smaller, pumping, heaters, and other

elements. Magnetic NPs in fluids of body can also be used as means of delivering drugs or radiotherapy and provide new cancer treatment technology. Due to the surface characteristics of NPs are more adhesive to cells of cancer than normal cells (Sha *et al.*, 2011).

2.7.2 Nanofluids thermal properties

Nanofluids contains a low concentration of NPs have much more effective thermal diffusivity values than those of pure fluids. In nanofluids the thermal diffusivity significantly increases with the increasing concentration of NPs. Moreover, it is found that the size and shape of NPs have an effect on the nanofluids thermal diffusivity. The result shows the thermal diffusivity of nanofluids significantly can be increased with increase the volume fraction of NPs. This is mainly due to the thermal conductivity of nanofluids has been found to be significantly greater than the thermal diffusivity of the base fluids and increases with the volume fraction of nanoparticle (Murshed *et al.*, 2005; Eastman *et al.*, 2001; Xie *et al.*, 2002) The results of thermal diffusivity, with using the measured of thermal conductivity and specific heat of nanofluids, and calculated the thermal diffusivity from these result, was reported by Wang *et al.*, in 2004, which it was showed a significant enhancement in the nanofluids thermal diffusivity.

2.7.3 Synthesis and Stability of Nanofluids

Preparation of nanofluids is the important parameter in investigation of the thermal properties of nanofluids. Preparation of nanofluid is not mean of the simple mixture

of liquid and nanopowder. The good dispersion methods of dispersed NPs in liquids or directly producing the stable nanofluids are crucial. Stability of nanofluid is produced by good dispersing NP materials into liquid such as water, ethylene glycol, or oil. There are primarily two methods for the synthesis of nanofluids, that are the two step process and single-step process as a direct synthesis of nanofluids.

The two-step method is achieved by first synthesis of dry NPs to the preferred size and shape. In the second step, these particles are carefully mixed into the required base fluid in the desired volume fraction, typically with some additives for stability of nanofluids. Thus, the small volume fraction of NPs and proper dispersion techniques are important for preparation stability of nanofluids by this technique. Many researchers have had successful in fabricating and testing nanofluids using the two-step preparation method (Wei *et al.*, 2012; Taylor *et al.*, 2011; Chen *et al.*, 2011). Due to the high surface area in NPs, they have the tendency to aggregation. The large degree of agglomeration in nanoparticle may result of using in this method. Thus, proper dispersion techniques, such as ultrasonic dispersion technique (Nguyen *et al.*, 2011; Huang *et al.*, 2008; Sato *et al.*, 2008) or fragmentation process of NPs using laser irradiation (Lapotko 2009; Robinson *et al.*, 2009; Resta *et al.*, 2006; Link *et al.*, 2000; Hodak *et al.*, 2000; Link *et al.*, 1999; Gonella *et al.*, 1996), in low concentration of NPs are important for production stability of nanofluids. Additionally, the other technique to enhance the stability of NPs in fluids is the use of surfactants. In summary, the optimization of thermal characteristics of nanofluids needs the stability of nanofluids, which can be achieved by synthesis and dispersion processes.

To reduce the agglomeration of NPs, several advanced techniques have been developed to produce nanofluids, using the one-step preparation methods (Kumar *et al.*, 2009) and (Zhu *et al.*, 2004). A novel combined synthesis of one step approach which is rapid, simple, and “green” for the synthesis of metallic nanostructures is that through MW irradiation.

2.8 Pyroelectric Detection Technique

During the last two decades, photothermal method has been widely used for determining of thermal parameters of material. This technique typically uses a modulation of the laser beam for induce the TW field in the sample. The obtained TW distribution has been detected by various photothermal methods, such as photoacoustic, photothermal radiometry, or PE detection (Matvienko & Mandelis, 2006).

The PE detection technique was introduced in 1984, as a powerful experimental setup for measurement of thermal properties of materials in high resolution (Coufal *et al.*, 1984; Mandelis *et al.*, 1984). In fact, the advantage of PE sensors makes them suitable for many applications such as, sensitive in a wide temperature range without the need of cooling, low power requirements, fast response and generally, low cost materials. The PE method can be applied to the high-resolution thermal characterization of sample, by measurement of the amplitude and phase lag of the TW signal as a function of distance (cavity length scan) or frequency scan. The first PE technical device designed for measuring TW propagation for fluid samples (liquid or gas), termed as the thermal-wave cavity TWC, was introduced in 1995. In

this technique, a modulation of the laser impinging on the thin metallic foil has been used as a TW generator. The TW generated in thin film then propagates through the intracavity medium and detected by a PE sensor, usually PVDF on the opposite side.

The thermal parameter directly resulting from the PE experiment is usually the “fundamental” ones: the thermal diffusivity and also the thermal effusivity. It is very clear that four thermal parameters can be connected by two relationships, $\alpha = k/C$ and $(e = k/\sqrt{\alpha})$, where, C , α , k , and e , the volume specific heat, the thermal diffusivity, conductivity, and effusivity, respectively. Concerning the PE detection configurations, two of them, “back” and “front” respectively, have been mainly applied for calorimetric purposes. In principle by using both of Back-PE and Front-PE configurations, source of information (amplitude PE signal and phase of PE signal), cavity scanning or frequency scanning, is possible to obtain both the thermal diffusivity and thermal effusivity.

2.8.1 Back-Pyroelectric Technique

In the Back-PE technique, named thermal TWC technique, a very thin metal film was illuminated by a modulated laser beam was illuminated and the PE cell was consisted of these two parallel walls; one the metallic foil as a TW generator and another the PE film as a PE signal detector which was placed parallel to the TW generator surface at a fixed cavity length as a function of frequency in frequency scanning, and at given frequency as a function of cavity length in cavity scanning, respectively. This various modifications in TWC technique can be increased the accuracy and the precise thermal properties measurements. This experimental device

has allowed the measurement of thermal properties of gas, (Shen & Mandelis, 1995) and liquid and liquid mixtures (Chirtoc *et al.*, 2001). This expression is typically based on the general theory of PE detection (Mandelis *et al.*, 1993) and has a range of changes based on the cavity length of the cavity of PE cell.

Almost, the theory of treatment takes relatively simple 1-D thermal wave field approaches (Mandelis & Zver, 1985) of the plane TW theory describing the detected signal. Although this assumption greatly simplified model, a 1-D approach might not be enough to describe the experimental results, if the Gaussian laser beam, w , is small enough in comparison to the diameter of the cavity diameter, or the thermal diffusion length is small compared to the cavity length.

The TW field of the PE technique can be tackled through two approaches: a mathematically computationally simple, conventional, 1-D approach and a 3-D approach, which was calculated in 2006 by Matvienko and Mandelis. This calculation shows the dimensionality of the field of TW in the cavity scanning depending on the lateral thermal boundary conditions and the relationship between the size of the laser beam illuminating on the metal film and the metal diameter itself as the TW generator in PE cell.

The first attempt to design the TWC technique to resolve the dimension of problem have been done by Azmi *et al.*, (2008) and termed as the “optical fiber - thermal-wave cavity (OF-TWC) technique”. In that study, the metalized optical fiber has been used as a light transfer and also as a TW generator for measuring thermal diffusivity of a small volume of liquid samples by using cavity length scanning. Attention was

given to the boundary condition in order to calculate the theory of 3-D signal in cylindrical coordinates. The other advantage of this simplification is the arrangement of the TW generator - PE detector, which did not necessarily need to be in a vertical position as the optical beam always guided through and illuminates the optical fiber metallized surface.

2.8.2 Front-Pyroelectric Technique

A Front-PE technique is the modification of the classical configuration of PE technique. In this technique, the TW is introduced to the rear of the PE detection (Chirtoc *et al.*, 2001). For the front detection configuration, two schemes were proposed, namely the configuration with thermally thin PVDF sensor and the optically opaque sensor (Dadarlat *et al.*, 1993), and the configuration with thermally thick and optically semi-transparent sensor using LiTaO₃ (Longuemart *et al.*, 2002). Concerning the front configuration, a simplified method to measure both of the thermal diffusivity and thermal effusivity (also called heat penetration coefficient) of sensor was proposed (Longuemart *et al.*, 2003). These thermal parameters were obtained from the TW amplitude and phase of thermal wave PE signal generated by the PE detection. However, this configuration presents some technical disadvantages as the very thick sensors (usually LiTaO₃) has to be coated with gold and this would allow only a fraction of the light energy to be absorbed. In this very thick sensor, typically 300 (Dadartat *et al.*, 1995) or 500.micron (Dadarlat *et al.*, 2009), one has to use a very low chopping frequency facility.

Balderas-Lopez *et al.*, (2003), applied the Front-PE configuration to perform high

precision measurements of thermal effusivity in transparent liquids in a very thermally thick regime. The overall methodology was based on the asymptotic behavior of the normalized PE signal, as a function of the modulation frequency, when the modulated beam impinges on the PE surface by crossing the liquid sample. A constant value for that normalized signal, which depends on the thermal effusivity of the liquid in question, was obtained for each case normalized by signal without liquid sample.

2.9 Application of Thermal wave Interferometry in Pyroelectric Technique

The photothermal methods are mainly based upon detection of fluctuation in temperature in the sample due to nonradiative de-excitation processes of the absorption of laser beam modulation. One of these techniques that called TW interferometry is based on the interference of TWs, which, first described by Bennett and Patty in 1982. This possibility was later demonstrated by Shen and Mandelis (Shen & Mandelis, 1995; Shen *et al.*, 1997) who succeeded in showing the feasibility of the PE sensor for TWs propagating across an air sample which is between PE sensor and the TW generator of the PE cell. The thermal diffusivity of air with very high accuracy was obtained by using PE sensor as the TW detection.

Esquef *et al.*, in 2006 developed a method consisting essentially in combining a photoacoustic cell and a PE cell enclosed in a single compact gas analyzer for the measuring of the thermal diffusivity and thermal effusivity. In this work applying the TW interferometry technique, they presented a combination two well established photothermal techniques for the measuring of the thermal diffusivity and thermal

effusivity of gas samples. The photoacoustic cell was used to measure thermal effusivity and PE cell for measurement of thermal diffusivity.

Streza *et al.*, in 2009 applied two PE detection configurations, “back” and “front,” to calorimetric studies of the some liquids (liquid mixtures, magnetic material nanofluids, liquid foodstuffs, etc). The report demonstrated that, if the back configuration using phase of PE signal in cavity scan method and in the front configuration using frequency scan, both thermal diffusivity and thermal effusivity could be measured.

2.10 Thermal Properties of Nanofluids Using Other Method

Thermal conductivity is the intrinsic property of nanofluids that has motivated the most number of research articles (Kebinski *et al.*, 2008; Trisaksri & Wongwises 2007). Much of the early work used a traditional 'hot-wire' method (THW) for measuring thermal conductivity and derived the thermal diffusivity from this measured value (Watanabe *et al.*, 1996). In this method a wire is heated and the fluid temperature is measured on the wire and usually at various distances away. By knowing the wire geometry, heat input, temperatures, time, and distances the following equation can be used to find the thermal conductivity regardless, the steady-state technique (Wang & Mandelis, 1999), temperature oscillation technique (Bhattacharya *et al.*, 2006) and the 3ω -wire method (Yang *et al.*, 2006), were used to investigate the thermal conductivity of nanofluids, however, the accuracy of the THW is more than these methods.

In practical application, this requires the achievement of a high precision measuring an absolute temperature increase in order to establish the thermal properties. However, in THW method, there are some technical difficulties to keep a homogeneous initial temperature of the samples in a rather long vessel.

In 2006 a new double THW method was developed for measuring the nanofluids thermal diffusivity by Murshed. (Murshed *et al.*, 2006) They prepared several types of nanofluids, TiO₂, Al and Al₂O₃ NPs in water, engine oil and ethylene glycol suspensions in different volume fraction (1–5%). The thermal diffusivity of nanofluid which was measured by hot-wire method was increased substantially with the increased NPs volume fraction in the base fluid and the resulted thermal diffusivity shows that it was more significantly than the calculated from the thermal diffusivity expression ($\alpha = k/(\rho c_p)$) by using the obtained thermal conductivity and volume specific heat of the convention hot-wire technique.

CHAPTER 3

THEORY AND BACKGROUND

3.1 Detection of Thermal-Wave

During the last two decades, the PE technique has attracted great attention, and become a useful analyzes and widely used to determine the thermal properties of materials in many aspects of science and technology. In overall, PE measurement is based on using a PE sensor to detect the amplitude and phase of the PE signal caused by a modulated laser beam to induce TW (periodic heating) of a 1-D layered sample-transducer assembly.

The first PE configuration is the Back-PE technique, which is designed to measure thermal properties of gases and liquids materials, called the thermal-wave cavity (TWC), and introduced by Shen and Mandelis in (1995). In this method, a modulated laser impinging on a thin metallic film (Balderas-Lopez *et al.*, 2002; Kwan *et al.*, 2007) or silver conductive paint (Azmi *et al.*, 2008) has been used as a TW generator and the induced TW is then propagated through the intracavity medium onto a PE sensor (usually polyvinilidene fluoride film, PVDF) at the opposing side. The TW is converted by PVDF into a voltage signal that can be measured. A modification in the method is the Front-PE technique (Dadarlat *et al.*, 2009; 2007). In this method, the TW is introduced to the back side of the PE sensor. This configuration has been widely used to measure thermal effusivity of gases and liquids (Kwan *et al.*, 2007).

To the best of our knowledge, these applications of the TWC measurement techniques are all adopted on a 1-D model of the plane TW theory describing the detected signal. Although this hypothesis greatly simplify the theory model, a 1-D approach may not be enough to explain the experimental results, if the spot size w of the Gaussian laser beam is sufficiently small compared to the cavity diameter, or the cavity length is large compared to the thermal diffusion length(Kwan *et al.*, 2007). The attempt to redesign the TWC technique in resolving the dimension issue was carried by Azmi *et al.* (2008) and was termed as the optical fiber – thermal wave cavity (OF-TWC) technique. Here, the metalized optical fiber was used as light transfer as well as TW generator of TWC was studied by using cavity length scanning. Attention was given to the boundary conditions of the calculations of the theoretical 3-D signal in cylindrical coordinates that developed by Matvienko and Mandelis in 2006.

3.2 Three-Dimensional Thermal-Wave Field

The approximation for cylindrical geometries applies in the case of fiber free end was shown in Figure 3.1. The 3-D Gaussian laser beam is transmitted through the inlet of single core polymer fiber (of spot size w) and is converted into TW at the other metalized end, while, the diameter of source was smaller than the conventional technique of using metal foil.

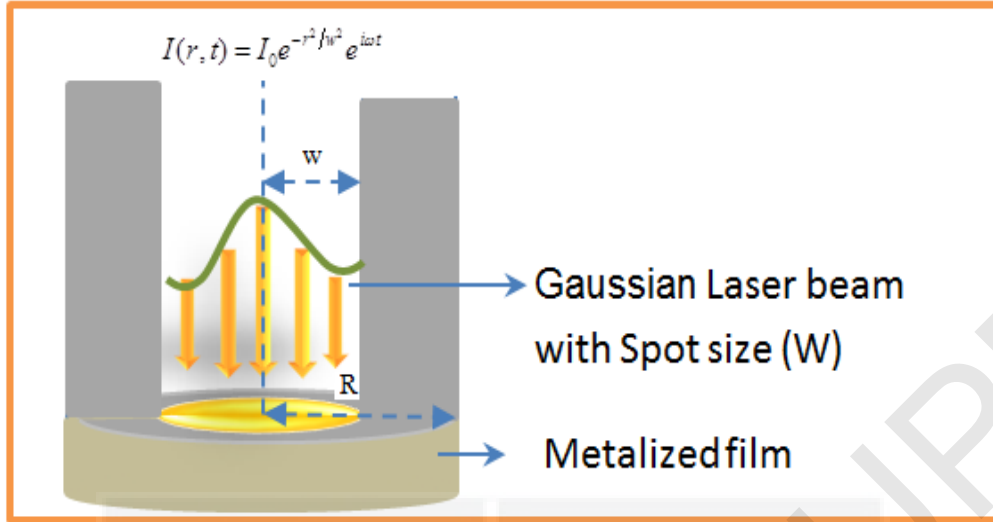


Figure .3.1 Schematic diagram of Optical Fiber- TWC, Gaussian laser beam is transmitted through the inlet of single core polymer fiber (of spot size w) and is converted into TW at the other metalized end

The detailed solution of 3-D thermal-wave field with appropriate boundary conditions for the cavity filled with a liquid sample can be found in the previous study (Azmi *et al.*, 2008). The simplified resulting TW field, can be written as (Matvienko & Mandelis, 2006).

$$T_l(r, z; \omega) = \frac{I_0}{2k_l R^2} \sum_{n=1}^{\infty} \frac{J_0[a_n(r/R)] F_n(R, w) (1 + \gamma_{sl}) \left\{ \exp(-\xi_n z) + \gamma_{lp} \exp[-\xi_n (2L_l - z)] \right\}}{\left\{ \xi_n \left[1 + (Bi/a_n)^2 \right] J_0^2(a_n) \left[1 - \gamma_{sl} \gamma_{lp} \exp(-\xi_n 2L_l) \right] \right\}} \quad (3.1)$$

Here, the following definitions are used:

$$a_n J_1(a_n) - \left(\frac{hR}{k_s} \right) J_0(a_n) = 0 \quad a_n = \lambda R \quad (3.2)$$

where,

$$\xi_n^2 = \frac{a_n^2}{R^2} + i \frac{\omega}{\alpha}, \quad b_{ij} = \frac{k_i \xi_i}{k_i \xi_j}, \quad \gamma_{ij} = \frac{1 - b_{ij}}{1 + b_{ij}}, \quad F_n(R, w) = \int_0^R \exp\left(-\frac{r_0^2}{w^2}\right) J_0\left(a_n \frac{r_0}{R}\right) r_0 dr_0 \quad (3.3)$$

where $Bi = hR/k_s$ (Biot number is the ratio of product of sample surface R and surface heat transfer coefficient h to thermal conductivity k_s), and w is the laser beam spot size, considering that for thermally thick condition where $|\exp(-\xi_n^2 2L_s)| \sim 0$, the temperature field at the liquid-solid interface, can be written as,

$$T_l(r, z; \omega) = C \sum_{n=1}^{\infty} \frac{J_0[a_n(r/R)] F_n(R, w)}{\left\{ \xi_n \left[1 + (Bi/a_n)^2 \right] J_0^2(a_n) \right\}} \exp(-\xi_n z) \quad (3.4)$$

Here, the coefficient C contains the instrumental transfer function and is independent of the samples thickness (Balderas-Lopez *et al.*, 2002). The comparison between 1-D and 3-D calculation revealed the influence of two main parameters that may give rise to the 3-dimensionality of the problem, namely w and Bi (Matvienko & Mandelis, 2006).

In this work, by using high thermal conductivity of silver foil ($k = 430$ W/m K), the heat transfer coefficient of the circumferential boundary of the Ag and water, between 200 and 600 W/m² K, and small TW generator radius $R = 1$ mm, the Biot number, $Bi=0$.

3.2.1 The Comparison of Temperature Filed In 1-D and 3-D

Figure 3.2 shows the plot of temperature field in 3-D and 1-D, with respect to scanning radial distance of cavity at different thickness, z , from 0 to 0.02 cm using laser spot size $w=0.05$ cm and TW generator radii, $R= 0.15$ cm It can be seen that the temperature filed in 1-D does not depend on the TW generator radius, on the other hand, in 3-D, the value of temperature filed is close to its value of 1-D as long as the TW generator in the vicinity of size of laser spot size, however, it is reduced and the signal is very noisy at the edge of the TW generator.

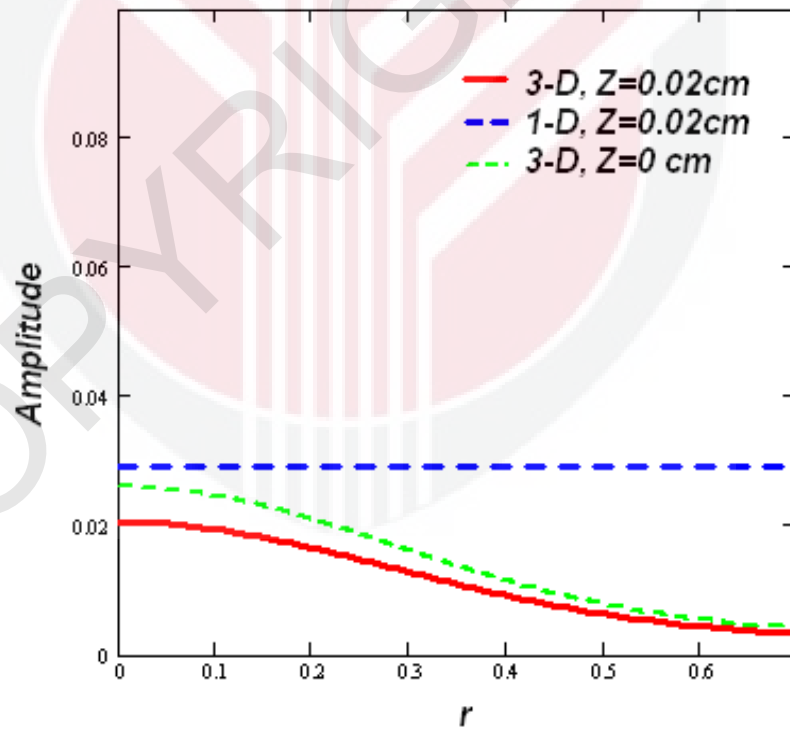


Figure 3.2. The plot of temperature field in 3-D and 1-D, with respect to scanning distance radius in water at different thickness, z , from 0 to 0.02 cm using laser spot size $w=0.05$ cm and TW generator radii, $R= 0.15$ cm

In order to use one-dimensional TWC theory for accurate thermal properties fits, one must ensure that the influence on the TW the distribution of lateral (radial) heat transfer through the cavity boundary is properly accounted for, and the beam size of the laser is large enough, in order to keep the TW field within the 1-D theory, thus significantly simplify and strengthen the quantitative importance of TWC technique. (Matvienko & Mandelis, 2006).

3.3 Application of Thermal Wave Interferometry for PE System in 1-D

One of the most important benefits to apply TW interferometry model in the analysis of PE signal is that the propagating TW can be modeled directly in a different kind of thermal condition and geometry, such as in the multilayer samples as well as for the backward-and forward- propagating TW in the spatial region of the multilayer case.

In this session, the TW field of the 1-D approach of the PE signal of the multilayer sample by using TW interferometry approach, which was first proposed by Bennett and Patty (1982), is first derived. Then monitoring of Back- and Front- PE configurations as the special cases correspond to different cell structures is analyzed.

3.3.1 Pyroelectric Effect in Multilayer Sample

The fundamental principle of TW interferometry is to illuminate a metallic opaque film with a modulated laser beam, in order to generate a plane TW in 1-D approach, the laser beam size have to be large enough. Here it is assumed that:

- This technique requires thermally thick and optically opaque of the solid sample layer, which absorbs a large fraction of the light modulation at its front side, thus generate TWs through the sample and the PE sensor, which located in good thermal contact with the sample's back side, detects the fraction of the heat flow variations that has diffused through the sample (Menon *et al.*, 2009).
- The diameter of the laser beam needs to be much larger than the thermal diffusion length of sample (Shen & Mandelis, 1995).
- The TW generator (copper, aluminum or silver) is perfectly flat and it could provide a 1-D plane TW.

The light source is assumed to be a modulated monochromatic laser beam incident on the solid sample with flux $I = I_0(1 + \cos \omega t) / 2$ where, I_0 is the source intensity, ω is the modulated angular frequency of the incident light. When a plane TW approaches the interface between two media, it is partially reflected back and refracted beyond (Lima *at el.*, 2001), some of parameters used in the derivation are: thermal diffusion length $\mu_i = \sqrt{\alpha_i / \pi f}$ and thermal diffusion coefficient $a_i = 1 / \mu_i$. T_{jk} and R_{jk} are TW transmission coefficient and TW reflection coefficient, respectively, at (j - k) interface, defined as

$$T_{jk} = \frac{2}{1 + b_{jk}}; \quad R_{jk} = \frac{1 - b_{jk}}{1 + b_{jk}}; \quad b_{jk} = \left(\frac{k_k}{k_j} \right) \left(\frac{\alpha_j}{\alpha_k} \right)^{1/2} \quad (3.5)$$

As shown in Figure 3.3 the sample is composed of N layers with indices 1 through N . The indices of the solid (TW generator) and detector are 0 and $N+1$, which also take the subscripts p and s , respectively. Layer i , with the rear and front interface located at l_{i-1} and l_i , has a thickness of $L_i = l_i - l_{i-1}$, where $i=0, 1, \dots, N$.

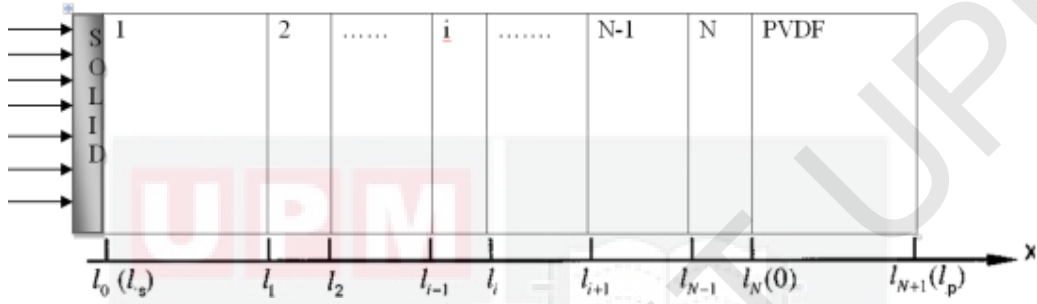


Figure 3.3. The cross section of multilayer sample

The first TW filed at solid-1th layer is, $\theta_0 = I_0/2k\sigma$, where, k is thermal conductivity of the material and σ is the complex TW diffusion coefficient $\sigma_j = (1+i)/\mu_j$. The TW filed at the interface $x=l_0$ was reflected in the solid thermally thin sample, and transmissions at $x=l_0$ in to the 1th layer. This TW filed consists of two parts transmitted, $\theta_0 e^{-\sigma_s L_s} T_{s1}$, and the reflected, $\theta_0 e^{-\sigma_s L_s} R_{s1}$. This transmissions at $x=l_0$, $\theta_{s \rightarrow 1} = T_{s1} \theta_0 e^{-\sigma_s L_s}$, consists of two parts transmitted to the next layer and the multiple reflected in to the 1th layer, at $x=l_1$ TW interference can be occurring between this reflected and transmitted, so the TW field at this surface is,

$$\theta_{s \rightarrow 1} e^{-\sigma_1 L_1}, \theta_{s \rightarrow 1} e^{-\sigma_1 L_1} (R_{s1} R_{12} e^{-2\sigma_1 L_1}), \theta_{s \rightarrow 1} e^{-\sigma_1 L_1} (R_{s1} R_{12} e^{-2\sigma_1 L_1})^2, \dots$$

$$\theta_{1 \rightarrow 2} = \theta_{s \rightarrow 1} e^{-\sigma_1 L_1} \sum_{n=0}^{\infty} (R_{s1} R_{12} e^{-2\sigma_1 L_1})^n$$

$$\theta_{1 \rightarrow 2} = \theta_{s \rightarrow 1} \frac{e^{-\sigma_1 L_1}}{1 - R_{s1} R_{12} e^{-2\sigma_1 L_1}} \quad (3.6)$$

In order to calculate the TW of the resultant reflected and transmitted of TW at the surface of PE detector (at the interface $x=0$). Since $\theta_{N \rightarrow P}$ is the surface temperature of the PE (the boundary of sample N and PE detector), is divided by two parts, partially reflected, in previous sample and partially transmitted, there will be many partially transmitted and reflected TWs. Figure 3.4 shows, the schematic geometry of the surface $N-1$, N and P , respectively, of the multilayer samples

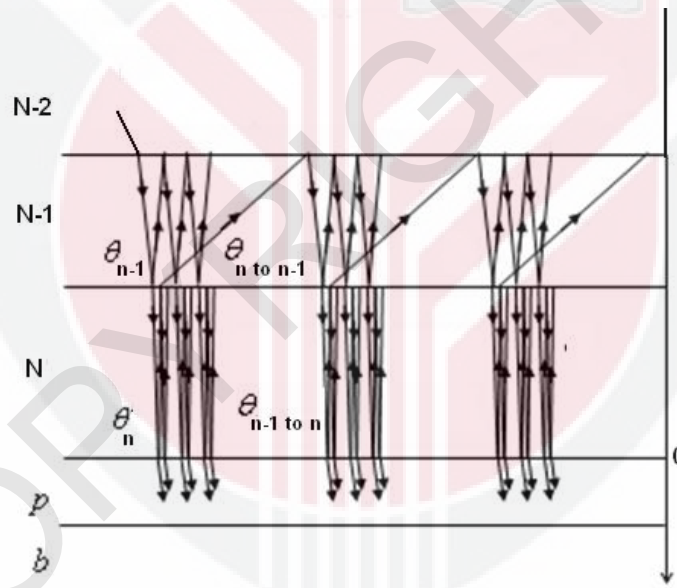


Figure 3.4. Schematic geometry of the surface $N-1$, N and P , respectively (Azmi et al., 2006), of the multilayer samples

The first term of the surface temperature of the PE at the interface $x=0$, that is transferred from the previous layer, (from the $N-1$ to N) called θ_{N_1} , the resultant

transmittance and reflected in series and the summation of all the partial reflections leads to the following expression

$$\theta_{N_1} = \theta_{N-1 \rightarrow N} e^{-\sigma_N l_N} \sum_{n=0}^{\infty} \left(R_{(N-1)N} R_{NP} e^{-2\sigma_N l_N} \right)^n$$

$$\theta_{N_1} = \theta_{N-1 \rightarrow N} \frac{e^{-\sigma_N l_N}}{1 - R_{(N-1)N} R_{NP} e^{-2\sigma_N l_N}} \quad (3.6)$$

where, $\theta_{N-1 \rightarrow N}$ is the TW of at the boundary of sample N and sample $N-1$, R_{NP} and $R_{(N-1)N}$ are the TW reflection coefficient The values of these coefficients can be obtained from the definitions of the Equation 3.5.

As shown in Figure 3.4, in the second term of the surface temperature of the PE sensor, partially of TW which was transmitted from $N-1$ to N reflected back at the interface between $N-1$ and N and partially of it then transmitted again at the interface $x=0$ From $N-1$ to N , etc.

For the partial of TW which reflected back at the interface between $N-1$ and N , the contribution was,

$$\theta_{N_1} e^{-\sigma_N l_N} T_{N(N-1)} R_{NP} \cdot \theta_{N_1} e^{-\sigma_N l_N} T_{N(N-1)} R_{NP} (R_{(N-1)N} R_{NP} e^{-2\sigma_N l_N}) \cdot \theta_{N_1} e^{-\sigma_N l_N} T_{N(N-1)} R_{NP} (R_{(N-1)N} R_{NP} e^{-2\sigma_N l_N})^2 \dots$$

$$\theta_{N_1} e^{-\sigma_N l_N} T_{N(N-1)} R_{NP} \sum_{n=0}^{\infty} \left(R_{(N-1)N} R_{NP} e^{-2\sigma_N l_N} \right)^n$$

$$\theta_{N \Rightarrow N-1} = \theta_{N1} \frac{e^{-\sigma_N l_N} T_{N(N-1)} R_{NP}}{1 - R_{(N-1)N} R_{NP} e^{-2\sigma_N l_N}} \quad (3.7a)$$

This transmitted waves, that is will undergo multiple reflections in the $N-1^{th}$ layer and transmission at $x=L_{N-1}$,

$$\theta_{N \Rightarrow N-1} \frac{R_{(N-2)(N-1)} T_{(N-1)N} e^{-2\sigma_{(N-1)l(N-1)}} e^{-\sigma_N l_N}}{1 - R_{(N-2)(N-1)} R_{(N-1)N} e^{-2\sigma_{(N-1)l(N-1)}}} \quad (3.7b)$$

The surface TW was obtained by summing all the TW arriving at the boundary of sample N and PE detector, at the interface $x=0$, so the previous two Equations (3.7a) and (3.7b) can be combined to generate it can be written as,

$$\theta_{N_2} = \theta_{N_1} \frac{R_{(N-2)(N-1)} R_{NP} T_{(N-1)N} T_{N(N-1)} e^{-2\sigma_{(N-1)l(N-1)}} e^{-2\sigma_N l_N}}{(1 - R_{(N-1)N} R_{NP} e^{-2\sigma_N l_N}) (1 - R_{(N-2)(N-1)} R_{(N-1)N} e^{-2\sigma_{(N-1)l(N-1)}})} \quad (3.8)$$

The series of TWs at PE surface is: $\theta_N = \frac{\theta_{N_1}}{1 - \theta_{N_2}}$ It can be obtained for another layer

also and after some calculation, the TW of PVDF interface can be written as,

$$\theta_N = \theta_{N_1} \theta_{N_2} + \theta_{N_1} \theta_{N_2}^2 + \theta_{N_1} \theta_{N_2}^3 + \dots$$

$$\theta_N = \frac{\theta_o T_{s1} \dots T_{(N-1)N} T_{Np}}{e^{-(\sigma_1 L_1 + \dots + \sigma_{(N-1)} L_{(N-1)} + \sigma_N L_N)}} \bigg/ 2k_1 \sigma_1 \left\{ \left[\left(1 - R_{12} R_{13} e^{-2\sigma_1 L_1} \right) \dots \left(1 - R_{(N-1)N} R_{(N-1)(N-2)} e^{-2\sigma_{(N-1)} L_{(N-1)}} \right) \left(1 - R_{Np} R_{N(N-1)} e^{-2\sigma_N L_N} \right) \right] \right\} \quad (3.9)$$

In this result there are many transmitted waves which come from this side of PVDF interface. However, the TWs are very weaker in intensity after a successive transmitted and reflected (Azmi *et al.*, 2006).

3.3.2 Temperature Distribution in PVDF Film in Multilayer Samples

After travelling through a distance L_p in PVDF film the wave will be partially transmitted into substrate and partially reflected into PVDF (Figure 3.5). The temperature distribution in PVDF film is divided into two parts (Mandelis *et al.*, 1993);

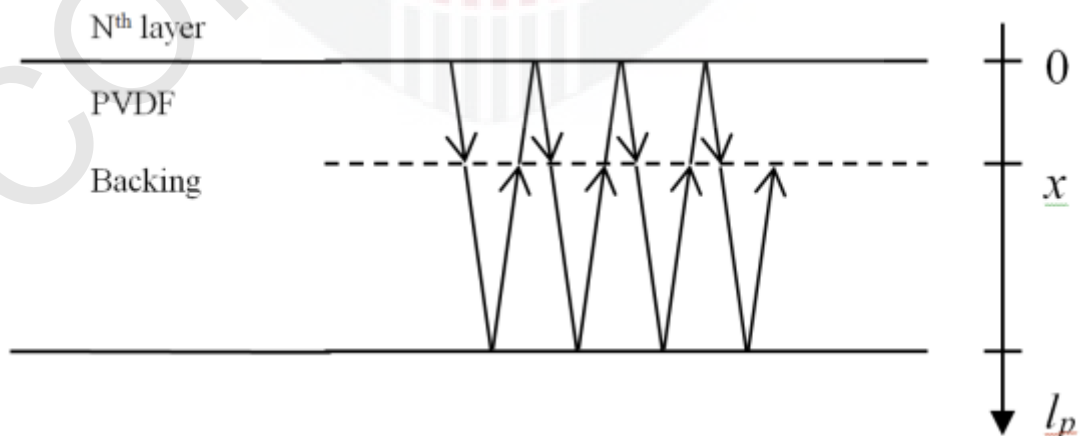


Figure 3.5. TW after travelling through a distance L_p in PVDF film partially transmitted into substrate and partially reflected into PVDF

Temperature distribution in PVDF film, from the PVDF film -backing interface the contribution is

$$\theta_{p-b}(f, x) = R_{pb} e^{-\sigma_p(2l_p - x)} \left(1 + R_{PN} R_{pb} e^{-2\sigma_p l_p} + (R_{PN} R_{pb} e^{-2\sigma_p l_p})^2 + \dots \right)$$

$$\theta_{p-b}(f, x) = \frac{R_{pb} e^{(-2\sigma_p l_p + \sigma_p x)}}{(1 - R_{pb} R_{PN} e^{-2\sigma_p l_p})} \quad (3.10)$$

Temperature distribution in PVDF film, from the PVDF film- N^{th} layer interface the contribution is $\theta_{p-N}(f, x) = e^{-\sigma_p x} \left(1 + R_{pb} R_{PN} e^{-2l_p \sigma_p} + (R_{pb} R_{PN} e^{-2l_p \sigma_p})^2 + \dots \right)$

$$\theta_{p-N}(f, x) = \frac{e^{-\sigma_p x}}{(1 - R_{pb} R_{PN} e^{-2\sigma_p l_p})} \quad (3.11)$$

Summing up the two contributions, consider infinite TW reflections in the PVDF film, can be written as

$$\theta_{p(Nb)}(f, x) = \theta_N \frac{T_{NP} \left(e^{-\sigma_p x} + R_{pb} e^{(-2\sigma_p l_p + \sigma_p x)} \right)}{(1 - R_{pb} R_{PN} e^{-2\sigma_p l_p})} \quad (3.12)$$

The average temperature field in the bulk of the detector is given by

$$\langle \theta_p(\omega, x) \rangle = \frac{1}{l_p} \int_0^{l_p} \theta_p dx \quad (3.13)$$

If P is the PE coefficient, l_p is the thickness of the PVDF detector, ε is the dielectric constant of the PE detector, ε_0 is the permittivity constant of vacuum. The average PE voltage is given by,

$$V(f, l) = \frac{P}{\varepsilon \varepsilon_0} \langle \theta_p \rangle$$

$$V(f, l) = P / \varepsilon \varepsilon_0 \left\langle \frac{\theta_N T_{NP} (1 - e^{-\sigma_p l_p}) (1 + R_{pb} e^{-\sigma_p l_p})}{(1 - R_{pb} R_{PN} e^{-2\sigma_p l_p})} \right\rangle \quad (3.14)$$

$$V(f, l) = \left\{ \frac{PT_{s1} \dots T_{(N-1)N} T_{Np}}{2k \sigma \varepsilon \varepsilon_0 \sigma_p} \left[\frac{\theta_p (1 - e^{-\sigma_p l_p})}{(1 + R_{pb} e^{-\sigma_p l_p})} \right] \right\} \left\{ \frac{(1 - R_{pb} R_{PN} e^{-2\sigma_p l_p})}{\left[\begin{array}{l} (1 - R_{12} R_{1s} e^{-2\sigma_1 l_1}) \dots \\ \dots (1 - R_{(N-1)N} R_{(N-1)(N-2)} e^{-2\sigma_{(N-1)l_{(N-1)}}}) \\ (1 - R_{Np} R_{N(N-1)} e^{-2\sigma_N l_N}) \end{array} \right]} \right\} e^{-2(\sigma_1 l_1 + \dots + \sigma_{(N-1)l_{(N-1)}} + \sigma_N l_N)} \quad (3.15)$$

In the case of PE thermally thick, $e^{-2\sigma_p l_p} \approx 0$, the average PE voltage is reduced to,

$$V(f, l) = C \times \left\{ \frac{\left(1 - e^{-\sigma_p l_p}\right) \left(1 + R_{pb} e^{-\sigma_p l_p}\right) e^{-(\sigma_1 L_1 + \dots + \sigma_{(N-1)} L_{(N-1)} + \sigma_N L_N)}}{\left[\left(1 - R_{12} R_{1s} e^{-2\sigma_1 L_1}\right) \dots \left(1 - R_{(N-1)N} R_{(N-1)(N-2)} e^{-2\sigma_{(N-1)} L_{(N-1)}}\right) \right] - \left[\left(1 - R_{Np} R_{N(N-1)} e^{-2\sigma_N L_N}\right) \right]} \left\{ R_{s1} T_{s1} R_{12} T_{1s} \dots R_{(N-1)N} T_{(N-1)N} R_{Np} T_{N(N-1)} e^{-2(\sigma_1 L_1 + \dots + \sigma_{(N-1)} L_{(N-1)} + \sigma_N L_N)} \right\} \quad (3.16)$$

where C is the constant values of the Equation 3.16. For the samples in thermally thick condition, $e^{-2\sigma_i l_i} \approx 0$ the Equation 3.16 can be written more simply as

$$V(f, l) = C \times \left(1 - e^{-\sigma_p l_p}\right) \left(1 + R_{pb} e^{-\sigma_p l_p}\right) e^{-(\sigma_1 L_1 + \dots + \sigma_{(N-1)} L_{(N-1)} + \sigma_N L_N)} \quad (3.17a)$$

The reliability of the general expression of PE signal for N-layered sample was investigated by reducing it to a one or two layered sample. The Equation 3.16 can be reduce for two-layer configuration that was between the TW generator and PE sensor

$$V(f, l) = C \times \frac{e^{-(\sigma_1 L_1 + \sigma_2 L_2)} \left(1 + R_{pb} e^{-\sigma_p l_p}\right)}{\left[\left(1 - R_{12} R_{1s} e^{-2\sigma_1 L_1}\right) \left(1 - R_{2p} R_{21} e^{-2\sigma_2 L_2}\right) - R_{12} T_{12} R_{2p} T_{21} e^{-2(\sigma_1 L_1 + \sigma_2 L_2)} \right]} \quad (3.17b)$$

This approach (Equation 3.17(b)) was successfully adopted and applied by the authors using PE technique to measure thermal properties of sample, (Azmi *et al.*, 2005). However:

- At high modulated frequency, the induced TWs have a short thermal wavelength and they are subjected to a large attenuation, do not reach another samples, and cannot in any way interfere in the cavity. The interference phenomenon becomes negligible.

- At low modulated frequency, the TWs induced on the first sample have a long thermal wavelength, thus, these long waves are subjected to a weak attenuation, but are able to reach the another sample

Reducing this Equation 3.17 to Back and Front PE configuration can be investigated as special limiting cases.

3.4 Monitoring of Back and Front Configuration as Special Cases

The theoretical special cases corresponding to different PE cell structures are analyzed in Back-PE and Front-PE configurations. The proposed technique is based on the concept of a TW interferometer.

3.4.1 Back-PE Configuration (TWC Technique) Theory

Four layers considered in the formulation of the 1-D model was presented in Figure 3.6, which contains of the sample (s), medium (m), PE detector (p) and the backing (b). The sample (s) converts the modulated laser beam into TWs. The induced TWs then transmit through the intracavity medium (m) by TW transmission and the reflection mechanism is detected by the PE sensor (p). The backing (b) is considered semi-infinite as it is thermally very thick.

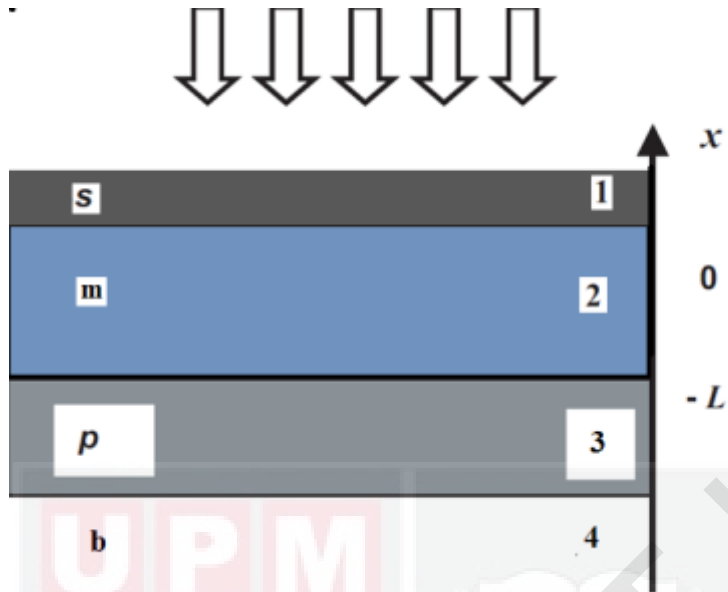


Figure 3.6. 1-D geometry of the TWC, (back-PE), for a cell structure (s/m/p/b)

The first transmitted and the reflected TW in the PE cell is shown in Figure 3.7, the temperature at the s-m surface was obtained from the first transmitted $T_A = \theta_0 e^{-\sigma_s L_s} T_{sm}$ and the reflected $R_A = \theta_0 e^{-\sigma_s L_s} R_{sm}$ wave in A,

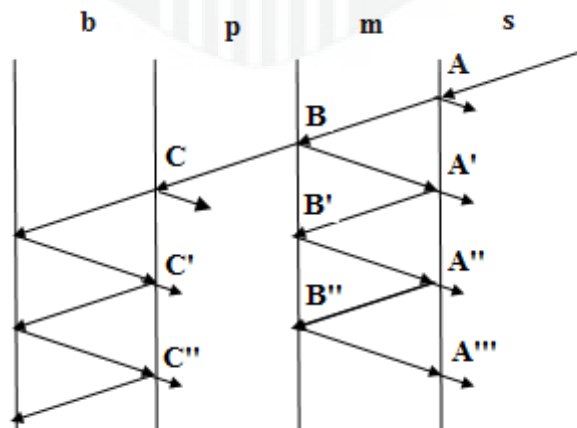


Figure 3.7. The first transmitted and the reflected TW in the PE cell

The temperature at the m - p surface was obtained by summing all the TWs arriving at this surface, Figure 3.7 shows the resultant waves, B, B', B'', \dots , from the right side of PVDF sensor,

$$\mathbf{B}: \begin{cases} T_B = T_A e^{-\sigma_m L_m} T_{mp} \\ R_B = T_A e^{-\sigma_m L_m} R_{mp} \end{cases} \quad (3.18a)$$

$$\mathbf{B}': \begin{cases} T_{B'} = T_A e^{-3\sigma_m L_m} T_{mp} R_{ms} R_{mp} \\ R_{B'} = T_A e^{-3\sigma_m L_m} R_{mp}^2 R_{ms} \end{cases} \quad (3.18b)$$

$$\mathbf{B}'': \begin{cases} T_{B''} = T_A e^{-5\sigma_m L_m} T_{mp} R_{ms}^2 R_{mp}^2 \\ R_{B''} = T_A e^{-5\sigma_m L_m} R_{mp}^3 R_{ms}^2 \end{cases} \quad (3.18c)$$

Thus the transmitted waves at the m - p surface, B, B', B'', \dots , give the series of transmitted terms to the PVDF film from the right

$$\theta_{pr} = \theta_0 e^{-\sigma_s L_s} T_{sm} T_{mp} \frac{e^{-\sigma_m L_m}}{1 - R_{ms} R_{mp} e^{-2\sigma_m L_m}} \quad (3.19)$$

Figure 3.7 shows the resultant waves, C, C', C'' from the left side of PVDF sensor, (3.20a)

$$\mathbf{C}: \begin{cases} T_C = T_A e^{-\sigma_m L_m} T_{mp} e^{-\sigma_p L_p} T_{pb} \\ R_C = T_A e^{-\sigma_m L_m} T_{mp} e^{-\sigma_p L_p} R_{pb} \end{cases}$$

$$\mathbf{C}': \begin{cases} T_{C'} = T_A e^{-\sigma_m L_m} T_{mp} T_{pb} e^{-2\sigma_b L_b} R_b T_{pb} \\ R_{C'} = T_A e^{-\sigma_m L_m} T_{mp} T_{pb} e^{-2\sigma_b L_b} R_b R_{pb} \end{cases} \quad (3.20b)$$

The total waves in the left side are the multiple transmission waves, C , C' , C'', from the left hand:

$$\theta_{pl} = \theta_0 e^{-\sigma_s L_s} e^{-\sigma_p L_p} T_{sm} T_{mp} \frac{e^{-\sigma_m L_m}}{1 - R_{ms} R_{mp} e^{-2\sigma_m L_m}} \left[R_{pb} + \frac{T_{bp} R_{bp} R_b e^{-2\sigma_b L_b}}{1 - R_{pb} R_b e^{-2\sigma_b L_b}} \right] \quad (3.21)$$

The average temperature field in the bulk of the detector is given by

$$\langle \theta_p(\omega, x) \rangle = \frac{1}{l_p} \int_0^{l_p} \theta_p dx$$

If P is the PE coefficient, l_p is the thickness of the PVDF

detector, ε is the dielectric constant of the PE detector, ε_0 is the permittivity constant

of vacuum. The average PE voltage is given by $V(f, l) = \frac{P}{\varepsilon \varepsilon_0} \langle \theta_p \rangle$

$$V(f, L_m) = \frac{P \theta_0 (1 - e^{-\sigma_p L_p}) (1 + R_{pb} e^{-\sigma_p L_p})}{\varepsilon \varepsilon_0 \sigma_p (1 - R_{pb} R_{pm} e^{-2\sigma_p L_p})} \times \frac{T_1 e^{-\sigma_m L_m}}{(1 - R_{ms} R_{mp} e^{-2\sigma_m L_m})}$$

$$V(f, L_m) = \underbrace{\frac{P \theta_0 T_1 (1 - e^{-\sigma_p L_p}) (1 + R_{pb} e^{-\sigma_p L_p})}{\varepsilon \varepsilon_0 \sigma_p (1 - R_{pb} R_{pm} e^{-2\sigma_p L_p})}}_{\text{Constant}} \times \frac{e^{-\sigma_m L_m}}{(1 - R_{ms} R_{mp} e^{-2\sigma_m L_m})} \quad (3.22)$$

If the chopping frequency is fixed and a single wavelength of excitation source is used the Equation 3.22 is reduced to

$$V(f, L_m) = C \times \frac{e^{-\sigma_m L_m}}{(1 - R_{ms} R_{mp} e^{-2\sigma_m L_m})} \quad (3.23)$$

In thermally thick condition $|e^{-2\sigma_l}| \ll 1$ and Equation 3.23 can be written more simply as (Balderas-Lopez *et al.*, 2000). The amplitude and the phase, respectively, are,

$$V(f, L) = \text{Constant}(f) e^{-\sigma L} \quad (3.24)$$

$$|V(f, L)| = \text{constant}(f) \times e^{-L/\mu} \quad (3.24a)$$

$$\phi(f, L) = \text{constant}(f) - L/\mu \quad (3.24b)$$

where, $\sigma_j = (1+i)/\mu_j$ is TW diffusion coefficient $\mu = (\alpha/\pi f)^{1/2}$ is the thermal diffusion length at frequency f and α is the thermal diffusivity of liquid sample. The thermal diffusivity of sample can be obtained by the slope liner fitting from the plot In amplitude and phase vs both cavity length (from the cavity scan) and frequency square (from the frequency scan).

The real (in-phase) and imaginary (quadrature) parts of Equation 3.24, as well as its amplitude and phase, are functions of the frequency or cavity length. The thermal diffusivity derived from the fit to the theory (Lima *et al.*, 2000).

$$\text{Re}[V(f, L)] = IP = A(\omega) e^{-a_l l} \cos(a_l l) \quad (3.25a)$$

$$V(L, \alpha, \omega) = A(\omega) e^{-aL} \longrightarrow$$

$$\text{Im}[V(f, L)] = A(\omega) e^{-a_l l} \sin(a_l l) \quad (3.25b)$$

3.4.2 Front-PE configuration

Usually, the Front-PE configuration can be obtained as shown in Figure 3.8, in the absence of the sample (s) and medium (m) $L_m=0$ or replaced by gas, and subscript (s) sample replaces to (b) backing. Then the cell structure (g/p/s) becomes another variant of PE technique, that is, the Front-PE configuration, the sensor directly is irradiated and the sample in contact with its rear surface (Delenclos et al., 2002).

Figure 3.8 shows the Front-PE configuration,

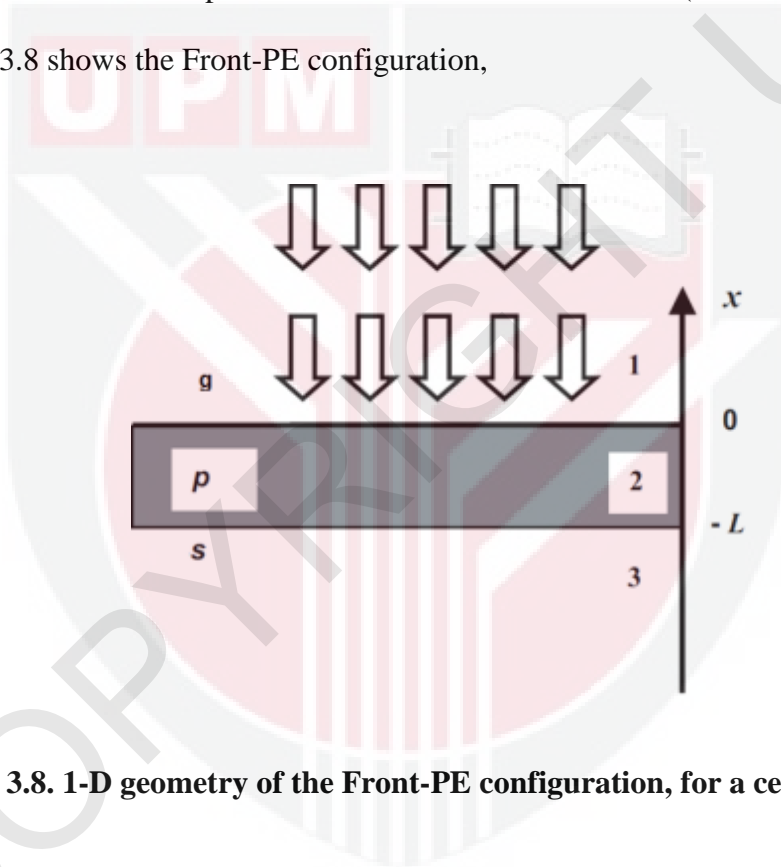


Figure 3.8. 1-D geometry of the Front-PE configuration, for a cell structure (g/p/s)

Under this assumption: Then, for a cell structure (g/p/s) Equation 3-22 simplifies to,

$$V(f, l) = V_s \frac{(1 - e^{-\sigma_p l_p})(1 - R_{ps} e^{-\sigma_p l_p})}{(1 - R_{ps} R_{pg} e^{-2\sigma_p l_p})} \quad (3.26)$$

where, $V_s(f) = P/\epsilon\epsilon_o \langle \theta_s \rangle$ with thermally thick sensor and sample, the signal

defined by,

$$V(f) = V_s \left[1 - (1 + R_{sp}) e^{-\sigma_p L_p} \right] \quad (3.27)$$

$$R_{sp} = (e_s - e_p) / (e_s + e_p) \quad (3.28)$$

where, e_s and e_p are the thermal effusivity of sample and PE sensor, respectively.

The normalizing signal is determined (by using air), the normalized signal becomes,

$$V_n(f) = 1 - (1 + R_{sp}) e^{-\sigma_p L_p} \quad (3.29)$$

The normalized phase of the signal defined by

$$\theta = \arctan \left[\frac{A e^{-L_p/\mu_p} \sin(L_p/\mu_p)}{1 - A e^{-L_p/\mu_p} \cos(L_p/\mu_p)} \right] \quad (3.30)$$

where $A = 1 + R_{sp}$, A the constant can be obtained by optimizing the fit performed on the experimental data with the normalized signal phase by using Equation 3.30. The amplitude of the signal is given by

$$|V_n(f)| = \left\{ \left[A \sin(L_p/\mu_p) e^{-L_p/\mu_p} \right]^2 + \left[1 - A \cos(L_p/\mu_p) e^{-L_p/\mu_p} \right]^2 \right\}^{1/2} \quad (3.31)$$

It can be shown that from the amplitude and phase of the normalized signal one can obtain the thermal effusivity of the liquid sample.

3.4.2.1 Combined Amplitude and Phase of PE Signal

The proposed method using combined amplitude and phase information, at a given frequency, lead to the same result. An alternative simplification of the Front-PE configuration is able to obtain information about all four thermal properties of PE sensor also can be used to measure the thermal effusivity of sample (Sahraoui *et al.*, 2003). From the amplitude and phase of the normalized signal at a single frequency, one can get the thermal diffusivity α_p and the thermal effusivity e_p (or e_s), to consider the quantity $1-V_n$ (Sahraoui *et al.*, 2003):

$$1-V_n(f) = (1+R_{sp})e^{-\sigma_p L_p} = Ae^{-i\phi} \quad (3.32)$$

Where,

$$A = (1+R_{sp})e^{-\alpha_p L_p} \quad \phi = \alpha_p L_p \quad (3.33)$$

A and ϕ are obtained from the normalized amplitude and phase of the PE signal V_n :

$$|A| = (|V_n|^2 + 1 - 2|V_n|\cos\theta)^{0.5} \quad (3.34)$$

$$\phi = \arctan\left(\frac{|V_n|\sin\theta}{1-|V_n|\cos\theta}\right) \quad (3.35)$$

Then, we obtain α_p and R_{sp}

$$R_{sp} = \frac{A}{e^{-\phi}} - 1 \quad \alpha_p = \pi f (L_p / \phi)^2 \quad (3.36a-b)$$

Thus by combining amplitude and phase of the PE signal, one can get both the thermal diffusivity and thermal effusivity of the PE sensor and thermal effusivity of sample from Equation 3.36 (a-b).

3.4.3 Thermal Effusivity of the Amplitude in Thermally Very Thick Regime

This type of Front-PE configuration can be obtained in the absence of the metal solid sample (s) and replaced by liquid sample as shown in Figure 3.6, and subscript (s) sample, replaces (m) medium. Then, a cell structure (s/p/g) becomes another variant of PE technique, front-PE configuration that is the sensor directly is irradiated and the sample is in contact with its rear surface (Figure 3.9). The upper surface of PVDF is painted, it is considered thermally thick and optically opaque.

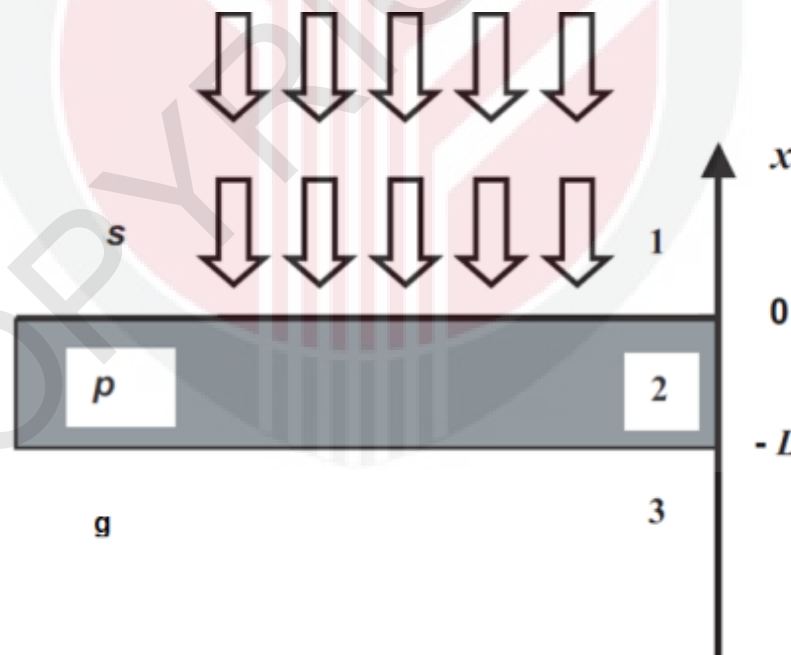


Figure 3.9. 1-D geometry of the Front-PE configuration, for a cell structure (s/p/g)

For the purpose of the Front-PE configuration to consider simplification of the situation where the detection cell is consisting of a sensor situated on a substrate, and the medium in front of the sensor is a transparent material (s) (Sahraoui *et al.*, 2003), as is shown in Figure .3.9

$$V(f) = \frac{V_0}{(b_{sp} + 1)} \frac{1 + R_{gp} e^{-2\sigma_p L_p} - (1 + R_{gp}) e^{-\sigma_p L_p}}{1 - R_{gp} R_{sp} e^{-2\sigma_p L_p}} \quad (3.37)$$

where V_0 is a factor depending on the PE coefficient of the sensor, The symbols s , p , and g refer to the front medium, PE sensor, and air, respectively. The latter is obtained from Equation 3.37 by considering water instead of front medium:

$$V_0(f) = \frac{V_0}{(b_{wp} + 1)} \frac{1 + R_{gp} e^{-2\sigma_p L_p} - (1 + R_{gp}) e^{-\sigma_p L_p}}{1 - R_{gp} R_{wp} e^{-2\sigma_p L_p}} \quad (3.38)$$

From the experimental point of view, the use of a liquid sample as a reference to normalize the signal that is with a known small thermal diffusivity value is needed to ensure its thermally thick behavior starts from the small frequency such as nanofluid sample. In this manner, any change of the normalized PE signal can be associated with the PE behavior of the sample, the thermal effusivity of which is to be measured (Balderas-Lopez *et al.*, 2002).

It is possible to determine the thermal eiffusivity of liquids by using of Equations 3.37 and 3.38. In particular, the normalize PE signal of nanofluids with the

corresponding signal from the water as a reference sample, a new PE method involves the linear simple fit to measure the thermal effusivity of the nanofluid is possible. The normalized signal,

$$V_n(f) = \frac{(b_{wp} + 1) 1 + R_{gp} e^{-2\sigma_p L_p} - (1 + R_{gp}) e^{-\sigma_p L_p}}{(b_{sp} + 1) 1 + R_{gp} e^{-2\sigma_p L_p} - (1 + R_{gp}) e^{-\sigma_p L_p}} \quad (3.39)$$

Equation 3.38 is still too complex to provide the practical PE measurement method of the thermal effusivity of material. However, a considerable simplification is achieved if the frequency is large enough so the substrate and front medium are thermally too thick. Through this, proceedings, the common proportionality factor and the instrument transmission function, are removed and this simple relationship is achieved:

$$N(f) = \frac{V_w}{V_n} = \frac{1 + e_n/e_p}{1 + e_w/e_p} \quad (3.40)$$

$$e_n = N(e_w + e_p) - e_p \quad (3.41)$$

where e_w and e_n are the thermal effusivity of the water and nanofluid under study, respectively. The thermal effusivity for a liquid can be found, once the asymptotic value N is known, from the Equation 3.40 and 3.41.

CHAPTER 4

METHODOLOGY

4.1 Introduction

In this chapter, the methods and materials that were used for the fabrication and characterization of metal and metal oxide NPs is presented. The detail of the experimental set up that was used to measure thermal diffusivity and thermal effusivity of nanoparticle is discussed. The detail of new design using Ag NPs-coated optical fiber to act as TW generator to develop OF-TWC method and enhancement of the PE signal is also discussed.

4.2 Green Synthesis of Ag Nanoparticles by using Microwave Irradiation

The monodispersed formations of Ag nanofluids was prepared by MW irradiation containing Ag NPs suspended in different base fluids to search for the Ag NPs which gives high increase of heat transfer. The MW irradiation technique was chosen because it is an efficient, more environmentally friendly, and economically viable technique to produce the NPs materials (Jia *et al.*, 2012) in large quantity. It is also very simple, rapid and clean to use and a possible route for the viable avenue for the greening of the synthesis of nano materials (Mohamed, *et al.* 2010; Bilecka *et al.*, 2009; Zhu *et al.*, 2000).

4.2.1 Synthesis of Ag NPs/ DW or Ag NPs/EG Nanofluid

MW irradiation was employed to synthesize water-based nanofluids, with polyvinyl pyrrolidone (PVP) as a surfactant in most reactions. This surfactant was widely used as an effective passivation agent in the fabrication of Ag NPs (Luo *et al.*, 2005). The characterizations on formation of Ag NPs suspensions were studied as a function of MW irradiation times. In order to make the comparison between MW and conventional heating, at the same apparent temperature, the same procedure was performed in the conventional heating. Silver nitrate (Merck, Darmstadt, Germany) 99.98%, 4.35 g/cm^3) was used as the source of silver NPs and PVP (MW-29000, K25, 1.2 g/cm^3 , Aldrich Chemistry) was used as a stabilizer for the Ag NPs fabrication. In the typical process, 0.3 g of AgNO_3 and 0.3 g of PVP were dispersed separately in 25 ml of DW (or EG) and was stirred for 15 minutes and then they were added together. This resulting solution was stirred for 10 minutes and allowed to cool down at room temperature in a 60 mL Pyrex glass cylinder container.

A series of Ag nanofluids were prepared in a MW oven (Panasonic, 1100W, 2.45 GHz, NN-K574MF, multi-mode) in various irradiation times. For the times, 20, 40, 60 and 90 s, the samples were quoted, for water as solvent as W1, W2, W3 and W4, and for ethylene-glycol as solvent as EG1, EG2, EG3 and EG4, respectively, with an intermittent pause every of 20 s to cool the reaction vessel. The sample temperature was controlled to about 60°C to prevent solvent intense boiling as well as aggregation of Ag NPs. After the irradiation the sample was allowed to cool at room temperature.

For the conventional technique, a portion of similar concentration of AgNO_3 and PVP in water was heated on a hot plate from room temperature to 60°C for 20 min. This was applied in order to give similar amount of heat energy input as MW heating but at slower heating rate. After heating, the mixture was allowed to cool at room temperature. The maximum output power of existing MW oven is 680 W, which is 61.8% of nominal value of 1100 W.

4.2.2 Comparison between Microwave and Conventional Heating

In order to make the comparison between MW heating and conventional heating more effective and more comparable; the synthesis conditions were kept as similar as possible, at the same apparent temperature. For thermal conventional heating, a 0.3 g AgNO_3 and 0.3 g PVP were each dissolved separately in 25 ml of water and stirring were continued for 15 min and then added together. The resultant solution was stirred for 10 min, after cooling to room temperature. The solution was heated on a hot plate and the temperature was found to reach 60°C from room temperature in 20 min, and the MW oven could reach 60°C in 20 s.

4.2.3 Ag NPs in Olive Oil

In order to search for thermal properties of Ag NPs in different base fluids, MW irradiation was employed to synthesize oil-based nanofluids. An amount of 0.3 g AgNO_3 was dissolved in 50 ml of olive oil, and was stirred for 20 min, then placed in a MW oven (Panasonic, NN-K574MF, 1100 W, 2450 MHz) for 10 s to reach 60°C . Then the mixture was cooled to room temperature.

4.3 Ag-NPs in Clay Suspension by Chemical Method

One of the successful methods to prevent agglomeration of NPs is by preparing it in clay matrices. In this method NPs are placed within the interlamellar space of clay and on its outer surfaces (Huang *et al.*, 2008; Patakfalvi *et al.*, 2003).

The Ag/Clay nanofluids were prepared in 0.1, 0.2, 0.5% vol of Ag NPs by adding constant amounts of clay (MMT, Kunipia-F, Japan), in various volumes of 1×10^{-3} M AgNO_3 and stirred for 24 h at room temperature. NaBH_4 (4×10^{-2} M) solution was then added to the AgNO_3 in order to make a constant molar ratio of 1:4 of $\text{AgNO}_3/\text{NaBH}_4$ and was stirred for 1 h. The suspension was finally centrifuged and washed with double-distilled water and dried under vacuum overnight. Because Ag/clay suspension has more free Ag ions, and NaBH_4 , it needs to be washed and then dried at room temperature to release these excess material. These powders were suspended again in water and dispersed with ultrasonicator. The ultrasound was used for between 0.5 h to ensure proper mixing of Ag NPs into the base fluids.

4.4 Preparation of Metal Oxide Nanofluids

In this section, nanofluids are prepared by dispersing pre-synthesized NPs into fluids, and if necessary, an appropriate amount of surfactants was added to keep NPs stable in the fluids. For the purpose of synthesizing stable nanofluids consisting of certain NPs and a given fluid, methods for NPs production, dispersion and fragmentation and size reduction of NPs have been developed.

Nanofluids were prepared using alumina and copper oxide particles dispersed in various base fluid, water, ethylene glycol and olive oil. Sources are listed in Table 4.1 together with the crystal phase and average particle size reported by the manufacturer.

Table 4.1. Sources of nano-powders and their properties provided by the manufacturer

Nanoparticle	Supplier	Average Particle (nm)
γ - Al_2O_3	Nanostructured and Amorphous Materials, Inc	11
CuO	ALDRICH	50
Stabilizer	Supplier	Purity
PVP	Aldrich Chemistry	(K25, MW-29000)
Solvent		
Deionized Water		
Ethylene glycol		
Olive oil	Monini, Spoleto-Italian	

To make a desired percentage volume concentration of NPs in nanofluids, the weights of deionized water and NPs were measured by an electric balance (Ohaus Adventurer Balances). For example, 3.97g of Al_2O_3 NPs, which is 1 ml based on the density provided by the vendor, were added to the 99g (99 ml) of deionized water (DW) to make 1 % volume concentration of Al_2O_3 /DW nanofluids.

4.5 Methods of Stability of Nanofluids, Dispersion/Aggregation State

In particular, NPs with different surface structure and surface interaction have much stronger aggregated tendency from the particles with micron size (Hidehiro *et al.*,

2010). Therefore, the methods for stability of nanofluids are necessary steps for particle validation. The following sections first, the different methods for particle separation and homogeneous nanofluids were proposed. Physical dispersion of powders in the liquid can be achieved by ultrasonic irradiation to achieve a homogeneous nanofluid with small size particles. Ultrasonication is universally employed to assist the dispersion and stabilization of nanofluids. However, currently there is no standard procedure for the sonication process.

4.5.1 Ultrasonication Dispersion Process

Physical dispersion of powders in the liquid can be achieved by ultrasonic irradiation, either in a bath, or direct irradiation by probe sonication method. Probe sonication has been studied to determine its effect on the particle characteristic such as the average agglomerate size and the surface charging (Richard *et al.*, 2008) The probe sonication is expected to move higher power to the suspension than the ultrasonic bath due to the directly probe immersion to the suspension. The bottles containing nanofluid are placed in the ultrasonic bath which was full of water.

The influence of the main parameter of ultrasonication such as irradiation types (probe and bath) to dispersion and reduced size was observed in the suspension of Al_2O_3 in low concentration suspensions in water. Al_2O_3 NPs (99%, 11 nm, Nanostructured and Amorphous Materials, Inc.) 0.5 wt% were dissolved in deionized water and magnetically stirred vigorously until a clear solution was obtained in about 1 h. The suspension is sonicated for 30 min using ultrasonic probe (VCX 500, 25

kHz, 500 W), called sample P, or bath ultrasonic (POWERSONIC, UB-405, 40 KHz, 350 W), called sample B, respectively.

As energy is transferred into the liquid, the liquid is heated and the cooling system to control temperature between 35 and 40°C is needed. This temperature is favourable to produce a large cavity field that greatly accelerates the integration of NPs in fluids. Unlike the bath sonication that was performed at room temperature, the tip probe sonication has higher amplitudes and more effective creation of cavitation and heating. In the case of the ultrasonic probe, the nanoparticle/ water mixture was placed in another larger container filled with ice cubes. This was to prevent evaporation of fluids caused by elevated temperature. It was found the most appropriate power and condition and is applied by probe ultrasonic to achieve the highest dispersion and long term stability.

4.5.2 Laser Fragmentation Process

In the study, for the first time to our knowledge, the characteristics of colloidal Al₂O₃ or CuO NPs, in terms of morphology, size and size distribution and also the behavior of thermal diffusivity of nanofluids under cw laser irradiated are presented. The nanofluids were prepared by dispersing of metal oxide NPs Powder (0.5 g) Al₂O₃ (11 nm, Nanostructured and Amorphous Materials, Inc) or CuO (50 nm, Nanostructured and Amorphous Materials, Inc) into 25 ml DW, 1vol% PVP was added to help stabilize the nanofluids. The samples were then subjected to ultrasonic processing to obtain uniform dispersions, under the ultrasonic frequency of 25 kHz using a probe ultrasonic.

The solutions were allowed to stir and irradiated along its vertical axis with a cw laser (532 nm diode pumped solid state laser (DPSS), maximum power 0.2W). This 10 Hz modulated laser was focused on around the 0.12 cm diameter of the solution surface in the quartz cuvette by a lens of 20 cm focal length (Figure 4.1.). Magnetic stirrer was used again to promote particle and to ensure homogeneous particle distribution. The process was repeated for 20 min and 90 min.

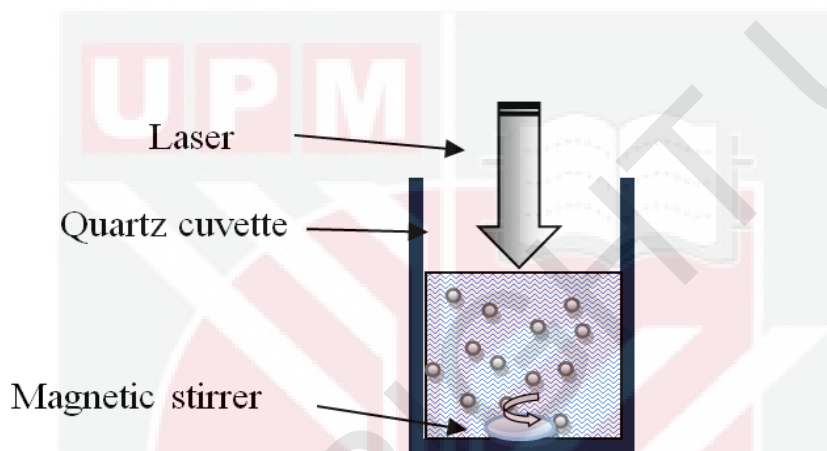


Figure 4.1. Schematic diagram of the process of laser fragmentation of nanofluids

The results of the laser fragmentation process were analyzed by transmission electron microscope (TEM, H-7100, Hitachi, Tokyo, Japan), the average colloidal NPs were estimated from the Nanophox Analyser (Sympatec GmbH, D-38678) and an average was taken from at least four measurements and optical absorption spectrum of the solution containing the NPs was investigated. The thermal diffusivity of each nanofluid was measured by OF-TWC technique in cavity scanning because it is rapid, robust, and was used successfully to thermal diffusivity measurement of nanofluids. Principle and detail of the technique measurement can be found elsewhere.

4.6 Sample Characterizations

Various techniques have been applied to analyze the chemical and physical properties of prepared nanofluids. Size, shape, and composition of these particles are of interest. The structure of the Ag-NPs was studied using powder X-ray diffraction (PXRD, Philips, X'pert, Cu K α). The morphologies of the deposits were studied using a (Hitachi, Tokyo, Japan), S-4700 field emission scanning electron microscope (FE-SEM), operating at 5.0 kV. We also determined the size, distribution and the morphology of the synthesized NPs via TEM (H-7100, Hitachi, Tokyo, Japan), and the particle size distributions were determined using UTHSCSA Image Tool software (version 3.00; UTHSCSA Dental Diagnostic Science, San Antonio, TX). In the characterization of prepared nanofluids, the particle size and size distribution of spherical NPs in colloidal form were measured by Nanophox Particle Size Analyzer (Sympatec GmbH System-Particle-Technik). This equipment is based on the principle of Dynamic Light Scattering, which provides mean particle size as well as particle size distribution. The Surface Plasmon or absorption maximum in the colloidal solution spectrum provides information on the particles average size, and the UV-Vis Spectrophotometer (Shimadzu-UV1650PC) was used. All the measurements of absorption spectra were carried out at room temperature for wavelength range 200-800 nm.

4.7 Pyroelectric Methods Experimental Set Up

The systematic experiments were to investigate the accuracy of thermal diffusivity and effusivity by the PE method in Back-PE and Front-PE configurations as special

case of the different structures of PE cell. The basic design of the analytical instrument consists of only a laser, a TW generator and a PVDF PE detector. Thermal diffusivity and thermal effusivity of nanofluids were obtained with designs of both Back- and Front-PE configurations which are;

- The Back-PE configuration, called Optical Fiber-TWC, which is an extremely attractive technique, was used to measure thermal diffusivity due to its requirement for only small liquid volume sample. The advantage of this technique is the small limited volume together with a short measurement time, thus, the concentration of nanofluid remains constant during the measurement process.
- In the Front-PE configuration, the metalized PVDF sensor in thermally thick regime for sensor and sample was used to measure thermal effusivity of sensor, a few liquid samples and nanofluids.
- In the Front- PE configuration in thermally very thick regime, when the modulated beam impinges on the PE surface and TW crossing the sample, the thermal effusivity of nanofluids was obtained.

4.7.1 Back- PE Configuration (Optical Fiber - TWC Set-up) and Experimental Conditions

Figure 4.2 shows the PE signal generation chamber or cell in the Back-PE configuration. A cell consists of two parallel walls: one wall is a metal foil exposed

to a modulated laser beam, acting as the TW generator, the other wall is a PE film in parallel with the TW generator surface at a fixed distance, generate an electrical signal proportion of the detected TWs transmitted through the intracavity (Matvienko & Mandelis 2008).

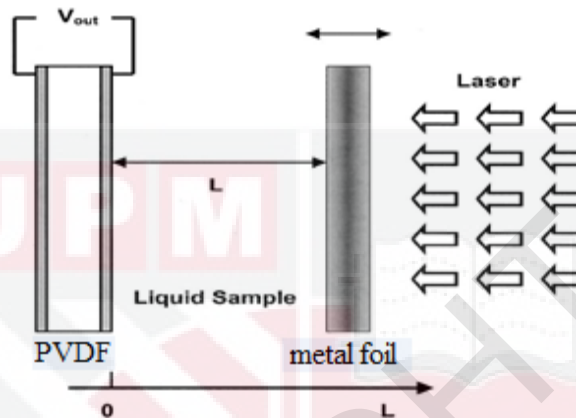


Figure 4.2. PE signal generation chamber in the Back-PE technique

In the Back-PE configuration, a newly developed optical fiber- TW resonant cavity (OF-TWC) sensor using a metalized optical fiber as both light-transmitting conductor and support of TW generator, was used as a powerful method for measuring thermal diffusivity of nanofluids. The advantage of the technique is that in the small limited volume together with a short measurement time, the concentration of nanofluid remains constant in the measurement process. Schematic diagram of the experimental set up is shown in Figure 4.3. In the present set-up, a 200 mW CW DPSS laser (MGL 150(10)) was modulated by an optical chopper (SR540). The beam then fixed onto an inlet of 2.25 mm of single core polymer fiber (RS 368-047, 1 mm core). The fiber consisted of a denser core surrounded by a cladding layer, as can be seen in Figure 4.3. In this case the laser beam was transferred through 1 mm diameter single core of optical fiber with minimum loss in transmission. Indeed,

moreover, for an optical beam of large diameter compared to thermal diffusion length of sample, the temperature field can be represented by 1-D model (Matvienko and Mandelis , 2006).

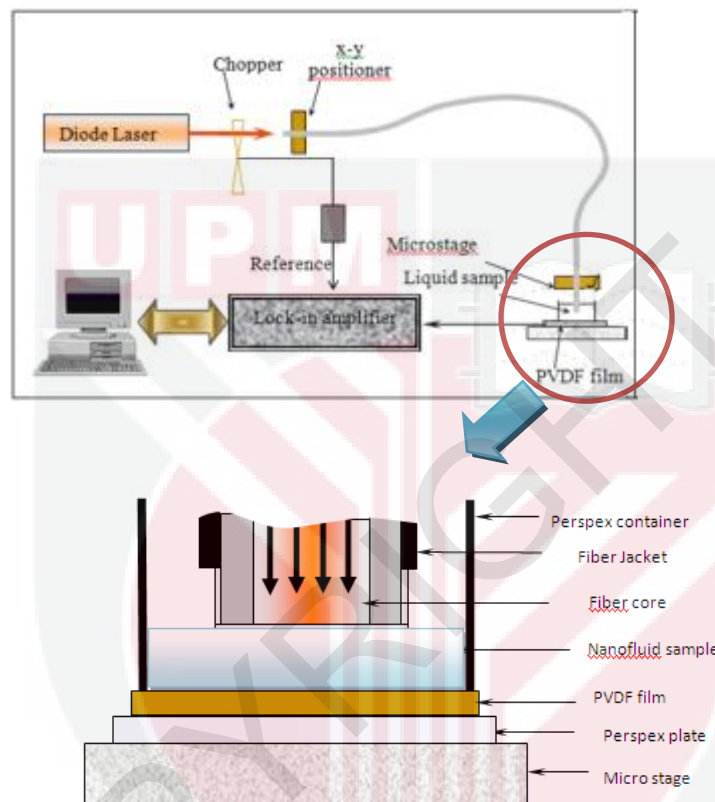


Figure 4.3. (a) Schematic diagram of OF-TWC technique and (b) the optical fiber and PE cell

In this study, the core polymer fiber diameter was bigger than the highest water thermal diffusion length, 0.08 mm, which can be achieved from 6.8 Hz, and was the lowest frequency used in this work. The modulated laser beam was channelled through one fiber tip entry to the other tip end to illuminate the inner side of the silver metalized layer coated to it. Before coating with silver conductive paint the

end surface was coated with a very thin matt black paint and polished to a reasonable flatness, typically less than 10 micron, to act as an efficient light-to-heat converter. The silver paint layer was totally thermally thin, due to the high conductivity and to very small thickness, hence the phase lag changes only slightly between the two faces of silver layer. The silver paint also was coated to the side of the fiber of about 3 cm from the tip upward to prevent the light from escaping the fiber end side that would introduce noise to the detecting signal. To avoid any possible and significant different in heat intensity, the optical fiber end is held in a fixed position. In the cell, the initiated TW propagate across the fluid and reach the PE transducer, which consisted of a 52 μm PVDF film (MSI DT1-028K/L). Since PVDF film was very flexible and any wrap of film and can caused a change of signal, it was fixed with silicon glue to Perspex substrate. On its top side, a plastic ring of 1 cm diameter was glued to it to act as sample container. The small volume liquid sample, less than 0.1 cm^3 , was simply filled in the inner side of the ring, with the sample depth or thickness of around 1 mm.

The PE signal generated by PVDF detector was analyzed by using a lock-in amplifier (SR 530) to produce PE amplitude and phase. To avoid vibrations and possible contributions of the PVDF sensor, its bottom rear face was attached to a Perspex container. The electromagnetic noise was reduced by eliminating all the ground loops via proper grounding. The experiment was done for both the cavity scan and frequency scan.

4.7.1.1 Tip of Fiber Optic Condition

During the design process it was noted that the end of the fiber after removing the jacket of fiber optic, the thickness of silver paint and its arrangement parallel to the PVDF film was very important and could affect the output signal substantially. Figure 4.4 presents the microscopic image of end of fiber after removing the jacket, the clean removal and the intensity of laser beam transferred from the end of fiber and the damaged fiber after removing the jacket thus reducing the intensity of the laser.

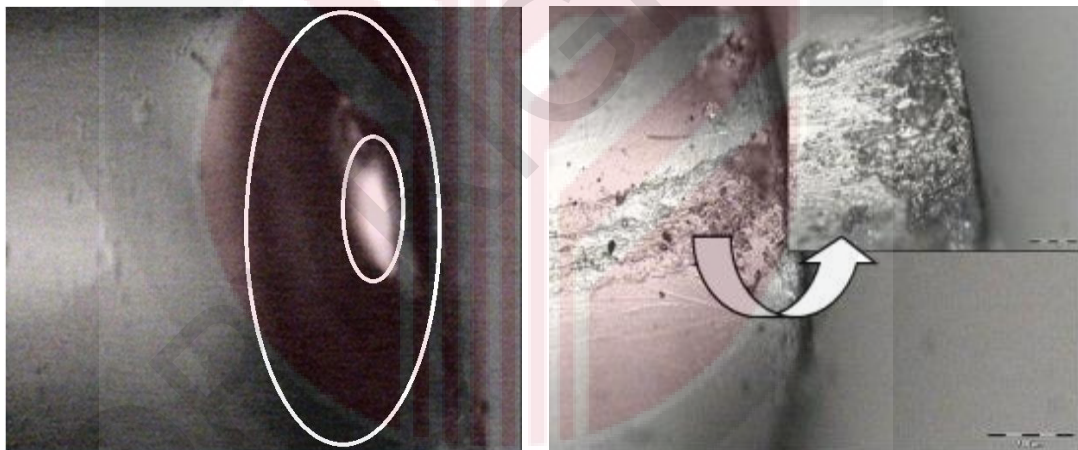


Figure 4.4. Microscopic image of end of fiber after removing the jacket, the clean removing (left) and the damaged fiber after removing the jacket (right)

4.7.1.2 Thermally Thick / Thin Condition

The most important parameters involved in this technique are the frequency, cavity length and PE signal. Coufal and Mandelis (1991) showed that different PE

information can be obtained from a PE experiment by careful selection of the modulation frequency of incident light for cavity length scanning and similarly for frequency scanning the suitable cavity-length should be chosen, in order for the sample to become thermally thick (de Albuquerque *et al.*, 2007) and information of the sample near the surface can be obtained, while at low chopping frequency where the sample is thermally thin and information of the sample comes from deeper within the sample (Thomas *et al.*, 1995). It was important to choose the optimal value of frequency for thermophysical measurements of nanofluids. The smaller the frequency, the better the output signals. Figure 4.5 displays the frequency behavior of the amplitude of signal obtained from the distilled water as a reference sample with known thermal properties.

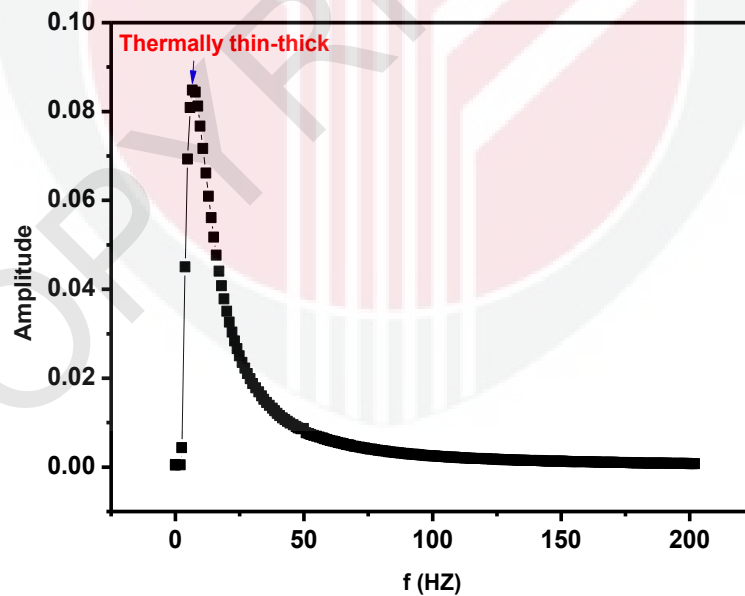


Figure 4.5. The frequency behavior of the amplitude of signal obtained from distilled water

It can be seen that, at frequencies below 6.5 Hz the effect of thermally thin becomes obvious, therefore for above 6.5 Hz, thermal diffusion length smaller than that of the thickness of PVDF film 52 μm , in this condition the PVDF film is thermally thick. Thus, the frequency behavior of the signal higher than 6.5 Hz was investigated. The noise level in the present set-up was about 75 μV . The TW in the sample attenuated rapidly to zero with increasing frequency or distance, the periodic temperature variation in the sample is effectively fully damped out. The LabVIEW software, installed in PC, was used to capture the amplitude and phase data and the data were analyzed using Origin 8. The following procedure describes the steps from the recorded experimental data up to obtaining thermal diffusivity of the test sample.

4.7.1.3 Slope Fitting Method (Cavity Scanning or Frequency Scanning)

In a thermally thick condition, the expressions for amplitude and phase, respectively, are (Lopez *et al.*, 2002),

$$|V(f, L)| = \text{constant}(f) \times e^{-L/\mu} \quad (4.1a)$$

$$\phi(f, L) = \text{constant}(f) - L/\mu \quad (4.1b)$$

where $\mu = (\alpha/\pi f)^{1/2}$ is the thermal diffusion length in frequency f and α is the thermal diffusivity of liquid sample. OF-TWC technique was used to measuring thermal diffusivity of nanofluid by: the slope liner fitting from the plot of the $\ln(\text{amplitude})$ and phase vs both cavity length (from the cavity scan) and frequency square (from the frequency scan). In order to obtain thermal diffusivity of sample in cavity

scanning condition, in this method the frequency was fixed and the Equation 4.1a can be written as,

$$|V(L, \alpha_m, \omega)| = \text{Const}(\omega) \times e^{-\sigma_m L_m} = \text{Const}(\omega) \times e^{-A L_m} \quad (4.2)$$

where $A = (\pi f / \alpha_m)^{1/2}$ to obtain this expression, and the thermal diffusivity was obtained from the slope fitting parameter A . It follows that the slope of amplitude and of phase vs cavity length allow for direct determine thermal diffusivity of sample. The thermal diffusivity of liquids can also be obtained by monitoring the PE signal as a function of cavity length in a semilog scale. In Figure 4.6 the typical behavior of the (a) $\ln(\text{amplitude})$ and (b) phase of the PE signal is shown versus the cavity length for distilled water. The experimental error was obtained by using the standard formula for error propagation,

$$\Delta\alpha/\alpha = |\Delta f/f| + 2(|\Delta A/A|)$$

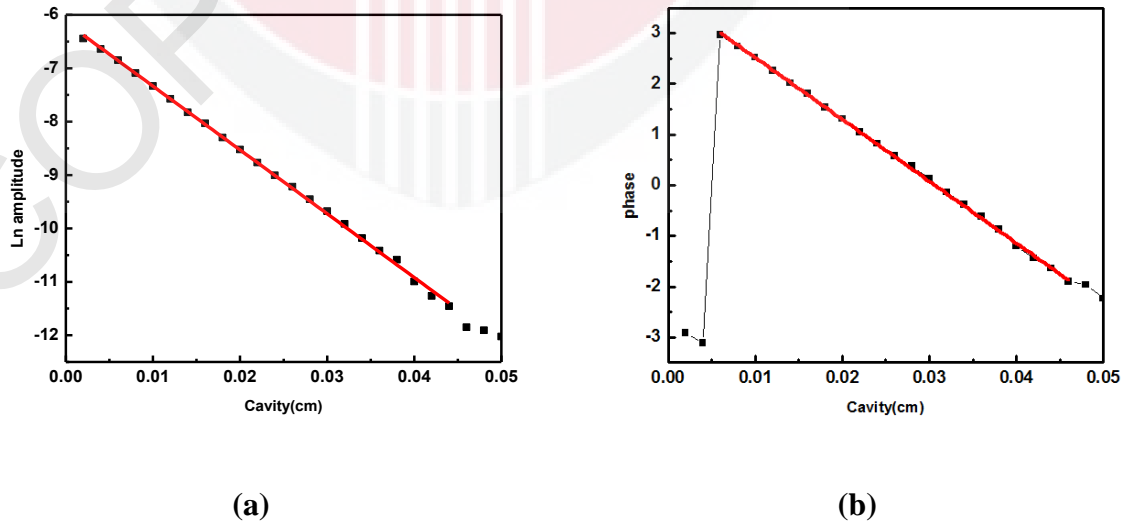


Figure 4.6. Typical result of the (a) amplitude and (b) phase vs cavity length for water, the thermal diffusivity was obtained from the slope fitting parameter $A = (\pi f / \alpha_2)^{1/2}$.

In frequency scanning method the cavity was at a fixed thickness L . By plotting the phase and $\ln(\text{amplitude})$ as a function of frequency scan, the same slope is obtained, from which the thermal diffusivity can be determined from one of the two relationships from PE amplitude and phase signals,

$$\alpha = \pi L^2 / \left(\frac{\ln(|v|)}{\sqrt{f}} \right)^2 \quad \alpha = \pi L^2 / \left(\frac{\varphi}{\sqrt{f}} \right)^2 \quad (4.3)$$

In the useful frequency range, curves are linear. The slope of curve ($V = \sqrt{\pi/\alpha L}$) depends on the thermal diffusivity and thickness. The experimental error was obtained by using the standard formula for error propagation,

$$\Delta\alpha/\alpha = 2(|\Delta L/L| + |\Delta V/V|) \quad (4.4)$$

4.7.1.4 In-Phase and Quadrature of Experimental Data

In Figure 4.7 the typical behavior of the (a) In-phase and (b) quadrature of signal is shown as a function of the cavity length of water. From the resulting dependence of the In-phase and quadrature of PE signal on the cavity length, the thermal diffusivity is obtained from the fit of the experimental data to Equations. 3.25 (a-b)

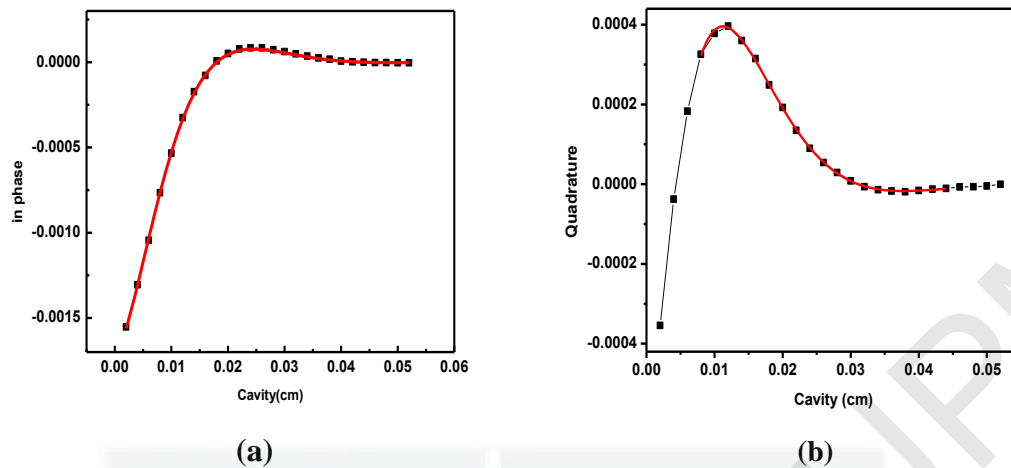


Figure 4.7. Typical results of the (a) In-phase and (b) quadrature of signal vs relative cavity length for distilled water. The thermal diffusivity from (a) In-phase using Equation. 3.25a, and (b) quadrature using Equation. 3.25b

4.7.2 Front Pyroelectric Configuration

In the new design, a simplified Front- PE configuration was set up by using a metalized PVDF, PE sensor as an excellent choice for signal detection, due to low cost, low weight, flexible and sensitive sensor. The comparison of normalized amplitude and phase of various sensors from the previous works was evaluated. By using the Front- PE configuration, the thermal effusivity of the PVDF sensor was measured by using amplitude and phase signals, and the thermal effusivity of a few liquid samples and nanofluids as a substrate in the detection cell were also measured.

A PVDF (polyvinylidenedifluoride (MSIDT1-028K/L)) sensor which is very sensitive for small changes in the heat flux, was metallized with black paint to provide a better light absorption and minimized reflections from the sensor surface to generate TW. The radiation source was a 30 mW He- Ne laser (MellesGriot 05-LHR-991) and the radiation was modulated by a mechanical chopper (SR540). The

signal from the PVDF sensor (52 μ m) was processed with a SR 530 lock-in amplifier. The sample simply filled a plastic ring, glued on the rear side of the sensor and the sample's thickness was 1 mm. As the sample thickness decreased, the contribution from the reflected thermal-wave power increased. A schematic view of experimental setup of Front-PE is presented in Figure 4.8.

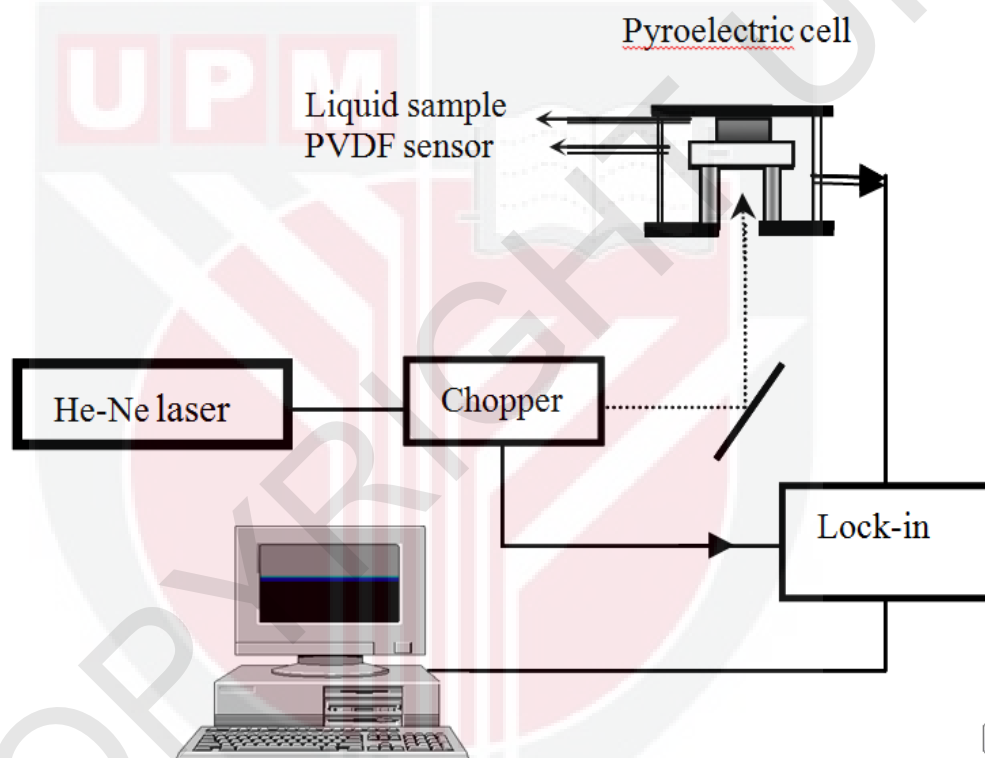


Figure 4.8. Schematic view of experimental setup of Front-PE configuration

The scan was performed in sample thermally thick condition in frequency range of 5 to 30 Hz with the step of 1 Hz. The S/N ratio of the experiment was more than 750. The LabVIEW software was used to capture the amplitude and phase data and the data were analyzed using Microcal Origin 8. The following procedure describes the steps from the recorded experimental data up to obtaining thermal effusivity of the

test sample. The measurement was performed immediately after prepare the nanofluid sample at room temperature. Therefore, due to the limited volume of the experimental cell and small time of measurement, the concentration of the nanofluids was not changed during the experiment. The advantages of this method are low cost in detection cell, ease of implementation and require the small volume of the sample. Additionally, scanning was completed within several minutes, thus, sedimentation and/or aggregation, if any, was avoided.

In the measurement of thermal effusivity of nanofluid by using Front-PE method, two methods were used: Fitting the normalized phase of PE signal vs frequency scan to obtain thermal effusivity (e_p or e_s) and combining the phase and amplitude of the Front-PE signal to obtain thermal diffusivity (α_p) and thermal effusivity (e_p or e_s).

4.7.2.1 Fitting the Normalized Phase Signal Vs Frequency Scan to Obtain Thermal Effusivity (sensor, e_p , or sample, e_s)

Thermal effusivity was measured from analysis of the phase or the amplitude of the PE signal generated by the sensor when it was periodically heated, in order to eliminate the parameters that were difficult to be estimated experimentally. The thermal effusivity value of sensor or sample testing was obtained through a fitting procedure. Figure 4.9 (a-b) displays the frequency behavior of the normalizing amplitude and phase of signal obtained from the distilled water as reference sample of known thermal effusivity, $1600 \text{ W s}^{1/2} \text{ m}^{-2} \text{ K}^{-1}$ (Caerels *et al.*, 1998), to determine thermal effusivity of PVDF sensor. Figure 4.9 (a-b) also contains the best fit performed on the experimental data with Equation 3-31 for normalizing amplitude signal and Equation 3-30 for normalizing phase signal, respectively.

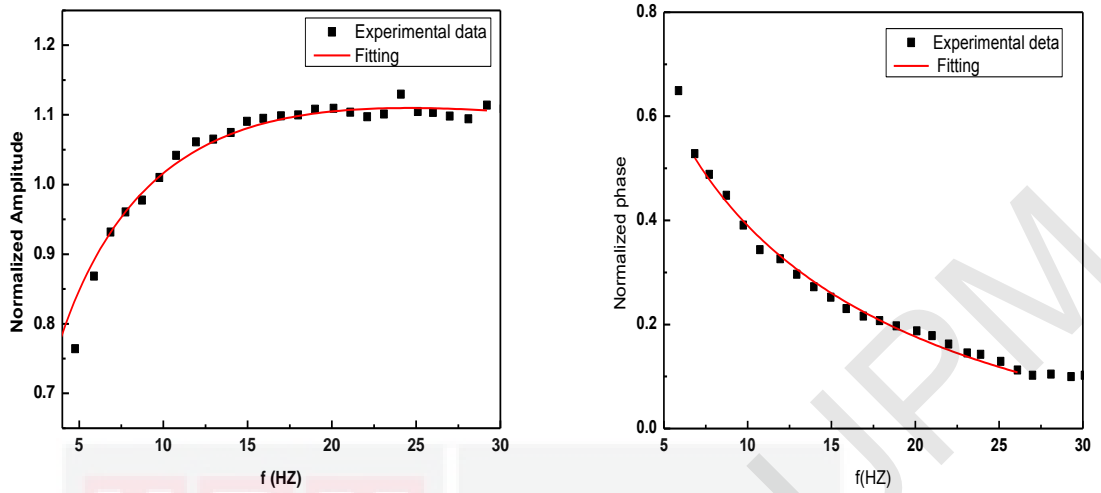


Figure 4.9. Frequency behaviour of the normalized (a) amplitude and (b) phase measured for the PVDF sensor with water as substrate. Solid lines are the best fit of amplitude to Equation 3-31 and phase to Equation 3-30, respectively.

In Figure 4.9 (a-b), at frequencies below 5 Hz the effect of thermally thin becomes obvious, thus, the frequency behavior of the normalizing signal amplitude and phase higher than 5 Hz was investigated. However, there was the difference between experimental data and the fitting at high frequency due to the reduction of S/N ratio. Therefore, the frequency range between 7-25 Hz was the best choice for fitting to find the parameters. Here, the phase was used instead of the amplitude because it produced more accurate results as it does not change with source intensity fluctuations.

The major characteristics of this method is responsible for the high precision results are (i) the information is contained in the phase of signal; (ii) the values of the thermal effusivity can be obtained from the fitting procedures, and no single measured data (Dadarlat *et al.*, 2008). The experimental error of e_p or e_s , significantly contributed to variation of A of Equation 3-30 and 3-31. The thermal

effusivity, Δe_p front of amplitude and the phase of signal are defined as follows:

$$\Delta A/A = \Delta e_p / e_p \quad (4.5)$$

4.7.2.2 Combining Phase and Amplitude to Obtain Thermal Diffusivity (α_p) and thermal effusivity (e_p or e_s)

The proposed method used combined amplitude-phase information, at a single frequency. From the amplitude and phase of the normalized signal using combined amplitude-phase information at a given frequency, Equation 3-36 one could get the thermal diffusivity α_p and the thermal effusivity e_p or e_s . (Sahraoui *et al.*, 2002)

Thermal diffusivity of PE sensor was obtained from the slope linear fitting from the plot the ϕ (which was obtained by using Equation 3-36 (b) vs square frequency (frequency scanning) and the thermal effusivity of PE sensor or sample (e_p or e_s) was calculated for given frequencies by using Equations 3-36 (a) and 3-28. The advantage in measurement by combining the phase and amplitude of the Front-PE signal method over fitting the normalized phase of PE signal technique was that combining the phase and amplitude of the Front-PE signal method involves a single modulation frequency (no different frequency was needed). The experimental error was obtained by using the standard formula for error propagation,

$$\frac{\Delta \alpha}{\alpha} = 2 \left(\frac{\Delta \text{slop}}{\text{slop}} \right), \quad \frac{\Delta R_{sp}}{R_{sp}} = \frac{\Delta e_s}{e_s} \quad (4.6)$$

4.7.3 Experimental Set Up for Front-PE Configuration in Thermally Very Thick Regime,

Front-PE configuration in thermally very thick regime experimental set up used in the present study consists of A DPSS cw laser (200 mW, MGL 150(10)), an optical chopper (SR540), a metalized PVDF (MSIDT1-028K/L) sensor (52 μm), and a lock-in amplifier (SR530). A mirror was used to focus or align the laser beam, (Figure 4.10).

A DPSS laser-modulated light crossing the liquid sample was incident on the metallized surface of a PVDF sensor (52 μm). The cw laser (Mitsubishi, Model ML1016R), equipped with a collimator lens system, and was left unfocused to illuminate a circular area of the PVDF surface, 5 mm in diameter. The optical energy of laser absorbed at the blackened PVDF film generated the PE signal that can be fed into the lock-in amplifier, the processed output signal in from of amplitude and phase signal were send to PC. In order to satisfy the thermally very thick regime for the sensor, and sample chopping frequencies higher than 50 Hz must be used. The normalized amplitude was recorded as a function of the modulation frequency from 50 to 100 Hz, in step of 1 Hz. This range of frequency is high enough to sample be in the cases of thermally thick, and also, this range of frequency is low enough to prevent strong attenuation of the signal and a good S/N ratio. At 50 Hz modulation frequency the PVDF film thermal diffusion length with $\alpha_p = 5.4 \times 10^{-8} \text{ m}^2\text{s}^{-1}$ was less than 20 μm , which was shorter than its physical thickness. The liquid thickness was approximately 1 mm above the upper surface of the PVDF sensor, which is much longer than the water thermal diffusion length in 50 Hz. The signal measured with the PE cell was normalized to the one obtained with

the water as a reference and another obtained with the nanofluid as sample. All the measurements were made at room temperature (22°C).

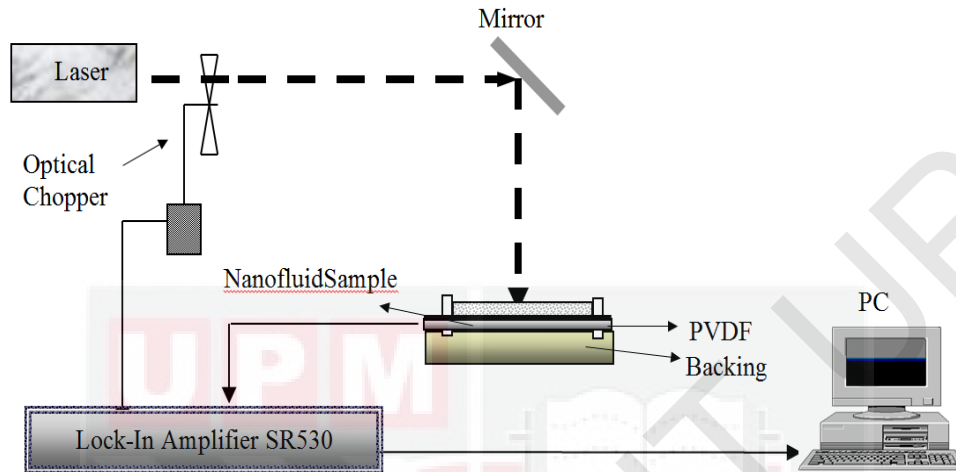


Figure 4.10. Schematic diagram of Front-PE configuration in thermally very thick regime

This methodology involves the thermally thick limit of the PE signal in the standard front-surface configuration. Signals at high modulation frequencies and their value, averaged over an experimental data set, were used for evaluating the sample thermal effusivity through a simple Equation 3.41. In the conventional method the value for the normalized signal, which directly depends on the thermal effusivity of the liquid sample, was obtained from the ratio of PE signals of liquid sample and air. The fact that air and liquids such as nanofluids are allowed to have different range of the frequency due to their different thermal diffusivity, the constant N can be obtained by taking the signal ratio in two different situations: one with the water as a reference, and the other with the liquid sample in place. The normalized signals obtained with water as a reference sample, make it a good choice for evaluating the nanofluids sample thermal effusivity through a simple equation, with higher accuracy.

The LabVIEW software was used to capture the amplitude data and data is analyzed using Microcal Origin 8. The following procedure describes the steps from the recorded experimental data up to obtaining thermal effusivity of the test sample.

From the PE sensor in the thermally very thick regime of two different situations: one with the water as a reference, and the other with the liquid sample in place, making the analytical procedure simpler and more reliable than those reported in the literature (Balderas-López & Mandelis 2003). The constant N , from Equation 3.40 is measured and its value, averaged over an experimental data set, is used for evaluating the sample thermal effusivity through a simple Equation 3.41, $e_n = N(e_w + e_p) - e_p$. The precision of the thermal effusivity measurement is thus directly related to the data-set standard deviation.

4.8 Designing the Ag NPs-Coated Optical Fiber as Thermal Wave Generator

In the case of a conventional (OF-TWC or TWRC) technique the TW generator were prepared by systematically applying two types of commercially available TW converter, conventional paint (silver conventional paint) on a fiber optic (Azmi *et al.*, 2008) or metal film (aluminium or copper) (Balderas-Lopez *et al.*, 2002) that can be used to make any surface conductive as a TW generator, although, for the study of thermal properties of samples, a simple and sensitive Optical Fiber-TWC (OF-TWC) technique has been designed and fabricated. An optical fiber- thermal wave cavity (OF-TWC) sensor using a metalized optical fiber as both of light-transmitting conductors and support of TW generator has been developed (Azmi *et al.*, 2010). Nevertheless, a great challenge for thermal properties measurement in this method is

the ratio S/N of PE signal.

The focus of this section is on developing PE technique to enhance its sensitivity for thermal measurement development, using colloidal Ag NPs efficiently to generate heat in the presence of optical beam, this process depends greatly on the Plasmon resonance and on the shape and concentration of NPs. The advantage of the enhancement in optical properties of noble metal NPs is utilized to fabricate the optical fiber TW generator in OF-TWC technique. The colloidal Ag NPs synthesis is used to coat the optical fiber and surface to enhance the PE signal in the OF-TWC sensor as a flexible photothermal device. Ultimately, it is the use of silver particle films which provide the most spectrally interesting results, while it is necessary to understand the physical processes which produce the spectra.

4.8.1 Synthesis of Colloidal Ag NPs

In preparing this case, the silver colloid used in this work was synthesized by MW irradiation method reported earlier. The composition of the silver colloidal suspension is as follows: Silver nitrate (AgNO_3 , 0.5 g) + water (10 ml) and contained 0.2 g PVP (BASF, molecular weight = 40,000) as the dispersing agent. In the final step, the Ag suspension was concentrated to ~ 20 wt % by using a centrifuge.

4.8.2 Modification of Optical Fiber (TW Generator)

The optical fiber tip or outlet end of 1 mm diameter core and 1.25 mm diameter cladding of single index polymer fiber, (RS 368-047) were cut into small pieces with

equal length of about 1 m. The surface of the fiber cores was then roughened using fine sandpaper. The roughened fibers were then coated. Before being coated with colloidal Ag NPs the end surface was coated with a very thin matt black paint and polished to a reasonable flatness, typically less than 10 micron, to act as an efficient light-to-heat converter. The coatings were prepared by dipping into a Ag NPs solution for 5 min and drying with a heat gun at about room temperature, this step leads to the formation of Ag NPs on the optical fiber surface as a low coverage NPs density, typically less than 5 μm . This procedure was performed repeatedly until a uniform coating with proper thickness about 15 μm , as a high coverage NPs density, was formed on the optical fiber surface after drying. The averaged thickness of Ag coated was measured by the mass of deposited silver on the surface area the thickness was confirmed by a digital micrometer.

4.8.3 Experimental Setup with Ag NPs-Coated Optical Fiber

In the study, we demonstrated the feasibility of an optical fiber-TWC technique. Schematic diagram of the experimental set up as shown in Figure 4.11. In the set-up, the cell design was modified on coating of Ag NPs onto the tip of a plastic optical fiber. In the previous OF-TWC method, this TW generator on the optical fiber tip was done by coating bulk silver paint (Electrolube - SCP03b - Silver Conductive Paint, 3g, average particle size less than 1 μm) (Figure 4.11)

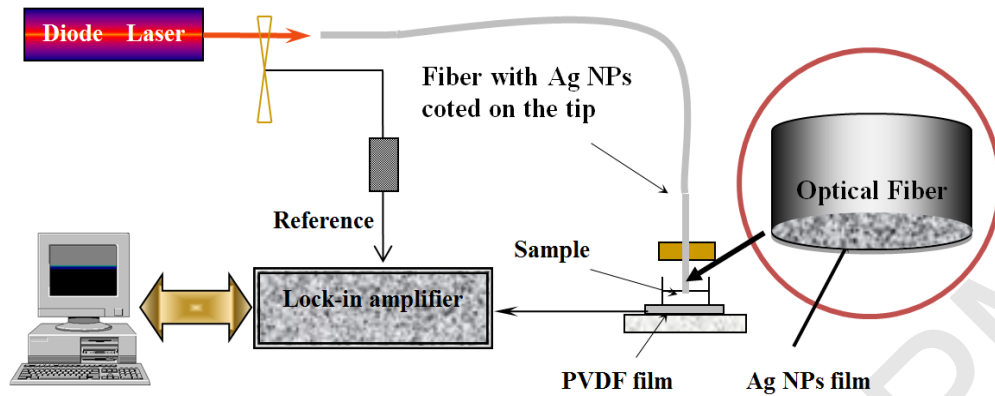


Figure 4.11. Schematic diagram of OF-TWC technique, the tip of optical fiber was coated by Ag NPs film as the TW generator

Once the laser illuminates the Ag NPs coated tip of the optical fiber (Ag NPs-coated optical fiber), the Ag NPs begin to generate heat due to photothermal effect. The Ag NPs-coated optical fiber, is excited by a modulated DPSS cw laser (green light of 532 nm, 0.2 W). The light does not only transmit within the fiber core but illuminates the fiber optic end surface directly to enhance the adsorption of photons. Therefore, the measured PE signal responsively depends only on the conversion of optical energy to thermal energy by the coating layer (Gilbert *et al.*, 2006). The layer is thermally thin so that its influence on the thermal transport process can be neglected (Marinelli *et al.*, 1994).

The TW generated photothermally on the Ag NPs-coated optical fiber is launched across the sample and reaches the PVDF sensor, located parallel to, and across from, the optical fiber. The amplitude signal and the phase shift between the sensor signals and the heating signals are measured by a lock-in amplifier by performing a frequency scan for given cavity length. The amplitude of signal is connected to a

PC, so the magnitude amplitude of signal can be recorded in various frequencies and all the measurements were made at room temperature.

Except for using the fiber end as TW generator, the experimental technique is similar to the OF-TWC technique. To complete the analysis, the method was tested on air sample as a reference sample to verify its accuracy. It was then applied to the study of thermal diffusivity of air with Ag NPs coated and also Ag paint coated TW generator. The thermal diffusivity of air was measured by performing a frequency scan of the OF-TWC device with Ag NPs. At 6.5 Hz the air thermal diffusion length was less than 1 mm while the cavity length scanning range was around 1.5 mm and the modulation frequency of the laser beam above 6.5 Hz to ensure the PVDF film, the sample and the backing medium are all in thermally thick regime during measurements.

CHAPTER 5

RESULTS AND DISCUSSION

5.1 Introduction

In this chapter begins by reporting the obtained results related to fabrication of Ag NPs in water and ethylene-glycol (EG) different solvents and different MW irradiation time at a moderate temperature, without any other reducing agent. The aim of this study is to improve the efficiency of this technique in fabricating Ag NPs. The possible progress of the formation of Ag NPs is also discussed.

Next, it presents the experimental results obtained from using the PE technique that was design at different configurations in the measurement of the thermal properties of nanofluids. The following result and discussion in this section are divided into three parts: (i) The back-PE configuration, in the OF-TWC set up to determine the thermal diffusivity of standard sample, Normal Grade and Winter Grade Biodiesel, and nanofluids containing Ag, Al₂O₃ and CuO NPs. (ii) The Front-PE configuration, in a simplified Front-PE configuration determine the thermal effusivity of the PVDF sensor, a few liquid samples, nanofluids of Al₂O₃ and CuO, and to determine the normalized combined amplitude and phase of signal to measure the thermal effusivity of Ag NPs dispersed in water or ethylene glycol, and the thermal diffusivity and thermal effusivity of PVDF sensor, and in thermally very thick regime to determine the thermal effusivity of Ag nanofluids in different solvents through a simple equation. (iii) The development of TW generator using colloidal Ag NPs to coat the optical fiber end in OF-TWC setup.

5.2 Green Synthesis of Ag Nanoparticles without Reducing Agent at Different Microwave Irradiation Times

The green synthesis of Ag NPs without reducing agent at different MW irradiation times has been carried out recently. This MW rapid heating method has been demonstrated for the preparation of Ag nanostructures, as the spherical NPs and also dendrites, in water and PVP as the stabilizer agent without any other reduction agent and this was compared with that synthesis of the conventional heating technique at the same apparent temperature. The color of prepared samples in various MW-irradiation times in a moderate temperature of 60 °C slowly change from colorless for AgNO₃/water (W0) to brown (W1, W2) and the end to dark brown (W3–W4) which indicated to the formation of Ag NPs in the water suspended (Figures 5.1). The Plasmon resonance of the colloidal Ag NPs causes colors in the visible spectrum, which, depends on a number of factors, including particle size and shape and the surrounding medium (Link *et al.*, 1999).

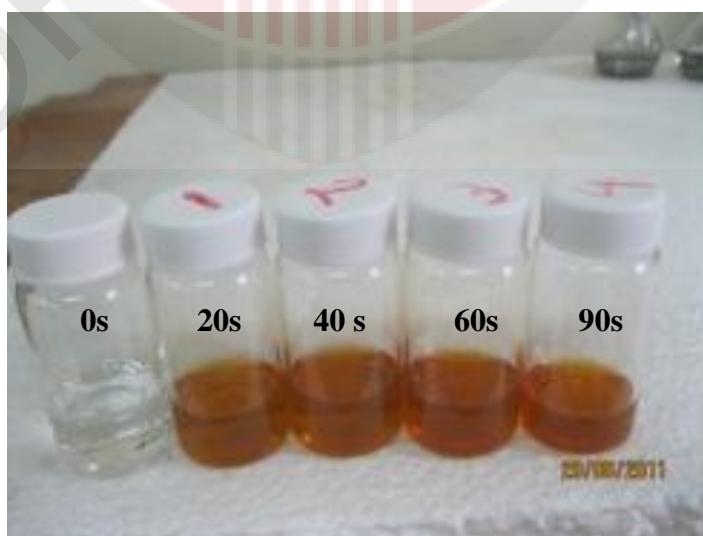


Figure 5.1. Synthesis Ag NPs dispersed in water using MW irradiation at 0, 20 s, 40 s, 60 s and 90s, left to right respectively

In order to determine the structure of synthesized Ag NPs, the XRD pattern of it was taken and as shown in Figure 5.2. All diffraction peaks correspond to the characteristic face centered cubic (FCC) silver lines (Raffi *et al.*, 2003). These lines observed at 2θ angle of 38.119, 44.305, 64.452 and 77.409 have respectively been indexed as (111), (200), (220) and (311).

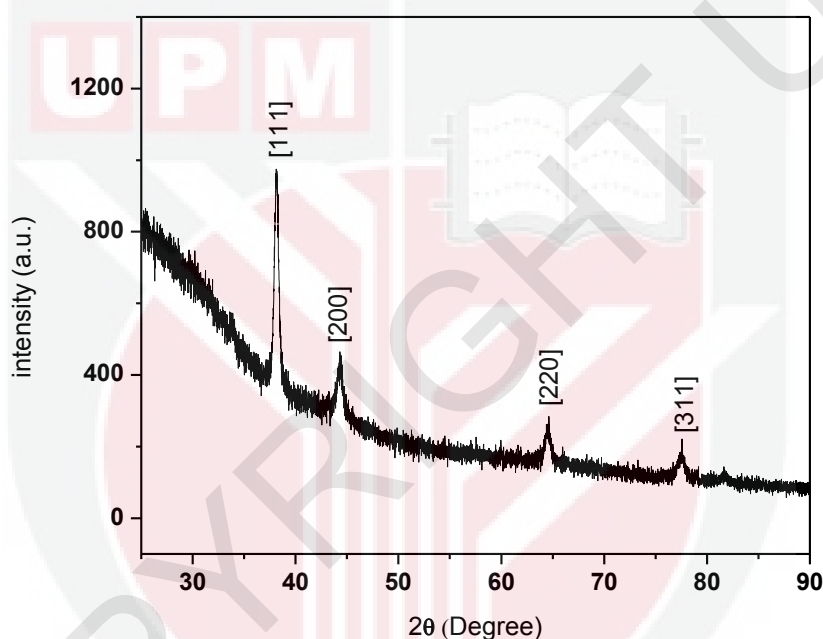


Figure 5.2. Synthesis Ag NPs dispersed in DW by using MW irradiation.

Figure 5.3 shows the TEM images and their size distributions of Ag NPs in the water under various MW irradiation times. When Ag nanofluids prepared under irradiation of 20 and 40 s, the mean diameters are about 7.14 ± 4.31 and 9.15 ± 3.71 nm (Figure 5.3A and C), respectively. As seen in Figure 5.3 (E and G), when the irradiation times increased to 60 and 90 s, the mean particles size was increased considerably to 10.1 ± 3.31 and 11.5 ± 2.59 nm, respectively.

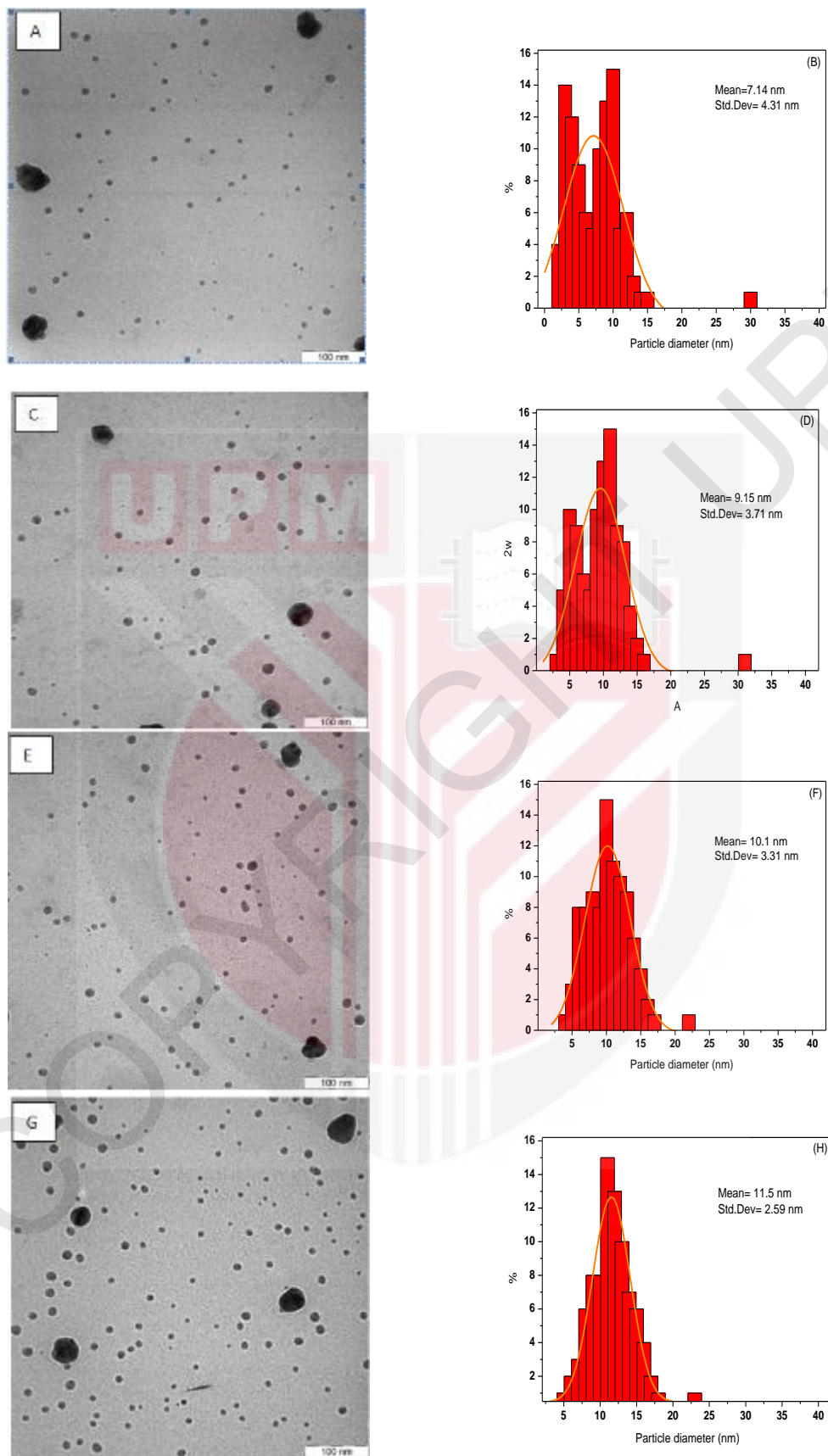
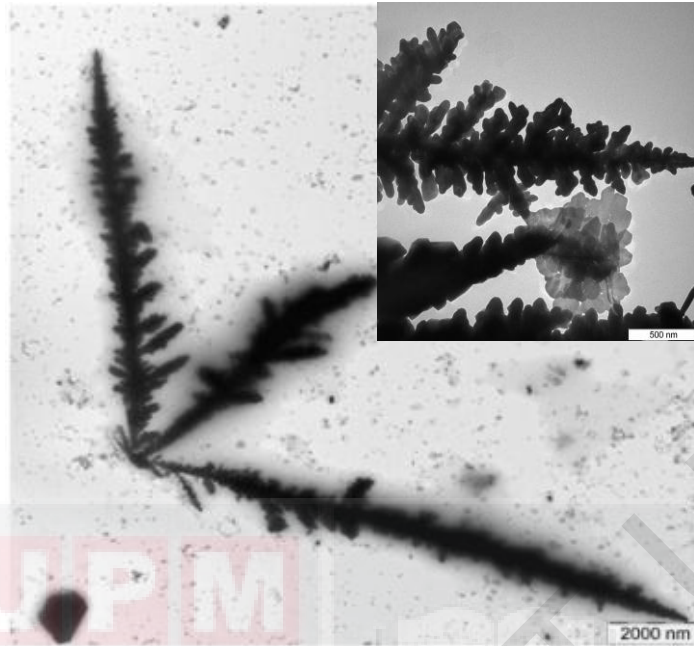


Figure 5.3. TEM images and their size distributions of Ag NPs at the different MW-radiation time: 20 (A, B), 40 (C, D), 60 (E, F), and 90 s (G, H)

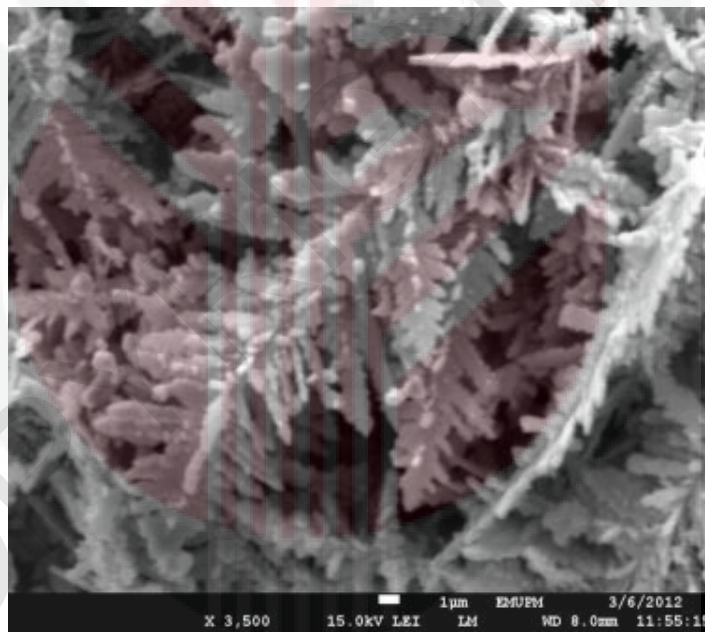
It can be seen that with the increased MW-irradiation time the Ag NPs mean diameter slightly increased in the solutions (Acharya *et al.*, 2011). However, a narrow size distribution and highly homogeneous of the Ag nanofluids prepared under MW irradiation of 90 s shows there is evident of increase in the concentration, due to increase in the amount of small NPs. From the TEM image can be seen that the particle size distributions obtained the combined effect of PVP therefore helps to control the particle size (Tripathi *et al.*, 2012).

5.2.1 Dendritic Nanostructures of Ag Nanoparticles

Figure 5.4 shows (a) TEM image and (b) FESEM image of Ag NPs that prepared under MW irradiation of 90 s in the solution. The formation of silver trees and dendritic nanostructure can be seen in Figure 5.4. Dendritic structure of Ag NP was formed and when the Ag NPs concentration was increased the large dendritic nanostructure was formed (Baruwati *et al.*, 2009; Agrawal *et al.*, 2008). The MW heating irradiation and PVP as a surfactant play important roles in the formation of Ag dendrites, Ag ion was reduced and metallic Ag NP was formed at the beginning of MW irradiation of AgNO₃ with the presence of PVP. Therefore, the interaction between Ag particles and MW energy lead to the growth of the NPs and an increase in temperature in the surrounding areas and can encourage new nuclei to appear at its boundary for further diffusion-limited growth. As the sphere grows, the spherical morphology becomes unstable and its shape becomes perturbed. The solid shape begins to express the preferred growth directions of the crystal. Consequently, this rate of nucleation and growth of crystals was allowed to form the Ag dendrites structure (Tsuji *et al.*, 2005).



(a)



(b)

Figure 5.4. (a) TEM micrographs (b) FESEM of the dendritic nanostructures to the formation of Ag trees

Figure 5.5 (a) shows, the absorption spectra of Ag nanofluids under various MW irradiation times. The UV-vis spectra shows a symmetrical peak of surface Plasmon resonance (SPR) at about 420.nm, and a long tail lengthening toward the lower wavelength (Tsuji *et al.*, 2002). However, the SPR absorption band obtained of

AgNO₃/water suspension (W₀), before the MW-irradiation, showed an absorption wide band at around 450.nm.

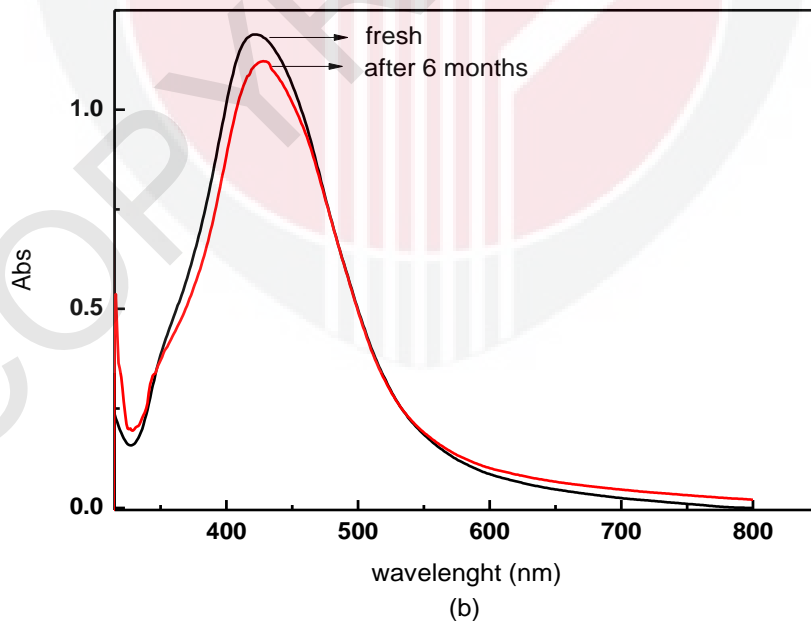
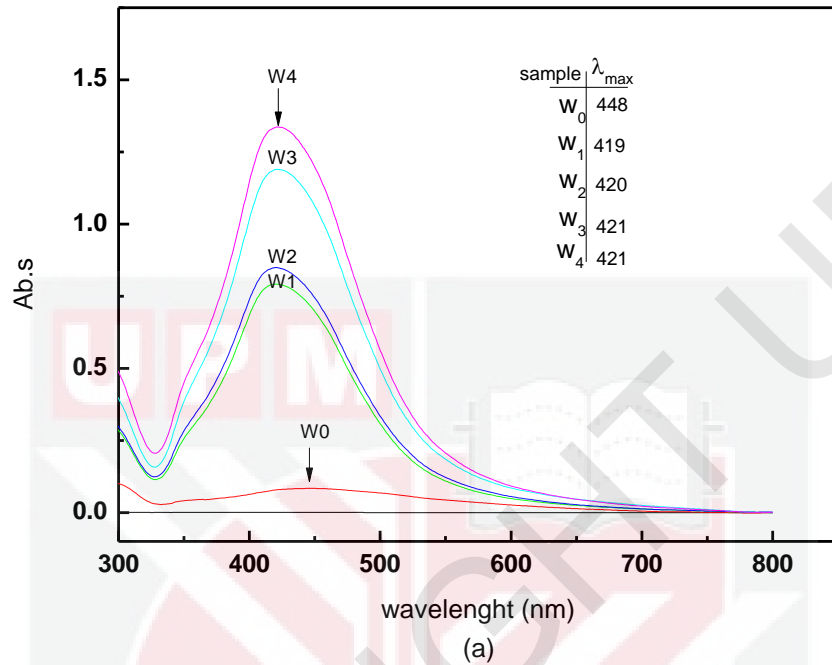


Figure 5.5. (a) UV adsorption during the formation of Ag+PVP nanofluids (W₀ , W₁ , W₂ , W₃ and W₄ at before and after 20, 40, 60 and 90s MW irradiation times) was on the traces. (b) UV adsorption of sample W₃, fresh and after six months storage

As shown in Figure, the absorption peaks of Ag NPs colloidal solutions increase sharply with the increase of irradiation time. Here, when the irradiation time increase to 20, 40, 60, and 90s, then the SPR peaks increase and are red-shifted to 419 (W1), 420 (W2), 421(W3), and 421(W4) nm, respectively. The result showed, a maximum absorption and narrow size distribution of the Ag NPs was reached after 90 s of irradiation time or highly homogeneous. The increase of absorbance is due to the increase in the number of NPs in the solution (Kappe *et al.*, 2004).

For stability testing of Ag nanofluid, the absorption spectra of sample W3 was taken after six months storage at room temperature (Figure 5-5b). The absorption peaks was slightly red shift only from 420 to 427.nm and the small decrement in dispersion intensity shows Ag NPs solution was quite stable. Therefore, Ag NPs prepared by MW irradiation produce stable Ag NPs over a long time.

5.2.2 Formation of Ag NPs under Conventional Heating

Figure 5.6 presents UV adsorption spectra of Ag nanofluids prepared under MW irradiation and conventional heating method. The absorption peak intensity of the sample obtained using MW heating was higher and was blue shift (from 435 to 421.nm) compared to that of conventional method. The shift and higher peak indicated that the size of Ag NPs prepared by using MW heating was smaller, more uniform in size distributions and was in a higher density (Mohamed *et al.*, 2010) compared with the conventional heating method. The concentration of the Ag NPs from MW irradiation and conventional heating confirmed by Atomic absorption

spectroscopy (AAS-S Series; Thermo Scientific, San Jose, CA) were 0.136 and 0.102 mg/L, respectively.

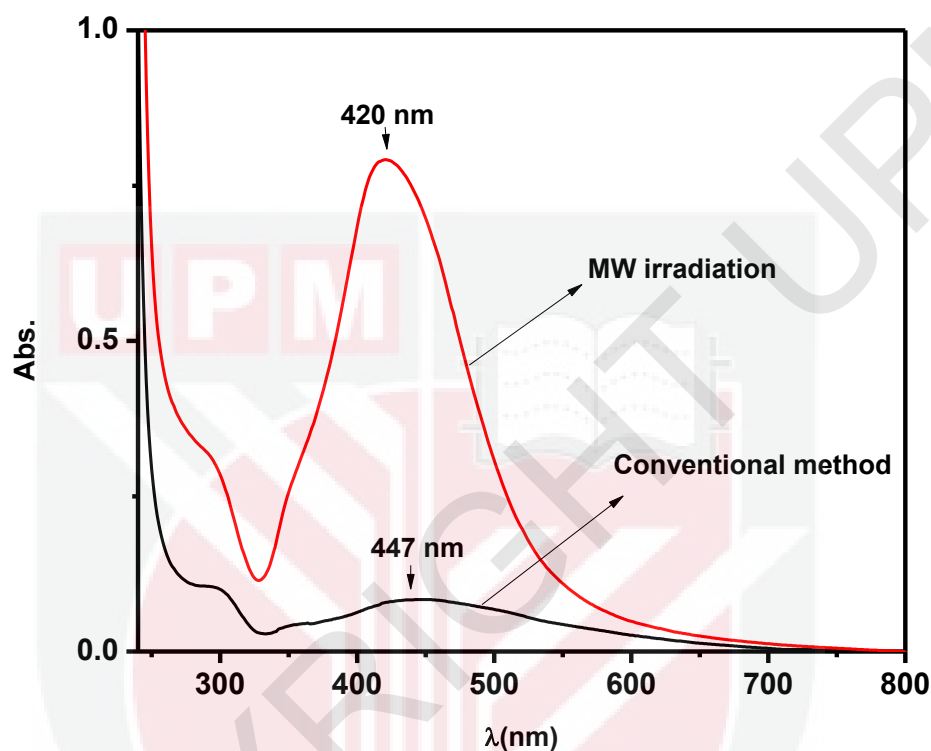


Figure 5.6. UV-vis adsorption spectra of Ag-NPs using MW irradiation and convention heating method in the same temperature, the concentration of Ag NO₃ and PVP are the same, while the temperatures reach to 60.°C.

From Figure 5.7, the TEM image and their size distributions clearly show the Ag NPs obtained from the conventional heating is bigger, 14.5.nm, than that of MW irradiation method based on large standard deviation, 7.73.nm and not uniform in size. The decrease in the size of Ag NPs prepared by using MW irradiation can be attributed to the efficient electromagnetic fields in heating of the polarization the water molecules. In the conventional heating, the solution was heated by conduction and convection, so there was a large temperature distribution within the solution

(Tsuji *et al.*, 2005). Rapid heating in MW irradiation can produce narrow sized distribution, homogeneous nucleation and subsequent crystal growth and indicating the superior yield of Ag NPs (Acharya *et al.*, 2011).

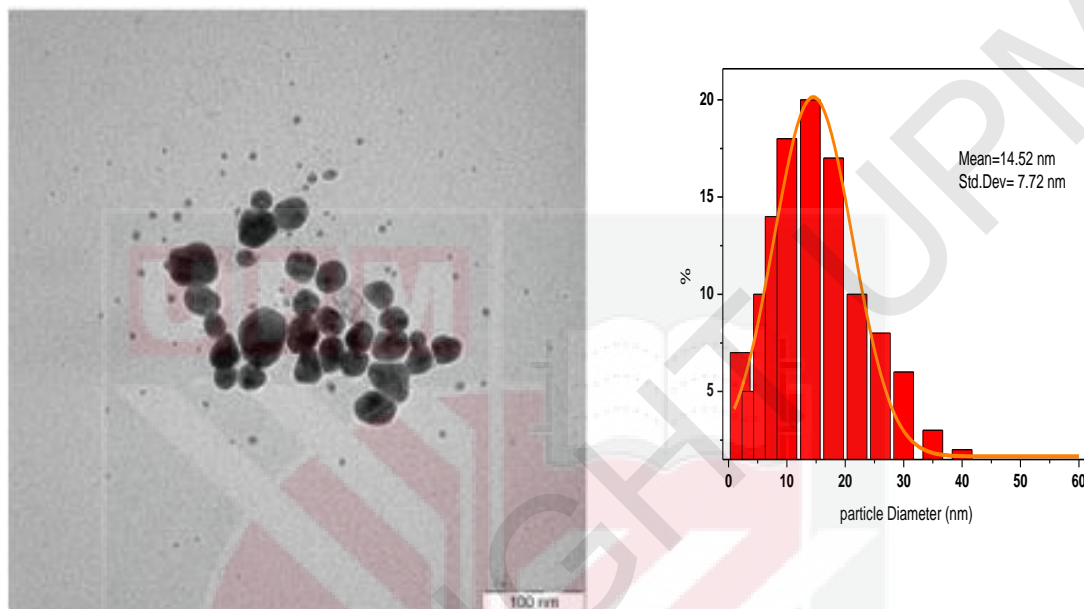


Figure 5.7. TEM images of Ag-NPs synthesized by conventional heating method

5.3 Synthesis of Ag NPs in Ethylene-Glycol at Different MW Irradiation Time

Choosing the right solvent is an important factor in the reactions, which MW irradiation to form Ag NPs. Therefore, ethylene-glycol (EG) was selected to act as both solvents and reducing agents to synthesize Ag NPs under irradiation MW at different times.

The color of the prepared samples at different irradiation times at a moderate temperature of 60 °C gradually changed from colorless for AgNO₃/EG suspension (EG0) to light yellow (EG1, EG2) and finally turned to dark yellow and light brown

(EG3– EG4) with the increase of irradiation time which indicated the formation of Ag NPs in the EG suspension, Figure 5.8. The light brown color indicated a higher concentration of Ag-NPs, which was confirmed by UV-vis absorption spectra. It has been suggested that the color of colloidal Ag depends both on the size and shape of clusters as well as the surrounding medium (Link *et al.*, 1999).



Figure 5.8. Synthesis Ag NPs dispersed in EG using MW irradiation at 20 s, 40 s, 60 s and 90s, left to right respectively

Figure 5.9 shows the absorption spectra of the colloidal Ag NPs under different MW irradiation times 0 s (EG0), 20 s (EG1), 40 s (EG2), 60 s (EG3) and 90 s (EG4) in ethylene glycol in the presence of PVP. The surface Plasmon absorption band obtained from AgNO₃/EG suspension (EG0), before the MW-irradiation, showed no sign of colloidal silver. The change of peak position and the shape of the absorption spectra were obvious during the irradiation MW time. The absorbance for the used range of wavelengths (200–800 nm) is the characteristic surface Plasmon resonance of spherical Ag NPs and a wide tail extending toward the lower wavelength (Durán,

Marcato *et al.*, 2010). The first peak appeared around the 300 nm as small Ag NPs (less than 2 nm) or their chemical compounds (Szymańska-Chargot *et al.*, 2009), but the second one was broadened at longer wavelengths from 443 nm to 428 nm for EG1 to EG3, respectively, and they exhibit tailing effect which could signify a variation in Ag NPs size.

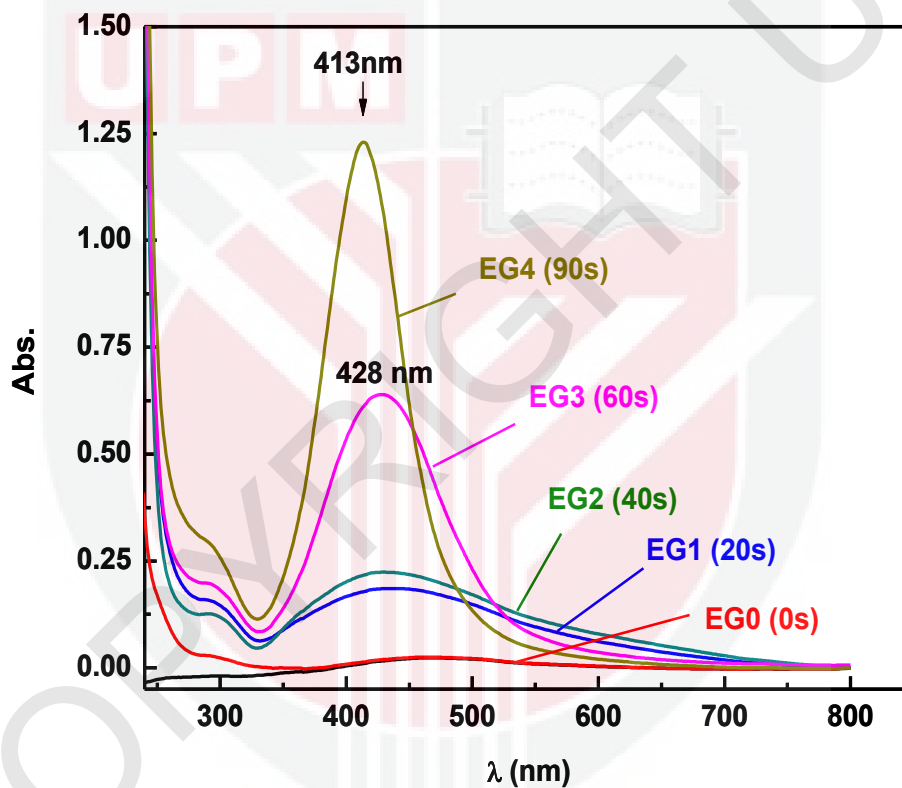


Figure 5.9. UV adsorption spectra during the formation of Ag nanofluids at the various MW irradiation times, the irradiation times was shown on the traces.

Figure 5.9 shows absorption spectra of the solution irradiated for 90 s the maximum of the peak appears at 413 nm, where the bands are sharper and more symmetrical, that reflects more uniform size distributions and higher silver concentrations. The

blue-shift of the Plasmon band for 90s irradiation may be due to the adsorption of Ag⁺ ions which are in excess in the solution (Patel *et al.*, 2005).

Figure 5.10 shows the TEM images and their corresponding particle size distributions of Ag nanofluids at the different MW-irradiation time: 20 (A, B), 40 (C, D), 60 (E, F), and 90 s (G, H). The mean diameter and their size distributions of Ag-NPs obtained by measuring the diameter and standard deviation of all particles in the images are shown beside each image, as seen in Figure 5.10. In the Ag-NPs solution prepared at 20 and 40 s, Ag NPs are formed with a broad size distribution and the mean particle size were about 12.8 ± 4.6 nm and 12.6 ± 4.3 nm, respectively (Figure 5.10 A and C). While for solution irradiated for 60 and 90 s (Figure 5.10 E and G), the mean particles size of Ag-NPs were decreased considerably to 12.03 ± 3.6 nm and 11.2 ± 2.3 nm, respectively.

This is probably because excess Ag⁺ ions produce more nuclei during the nucleation period, thus leading to formation of smaller NPs. It can be seen that larger Ag-NPs were obtained under shorter irradiation time, because usually more crystal nuclei were provided under further irradiation. The TEM result of decreasing in the particle size of Ag-NPs at 90 s is in accordance with the blue-shift of its absorption peak as shown in Figure 5-9.

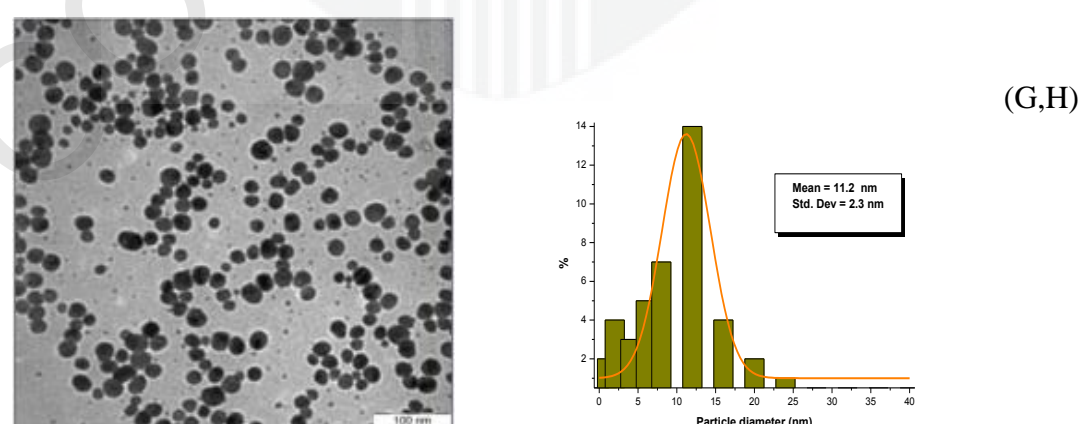
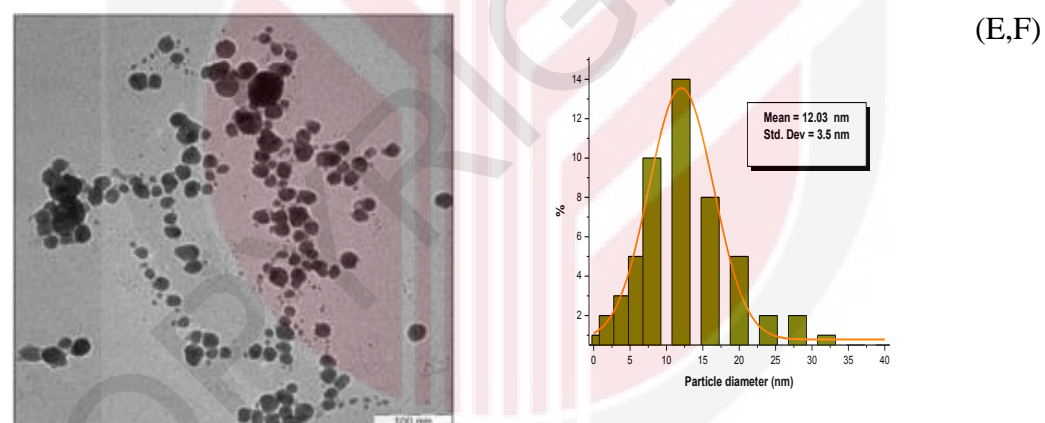
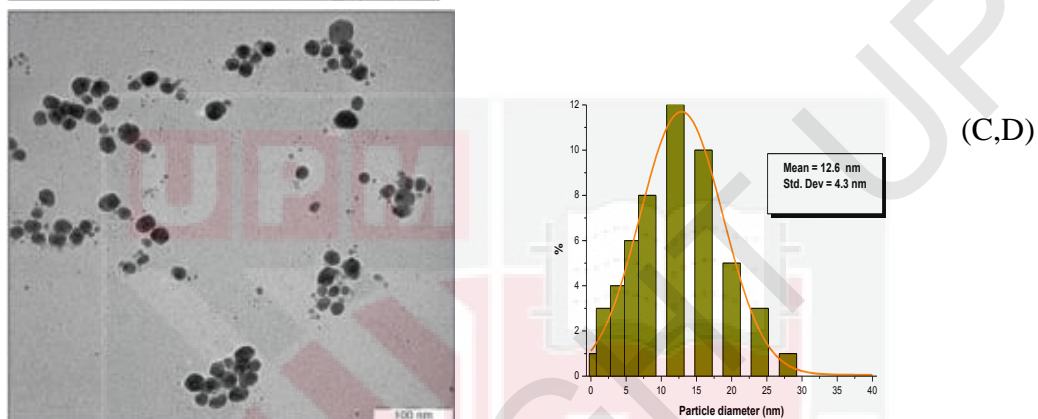
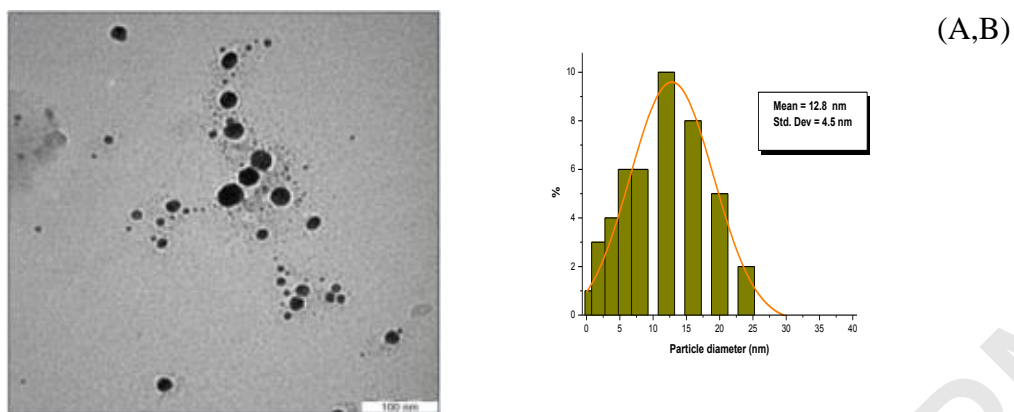


Figure 5.10. TEM images and their size distributions of Ag NPs at different MW-radiation time: 20 (A, B), 40 (C, D), 60 (E, F), and 90 s (G, H).

5.3.1 Self-Assembling of Ag NPs

As shown in the TEM images (Figure 5.11), the case images revealed surprising effect. It can be observed as evidence of individual spherical nanostructure of self-assembled Ag NPs, of about 1 micron, that are well-dispersed and nearly monodisperse.. For solution irradiated by MW for 90 s (Figure 5.10G), the amount of silver individual spherical nanostructure was large and it has tendency to aggregate in one place (Szymańska-Chargot *et al.*, 2009).

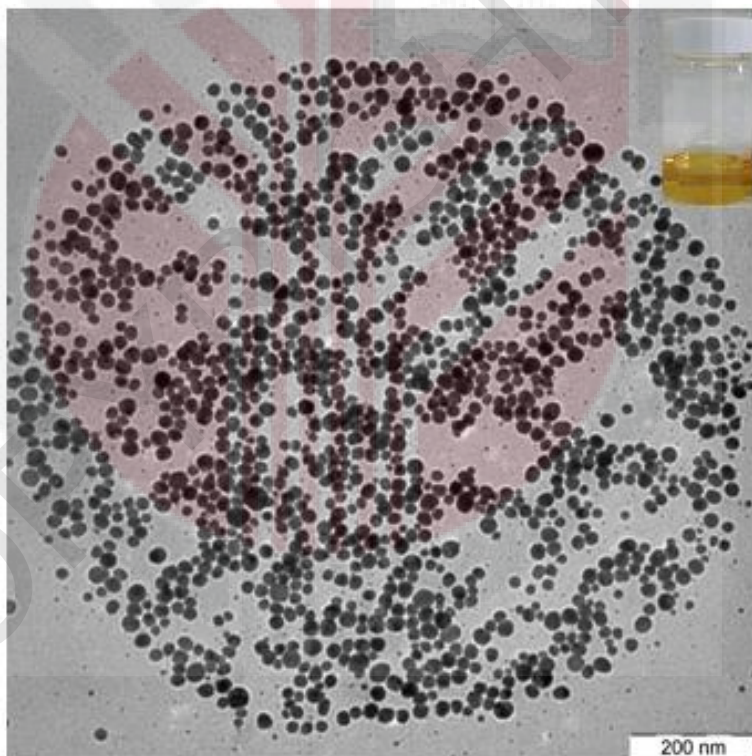


Figure 5.11: TEM images of the individual spherical nanostructure self-assembled of Ag colloids in EG solution

5.3.2 Comparison between Ag NPs in Water and Ethylene-Glycol as a Solvent

The MW irradiation on AgNO₃ dissolved in two different solvents (water and EG), produce particles of metallic silver of different sizes. Most of the Ag NPs nanofluids, prepared in water under MW irradiation, are spherical and distributed uniformly. The small size and low concentration of Ag NPs can also be seen from the TEM images in Figure 5.3. On the other hand, Figure 5.10, the silver colloids, which were obtained in EG under MW irradiation, are nearly uniformly spherical in shape, well-dispersed, with high Ag NPs concentration and a narrow size distribution.

The spectra obtained in Figure 5.9 with those in Figure 5.5 clearly show that the adsorption of EG was sharper and of smaller wavelength compared to the water solution. In both Figures 5.5 and 5.9 peaks are sharp and symmetrical which could signify a narrow distribution in size and morphology of Ag NPs (Zhang, *et al.* 2006). The high concentration and uniform distribution in the EG solution may be attributed to the size of Ag NPs, in which some aggregation can also be observed (Figures 5.10 and 5.3), which is consistent with the TEM results. In the present work, metallic Ag NPs prepared in EG were well-dispersed, high concentration and its solution was much more stabilized than those in water under identical MW irradiation conditions.

The observed difference between formation of Ag NPs in water and ethylene-glycol may be ascribed to:

- (i) The difference in the boiling points: the boiling points of the solvents have an important effect on the crystallinity of the Ag NPs (He *et al.*, 2002). Higher boiling point of EG (197.3 °C) is advantageous to the higher crystallinity of

the Ag NPs, and this could be the reason why EG is the favoured solvents for the formation of silver crystals under MW irradiation. The low boiling point of water does not favour the growth and ripening of crystals. Most of the isolated particles in the sample prepared in water are spherical and a few faceted nanocrystals can also be seen from TEM (Figures 5.3).

- (ii) The difference in the molecular weight: In general, liquids of large molecules have high viscosity. In the case of using EG as solvent, the behaviour of large molecular weight and long EG chains is easily adsorbed onto the surface of particles, due to high viscosity of EG $1.61 \times 10^{-2} \text{Pa s}$ (Dobryszyci *et al.* 2001) and hence assisted in their stabilization to achieve the narrow size distributions. This could also lead to growth of crystal, while the larger silver particles are also formed at high concentration. These results are consistent with the TEM observations (Figure 5.10).
- (iii) The difference in the dielectric loss: The higher dielectric loss of EG (49.950) compared to that of water, (9.889), may be the reason to the reaction proceeds at a much faster rate. Thus, the particle size in EG grows larger with a continuous nucleation of Ag. As a result for both solvents (water and EG), the effect of MW irradiation time mainly affects the particles distribution, rather than the size. This is probably because irradiation time produces a large number of nuclei leading to the formation of narrow particle size distribution with small average size.

5.4 Back Pyroelectric Configuration Technique and its Applications

In this section, calibration and validation of the set up was carried out in the cavity- and frequency- scans. The frequency-scan experiments are performed to measure the thermal diffusivity of both Normal Grade and Winter Grade Biodiesels. The cavity-length scan has shown further advantages in terms of precision and improving the S/N ratio (Shen & Mandelis, 1996). The thermal diffusivity of each nanofluid is measured by cavity-scan as it is rapid, robust, and was used successfully to measure the nanofluids thermal diffusivity.

5.4.1 Preliminary Work (Optimization and Calibration of System)

To optimize the measurement, different modulation frequencies and cavity length can be considered. Precise determination of resonant peak positions standing TW is critical in the cavity- and frequency-scans experiments. Understanding-wave conditions, significant TW- field enhancement may be expected to occur at resonances of the cavity. The Simulated of in-phase (IP) TW signal is calculated for different cavity length in frequency scan and similarity different frequency in the cavity-length scan.

5.4.1.1 Resonant Peak -Position Determination Method

Figure 5.12 shows, the Simulated of IP signal according to Equation 3.25, of the water as a function of cavity length in (a) 5 Hz and (b) 100Hz frequency. It can be seen that, the S/N ratio is higher for lower frequency, while, the peak is too flat for

precise determination of its maximum (Figure 5.12(a)). However, the peak is quite sharp for the higher frequency (Figure 5.12(b)), but produces a smaller output signal, which makes identification of the peak position difficult (Wang & Mandelis, 1999). It was experimentally found that with 6.7 Hz as the operating frequency, the S/N ratio is good with frequencies in the range of 0-0.04 cm cavity length, to measure liquid sample thermal diffusivity.

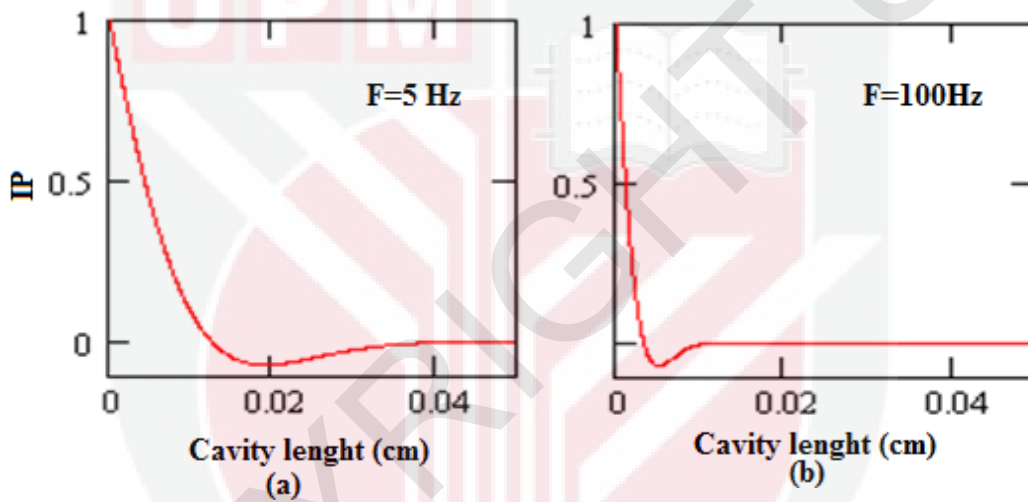


Figure 5.12. Simulated IP of signal and the first overtone resonances as a function of cavity length with (a) $f=5$ Hz, (b) $f=100$ Hz, water thermal diffusivity ($\alpha_w=0.00145 \text{ cm}^2 \cdot \text{s}^{-1}$)

Figure 5.13 (a-b) shows, the simulated IP signal of water, according to Equation 3.25, as a function of frequency at, (a) $L=0.005\text{cm}$ and (b) $L=0.015\text{cm}$ cavity length. In Figure 5.13 (a-b) exhibits a strong and narrow minimum but low resonant frequency (low S/N ratio) in the big cavity (b), whereas a much weaker minimum and has the high resonant frequency (high S/N ratio) and better the output signal in the low cavity (a) (Shen & Mandelis, 1995).

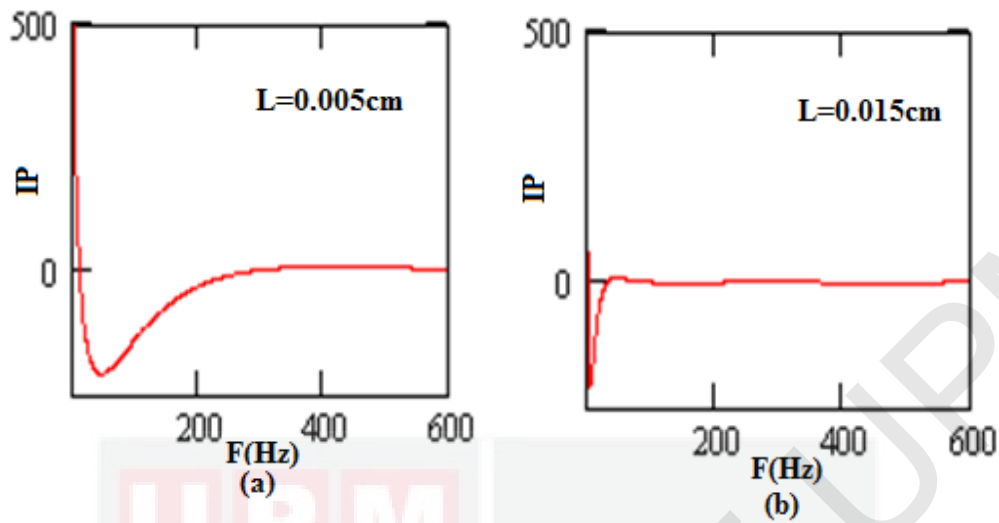


Figure 5.13. Simulated IP of signal and first overtone resonances as a function of modulated frequency with (a) $L=0.005\text{cm}$, (b) $L=0.015\text{cm}$, water thermal diffusivity ($\hat{\alpha}_w=0.00145\text{ cm}^2\text{s}^{-1}$)

In the experiment, one should carefully choose the modulation frequency in order to get a sharp resonant peak (actually a trough), which is necessary for precise diffusivity determinations. It has been experimentally found that the S/N ratio is good with the frequency, in the range of 7 to 25 Hz.

5.4.1.2 Calibration and Error Estimation of Setup by Cavity Length- Scanning

The experimental system of thermal diffusivity of water as a base fluid is calibrated using cavity length-scan. Figure 5.14 (a-b) shows the plots of logarithmic amplitude and phase versus the cavity length of water. The thermal diffusivity is obtained from the slopes of the PE signal ($\ln(\text{amplitude})$ and phase), and the thermal diffusivity values measured in the present work are summarized in Table 5.1.

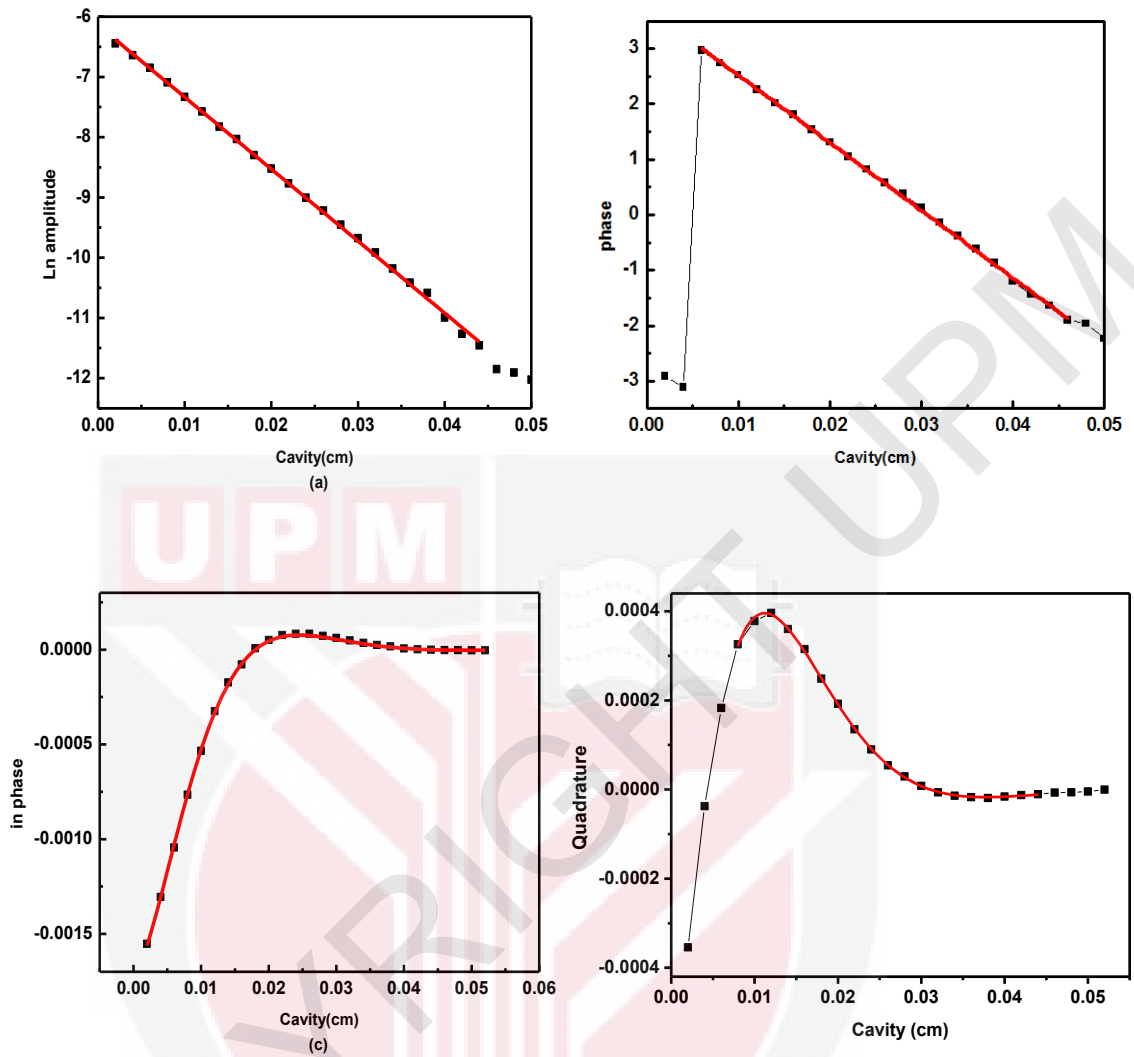


Figure 5.14. (a-b): The plots of logarithmic amplitude and phase versus the cavity length , and (c-d) shows the real (ln-phase) and imaginary (quadrature) of signal versus the cavity length in water

Both plots are linear with respect to cavity length. The average thermal diffusivity of water differs by only 0.7% with values described in the literature, $1.456 \pm 0.008 (\times 10^{-3} \text{ cm}^2/\text{s})$ (Balderas-Lopez *et al.*, 2000). Figure 5.14 (c-d) shows the real (ln-phase) and imaginary (quadrature) of signal versus the cavity length of water. The experimental data are fitted to the theoretical Equation 3.25 a-b, and the thermal diffusivity values measured in the present work are summarized in Table 5.1.

Table .5.1 The thermal diffusivity values of water measured in the present work

Method for fitting	Parameter of fitting	Thermal diffusivity ($10^{-3} \text{ cm}^2/\text{s}$)	Relative error%
Slope			
In amplitude	121.967 ± 0.609	1.426 ± 0.007	0.49
Phase	119.446 ± 0.768	1.486 ± 0.009	0.61
Fitting			
In phase	122.838 ± 1.623	1.405 ± 0.01	0.71
Quadrature	118.606 ± 0.787	1.507 ± 0.01	0.66

In terms of thermal diffusivity values, one can see only minor difference between the thermal diffusivities obtained from amplitude and phase curves, $\Delta\alpha = 0.061 \times 10^{-3} \text{ cm}^2 \text{ s}^{-1}$, while, that from In-phase and Quadrature is $\Delta\alpha = 0.102 \times 10^{-3} \text{ cm}^2 \text{ s}^{-1}$. Consequently, thermal diffusivity is more precise than that obtained from the slopes of the PE signal (Ln(amplitude) and phase).

In this study the average thermal diffusivity obtained from the four curves, $\alpha_{average} = 1.456 \times 10^{-3} \text{ cm}^2 \text{ s}^{-1}$ was in agreement with the literature $\alpha = 1.448 \times 10^{-3} \text{ cm}^2 \text{ s}^{-1}$ (Matvienko & Mandelis, 2005) and the difference is about 0.5-0.7%. This fact coupled with a small experimental error, $10^{-5} \text{ cm}^2/\text{s}$, indicate the accuracy of this technique in measuring the liquid thermal diffusivity of small volume samples. As can be seen in the figures, with increase the cavity length, the signal reaching the PVDF detector becomes smaller. However, the signal still has high magnitude even at the cavity length $L=0.05\text{cm}$.

5.4.1.3 Pyroelectric Signal Respect to Time

The typical PE signal was measured with respect to time to investigate the steady-state of the signal. The sensitivity of TWC technique was tested by maintaining the cavity length at about 100 μm , and the PVDF signal was recorded over 300 s. The experiment was carried out with a single drop of distilled water, Figure 5.15, and it can be seen that the PE signal is quite stable around 1.49×10^{-3} V with standard deviation 5.12×10^{-5} V.

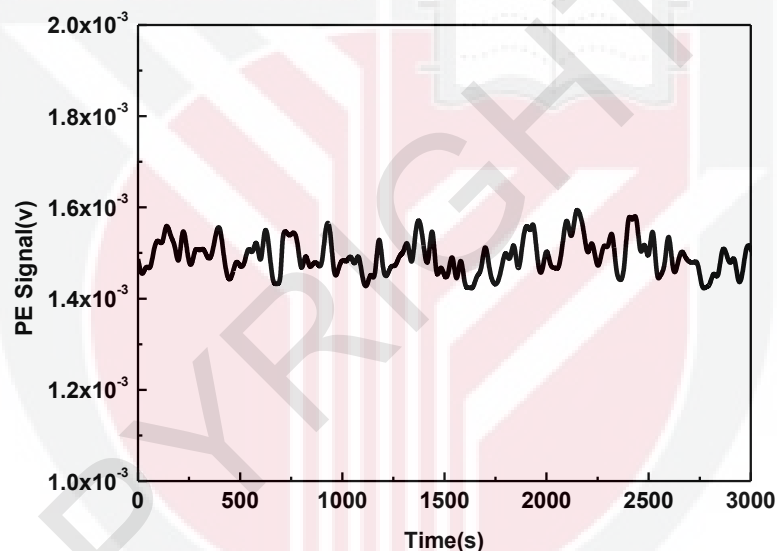


Figure 5.15. PVDF signals recorded vs. time for distilled water, the baseline is a steady-state signal various the times

5.4.2 Thermal Diffusivity and Conductivity Determination of Clay Containing Ag-NPs; Volume Fractions Effect

5.4.2.1 Sample Preparation and Characterization

As the first step of this study the thermal diffusivity of Ag NPs in clay suspension as a function of Ag NPs volume fractions was investigated. The thermal diffusivity

measurement was determined by the slope of the PE signal (Ln(amplitude) and phase) versus cavity length, and the thermal conductivity by the product of the volumetric specific heat and thermal diffusivity. The Ag/Clay nanofluids were prepared of 0.1, 0.2, 0.5% vol of Ag NPs, constant amounts of clay (MMT, Kunipia-F, Japan), were suspended in different volumes of 1×10^{-3} M AgNO_3 aquatic solution and were stirred for 24 h at room temperature. Freshly prepared NaBH_4 (4×10^{-2} M) solution was then added to the AgNO_3 in order to make a constant molar ratio of 1:4 of $\text{AgNO}_3/\text{NaBH}_4$ and stirring was continued for one hour. The suspensions were finally centrifuged, washed with double-distilled water and dried under vacuum overnight. Because Ag/clay suspension has more free Ag ions, and especially free NaBH_4 , therefore it needed to be washed and then dried in room temperature to release the excess materials, and then these powders were suspended again in water and dispersed with ultrasonicator in fluid forms. The ultrasound was used for between 0.5 and 1 h to ensure proper mixing of Ag NPs into the base fluids. All types of Ag NPs were found to be well dispersed into the base liquids and formed stable suspensions.

Figure 5.16 (a-c) shows the TEM images of Ag NPs with the corresponding average particle sizes of 4.19, 6.74, and 9.17 nm for Ag NPs volume fraction 0.1, 0.2 and 0.5 vol%, respectively. Ag NPs have spherical shapes in the TEM images, but clay has nanofiber shapes that can only be shown with HRTEM (Ahmad *et al.*, 2009). After synthesis Ag NPs between clay layers these layers exfoliation in the suspension, because their layered structure with high active surface area. The Ag NPs capped with the interlayer space of clay layers, therefore Ag NPs synthesis separately without any agglomeration with others NPs because nano-fiber structures of clay as

nanocomposites separate each one of the Ag NPs. Therefore the preparation of Ag/clay, as a very stable suspension in colloid form, is a suitable way to prepare practically applicable supported Ag particles as well as to control the particle size (Ahmad *et al.*, 2009). Increasing the volume fraction increased the sizes of Ag NPs, this statistical increase of particle size relative to the Ag NPs volume fraction can be attributed to the action of clay as an effective protective reagent. By adding increasing concentration, some of the Ag NPs are adsorbed on the basal plane of the clay layers and the rest is free in bulk solution. (Fan *et al.*, 2010)

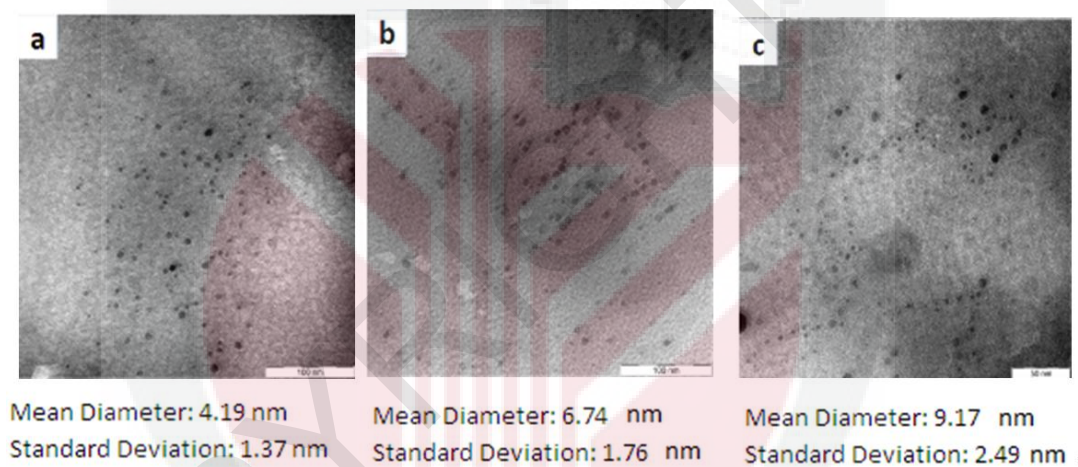


Figure 5.16. TEM images and the corresponding particle size distributions of prepared Ag NPs in clay suspension at different volume fractions [(a) 0.1, (b) 0.2, and (c) 0.5 vol%]

5.4.2.2 Thermal Diffusivity and Thermal Conductivity Measurement

The experimental system was calibrated using water and the thermal diffusivity was determined by using Equation 3.24 a-b, while, its thermal conductivity by using Equation 1.1. The clay suspension thermal conductivity as base fluid was calculated using the water heat capacity and density values of 4.15.J/gK and 1000.kg/m³,

respectively (Almond *et al.*, 1996). This assumption is being considered reasonable since only a small amount of clay was introduced in the water, i.e. 1 g clay in 1 liter of water. Table 5.2 shows a comparison of the measured and standard values of thermal diffusivity and thermal conductivity for water and clay suspension.

Table 5.2. Results of calibration with water and clay suspension

Fluid	Experiment		literature		Deviation (%)	
	α (10^{-3} cm ² /s)	K (W/mK)	α (10^{-3} cm ² /s)	K (W/mK)	α	K
water	1.439 ± 0.019	0.597 ± 0.019	1.445 ^[b]	0.60 ^[a]	0.4	0.5
clay	1.403 ± 0.021	0.582 ± 0.021	-	-	-	-

(Murshed *et al.*, 2005)^[a] (Balderas-Lopez *et al.*, 2000)^[b]

In this study thermal conductivity of water was 0.597 W/mK, and differed only by 0.5% with values described in literature. This fact coupled with a small experimental error, 0.019 W/mK, indicates high accuracy of this technique in measuring liquid thermal conductivity of small volume samples. The thermal conductivity of clay suspension, 0.582 W/mK, is slightly lower than that of water and this can be associated with larger clay suspension molecules which were introduced into the water, reducing the thermal conduction (Azmi, *et al.* 2006).

Figure 5.17 (a-b) shows the plots of logarithmic amplitude and phase versus the cavity length of Ag/Clay nanofluids at different Ag NPs volume fractions from 0 to 0.5 vol% in a thermally thick condition. The slopes of the PE signal (Ln(amplitude) and phase), and the thermal diffusivity values measured in the present work are summarized in Table 5.3. Both plots are linear with respect to cavity length and the curve of low Ag NPs volume fraction, 0.1 vol%, was close to that of clay suspension

at 0 vol %. As indicated by the gradient, the thermal diffusivities at low volume fraction are very close to each other except at highest Ag NPs volume fraction of 0.5 vol %.

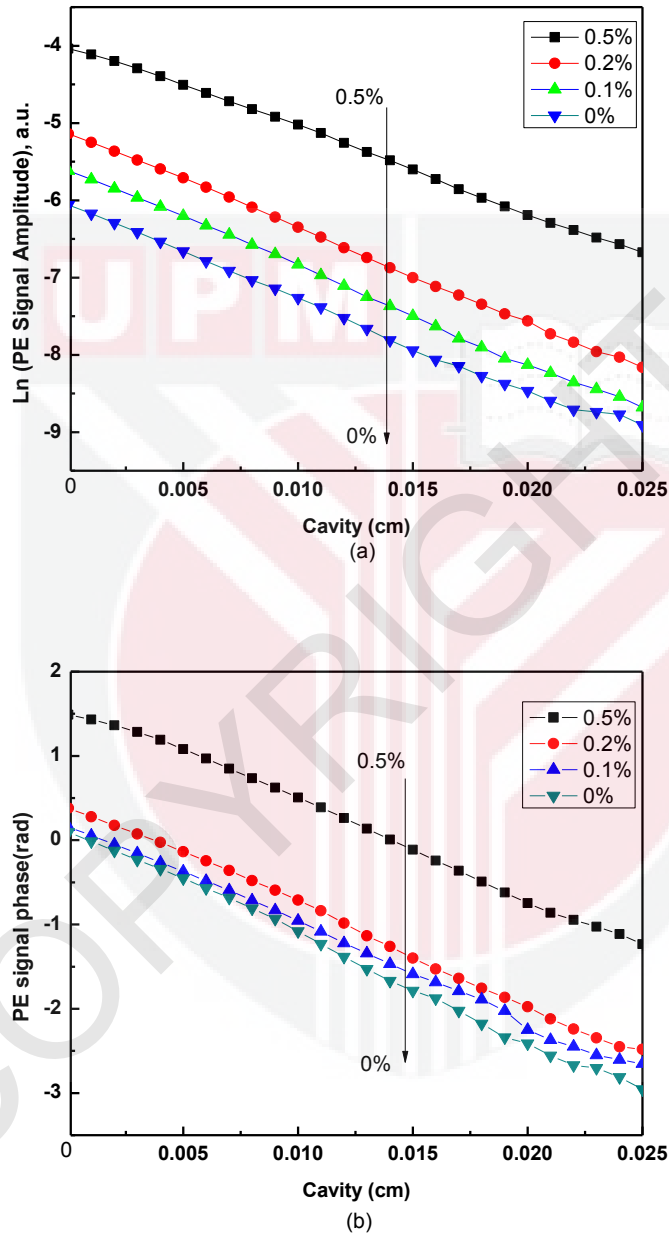


Figure 5.17. Typical (a) logarithmic amplitude and (b) phase as a function of the relative cavity length of Ag/clay nanofluids at different Ag NPs volume fractions [0, 0.1, 0.2, and 0.5 vol%]

Some of the data in Figure 5.17 can be redrawn into Figure 5.18 (a-b) which shows an overlay comparison of six similar cavity lengths from 0 to 0.025 cm of the logarithmic amplitude and phase for water and for five different Ag NPs volume fractions of Ag/Clay nanofluid from 0 to 0.5% vol.

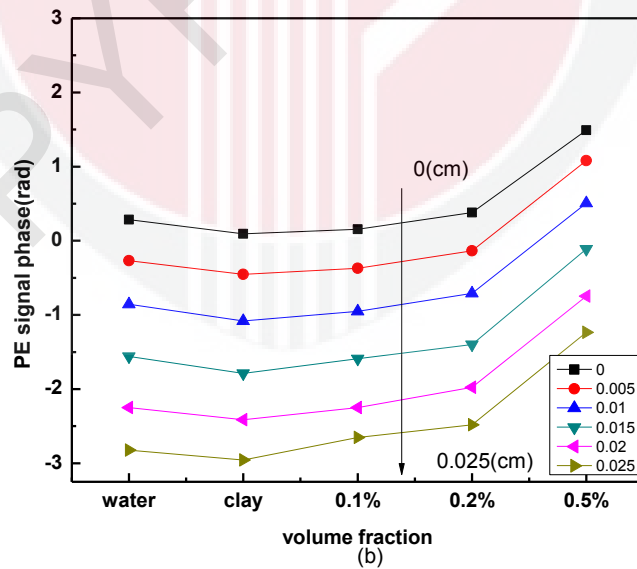
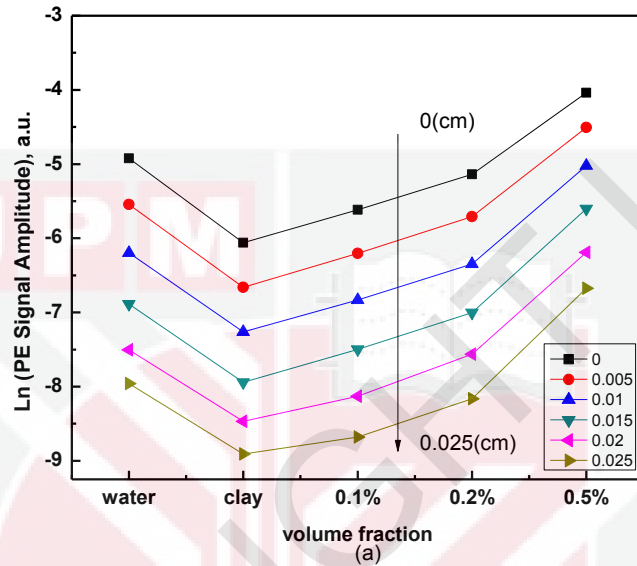


Figure 5.18: Comparison of six cavity length (0-0.025 cm) of the (a) logarithmic amplitude and (b) phase of water and Ag/clay nanofluids at different Ag NPs volume fractions [0, 0.1, 0.2, and 0.5 vol%]

In all samples, the reductions of PE amplitude and phase signals become obvious when the cavity length increases from 0 to 0.025 cm. The lowest signal limit is from clay suspension at 0.025 cm cavity length, which is closed the noise level and having an SNR of about 1.6. It can be seen also that the logarithmic amplitude and phase of clay suspension become reduced compared to that of water. This effect can be attributed to the larger molecules of clay suspension compared to the pure water, which results in reduction the heat conduction (Fan *et al.*, 2010). Both amplitude and phase signals from the nanofluids increase with the increases in Ag NPs volume fractions. It is worthwhile to note here that in OF-TWC technique, there are several factors that influence the linear behavior of the amplitude and phase data: laser intensity, cavity length, modulation frequency and thermal properties of the sample. The measurements were carried out under the similar condition of the experiment, such as cavity length and using fixed frequency. From Figure 5.18, it is clear that for all the nanofluids the difference between curves is due to the difference between Ag NPs volume fractions.

From analysis of Figure 5.17, the thermal diffusivity ratio of Ag/Clay nanofluids with respect to base fluid, $\alpha_{nanofluid}/\alpha_{basefluid}$, can be obtained, Figure 5.19. Here, the ratio increases substantially with Ag NPs volume fraction in clay suspension. Following this, the plots of thermal conductivities within the nanofluids for Ag NPs volume fractions of 0 - 0.5 %vol, Figure 5.20, can be determined. In the calculation, the effective volumetric specific heat of nanofluids can be determined by, (Murshed *et al.*, 2011)

$$(\rho C_p)_{eff} = [\phi_p \rho_p C_{p(p)} + (1 - \phi_p) \rho_f C_{p(f)}] \quad (5.1)$$

where C_p and ρ_i are the specific heat and density, respectively; p and f subscripts refers to particle and base fluid, respectively. From Table 5.3, the rate of thermal conductivity increment of this nanofluid system with respect to %vol Ag is about 0.38 W/m K per vol %. From this it can be said that the thermal conductivity of small volume of nanofluid have been successfully obtained by using OF-TWC technique.

Table 5.3. Summarized results for thermal properties of Ag NPs/ clay nanofluids at different AgNPs volume fraction

Volume fraction (%)	Δ_{phase}	$\Delta_{\text{amplitude}}$	Δ_{average}	α ($10^{-3} \text{ cm}^2/\text{s}$)	K (W/mK)	K_{HC}
0	126.48 ± 1.19	123.36 ± 0.75	124.92 ± 0.97	1.40 ± 0.02	0.582 ± 0.009	0.582
0.1	121.64 ± 0.86	118.14 ± 0.97	119.89 ± 0.91	1.52 ± 0.02	0.632 ± 0.009	0.584
0.2	119.98 ± 0.98	117.06 ± 1.27	118.46 ± 1.13	1.56 ± 0.03	0.646 ± 0.012	0.586
0.5	113.17 ± 0.89	108.21 ± 0.47	110.69 ± 0.68	1.79 ± 0.02	0.741 ± 0.009	0.591

The plot of effective thermal conductivities of experimental results compared to that calculated using HC model can be seen in also in Figure 5.20. The effective thermal conductivity, by HC model is expressed as, (Zhang *et al.*, 2006)

$$K_{\text{eff}} = K_f \frac{[K_n + (n-1)K_f - (n-1)(K_f - K_n)\phi_p]}{[K_n + (n-1)K_f + (K_f - K_n)\phi_p]} \quad (5.2)$$

Here, K_f and K_n are the thermal conductivity of fluid and particle respectively, and n for spherical particles is equal to 3. The HC model included the effect of particle shape and particle volume fraction on thermal conductivity of suspensions and does

not include the effect of particle size (Murshed *et al.*, 2011).

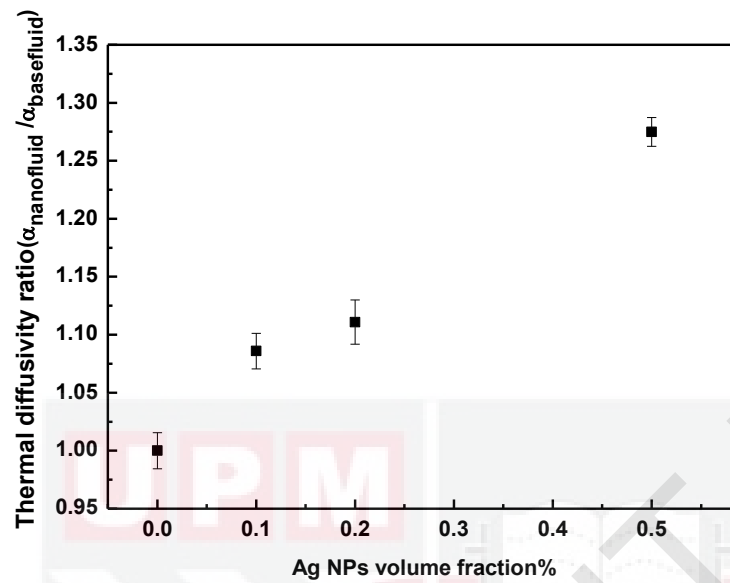


Figure 5.19. Thermal diffusivity ratio of Ag/clay nanofluid at different Ag NPs volume fractions [0, 0.1, 0.2 and 0.5 vol %]

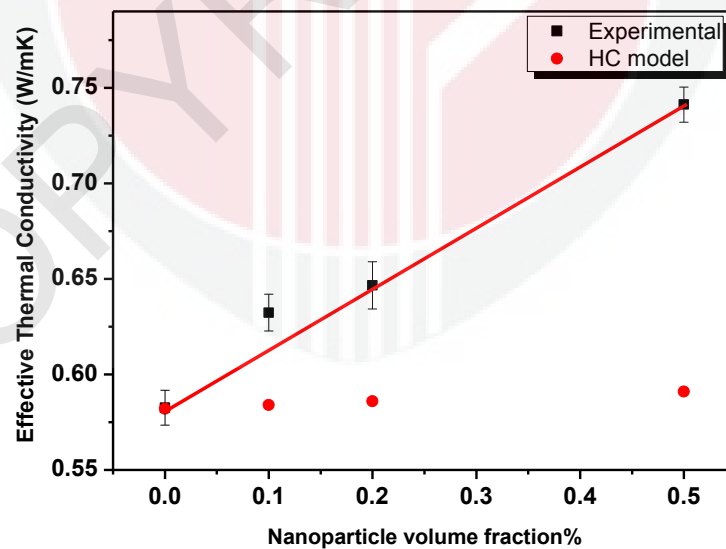


Figure 5.20. Thermal conductivity of Ag/clay nanofluid at different Ag NPs volume fractions [0, 0.1, 0.2 and 0.5 vol %] and the comparison with HC model

To calculate the effective thermal conductivity of Ag/clay nanofluid using HC

model, the Ag heat capacity, density, and thermal conductivity values of 0.233.J/gK, 10489.kg/m³, and 429.W/mK, respectively (Almond *et al.*, 1996). Results of these studies are presented in Table 5.4. The enhancement of effective thermal conductivity of suspension with nano particle size cannot be explained by HC model. This is because the HC model was developed only for milli- or micro-sized particles rather than for NPs size (Murshed *et al.*, 2011), taking in to consideration that the thermal conductivity in high agglomeration of NPs may agree well with the values predicted by the HC model (Zhang *et al.*, 2006). During the stochastic motion of the NPs suspension, aggregation and dispersion may occur between NP clusters and each nanoparticle. HC model gives a good description of systems with micrometer or larger-size particles, but fails to predict the measured thermal conductivity of nanofluids.

5.4.3 Agglomeration Effect on Thermal Diffusivity of Ag/Clay

In order to investigate the effect of NPs agglomeration on the thermal diffusivity of nanofluid, the container of PE cell was filled with 0.5% volume fraction of Ag/clay suspension and the PE signal of that liquid were then at 0 and after 1, 2 and 3 h. The thermal diffusivity was obtained by measuring the variation of the signal with cavity length, Figure 5.21. Various slope of the curve indicate different thermal diffusivity of nanofluid, and the results show a decrease in thermal diffusivity with the increase time of leave. The results of thermal diffusivity are summarized in Table 5.4. The thermal diffusivity and the thermal diffusivity enhancement ratio of the Ag/Clay 0.5 vol % after 1, 2, and 3 hours is shown in Figure 5.22 (a-b). It is clear that immediately after dispersion (0 h) the thermal diffusivity is at the highest value,

$(1.571 \pm 0.011) \times 10^{-3} \text{ cm}^2/\text{s}$, and thermal diffusivity of nanofluid decreases with increasing time of leave, and it returns to its base fluid thermal diffusivity value over time, the thermal diffusivity ratio close to 1 (Figure 5.22b). This value reaches to $(1.456 \pm 0.007) \times 10^{-3} \text{ cm}^2/\text{s}$ at 3 hours after dispersion. It is defined as agglomeration effect in that the thermal diffusivity gradually decreases around 7.3% after 3 h time of leave.

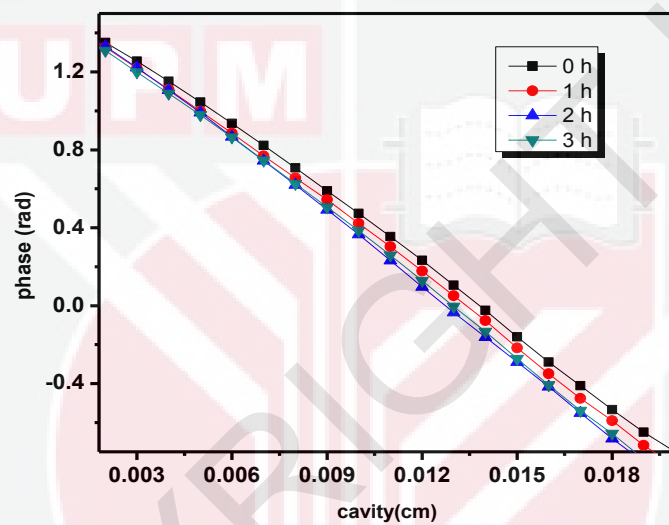


Figure 5.21. Phase of signal for measuring thermal diffusivity of Ag/clay nanofluid in 0.5% vol in various times (0, 1, 2, 3 h) after dispersion, the slope gradient of PE phase was changed in nanofluid of different time of leave.

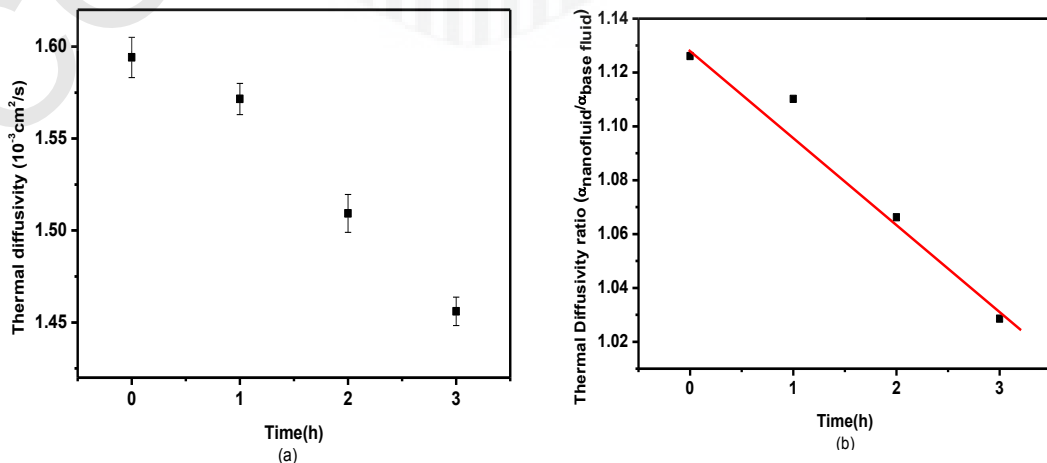


Figure 5.22. (a) Thermal diffusivity (b) and Thermal diffusivity ratio of Ag/clay nanofluid at different time of leave (0, 1, 2, and 3 h)

Table 5.4. Summarized results for thermal properties of Ag NPs/ Clay nanofluids at different different time of leave (0, 1, 2, and 3 hours).

Time h	A_{phase}	$A_{\text{amplitude}}$	A_{average}	α ($10^{-3} \text{ cm}^2/\text{s}$)	$\frac{\alpha_{\text{nanofluid}}}{\alpha_{\text{basefluid}}}$
0	116.4 ± 1.0	117.9 ± 0.6	117.2 ± 0.8	1.594 ± 0.011	1.126
1	117.3 ± 0.8	118.7 ± 0.5	118.0 ± 0.6	1.571 ± 0.008	1.110
2	119.4 ± 0.6	121.4 ± 1.0	120.4 ± 0.8	1.509 ± 0.010	1.066
3	121.6 ± 0.7	123.6 ± 0.5	122.6 ± 0.6	1.456 ± 0.007	1.029

The smaller the radius of gyration of the clusters suspended in the fluid, the larger the thermal diffusivity of the nanofluid because of the fact that the smaller clusters move faster, therefore, the energy transport inside the liquid becomes stronger, due to the Brownian theory (Okeke *et al.*, 2011).

5.4.4 Dispersion and Fragmentation Effect on Thermal Diffusivity of Nanofluids

Most scientists use commercially-available metal oxide NPs. By using these NPs, the nanofluids can be synthesized by using simple process of two steps; in this process, dry NPs are dispersed into a fluid. This method may result in a large degree of nanoparticle agglomeration. To reduce the agglomeration, several techniques are developed; the ultrasonic dispersion technique or the NPs fragmentation processes using laser irradiation technique, in low concentration of NPs are important to produce stable nanofluids.

5.4.5 Effect of Ultrasonication on Thermal Diffusivity of Al₂O₃ Nanofluids

In the dispersion of nanopowders into base fluid with stirring or ultrasonication, many studies on the potential uses of ultrasound baths have been reported in the literature (Xuan & Li., 2000; Nguyen *et al.*, 2011; Huang & Yang, 2008) in this study, the influence of irradiation modes (bath-sonication and probe-sonication) of ultrasonication on nanofluid thermal diffusivity of nanofluids and also cluster size of Al₂O₃ NPs in low concentration in water were investigated.

5.4.5.1 Sample Preparation and Characterization

Al₂O₃ NPs (11nm, 99%, Nanostructured and Amorphous Materials, Inc.) 0.5 wt% were dissolved in deionized water and magnetically stirred vigorously until a clear solution in about 1 h the suspension is ultrasonicated for 30 min using probe ultrasonic (VCX 500, 25 kHz, 500 W), called sample P, and using bath ultrasonic (POWERSONIC, UB-405, 40 KHz, 350 W), called sample B, respectively. Unlike the bath sonication that was performed at room temperature, the tip probe sonication has higher amplitudes and more effective creation of cavitation and heating. Thus, the sample was allowed to cool using ice-water during the sonication process. After each ultrasonication, the mean particle size was measured using Nanophox Machine (Sympatec GmbH, D-38678) and an average was taken from at least three measurements. The morphology of the alumina clusters was characterized by TEM and the absorption properties of the Al₂O₃ nanofluids were analyzed using UV–Vis spectrophotometer.

Figure 5.23 shows the particle size distribution (PSD) of Al_2O_3 suspensions, 0.5% vol, in the treatment by bath (sample B) and probe (sample P) sonication. PSD of sample B have smaller density distribution and larger NPs agglomerates size than PSD of sample P. The significant broadening FWHM of the size distribution of sample B would suggest the formation of small clusters and indicates a greater degree of polydispersity (Hassen & Davis , 1989).

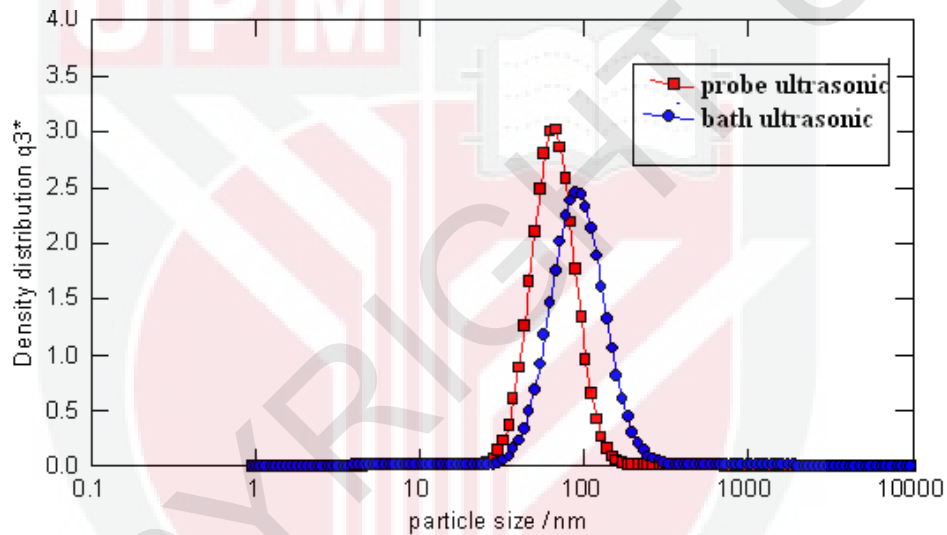


Figure 5.23. PSD of alumina suspensions in the treatment by bath (sample B) and probe (sample P) sonication.

Figure 5.24 shows the distribution density function and the cumulative distribution of sample P. The center of gravity of the density curve gives the mean sphere diameter $x = 62$ nm with a standard deviation of 3 nm. Using the probe sonication on sample P, the peak shifted towards the smaller fragments size and the size distribution remained relatively sharp, due to large agglomerates were completely broken down into smaller components, so their size has a reasonably uniform distribution.

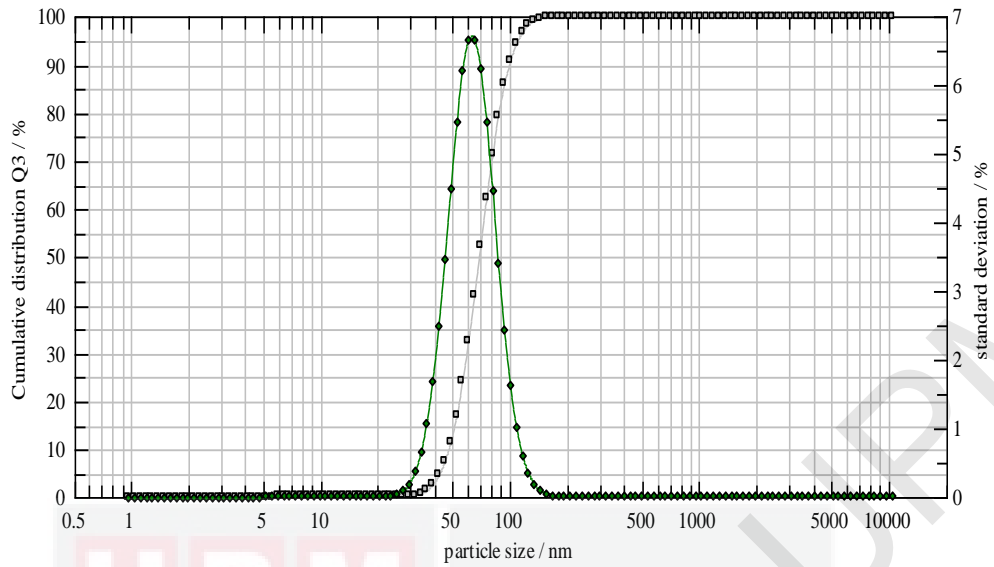


Figure 5.24. Distribution density function of sample P, in the treatment by probe sonication, measured with Nanophox Machine

The measurement of the absorbency has become an important evaluation for understanding the dispersion behavior of alumina particles in a liquid medium (Zhu *et al.*, 2009). The absorption spectra of the Al_2O_3 obtained from bath and probe sonications were shown in Figure 5.25. The height of absorption peak increases from sample in the treatment by probe ultrasonic, which may be attributed to the increase of quantity of Al_2O_3 NPs assembled within the fluid, as proven by the Nanophox results.

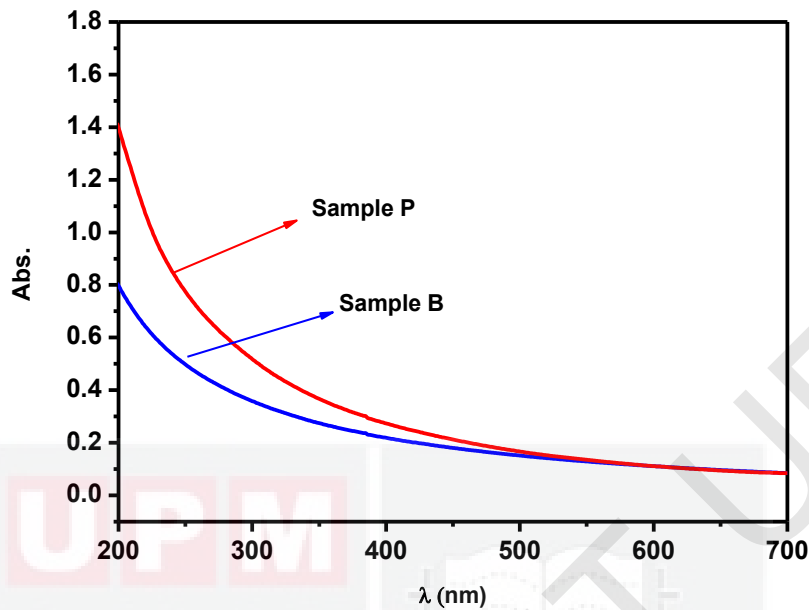


Figure 5.25. UV–Vis absorption spectra of the Al₂O₃ nanofluids, in the treatment by bath (sample B) and probe (sample P) Sonication, respectively

Figure 5.26 shows the TEM analysis of the morphology of the synthesized Al₂O₃ nanofluids using (a) bath and (b) probe sonications at 30 min. As it can be seen in the TEM image, most of the Al₂O₃ particles are spherical and are connected to each other to form a porous structure ranging in size from 1 μm to larger (Figure 5.26 (a)) and the probe sonication effectively reduced the particle size to below 100 nm (Figure 5.26 (b)). As seen in the figures, the ultrasonic bath sonication proved to be almost ineffective in size reduction, while, the ultrasonic probe was more effective in reducing particle size. However, in all nanofluids cases, the measured particle sizes are larger than the nominal particle size claimed by the vendor. This indicates that oxide NPs in water are agglomerated and that the hard aggregates cannot be broken down into individual NPs under these operating conditions or even at very high energy input (Nguyen *et al.*, 2011).

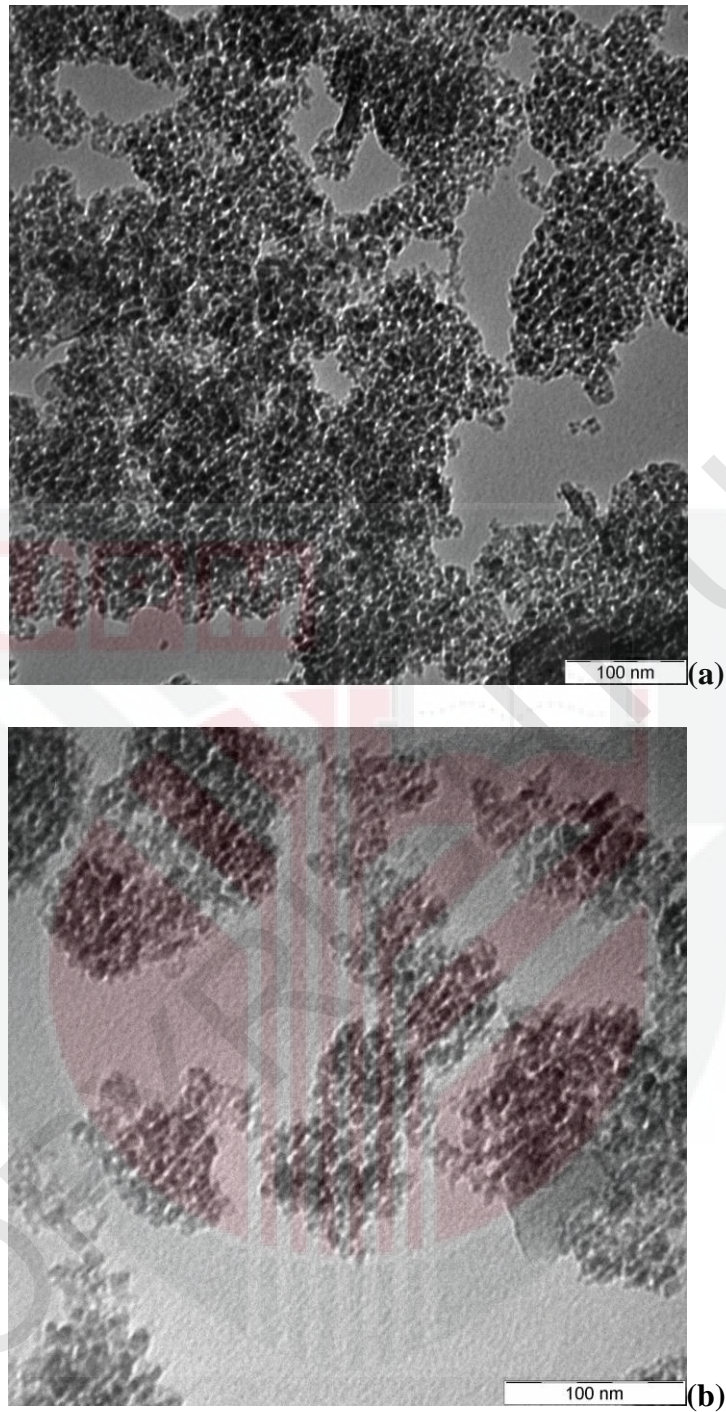


Figure 5.26. TEM images of alumina NPs (a) bath (b) probe ultrasonication at 30 min of sonication

5.4.5.2 Thermal Diffusivity Measurement

Figure 5.27 (a-b) shows the plots of logarithmic amplitude and phase, versus the cavity length at 6.8 Hz, of Al_2O_3 nanofluids in the treatment by bath (sample B) and

probe (sample P) sonications, respectively. The thermal diffusivity values were calculated from the slopes of the linear part of the logarithmic amplitude of the signal curves. The result of thermal diffusivity of these samples is summarized in Table 5.5.

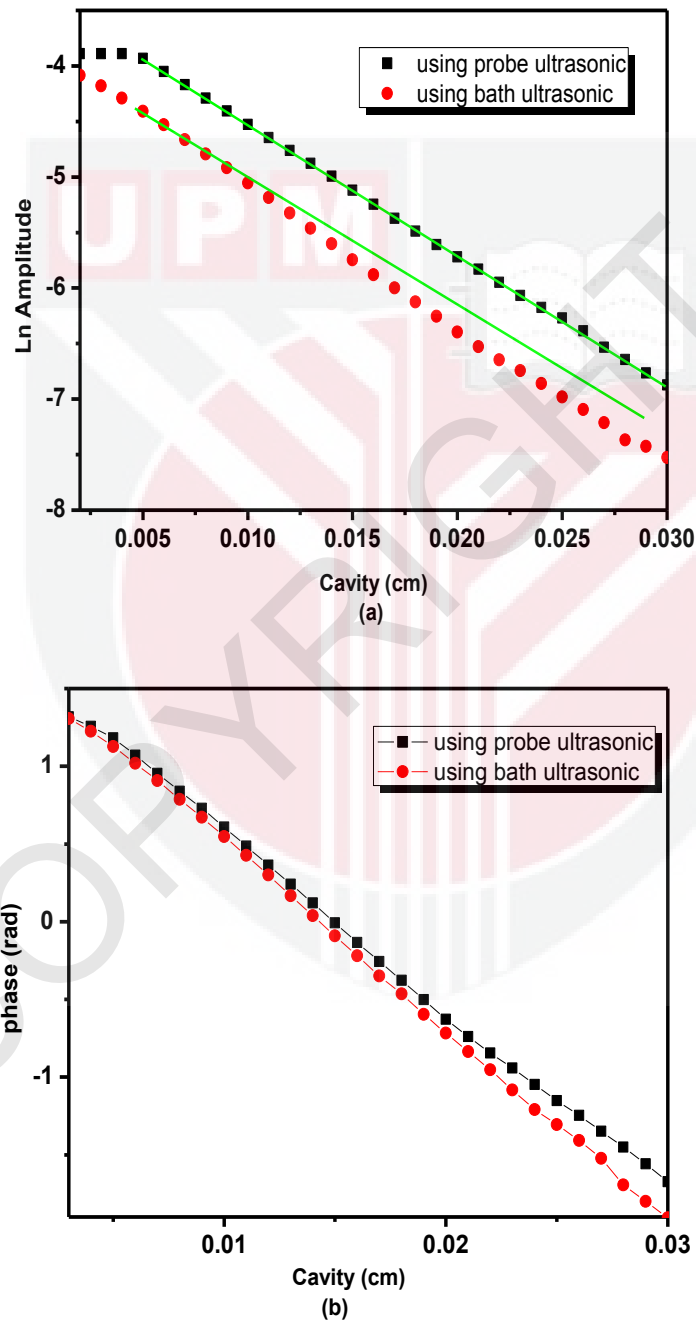


Figure 5.27. Typical (a) logarithmic amplitude and (b) phase as a function of relative cavity length of Al_2O_3 nanofluids in the treatment by bath (sample B) and probe (sample P) Sonication, respectively

Table 5.5. Summarized results of thermal diffusivity of Al₂O₃ nanofluids in the treatment by bath (B) and probe (P) Sonication

Code of Sample	Slope	Thermal diffusivity (cm ² /s) × 10 ⁻³	Error Δá
P	115.222	1.609	0.037
B	119.391	1.498	0.035

The results show that the thermal diffusivity of sample B ($1.498 \times 10^{-3} \text{ cm}^2/\text{s}$) and of sample P ($1.609 \times 10^{-3} \text{ cm}^2/\text{s}$) are higher than that of water ($1.445 \times 10^{-3} \text{ cm}^2/\text{s}$) (Balderas-López *et al.*, 2001). This is because the particle surface (the heat transfer area) becomes larger due to NPs more widely dispersed into water through probe sonication (Zhu *et al.*, 2009).

5.4.6 Effect of Laser Irradiation on Thermal Diffusivity of Al₂O₃ and CuO Nanofluids

Since the size of NPs in a nanofluid critically affects their thermal properties, particle fragmentation processes that reduce the particle size can be employed to enhance the thermal properties of nanofluids (Hong *et al.*, 2007). For example, CuO, Al₂O₃, TiO₂, ZnO, MgO, CaO, Ag₂O, and CeO₂ that have been tested for their antimicrobial activity (Raghupathi *et al.*, 2011; Ravikumar *et al.*, 2011) are used in a cell environment with laser irradiation. Therefore, investigation of the stability and localized heating effect due to the laser irradiation on the particle is required (Honda *et al.*, 2011). The effect of laser light on NPs in solution has been studied to change the size, melt, or fragment NPs (Inasawa *et al.*, 2005, Gonella *et al.*, 1996, Hodak *et al.*, 2000, Link *et al.*, 2000), but so far in most experiments only ns pulsed laser light at different wavelengths with pulse laser has been proposed by a number of researchers (Liu *et al.*, 2009; Bosbach *et al.*, 1999). In the case of the pulse of laser irradiation the NP is limited and heated only during each pulse, and a pulse plays a self-limiting

role for the formation of NPs and also the efficiency of NPs production. Therefore, a large number of laser pulses as well as long irradiation times (typically ranging from 15 to 120 min) are required to change the morphology, size and size distribution of NPs.

5.4.6.1 Sample Preparation and Characterization

In this section, for the first time to our knowledge, fragmentation of colloidal NPs by cw laser was investigated to study the morphology, size and size distribution and also the behavior of thermal diffusivity of colloidal Al_2O_3 and CuO NPs under CW laser irradiation time. For this purpose, Nanofluids were prepared by dispersing 0.5 g metal oxide NPs powder Al_2O_3 (11nm) or CuO (50 nm) into 25ml DW and 1vol% PVP was added to help stabilize the nanofluids. The samples were then subjected to probe sonication to obtain uniform dispersions. The solutions were stirred and irradiated along the vertical axis with a cw DPSS laser (532 nm) with a maximum power of 0.2W. The laser at 10 Hz was focused on around 0.12 cm of the solution surface in the quartz cuvette by a lens with a focal length of 20 cm.

The results of laser fragmentation process are analyzed by TEM images, the average colloidal NPs was estimated from the Nanophox analyzer and an average was taken from at least four measurements, in conjunction with TEM, to evaluate irradiation effects of agglomeration change in the presence or absence of a laser beam. The optical absorption spectrum of the solution containing the NPs was also investigated. The thermal diffusivity of each nanofluid was measured by cavity scanning.

5.4.6.1.1 Laser Irradiation on Al₂O₃ Nanofluids

The TEM images photographs of Al₂O₃ NPs in DW solutions taken before and after irradiation with 20 min and 90 min duration laser are shown in Figure 5.29.

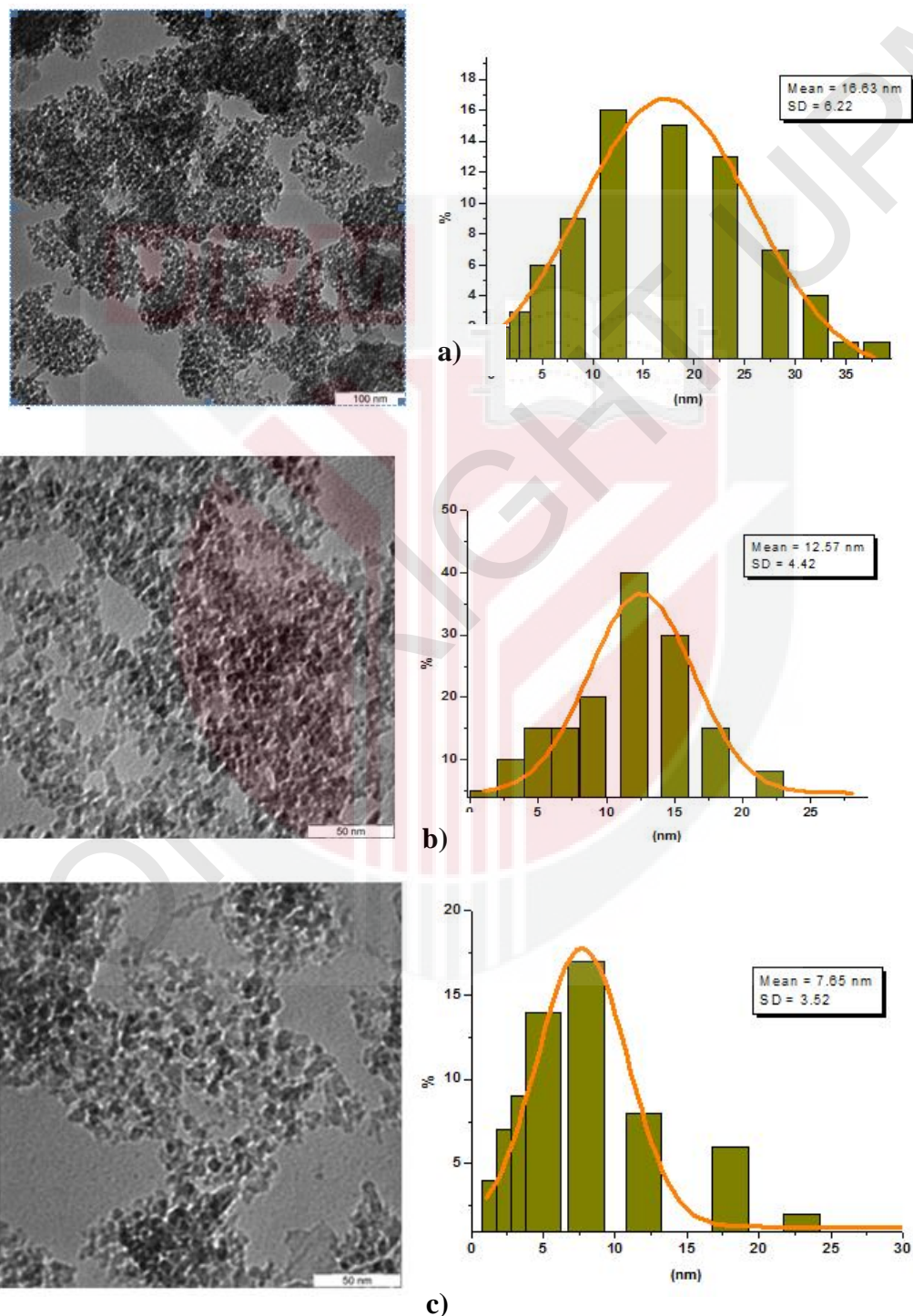


Figure 5.28. The TEM images and the relative size histograms of the Al₂O₃-NPs (a) before (16.63±6.22 nm), and after (b) 20 (12.67±4.42 nm) and (c) 90 min (7.65±3.52 nm), respectively, of laser irradiation

It can be seen that the collected material is composed of clusters of near spherical shape particles, dispersed in a highly porous material and sized from 100nm or larger observable in Figure 5.28 (a). After irradiation of 20 and 90 min of Al₂O₃ nanofluid the porous material range was brought down to below 50 nm, Figure 5.28 (b-c). Figure 5.28 (c) shows Al₂O₃ NPs almost uniform size and narrow size by distribution after 90 min irradiation as a result of absorption of laser energy and leading to fragmentation of particles (Liu *et al.*, 2009).

The hydrodynamic diameters of Al₂O₃ particles and the relative dispersion of NPs in deionized water solution in 3 times measurement were monitored and recorded by Nanophox analyzer. The hydrodynamic diameters from sample without irradiation exhibited significant NPs dispersion size from 69 to 97 nm. In the sample after 20 min irradiation the dispersion size shifts to closer size 75 to 96 nm, and for 90 min irradiation the PSD shifts very close together from 91 to 95, due to decrease of the clusters size. As can be seen in Figure 5.29, the changes in hydrodynamic diameter of particles in sample after 90 min irradiation made the solution more homogeneous than the others. However, hydrodynamic diameter mainly indicates the NPs agglomeration and was different compared to diameters measured via TEM, because only if the number of particles is high enough, they can be represented in the measured hydrodynamic size distribution. Figure 5.30 shows the distribution density function and the cumulative distribution of nanoparticle suspension (a) in before (b) after 20 min and (c) after 90 min irradiations. The gravity of the density curve gives the mean sphere diameter. In addition, a narrow PSD is obtained, the particles for 90 min irradiation had a sharp interface indicating a narrow distribution of particle diameters shapes (Figure 5.30c), while the particles before irradiation had a broadly spread interface indicating a greater degree of polydispersity (Figure 5.30a).

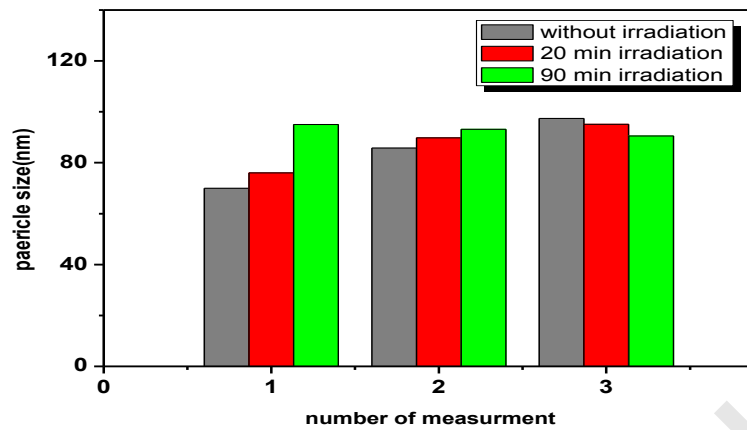


Figure 5.29. The hydrodynamic diameters of Al₂O₃ nanofluids measured 3 times before irradiation, after 20 min and after 90 min irradiation

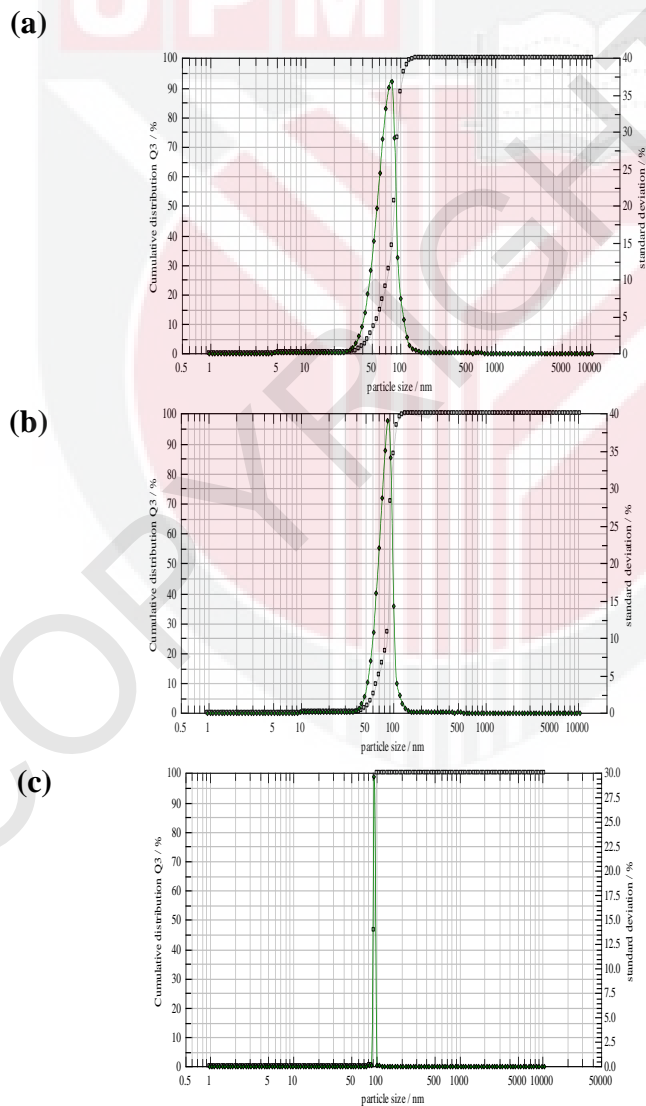


Figure 5.30. The distribution density and the cumulative distribution of Al₂O₃ NPs suspension (a) before (b) after 20 min and (c) after 90 min irradiation. The center of gravity of the density curve gives the mean sphere diameter.

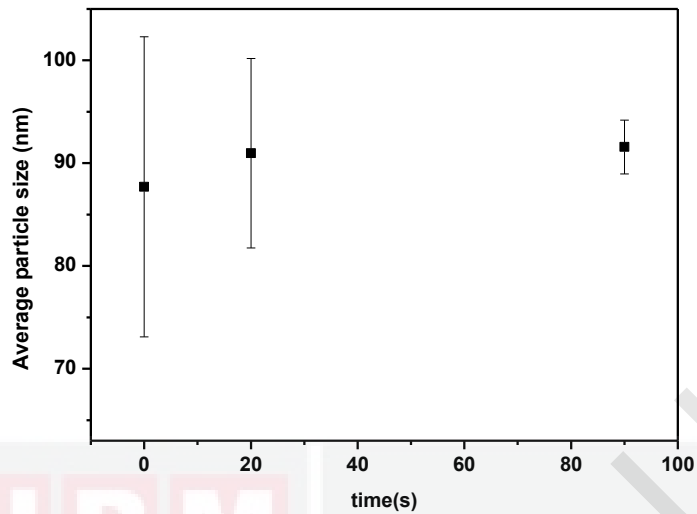


Figure 5.31. Hydrodynamic diameter distribution of Al₂O₃ NPs from Nanofluid before irradiation of 87.7±14.59 nm, after 20 min of 90.97±9.21 nm, and after 90 min irradiation of 91.57±2.61 nm.

Figure 5.31, shows the hydrodynamic diameter distribution of Al₂O₃ particles from nanofluids with diameter of 87.7±14.59 nm, 90.97±9.21 nm 91.57±2.61 nm for the before, 20 and 90 min irradiations, respectively. The standard deviations, σ , in the particle diameter are 16.6% (without irradiation), 10.1% (20 min irradiation), and 2.8% (90 min irradiation). Following a convention advocated by Murray and Bawendi (2000), samples with $\sigma < 10\%$ in diameter are referred to as monodisperse. This can confirm the stability of the sample prepared under 90 min irradiation. Also, the standard deviations of NPs are reduced exponentially by increasing laser irradiation time, where the standard deviations of NPs can be given as, $\sigma = \sigma_0 e^{-kt}$, where, σ_0 is the standard deviations of NPs before irradiation, t is the irradiation and k is the constant value. Figure 5.32 shows the plot of $\ln(\sigma/\sigma_0)$ vs laser irradiation time of Al₂O₃ nanofluid. The plot is linear with respect to irradiation time, with a constant value $k = -0.018 \text{ min}^{-1}$.

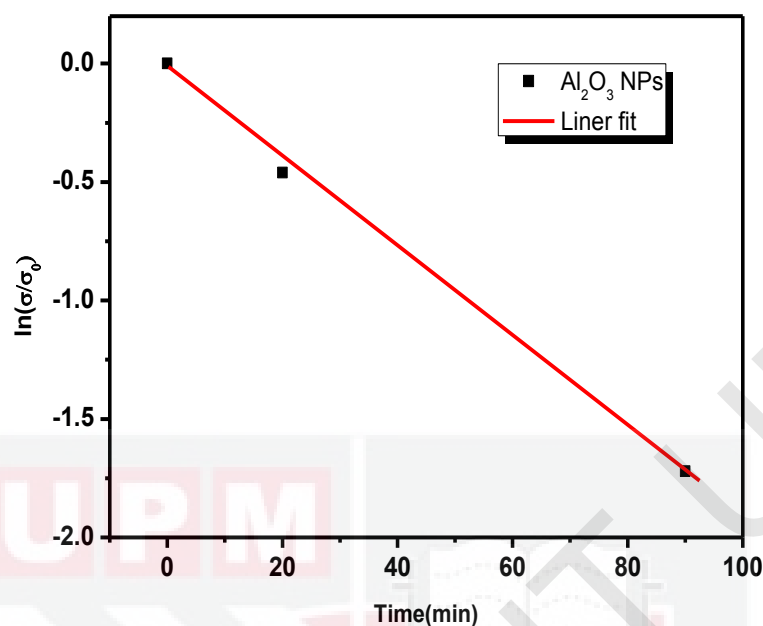


Figure 5.32. $\ln(\sigma/\sigma_0)$ vs laser irradiation time of Al_2O_3 nanofluid

Therefore, the obtained results show the ability of laser irradiation to reduce size distribution and therefore, size controller. However, the effect of laser irradiation on the distribution size is more than on the size of particles (Tsuji *et al.*, 2003). The comparison of the size information obtained by using TEM and Nanophox analyzer suggests that the TEM provides a number average diameter of the dry particles, while Nanophox analyzer provides an intensity weighted average diameter that is always larger than the number of average diameters of that sample due to the hydrodynamic layer on the particles. Figure 5.33 shows the UV-Vis absorption spectra of the Al_2O_3 nanofluids from without and with 20 and 90 min laser irradiation. Optical spectra of the original Al_2O_3 nanofluid (without irradiation) as a reference, exhibit strong absorptions in the UV range and its low absorption below wavelengths of 300 nm, which are consistent with other literature (Kusuma *et al.*, 2009).

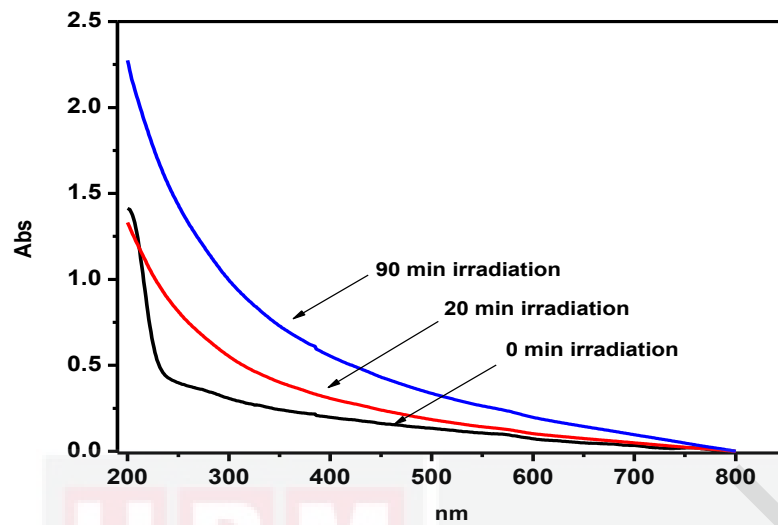


Figure 5.33. Optical absorption spectra of the Al_2O_3 NPs prepared in DW at various irradiation times

As shown in Figure 5.33, the absorbance was found to increase exponentially with the increasing laser irradiation, and the slope of curve increases with the increase in irradiation time, which may be attributed to the increases of the quantity of Al_2O_3 NPs assembled within the fluid, hence more stable the suspension (Zhu *et al.*, 2009), as proven by the Nanophox results. For a sample with poor stability, the absorption of nanofluids is at the minimum, therefore agglomeration between particles and the dispersion stability is poor. This spectral change indicates that the agglomerations of NPs are reduced more under irradiation of the laser (Mafuné *et al.*, 2001).

5.4.6.1.2 Laser Irradiation on CuO Nanofluids

Figure 5.34 shows the TEM images and the relative size histograms of the CuO-NPs in deionized water solutions taken before and after 20 and 90 min of laser irradiation (a): 0 min (47.45 ± 26.15 nm), (b): 20 min (47.15 ± 20.71 nm) and (c): 90 min

(45.65±17.4 nm), respectively.

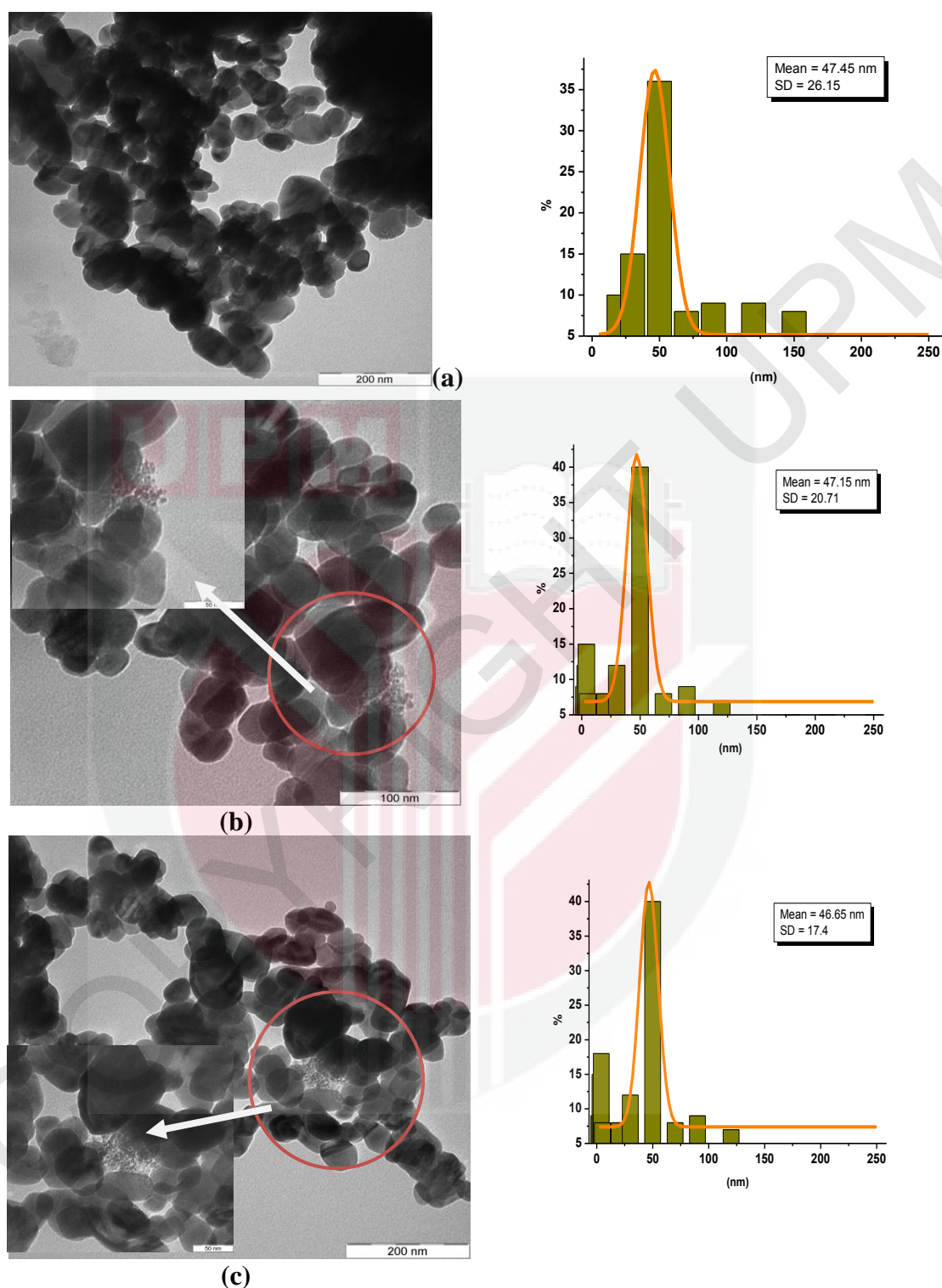


Figure 5.34. TEM images and the relative size histograms of the CuO-NPs before and after 20 and 90 min of laser irradiation (a): 0 min (47.45±26.15 nm), (b): 20 min (47.15±20.71 nm) and (c): 90 min (45.65±17.4 nm), respectively. Clearly (b) and (c) shows some small particles resulting from the fragmentation process and the breakup of these aggregations

The CuO nanofluid before irradiation was formed with a high agglomeration, Figure 5.34 (a). Figure 5.34 (b-c) shows some small particles resulting from the fragmentation process and the breakup of these aggregations, but there is no change in the NPs shapes, but there is a slight reduction in the mean size.

In Figure 5.35 the hydrodynamic diameters of CuO particles and the relative dispersion of NPs in solution measured three times were monitored and recorded by Nanophox analyzer. The hydrodynamic diameters from sample without irradiation exhibits significant dispersion size of particles from 93 to 187 nm. In the sample after 20 min irradiation the dispersion size shifted close to size 85 to 179 nm, and after 90 min irradiation the particles size dispersion shifted very close together from 159 to 182 nm, due to decrease of clusters size.

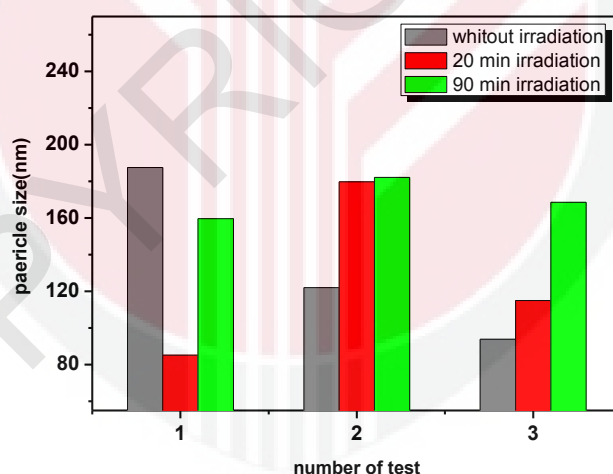


Figure 5.35. The hydrodynamic diameters of CuO nanofluids measured 3 times for before, after 20 min and after 90 min laser irradiations

In Figure 5.36, the distribution density function and the cumulative distribution of nanoparticle suspension in the (a) before (b) after 20 min and (c) after 90 min irradiation are shown. The particles after 90 min irradiation have a sharp interface indicating a narrow distribution of particle diameters (Figure 5.36(c)).

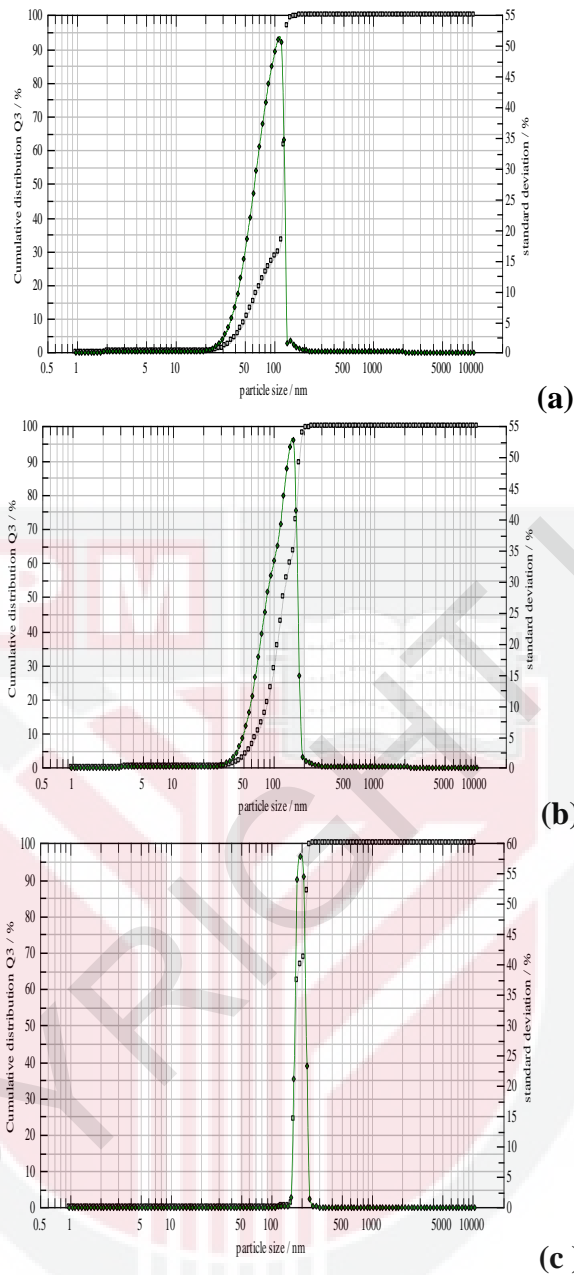


Figure 5.36. The distribution density and the cumulative distribution of CuO nanoparticle suspension in the (a) before (b) after 20 min and (c) 90 min irradiation. The center of gravity of the density curve gives the mean sphere diameter.

Figure 5.37 shows average CuO particle size of TEM result and Nanophox results (Hydrodynamic diameter distribution) of particles before irradiation and after 20 and 90 min irradiation. The TEM results shown, the changes in particle size is negligible in sample as a function of irradiation time, this supports the realization that the laser light inhibits the growth of the nanoparticles, the mechanism of the particle

fragmentation was also proposed. The hydrodynamic diameter distribution of CuO nanofluids are 134.49 ± 55.39 , 132.32 ± 35.51 , and 150.84 ± 15.31 nm for before, after 20 min, and after 90 min irradiations, respectively. The standard deviations in the particle diameters shown in the figure are 41.1, 26.8, and 10.1% for before, after 20 and 90 min irradiations, respectively. Historically, most oxide particles with $\sigma < 10\%$ in diameter are referred to as monodisperse. This can confirm the stability of the sample prepared under 90 min irradiation times.

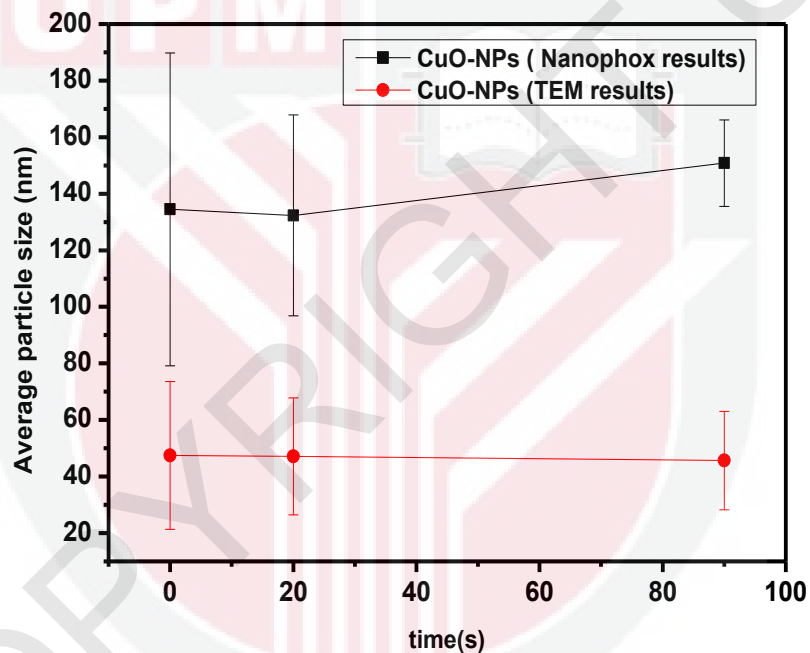


Figure 5.37. Average CuO particle size of TEM result and Nanophox results (Hydrodynamic diameter distribution) of particles before irradiation and after 20 and 90 min irradiation.

Figure 5.38 shows the plots of $\ln(\sigma/\sigma_0)$ vs laser irradiation time of CuO nanofluid, plot is liner with respect to irradiation time with a constant value $k = -0.014 \text{ min}^{-1}$.

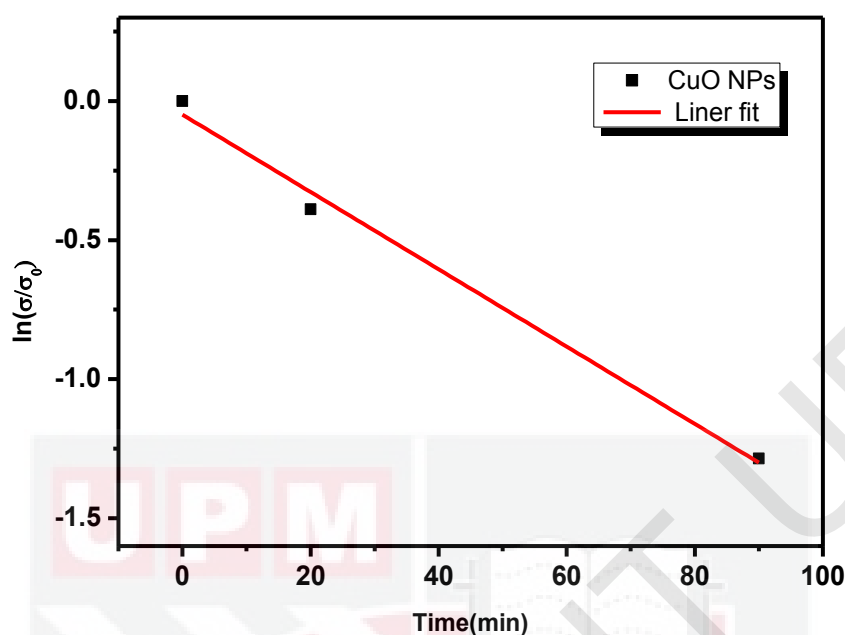


Figure 5.38: $\ln(\sigma/\sigma_0)$ vs laser irradiation time of CuO nanofluid

The absorption spectrum obtained for the CuO nanofluid before, after 20 min and after 90 min irradiation is shown in Figure 5.39. The characteristic CuO of SPR band was detected around 200 nm, while, CuO was characterized by sharp peak appearing at around 250 nm (Dadgostar *et al.*, 2008), this might be due to smaller particle size in this examination and sharp peak indicating that the particles have relatively narrow size distributions. Since only one absorption peak was obtained, the particles were mainly spherical (Pyatenko *et al.*, 2007), in agreement with previously discussed TEM results. Absorption spectra show that the intensity of the absorption peak due to the SPR of CuO NPs increases with increased irradiation time. The peak due to SPR became more pronounced and highly symmetrical, showing the presence of monodisperse CuO NPs after 90 min irradiation.

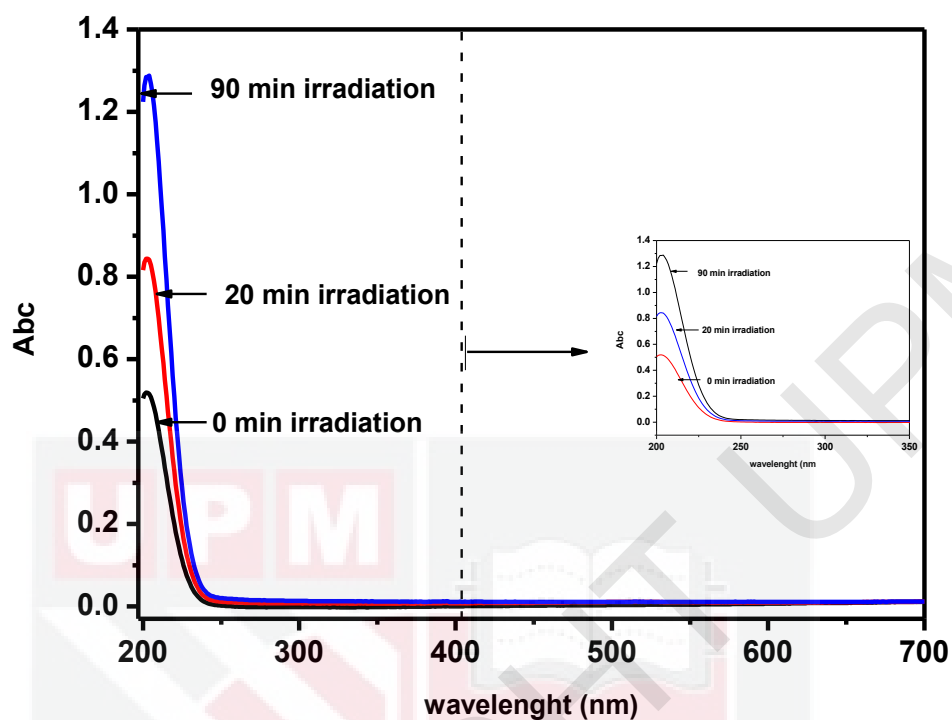


Figure 5.39. Optical absorption spectra of the Al_2O_3 NPs prepared in DW at various irradiation times

As shown in the UV–vis spectra, the SPR peak increases as the laser irradiation time increases, indicating an increase in the amount of CuO particles with very small sizes or the efficiency of particle formation increases at higher repetition rates (Darroudi *et al.*, 2011). In principle, irradiation with a given laser photon energy excites and heats NPs of certain sizes or/and shapes and leads to diffusion and evaporation of surface atoms. Thus, suitable size of NPs can be achieved.

5.4.6.2 Mechanism of Fragmentation

The mechanism of fragmentation can be summarized as in Figure 5.40. In principle, the NPs were excited and heated by irradiation of a given laser photon energy with some heat loss to the surrounding water, while absorption of energy of laser light by

the particles can cause further fragmentation of the particles (Akman *et al.*, 2011). This would suggest that there was absorption of the laser energy by the NPs in the longer exposure time (Liu *et al.*, 2009). The fragmentation of the agglomerates takes place via a direct absorption of the laser with an end result of almost uniform in size distribution as seen in figures of Nanophox and TEM results.

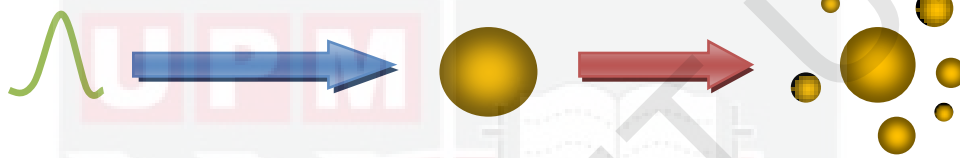


Figure 5.40. The NPs after laser irradiation into smaller fragments; the mechanism of fragmentation

The NPs size decreases toward the smallest possible diameter as the laser time irradiation increases. In addition, the distribution of particle also decreases to the increase of laser irradiation time, as also has been reported by Kamat *et al.* (Kamat *et al.*, 2002). Hence, considerable research has been directed towards decreasing the size of particles using various nanosecond and femtosecond lasers running at different wavelengths (Akman *et al.*, 2011; Liu *et al.*, 2004; Saetveit *et al.*, 2007). Coincidentally, the exactly the same result was obtained. As a result for both the nanofluids (Al_2O_3 and CuO) the laser irradiation time affected mainly the particles rather than their size. This is probably because effect of the laser irradiation on fragmentation of agglomerated particles to the smaller NPs and increasing the total number of particles in the solution.

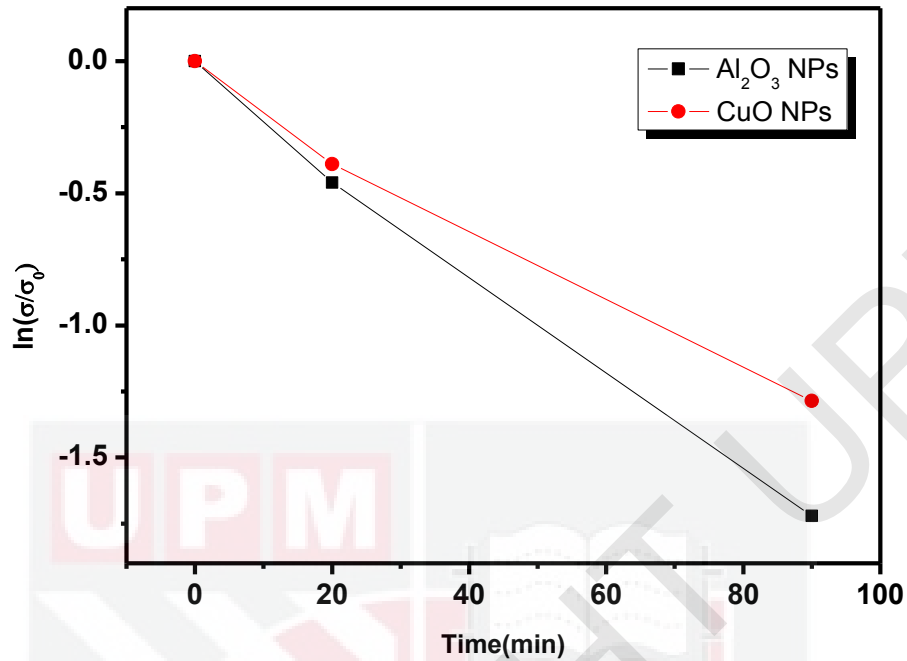


Figure 5.41. $\ln(\sigma/\sigma_0)$ vs laser irradiation time of Al₂O₃ and CuO nanofluid

Figure 5.41 shows the varied size distribution of the of Al₂O₃ and CuO nanofluids in different laser irradiation times, thus indicating the effectiveness of laser irradiation on the fragmentation of Al₂O₃ NPs in fluid is more than CuO NPs in fluid. The reason for this could be the higher density of CuO compared to Al₂O₃, which may explain the low fragmentation by laser irradiation.

5.4.6.3 Thermal Diffusivity Measurement

In order to measure thermal diffusivity of nanofluids before and after laser irradiation, first, the experimental setup need to be calibrated by using distilled water as a standard liquid. The calculated average from PE amplitude and phase of distilled water is $(1.446 \pm 0.011) \times 10^{-3}$ cm²/s, with deviations from the literature

(Balderas-López *et al.*, 2001). Measurements were repeated 5 times for a particular sample and the averaged thermal diffusivity value was taken. The experimental errors in the measurements were between 0.6 and 0.8%. These results demonstrate that the experimental setup used in the present study can produce a reliable data. Figure 5.42 (a-b) shows the plots of logarithmic amplitude and phase versus the cavity length of Al₂O₃ nanofluids at different laser irradiation from 0 to 90 min in a thermally thick condition. The slopes of amplitude and phase of signal, $A = (\pi f / \alpha)^{1/2}$, and the thermal diffusivity values measured in the present work are summarized in Table 5.6.

Table 5.6. Summarized results for thermal properties of Al₂O₃ and CuO nanofluids at different laser irradiation times.

Sample	Time (Min)	A _{phase}	A _{amplitude}	A _{average}	α (10 ⁻³ cm ² /s)
Al ₂ O ₃	0	120.6 ± 0.8	122.6 ± 0.6	121.6 ± 0.7	1.444 ± 0.008
	20	119.4 ± 0.6	121.8 ± 1.0	120.6 ± 0.8	1.468 ± 0.011
	90	118.4 ± 0.9	120.4 ± 0.6	119.4 ± 0.7	1.498 ± 0.009
CuO	0	119.2 ± 0.9	121.2 ± 0.9	120.2 ± 0.9	1.477 ± 0.011
	20	118.9 ± 0.8	120.2 ± 1.1	119.5 ± 0.9	1.494 ± 0.012
	90	116.7 ± 0.9	119.0 ± 0.9	117.9 ± 0.9	1.537 ± 0.013

Both plots are linear with respect to cavity length and the curve of 20 min laser irradiation was close to that of nanofluid without laser irradiation except at 90 min of laser irradiation. Similar PE signals evolution were obtained for CuO nanofluids at

different laser irradiation from 0 to 90 min and their corresponding, the slopes of amplitude and phase of signal and the thermal diffusivities were also obtained and are tabulated in Table 5.6.

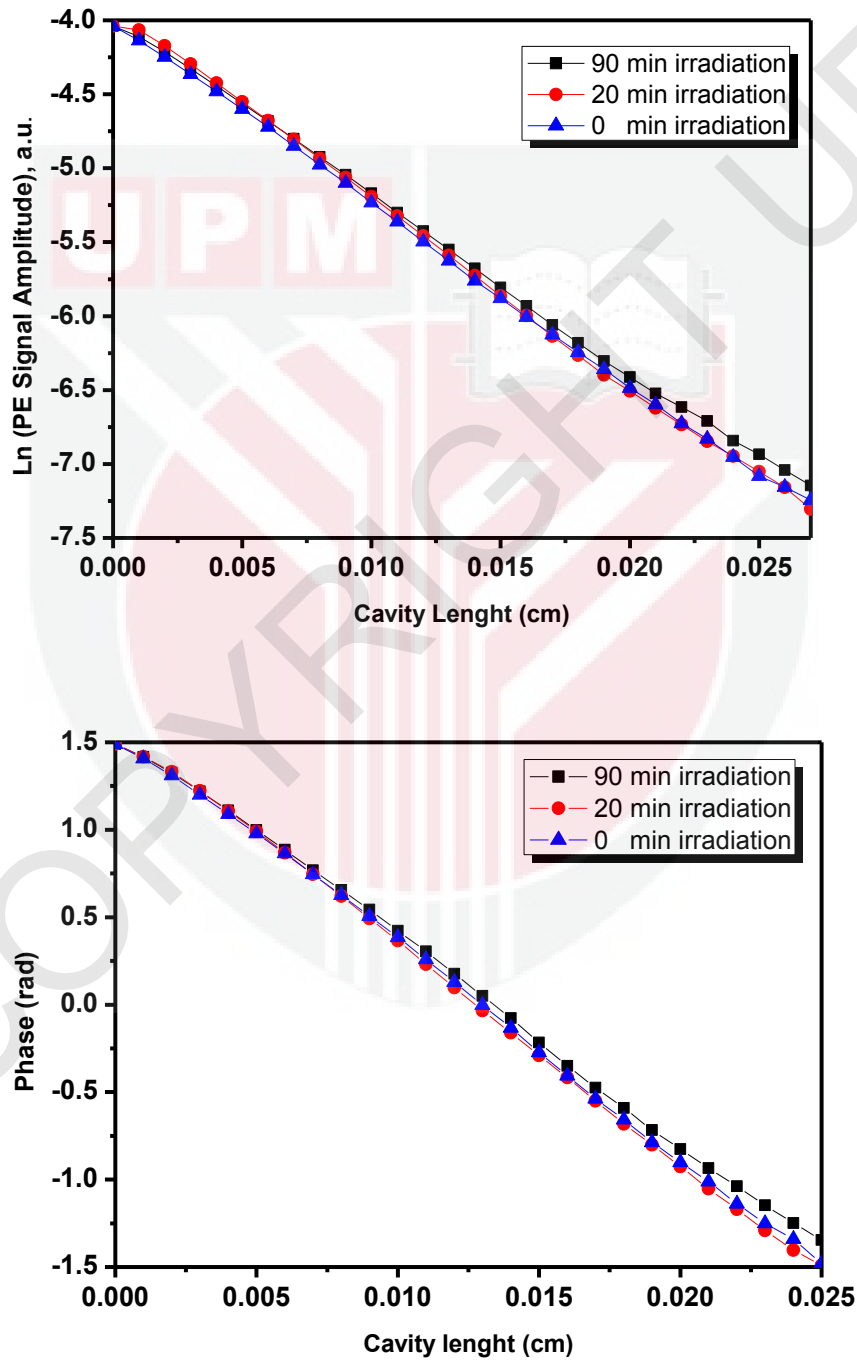


Figure 5.42. Typical Ln(Amplitude) (a) and phase (b) as a function of the relative cavity length of Al_2O_3 nanofluids at different irradiation times (0, 20 and 90 min)

Figure 5.43 shows the thermal diffusivity values for Al_2O_3 and CuO nanofluid at different irradiation time. It is clear that in all of nanofluids, the thermal diffusivity increases gradually by dispersing Al_2O_3 or CuO NPs in the water and then increases with the increase of irradiation time. From results of nanofluid samples, the nanoparticle material has a stronger effect on the thermal diffusivity of nanofluids, as a consequence of the lower thermal diffusivity of the nanofluids with respect to that of the Al_2O_3 nanofluid. It is defined as an aging effect in that the thermal diffusivity gradually increases around 3–6% after laser irradiation (Balderas-López *et al.*, 2001).

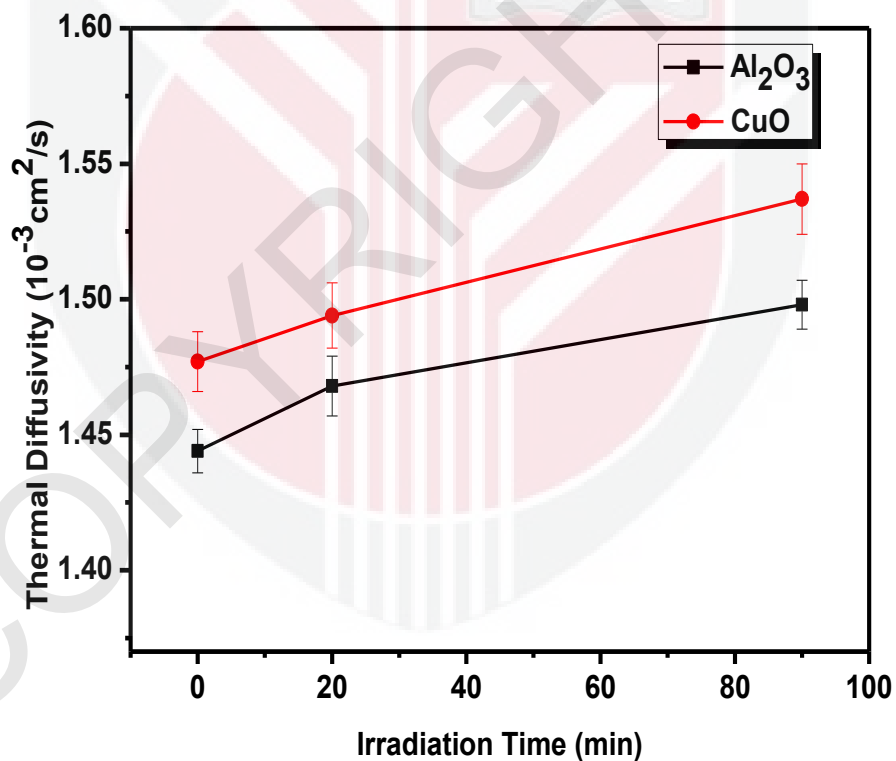


Figure 5.43. The thermal diffusivity values for Al_2O_3 and CuO nanofluid at different irradiation times.

The increase in the thermal diffusivity with increased irradiation time is a consequence of the decrease in the clusters and agglomerate size, due to the fragmentation of larger NPs (Jonggan *et al.*, 2007). Generally the density of the

particle number or volume fractions of the particles will be increased, it is thus evident that particle size reduction increases the nanoscale mixing effects, such as Brownian motion (Jonggan *et al.*, 2007). Therefore, it may help to enhance the thermal diffusivity of nanofluids.

The thermal effusivity as a suitable parameter for thermal characterization of the nanofluids sample that can be measured by the Front-PE technique is discussed in the next section.

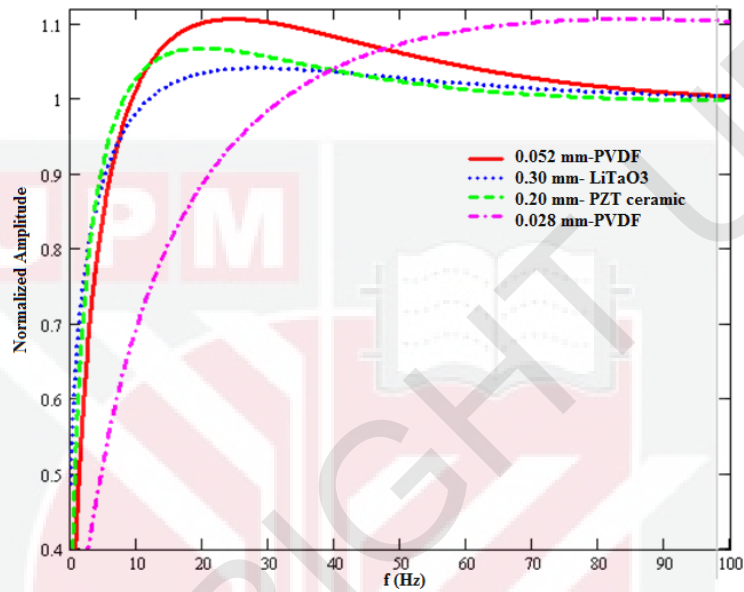
5.5 Front Pyroelectric Configuration Technique by Using PVDF as a Sensor

The Front-PE is based on the information contained in the amplitude and phase signal. In the next section, it is proposed to use a metalized PVDF sensor as a thermally thick sensor instead of a very thick in the conventional front PE configuration. Instead of typically 300 μm (Dadarlat *et al.*, 2007) or 500 μm (Dadarlat *et al.*, 2009), is an excellent choice for signal detection, due to its low cost, light weight, flexibility, and sensitivity. The Front-PE technique was performed to measure the thermal effusivity of the PVDF sensor, a few liquid samples and nanofluids containing Al_2O_3 and CuO NPs in different base fluid. Finally with using Combined the amplitude- phase, was measured the thermal effusivity of Ag NPs dispersed in DW or EG.

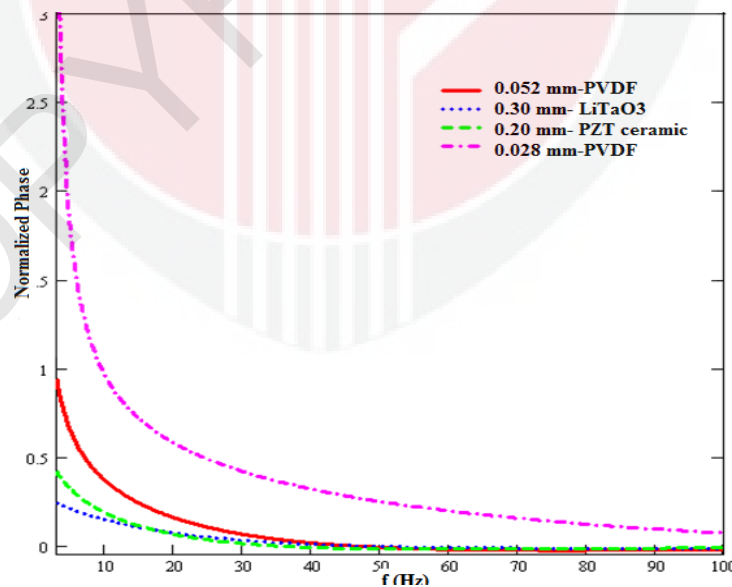
5.5.1 Thermal Effusivity Measurements of Pyroelectric Sensor and Sample

Figure 5.44 shows the simulated frequency dependence of the normalized PE signal: (a) amplitude and (b) phase according to Equations 3.31 and 3.30, respectively, for

PVDF sensors (52 μm and 28 μm), LiTaO₃ ;(300 μm) and PZT (200 μm) as a function of frequency, to see the comparison of their phases and amplitudes for water as liquid sample. The values of the respective sensor thermal parameters reported in the literature are presented in Table 5.7.



(a)



(b)

Figure 5.44. Simulated frequency dependence of the normalized PE signal: (a) amplitude and (b) phase according to Equations 3.31 and 3.30, respectively, for PVDF sensors (52 μm and 28 μm), LiTaO₃ ;(300 μm) and PZT (200 μm); water as liquid sample

Table 5.7. Thermophysical parameters from literature values of the PE cell components used for the calculation with water as the liquid sample

Material	Thermal diffusivity ($10^{-8} \text{ m}^2 \cdot \text{s}^{-1}$)	Thermal effusivity ($\text{W} \cdot \text{s}^{1/2} \cdot \text{m}^{-2} \cdot \text{K}^{-1}$)
Water[a]	14.5	1600
PVDF [b]	4.16	490
LiTaO ₃ [c]	150	3700
PZT ceramic [d]	49.5	1660

(Balderas-López et al., 2001)^[a] (Dadartat et al., 1995)^[b] (Sahraoui et al., 2002)^[c] (Sahraoui et al., 2003)^[d]

Figure 5.45 displays the frequency behavior of the normalized amplitude and phase of the signal obtained from distilled water as a reference sample of known thermal effusivity, $1600 \text{ W} \cdot \text{s}^{1/2} \cdot \text{m}^{-2} \cdot \text{K}^{-1}$ (Caerels et al., 1998), to determine the thermal effusivity of the PVDF sensor

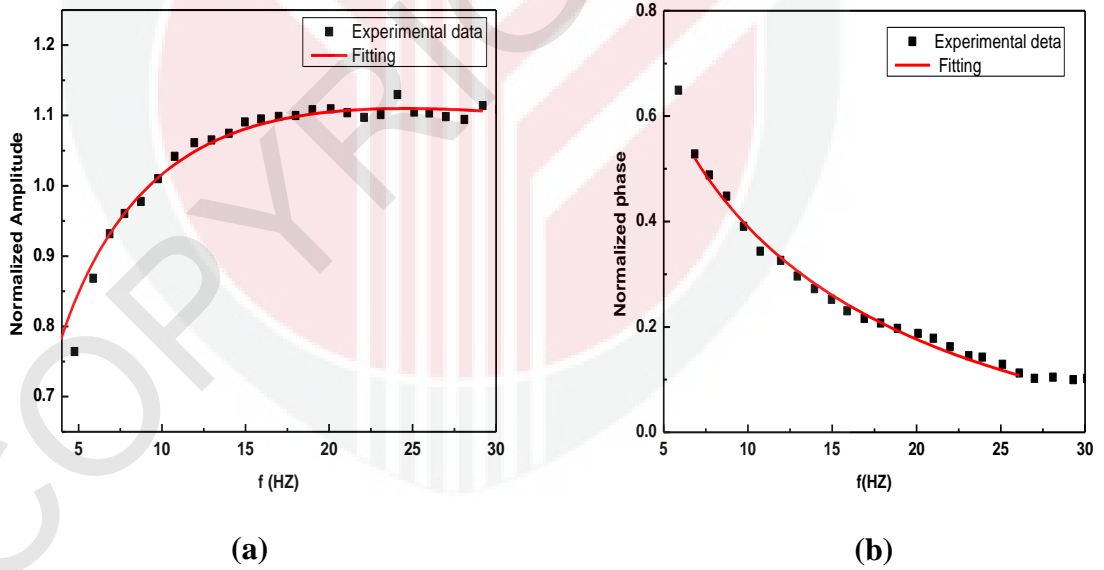


Figure 5.45. Frequency behavior of the normalized (a) amplitude and (b) phase obtained for the PVDF sensor with water as the substrate. Solid lines are the best fit of amplitude to Equation 3.31 and phase to Equation 3.30.

It also shows the best fit performed on the experimental data with Equation 3.31 for the normalized amplitude signal (Figure 5.45 (a)), and with Equation 3.30 for the normalized phase signal (Figure 5.45 (b)). At frequencies below 5 Hz, the effect of a thermally thin sensor becomes obvious, thus, the frequency behavior of the normalized amplitude and phase signals higher than 5 Hz was investigated. However, there is a significant difference between experimental data and the fit at high frequencies due to the reduction of S/N ratio. Therefore, the frequency range between 7 and 25 Hz is the best choice for fitting to find the parameters. In the setup, the S/N ratio at high frequency was better than 750.

From Figure 5.45 (a), the thermal effusivity of the PVDF sensor, e_p , calculated from the normalized amplitude signal by using Equations 3.31 and 3.28 is $(464.502 \pm 1.201) \text{Ws}^{1/2} \text{m}^{-2} \text{K}^{-1}$. From Figure 5.45 (b) the thermal effusivity calculated from the normalized phase signal by using Equations 3.30 and 3.28 is $(479.146 \pm 1.309) \text{Ws}^{1/2} \text{m}^{-2} \text{K}^{-1}$. The thermal effusivities obtained are close to each other. However, one can see that the results based on the phase are better than those on the amplitude, due to the high sensitivity of the amplitude to the radiation source intensity fluctuations (Longuemart *et al.*, 2003). The experimental errors of e_p obtained from both signals are less than 0.3% and the average value differs by less than 4.% compared to the literature, in Table 5.8.

In order to obtain thermal effusivity of liquid, this configuration can be used to measure of the liquid thermal effusivity (e_s) by normalizing the phase of PE signal if the sensor thermal properties, α_p and e_p , are known. Here, the phase instead of amplitude signal was used because it produces more accurate results since it does not

change with source intensity fluctuations (Dadarlat *et al.*, 2007). The thermal effusivity of a variety of liquids such as glycerol (Alfa Aesar, USA), soya bean oil (Mazola, CPC/AJI, Malaysia), and olive oil (Monini, Spoleto-Italian) were obtained. The frequency behavior of the normalized phase signal for different samples is presented in Figure 5.46.

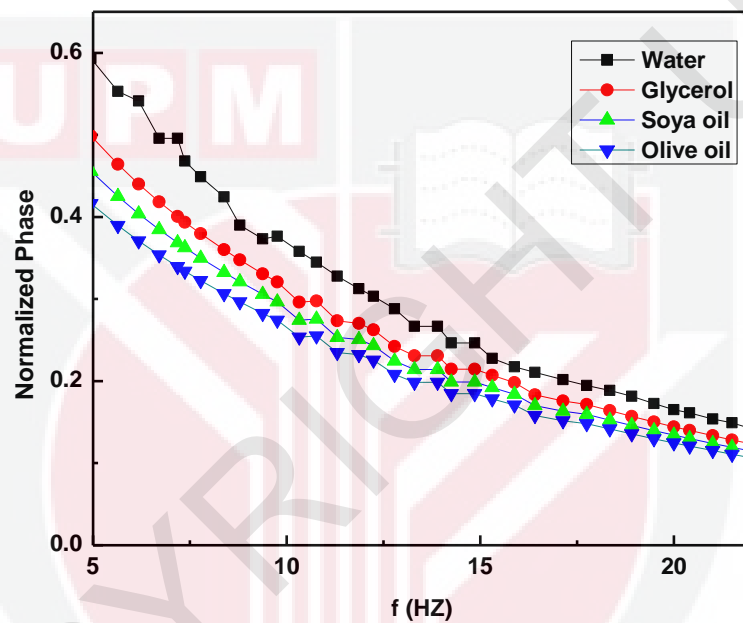


Figure 5.46. Frequency behavior of the normalized phase of the PE signal for the different substrates: water, glycerol, soya oil, and olive oil

Table 5.8 Thermal effusivity of some liquid samples (substrate), obtained from the phase of the PE signal, with PVDF sensor (52 μ m)

Material	Parameter A	Effusivity (measured) (W s ^{1/2} m ⁻² K ⁻¹)	Effusivity (literature) (W s ^{1/2} m ⁻² K ⁻¹)
Glycerol	1.310 \pm 0.003	930 \pm 2	924 ^[a]
Soya oil	1.209 \pm 0.003	749 \pm 2	-
Olive oil	1.175 \pm 0.002	697 \pm 1	621 ^[b]

^a(Lide *et al.*, 1997)

^b(Gutiérrez-Juárez *et al.*, 2008)

It can be seen that the normalized phase curve decay depends on the ratio, where very quick decrease of the normalized phase comes from the olive oil due to its smaller ratio. Table 5.8 displays the effusivities of samples with the corresponding standard deviations obtained from the signal phase. The thermal effusivity of glycerol is found to be in good agreement with the literature (Lide *et al.*, 1997); however, for olive oil, the value differs greatly from the literature due to its impurity. The standard deviation for glycerol is higher than that of olive oil because its thermal effusivity is higher than that of olive oil (Gutiérrez-Juárez *et al.*, 2008).

5.5.2 Thermal Effusivity of Nanofluids Containing Al₂O₃ and CuO NPs in different base fluid

Here, a study on the thermal effusivity and structure of two metal oxide NPs, Al₂O₃ and CuO, dispersed in three different base fluids, DW, EG and olive oil is reported.

5.5.2.1 Sample Preparation and Characterization

In order to prepare the Al₂O₃ nanofluid sample, 0.125 wt% of Al₂O₃ (11 nm, 99%, Nanostructured & Amorphous Materials, Inc.) were dissolved in each base fluid and was stirred vigorously with magnetic stirring for 1 h until a clear solution was obtained. Then this solution was sonicated by a probe sonication (VCX.500, 20 kHz, 500 W) for 30 min to ensure the uniform dispersion of NPs in the fluids. The similar procedure was followed to prepare of CuO NPs (50 nm, 99%, Nanostructured & Amorphous Materials, Inc.) sample. Average particle size was provided by manufacturer was typically determined by surface area measurements of the dry

powder. However, different lots of particles can have different sizes, and this measurement provides no guaranteed information regarding the size distribution of the particles. Thus, TEM were employed to obtain images of CuO and Al₂O₃ particles and to determine the average particle size. The individual particle size and distribution was determined using the UTHSCSA Image Tool software, version 3.0 (The University of Texas Health Science Center: San Antonio, TX, USA).

Figure 5.47 shows TEM images and their corresponding size distributions of CuO and Al₂O₃ NPs in water. The mean diameter and the size distribution of NPs in the images are shown beside each image. CuO and Al₂O₃ nanofluids showed excellent stability with 30 min of sonication as can be seen to remaining stable with only minor settling after a week at room temperature. However, according to TEM images, NPs were not well dispersed and some agglomerates were present (Figure 5.47) as the image measurement requires a dry sample under high vacuum conditions. The mean particle sizes of CuO and Al₂O₃ NPs observed in TEM images are about 7.5 ± 2.5 and 52.3 ± 4.2 nm, respectively; indicating that these commercial metal oxide particles are in the nanoscale range. However, the particle sizes of these commercial NPs determined from TEM images are slightly different from those reported by the manufacturers. Particles in each sample were aggregated to some degree. While CuO particles have a spherical shape with some uniform size distribution as reported by the producer, the alumina particles are irregularly shaped with considerable polydispersity and probably porous morphology.

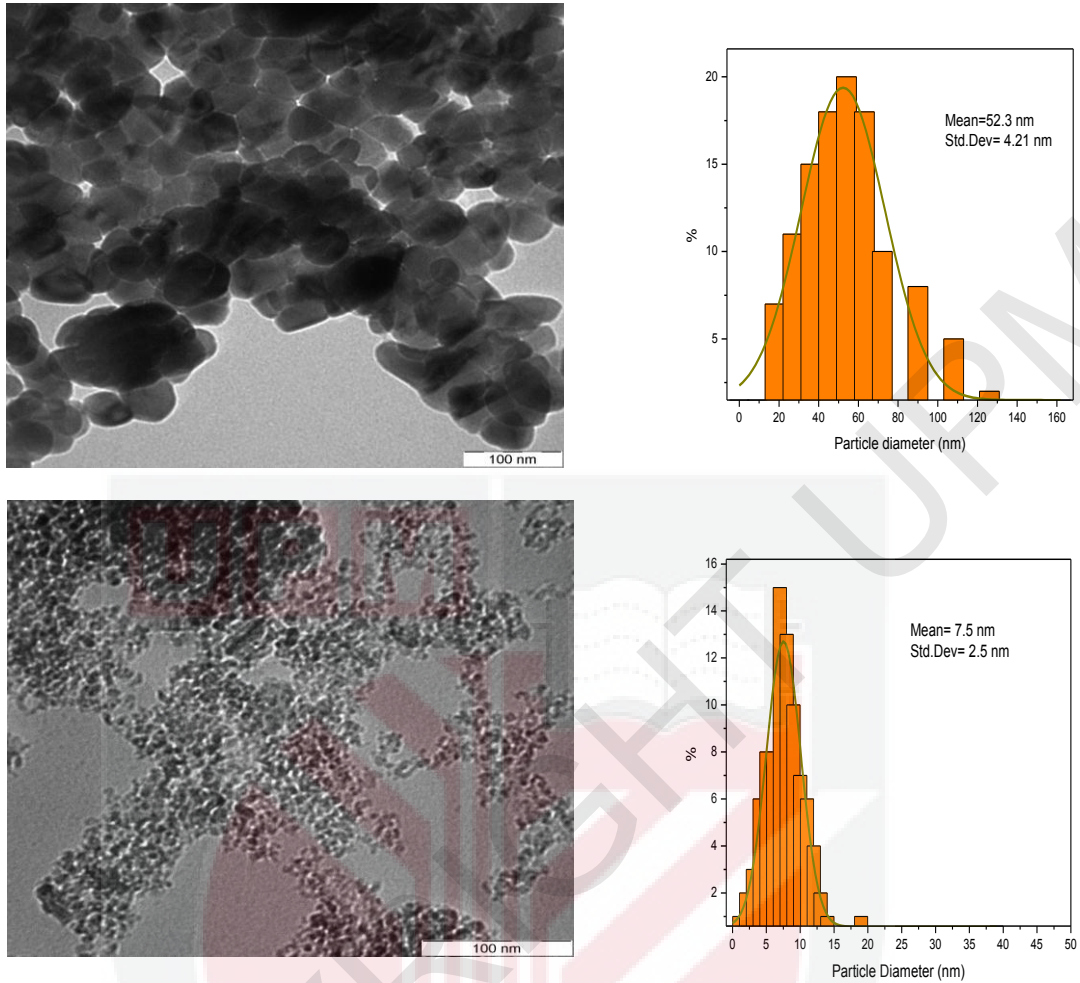


Figure 5.47. TEM images and their size distributions of (a) CuO particles and (b) alumina particles

5.5.2.2 Thermal Effusivity Measurement

Figure 5.48 shows the PE normalized phase of (a) Al_2O_3 + olive oil and (b) CuO + olive oil as a function of the frequency in a frequency range between 5 to 25 Hz. From this fit the parameter $A = (1.112 \pm 0.005)$ and (1.175 ± 0.006) were obtained, corresponding to thermal effusivities value of $(0.614 \pm 0.003) \times 10^3 \text{ W s}^{1/2} \text{ m}^{-2} \text{ K}^{-1}$ and $(0.697 \pm 0.003) \times 10^3 \text{ W s}^{1/2} \text{ m}^{-2} \text{ K}^{-1}$ for olive oil that contained Al_2O_3 and CuO NPs,

respectively, obtained by using Equation 3.30. The thermal effusivity of all nanofluids and their comparison with pure solvents are in Table 5.9 and Figure 5.49.

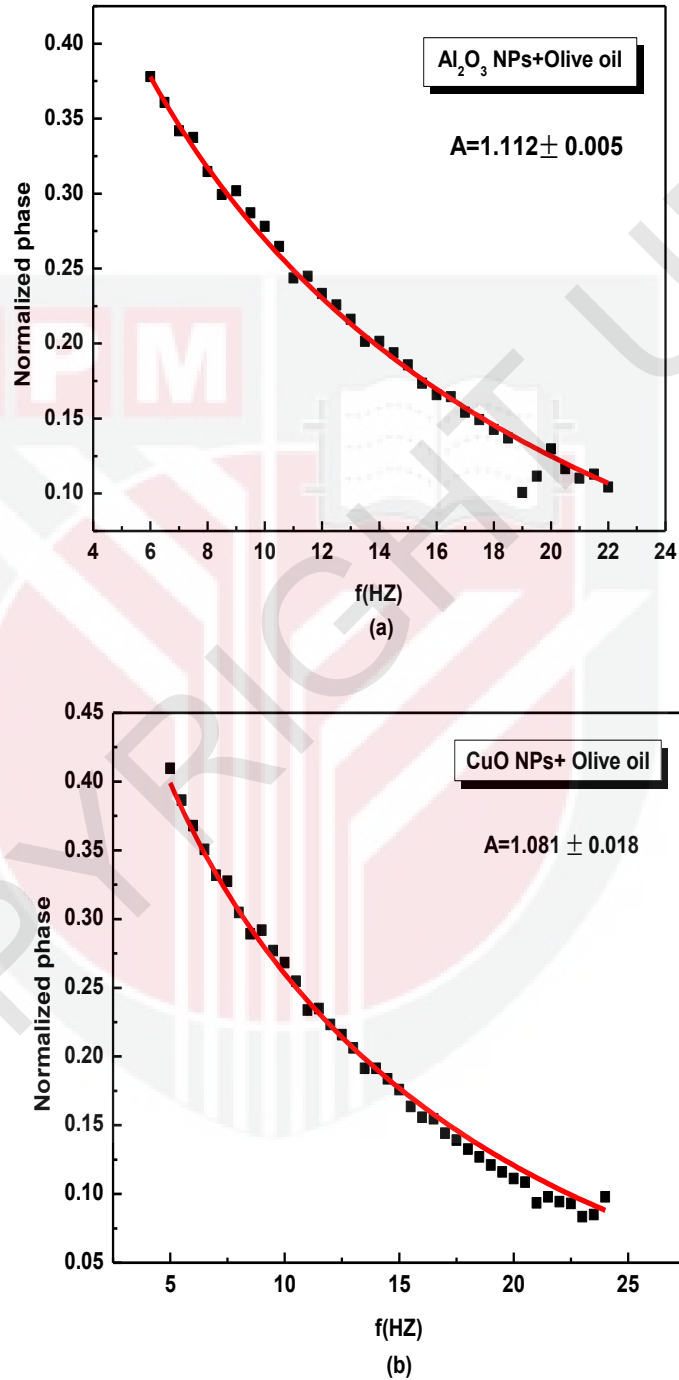


Figure 5.48. The PE normalized phase of Al_2O_3 + olive oil (a) and CuO + olive oil; (b) as a function of the light modulation frequency. Dots are experimental data and the solid line is the best fit to Equation 3.30.

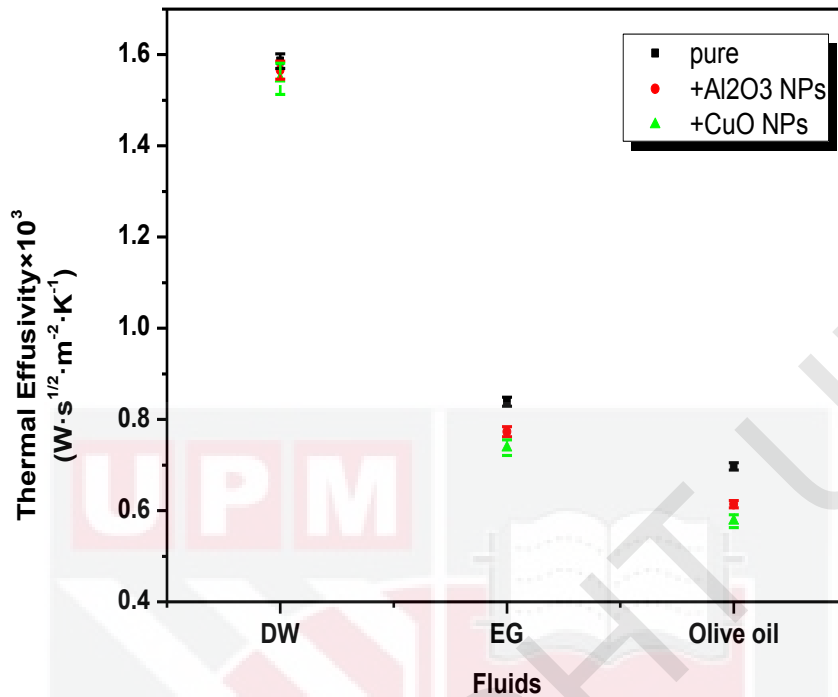


Figure 5.49. Comparison of the thermal effusivity of Al₂O₃ and CuO nanofluids with (DW, EG and olive oil) and the pure solvents.

Table 5.9. Experimental thermal effusivity for solvents with Al₂O₃ and CuO NPs and thermal effusivity values of pure solvents from the literature.

NPs	Base fluid	Fitting parameter(A)	Thermal effusivity × 10 ³ (Ws ^{1/2} m ⁻² K ⁻¹) measurement	Relative error%	Thermal effusivity × 10 ³ (Ws ^{1/2} m ⁻² K ⁻¹) Literature
Al ₂ O ₃	water	1.523 ± 0.014	1.566 ± 0.015	0.95	-
Al ₂ O ₃	EG	1.223 ± 0.009	0.773 ± 0.006	0.77	-
Al ₂ O ₃	olive	1.112 ± 0.005	0.614 ± 0.003	0.48	-
CuO	water	1.519 ± 0.028	1.547 ± 0.029	1.87	-
CuO	EG	1.202 ± 0.021	0.738 ± 0.012	1.75	-
CuO	olive	1.081 ± 0.018	0.577 ± 0.009	1.56	-
-	water	1.528 ± 0.011	1.586 ± 0.011	0.69	1.579 ^[a]
-	EG	1.263 ± 0.008	0.839 ± 0.005	0.59	0.810 ^[b]
-	olive	1.175 ± 0.006	0.697 ± 0.003	0.43	0.621 ^[c]

(Neamtu, 2009)^[a], (Balderas-Lopez, 2007)^[b], (Kulkarni, 2009)^[c]

5.5.3 Thermal Effusivity Measurement Using Combined the Amplitude and Phase

With the proposed method using combined amplitude-phase information of the normalized signal at given frequency to measure thermal effusivity of liquid, one can get the thermal diffusivity, a_p , of PVDF sensor and thermal effusivity of PVDF sensor or nanofluid sample, e_p (or e_s). Thus by combining the amplitude and phase of the PE signal, and using A and ϕ derived from the amplitude and phase of normalized PE signal, one can get both the thermal diffusivity and effusivity of PE materials (Sahraoui *et al.*, 2002).

5.5.3.1 Thermal Diffusivity and Thermal Effusivity of PVDF Sensor

Figure 5.50 shows the behaviour of ϕ vs square frequency, ϕ is derived from the amplitude and phase of the normalized PE signal, using Equation 3.35. The plot is linear with respect to frequency scanning, the thermal diffusivity of PE is obtained from the slope of this curve, $\text{slope}_{(\phi, f^{1/2})} = L_p (\pi/\alpha)^{1/2}$ and ϕ obtained by using Equation 3.36(b). The thermal diffusivity of PVDF sensor, $(0.578 \pm 0.01) \times 10^{-3} \text{ cm}^2\text{s}^{-1}$, differed by only 1.7% with values described in the literature. The thermal effusivity e_p is calculated for different frequencies by using Equation 3.36(a). The mean values of e_p and a_p are reported in Table 5.10.

Table 5.10. Experimental thermal diffusivity and thermal effusivity of PVDF sensor and its literature values

Experimental data	literature	Experimental data	literature
Slop of ϕ	Thermal diffusivity	R_{sp}	Thermal effusivity
	$\times 10^{-6} \text{ m}^2/\text{s}$		$\text{Ws}^{1/2}\text{m}^{-2}\text{K}^{-1}$
0.383 ± 0.004	0.057 ± 0.001	0.477 ± 0.051	565.2 ± 28.3
	0.056		559.4

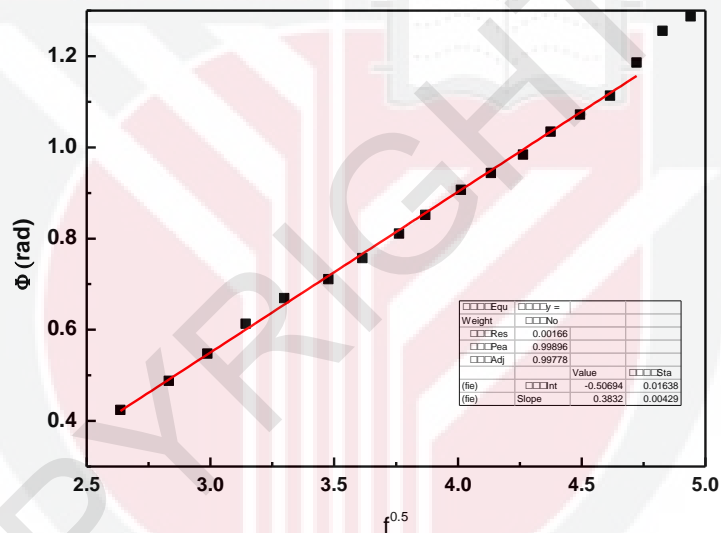


Figure 5.50. The behaviour of ϕ vs the square frequency, the thermal diffusivity of PE sensor was obtained from the gradient of this curve

In order to demonstrate the applicability of this technique, the thermal effusivity of Ag NPs dispersed in DW or EG at a given frequency were measured without carrying out a frequency scan, when the sensor thermal diffusivity and thermal effusivity are known.

5.5.3.2 Thermal Effusivity Measurement of Ag NPs in Different Base Fluid

In this section the thermal effusivity of the Ag NPs dispersed in DW or EG at different MW irradiation time, 20, 40, 60 and 90 s was investigated, has been mentioned in section 5.5.3. The samples were quoted, for DW as a solvent, W1, W2, W3 and W4 and for EG as a solvent, EG1, EG2, EG3 and EG4.

The thermal effusivity of Ag nanofluid is calculated for different frequencies by using Equations 3.36a and 3.28 and taking the well-known value for the thermal effusivity of PVDF $e_p = 559.4 \text{ W s}^{1/2} \text{ cm}^{-2} \text{ K}^{-1}$. The resultant values of the thermal effusivity obtained for Ag NPs dispersed in DW and EG as a base fluid are listed in Table 5.11. It is clear that the correct value of the thermal effusivity minimizes with increased of standard deviation of R_{sp} . The result shows that the relative error of the measurement is less than 2.5%.

Table 5.11. Experimental thermal effusivity of Ag NPs dispersed in DW or EG at different MW irradiation time, 20, 40, 60 and 90 s

Code of Sample	$R_{sp} \pm$ Standard Deviation	Thermal effusivity $\text{W s}^{1/2} \text{ m}^{-2} \text{ K}^{-1}$	relative error%
Ag/W1	0.4651 ± 0.0598	1531 ± 33	2.1
Ag/W2	0.4504 ± 0.0512	1475 ± 28	1.8
Ag/W3	0.4210 ± 0.0553	1371 ± 28	2.0
Ag/W4	0.4112 ± 0.0455	1339 ± 25	1.8
Ag/EG1	0.1851 ± 0.0330	812 ± 19	2.3
Ag/EG2	0.1723 ± 0.0261	791 ± 14	1.7
Ag/EG3	0.1642 ± 0.0273	778 ± 15	1.9
Ag/EG4	0.1564 ± 0.0337	766 ± 18	2.3

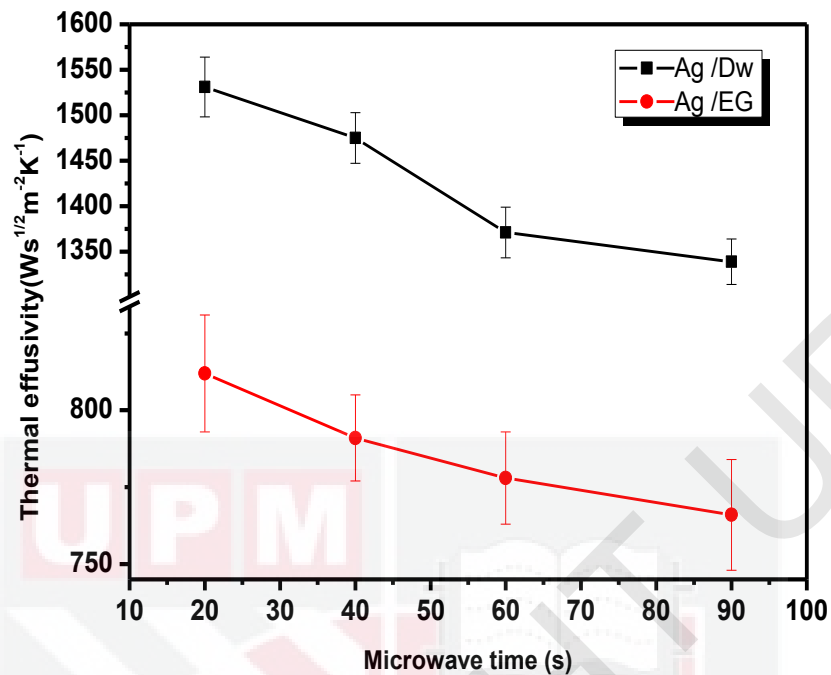


Figure 5.51. The thermal effusivity of Ag /DW and Ag/EG in 20, 40, 60 and 90 s MW irradiation times, respectively

Figure 5.51 shows the thermal effusivity values for Ag/DW and Ag/EG nanofluids at different MW irradiation times. Figure 5.51 shows the variations in thermal effusivity of Ag disperse in water between 0.1339-0.1531 Ws^{1/2}cm⁻²K⁻¹ and Ag disperse in EG between 0.0766-0.0815 Ws^{1/2}cm⁻²K⁻¹. It is clear that, the thermal effusivity of Ag nanofluids decreases with the increase of MW irradiation times, due to production of a bigger number of NPs in the solution. (Tu *et al.*, 2000)

It can be seen that the thermal effusivity has a behavior as opposed to the results of thermal diffusivity, which was due to the fact that both physical properties were inversely proportional ($e = k/\sqrt{\alpha}$) (Jiménez-Pérez *et al.*, 2009).

5.6 Thermal Effusivity of Ag NPs in Different Solvent Using Front-PE in Thermally Very Thick Regime

Recently, the amplitude of Front-PE in high frequency and thermally very thick regime, for thermal effusivity measurements in transparent liquids has been reported (Balderas-Lopez *et al.*, 2002). In the conventional method, a (theoretically constant) value for the normalized signal, which directly depends on the thermal effusivity of the liquid sample, has been obtained from the ratio of PE signals of liquid sample and air, respectively.

In this section of work, the amplitude of Front-PE technique in thermally very thick regime was modified to propose as an alternative for thermal effusivity measurement of nanofluid. This simple and high accuracy process of measuring thermal effusivity was obtained through a simple equation by normalizing the PE signal with the corresponding signal from the water as a reference sample. The normalized signal gives a constant value, N , from Equation 3.40. The normalization in this modification, due to close thermal diffusivity of water and testing sample, no need to use external frequency and it can be used at the needed frequency range for both reference sample and testing sample. Another important characteristic of this system is ability to work from low frequencies, due to low thermal diffusion in the nanofluid sample. In other words, the normalized signals obtained with water as a reference sample, make it good choice for evaluating the thermal effusivity of the nanofluids sample through a simple equation with a high accuracy. The thermal effusivity of the Ag NPs dispersed in DW or EG at different MW irradiation time, 20, 40, 60 and 90 s, which has been mentioned in section 5.5.3, was investigated. The samples were

quoted, for DW as a solvent, W1, W2, W3 and W4 and for EG as a solvent, EG1, EG2, EG3 and EG4.

In Figure 5.52 the horizontal lines represent the corresponding asymptotic values, N from Equation 3.40, for the normalized PE signal for Ag/W1 and Ag/EG1 nanofluids. The normalized amplitude was recorded as a function of the modulation frequency from 50 to 100 Hz, in steps of 1 Hz. In order to satisfy the thermally very thick regime for the sensor and sample chopping frequencies higher than 50 Hz have been used. The lower limit was imposed by the thermally thick regime restriction in sample, by the deterioration of S/N ratio.

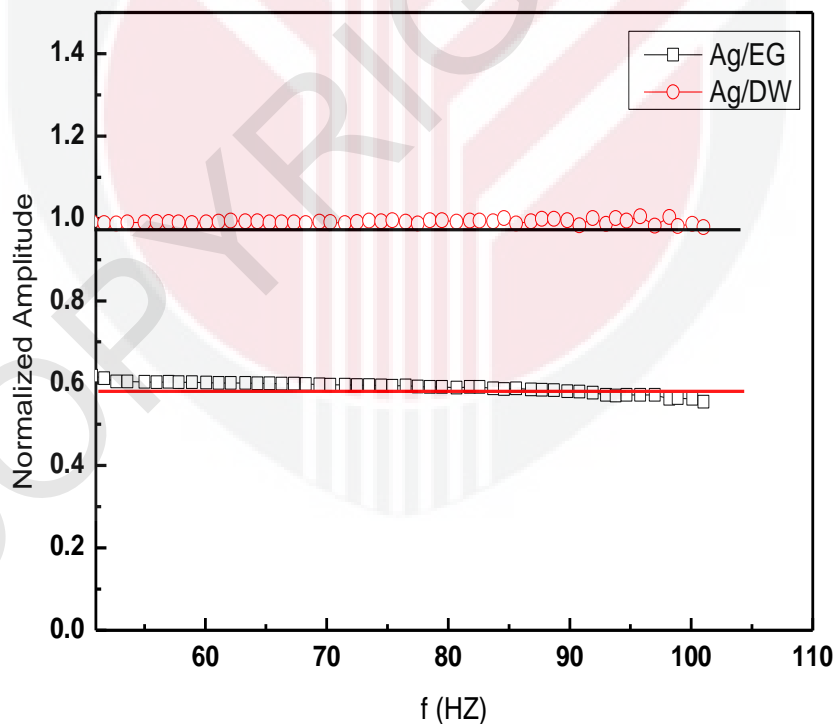


Figure 5.52. The horizontal line represents the corresponding asymptotic values, N , for the normalized PE signal as a function of the modulation frequency from 50 to 100 Hz, in steps of 1 Hz, for Ag/ W1 and Ag/EG1 nanofluids.

The maximum thickness of sample, including the thermally thick of sample was about 1mm. Using the known thermal effusivity for PVDF and water, $e_p = 0.05594$ and $e_w = 0.1579 \text{ W s}^{1/2} \text{ cm}^{-2} \text{ K}^{-1}$, the thermal effusivity of nanofluids sample can be easily evaluated from Equations 3.40 and 3.41. The experimental error of thermal effusivity measurements was estimated by using the usual formula for error propagation of the standard deviation for N measurements. The results are summarized in columns 2 and 3 of Table 5.12.

Table 5.12. The corresponding asymptotic values, N, for the normalized PE signal for Ag/w1 and Ag/EG1 nanofluids and their thermal effusivities

Code of Sample	N	Thermal effusivity ($\text{Ws}^{1/2} \text{ m}^{-2} \text{ K}^{-1}$)
AgNPs/DW		
W1	0.980 ± 0.009	1538.685 ± 4.851
W2	0.976 ± 0.006	1529.441 ± 2.994
W3	0.967 ± 0.005	1510.407 ± 2.563
W4	0.956 ± 0.011	1488.225 ± 5.468
Ag NPs/EG		
EG1	0.628 ± 0.018	810.387 ± 8.889
EG2	0.617 ± 0.006	787.938 ± 3.0978
EG3	0.591 ± 0.015	732.272 ± 7.302
EG4	0.563 ± 0.016	675.405 ± 7.747

Figure 5.53 shows the thermal effusivity values for Ag/DW and Ag/EG nanofluids at different MW irradiation times, using the front-PE technique at thermally very thick regime. It shows that with increase of irradiation time, the values of thermal effusivity of nanofluids decrease. This behavior of the experimental data has also been shown in Al_2O_3 nanofluids.

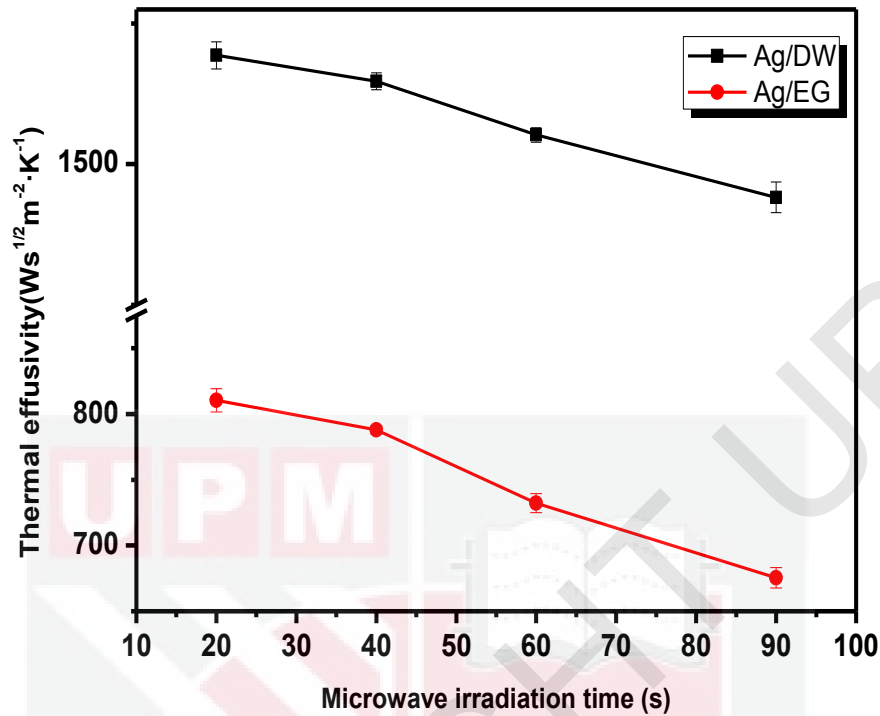


Figure 5.53: The thermal effusivity of (a) Ag NPs/DW and (b) Ag NPs /EG in 20, 40, 60 and 90 s irradiation microwave time, respectively.

5.6.1 A Comparison between Combining the Amplitude and Phase Signal and Front-PE in Thermally Very Thick Regime Method

In this section, the thermal effusivity measurement from two previous methods, by combining the phase and the amplitude of signal and PE configuration in thermally very thick regime was compared. A comparison between the values of thermal effusivity measured for Ag/DW and Ag/EG nanofluids at different MW irradiation time at 20, 40, 60, and 90 s, is summarized and compared between two different methods as shown in Table 5.13. It can be seen that the values of the thermal effusivity obtained from the combination of the phase and the amplitude of the PE signal in thermally very thick regime are in good agreement and also agree with the corresponding values reported in the literature such as, DW and EG.

Table 5.13. Thermal diffusivity and the comparison between two methods for respective samples

Code of Sample	Combining the phase and the amplitude	standard front-surface configuration	Literature
	Thermal effusivity $\times 10^3$ ($W s^{1/2} m^{-2} K^{-1}$)		
DW	1.559 ± 0.027	1.566 ± 0.005	1.579^a
W1	1.531 ± 0.033	1.538 ± 0.004	
W2	1.475 ± 0.028	1.529 ± 0.002	
W3	1.371 ± 0.028	1.510 ± 0.002	
W4	1.339 ± 0.025	1.488 ± 0.005	
EG	0.856 ± 0.022	0.832 ± 0.009	0.810^b
EG1	0.812 ± 0.019	0.810 ± 0.009	
EG2	0.791 ± 0.014	0.787 ± 0.003	
EG3	0.778 ± 0.015	0.732 ± 0.007	
EG4	0.766 ± 0.018	0.675 ± 0.008	

(Neamtu, 2009)^[a], (Balderas-Lopez, 2007)^[b]

However, a better accuracy and reproducibility of the measurement is observed when the information is taken from the PE configuration in thermally very thick regime. A major advantage of this methodology is the possibility to carry out fast estimates of the thermal effusivity of liquids, and as this high accuracy process is obtained through a simple equation. It is inevitable to work on high frequency as predicted by the theory. However, this condition is not always easy to be fulfilled due to the large damping of the amplitude signal at high frequency resulting in reduce in the S/N ratio. The thermal effusivity of the liquid sample can also be calculated by combining phase and amplitude, at a given frequency, without carrying out frequency scan. The influence of R_{sp} on the signal is independent of frequency. This procedure is suitable also for the study of thermal diffusivity and thermal effusivity of PE material.

5.7 Application of Ag NPs-Coated Optical Fiber to Enhance Thermal-Wave Generation in OF-TWC Technique

5.7.1 Surface Plasmon Resonance of Ag Nanoparticles

For investigation of the optical properties of Ag from NPs to large particles, Ag nanofluid six months storage at room temperature was subjected to UV-Vis spectroscopic analysis. During this time, the initial dark yellow colour was observed to change to aqua green colour. The exact position of this micro particle peak seemed unstable.

Figure 5.54 shows the absorption of Ag NPs solution measured by UV-vis absorption spectrometer for a fresh (just prepared) and after storage for six months. It can be seen that, the initial fresh colloidal Ag NPs have a strong absorption maximum in spatial wavelength, 412 nm, due to metallic NPs with dimensions that place them in the quantum size (Petryayeva *et al.*, 2011). Following a six month period of storage and with particle sizes increased there was broadening of absorption peak and also red shifted to 563 nm. The UV-Vis spectra clearly showed the reduced initial silver colloid absorbance, meaning the high significant change in particle size to the range to micron size due to electromagnetic retardation in the larger particles (Zheng *et al.*, 2010).

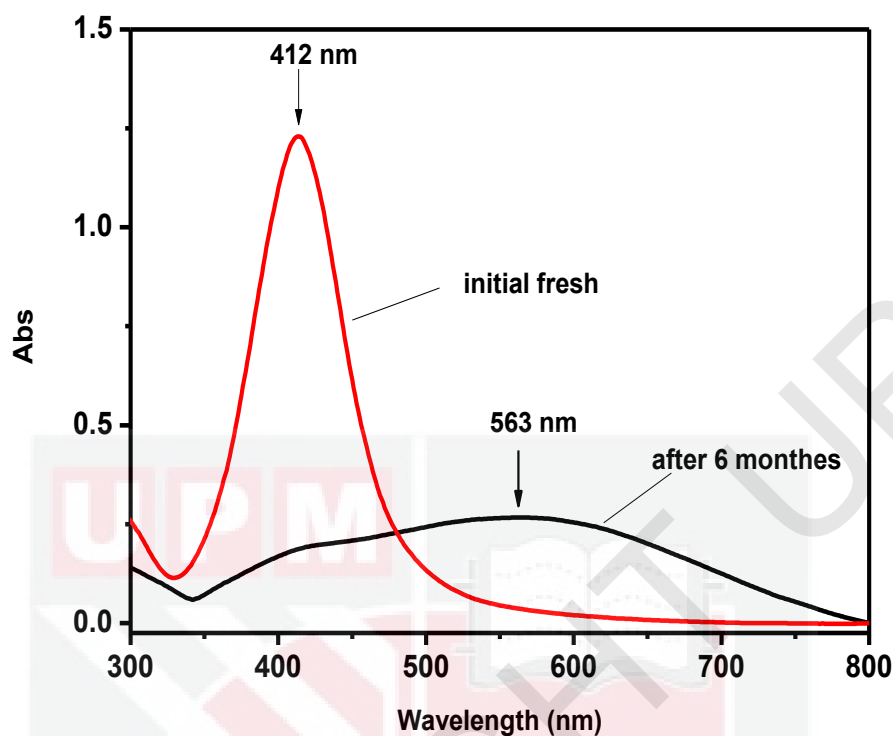


Figure 5.54. The corresponding UV-Vis spectra of the Ag NPs colloid, initial fresh; the optical absorption of Ag NPs is very high in spatial wavelength, and storage over approximately 6 months; absorption peak was red-shifted and broadened

To monitor the effect of the coverage densities of Ag NPs on optical absorption of Ag film, additional similar films were prepared onto two glass cover slip ($1\text{ cm} \times 1\text{ cm}$). To prepare the films, $20\ \mu\text{L}$ and $50\ \mu\text{L}$ of Ag NPs colloid were dropped and spread on glass and dried at room temperature, as low coverage and high coverage densities of Ag NPs. The corresponding UV-Vis spectra of the samples were recorded, Fig.5.55. Here, great similarities between the SPR spectra were observed, but the intensities of the bands increase with the increase of coverage density of the Ag NPs (Badr *et al.*, 2005).

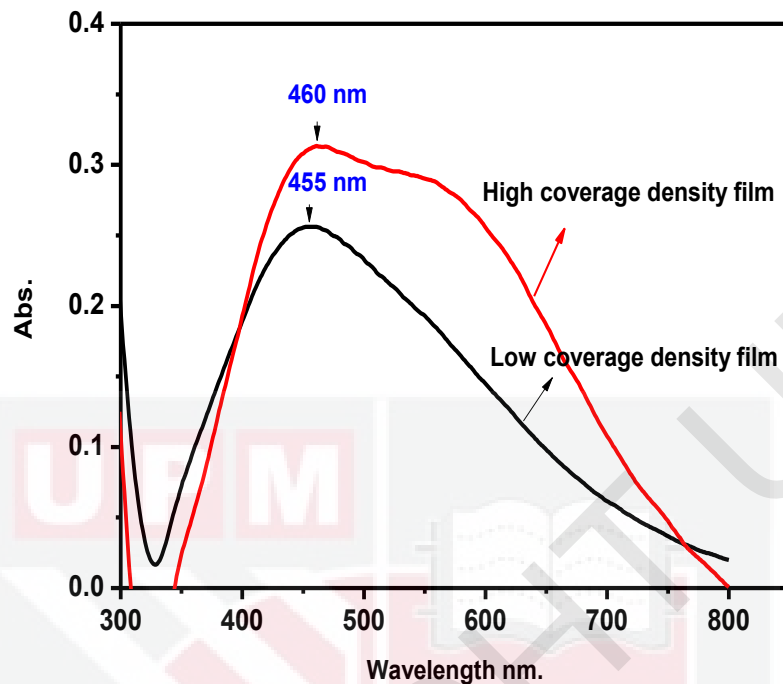


Figure 5.55. The corresponding UV-vis spectra of the Ag NPs colloid were dropped onto two 1 cm × 1 cm glass slides with different amount of Ag NPs coating, low coverage film (20 μ L) and high coverage film (50 μ L) densities of Ag NPs, and dried at room temperature

For the sample of high Ag NPs coverage density film, the primary peak located at about 460 nm in the spectrum. The absorption band of high coverage density film is rather broad and red-shifted compared with that of low coverage density film.

For the sample with low coverage density film, an obvious blue shift is clearly seen at 455 nm. Meanwhile, the absorption intensity decays dramatically. The blue shift and weak peak are due to the low coverage density of the Ag NPs indicating the smaller particle size of Ag NPs and the narrow range of size distribution. Usually, the addition of the Ag NPs leads to the aggregation of Ag NPs in the colloid, and causes the red-shift of the corresponding SPR peak (Wang *et al.*, 2012). The

increased absorption is attributed to the thickness effect, which is a common phenomenon observed in thin films. It is well known that the changes in the peak position due to different thickness can be used to study the photothermal effect of the metallized nanoparticle film.

A very important photothermal effect in metal NPs is improved when the metal NPs is excited by the laser of which the wavelength is resonant with SPR maximum of the substrate. As a result of UV-vis spectra, the general optical properties of NPs differ significantly from those that are observed in bulk material (Figure 5.54). This provides a large margin for enhancing the light excitation sensitivity. Another unique property of SPR of Ag NPs is that it can be tuned by changing the nanostructure size, shape, concentration or environment, in order to suit the scientific application (Figure 5.54 and 5.55).

The heating of NPs depends on their light absorption, which can be strongly enhanced from increased coverage density of Ag NPs. This effect was clearly observed in the UV-vis experimental study (Figure 5.55). The mechanisms of heating process of NPs are: (a) concentration effect and (b) the NPs formation and their interactions. The addition of NPs respects the additional heat fluxes generated by single NPs, as a sum of all NPs thermal source. The more NPs, the stronger the temperature increases that appears in the system. Consequently, the UV-vis spectra demonstrate that the heating of Ag NPs by laser irradiation, leading to SPR property change of Ag NPs causes the TW generator in OF-TWC technique.

5.7.2 The Effect of Laser Irradiation on Morphology of Ag NPs Film

A representative TEM image of Ag NPs before coating the fiber optic and surface is shown in Figure 5.56 (a) which confirms the generation of highly crystalline NPs with a spherical shape. Figure 5.56 (b) shows a histogram of the particle size distribution, with the mean particle diameter of 39.3 nm and standard deviation of 4.2 nm.

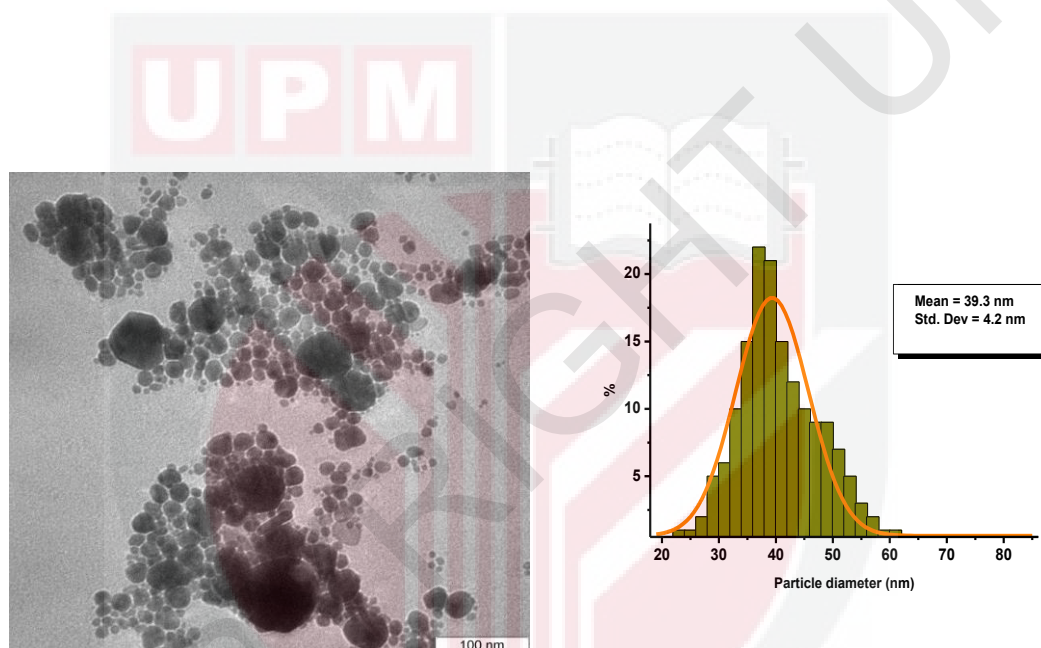


Figure 5.56. (a) TEM image of Ag NPs and (b) histogram distribution of the particle size

FESEM (Nova NanoSEM 30 series) was used to investigate the surface morphology.

Figure 5.57 (a) and (b) shows the low to high magnified images of Ag NPs on tip of optical fiber, where the average diameters are close to 39.3 ± 4.2 nm. It is clearly revealed from it that the synthesized products are of spherical NPs shape and are in a very high-density and possessing almost uniform shape. It shows clearly the homogeneous packing of the spherical Ag particles with some agglomerations.

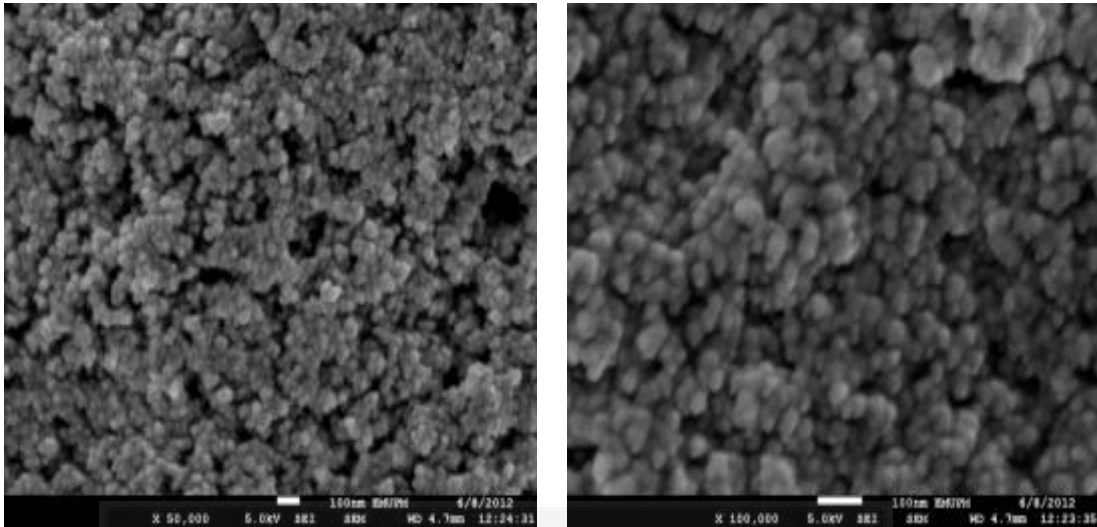


Figure 5.57. (a) low and (b) high magnification FESEM images of Ag NPs coated on tip of optical fiber (Ag NPs-coated optical fiber)

It should be necessary to investigate the effect of laser irradiation on the morphology of Ag NPs, which might reveal the interaction between the photons and the excited surface Plasmon's of the NPs. Figure 5.58 shows the concept of the fabrication processes by Ag nanoparticle film. Due to Photothermal effect of NPs, to convert light into heat, a focused laser beam as a local heat source can induce nanoparticle-selective melting, forming the metallic conductive thin film.

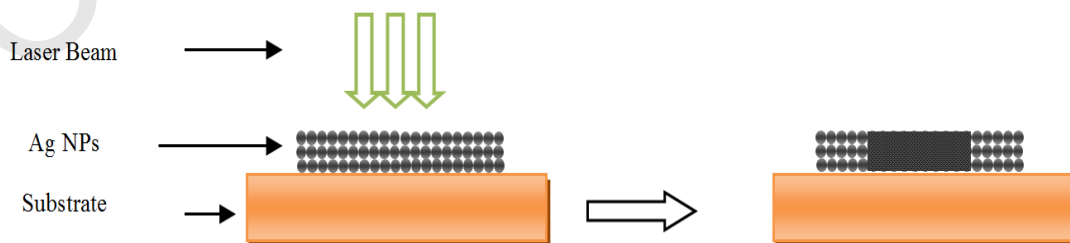


Figure 5.58. The concept of the fabrication processes of Ag NPs film; the effect of laser irradiation on the morphology of Ag NPs

The optical fibres coated with Ag NPs have the potential for the TW source application. To explore this exciting opportunity, the morphology of the Ag NPs-coated optical fiber have been investigated before and after 10 min laser irradiation (cw green light of 532 nm, 0.2W) at frequency range of 5-50 Hz (the condition of experiment). The typical results are shown in Figure 5.59.

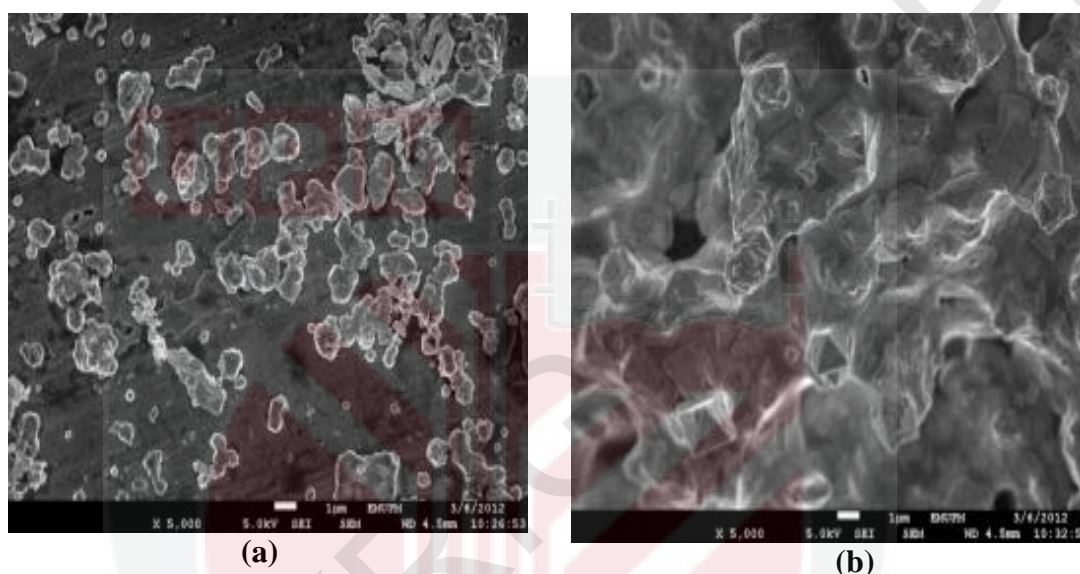


Figure 5.59. FESEM images of sample 1, Ag NPs-coated optical fiber (low density film) (a) before and (b) after 10 min laser irradiation in 10 min at range of frequency 5-50 Hz (at the condition of experiment)

Figure 5.59 shows the FESEM images of sample 1, Ag NPs on the fiber optic end surface (low coverage density of Ag NPs) (a) before and (b) 10 min after laser irradiation (at cw green light of 532 nm, 0.2w) in 10 min at range of frequency 5-50 Hz (at the condition of experiment). The nanoparticle morphology of Ag NPs can be clearly distinguished from one particle and the other is shown in Figure 5.59 (a). Whenever the cw laser illuminates the Ag NPs thin film, the Ag NPs begin to generate heat due to Photothermal effect. As soon as the temperature surrounding the Ag NPs exceeds the melting point of Ag NPs, the shape of the Ag NPs becomes flat and smooth, as in Figure 5.59 (b) (Samyn *et al.*, 2011).

On the other hand, in thicker Ag NPs film, the formed Ag film on the surface which is nearest to the light source surface has already been bulk material compared to Ag NPs at the surface free area at the fiber optic tip. Hence thermal conductivity of bulk material is higher than thermal conductivity of NPs, this indicated that Ag NPs gradually melt and connect together to form a conductive Ag film in thicker Ag NPs film (high coverage density of the Ag NPs), as shown in Figure 5.60. This is because of the lack of optical density, so that it was below the threshold-induced NP partial melting or surface melting, and NPs start to grow via Ostwald ripening to generate large agglomerated NPs, and the nanocrystal remaining in their original size even after laser irradiation (Graebner *et al.*, 1992), as can be seen in Figure 5.60.

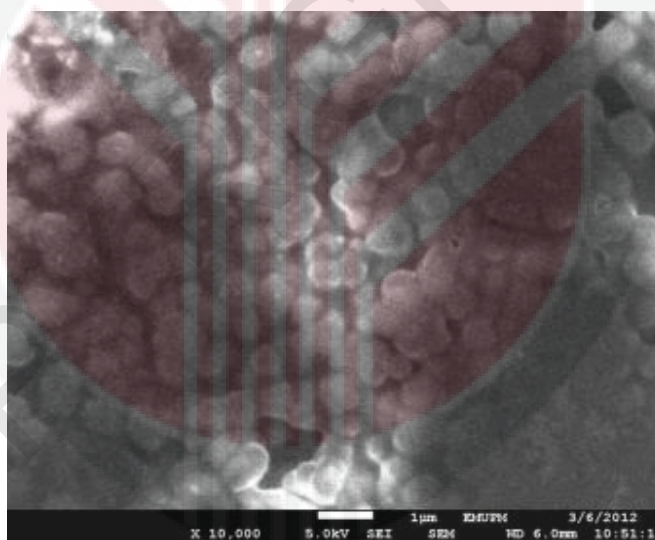


Figure 5.60. FESEM image of sample 2, Ag NPs-coated optical fiber (high density film) after laser irradiation at range of frequency 5-50 Hz (the condition of PT experiment)

5.7.3 Ag NPs-Coated Optical Fiber to Enhancement PE Signal

Two series of measurements were carried out in air at room temperature ($25 \pm 0.5^\circ\text{C}$). The first was to illustrate the range of PE signal which was determined by

the development of TW generator and the second was to compare the thermal diffusivity of air results obtained by this technique with those obtained by the traditional OF-TWC method. Frequency scanning measurement with the TW cavity filled with air sample was performed. The experimental PE signal was detected in an especially developed PE cell (Figure 5.61) the construction of which was optimized to yield maximum signal protection from the surroundings with a good S/N ratio.

As shown in Figure 5.61 (a), the PE amplitude vs modulation frequency for air responses to Ag NPs coating and Ag paint film coating as the TW generator, and Figure 5.61 (b) and 5.61 (c) show the Ln(Amplitude) and phase vs. square root of modulating frequency in air, responses of Ag NPs film coating and Ag paint film coating. The first part of Fig 5.61 (a) shows the gradual changes from the thermally thin regime to the thermally thick regime, this change was followed by an inflection point in the figure and the TW decay rate of PE signal amplitude from the Ag NPs film was faster than that of the Ag paint film. This behaviour was followed by the TW domination of the signal in high modulation frequency (López *et al.*, 2000). Here the oscillatory thermal expansion of the Ag paint sample is proportionally smaller than that of the Ag NPs sample. It can be seen in Figure 5. 61 (b) the amplitude in the PE chamber is stronger for the Ag NPs film. The Ag paint film significantly changes the slope of the PE phase difference curve for frequencies up to 25 Hz, is shown in Figure 5. 61 (c). This shows that the Ag paint film can be used at relatively low frequency as a significant component of PE signal for liquid materials. The signal under silver particles film is higher relative to that of Ag paint film.

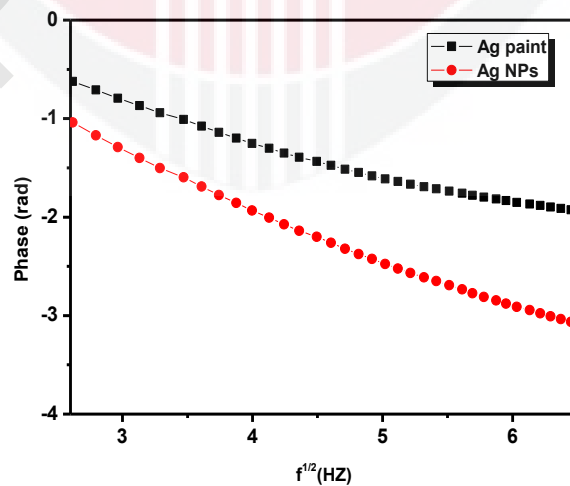
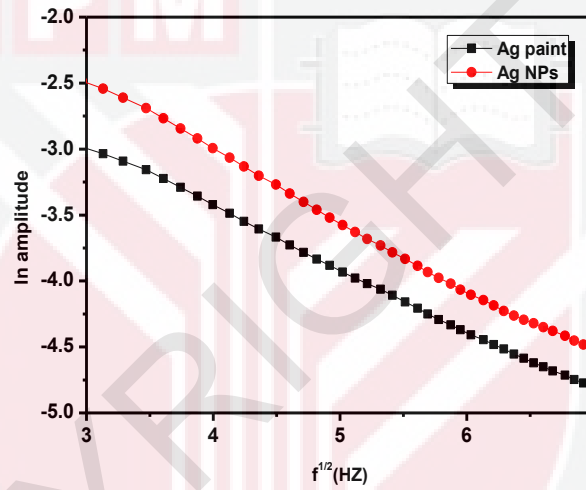
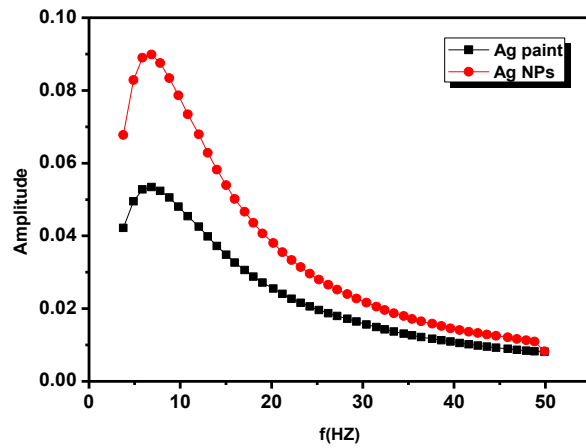
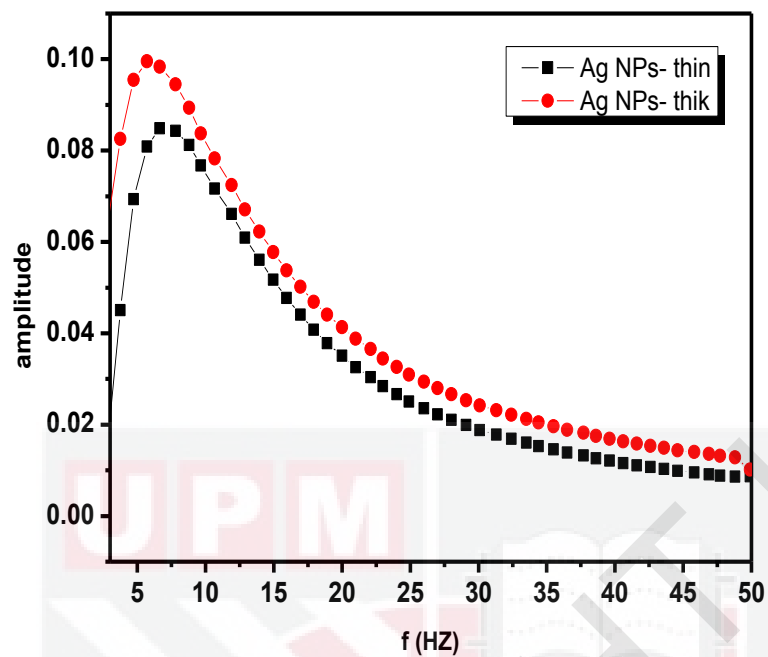
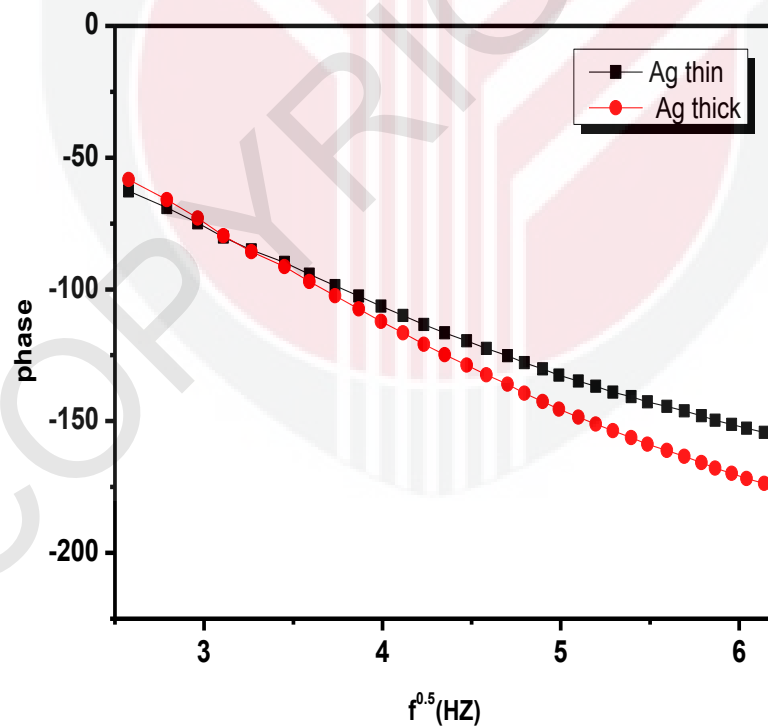


Figure 5.61. (a) Amplitude as a function of the modulation frequency, and linear (b) \ln (amplitude) and (c) phase as a function of square root of frequency, responses of the coated optical fiber (Ag NPs and Ag paint films)



(a)



(b)

Figure 5.62. (a) Amplitude as a function of modulation frequency, and linear (b) phase as a function of square root of frequency, responses of the Ag NPs-coated optical fiber (Ag NPs thin and thick films)

Figure 5.62 shows the two PE (a) amplitudes and (b) phase responses of the Ag NPs-coated optical fiber (Ag NPs film thinner and thin film coating) as a function of the modulation frequency for air. The analysis showed that the Ag NPs thin film had very small influence on the thermal characteristics and the Ag NPs thin layer model could be used in enhancement of the PE signal.

To complete the analysis, the method was tested on air sample to verify its accuracy. It was then applied to the study of thermal diffusivity of air with both thickness of Ag NPs coated and also Ag paint coated films. The thermal diffusivity of air was measured by performing a frequency scan of the OF-TWC set up.

5.7.4 Thermal Diffusivity Measurement of Air Using Ag NPs-Coated Optical Fiber

Figure 5.63 shows, Ln(amplitude) and phase vs. square root of frequency for air with TW generator; (a) Ag paint (b) Ag NPs 1(low density) (c) Ag NPs 2 (high density), respectively. The slope of curves, $V = \sqrt{\pi/\alpha L}$, depended on the thermal diffusivity and thickness, where $L=1.5$ mm. The thermal diffusivity values measured are summarized in Table 5.14.

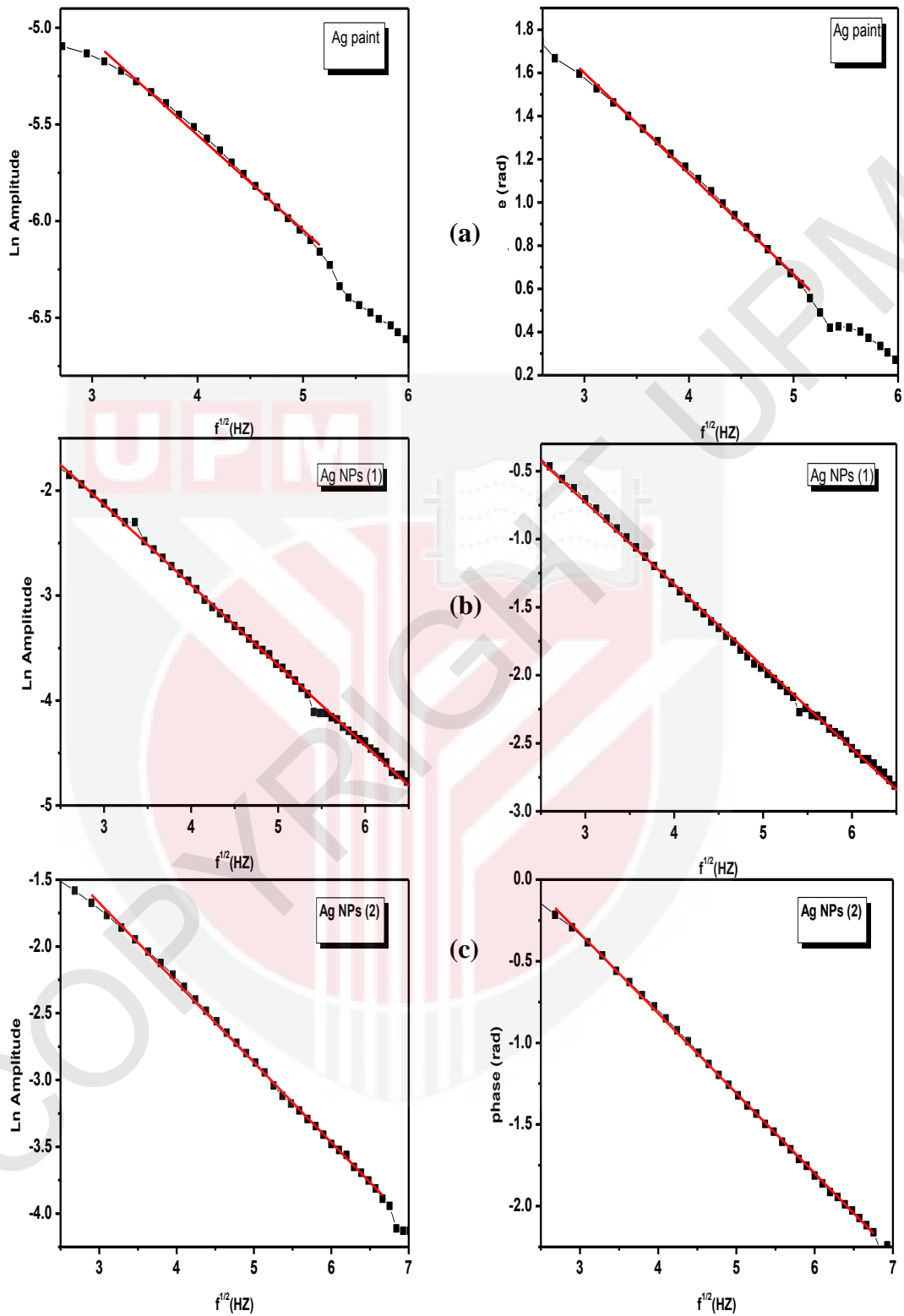


Figure 5.63. Amplitude and phase vs. square root of frequency for air sample with TW generator: (a) Ag paint (b) Ag NPs 1 (low density) (c) Ag NPs 2 (high density) films, respectively.

Table 5.14. Average value of Thermal diffusivity of air obtained from amplitude and phase of signal, with Ag NPs and Ag paint film as TW generator and comparison with literature values

Coated optical fiber	A_{average}	α_{average}	$\alpha_{\text{literature}}$	Standard deviation %
			$10^{-3} \text{ cm}^2/\text{s}$	
Ag NPs thick	0.565 ± 0.002	0.222 ± 0.003	0.19^{a} 0.221^{b}	1.3
Ag NPs thin	0.557 ± 0.005	0.227 ± 0.009	0.223^{c}	4.4
Ag paint	0.544 ± 0.008	0.239 ± 0.001		0.42

^a(Touloukian *et al.*, 1973) ^b(Holman *et al.*, 1990) ^c(Shen *et al.*, 1996)

The literature values of the thermal diffusivity of air at room temperature lie between 0.19 and $0.223 \text{ cm}^2\text{s}^{-1}$ (Touloukian *et al.*, 1973; Holman *et al.*, 1990; Shen *et al.*, 1996). The results of this work, $\alpha_{\text{air}} = 0.222 \pm 0.003$ and $0.227 \pm 0.01 \text{ cm}^2\text{s}^{-1}$, responses of the Ag NPs-coated optical fiber film of low density and that of high density, respectively, are in a very good agreement with them and also indicate the high sensitive, accurate.

In the end, analysis of these results highlights some important points:

- The Ag NPs-coated optical fibers show a more significantly enhanced PE signal than the Ag bulk paint optical fibers. Conceptually, the significant enhancement of PE signal could be explained by SPR (Cheng, *et al.* 2009). Indeed, the amplitude signal, Figure 5.61 (a), indicates that the Ag NPs have a much bigger SPR compared to the reported bulk Ag paint, Figure 5.61 (b), which suggests that absorption might play an important role to lead the enhancement in the PE signal as well. This indicates Ag NPs-coated optical fibers gradually melting and connecting together to form a conductive Ag

film and form continuous smooth film, which can be attributed to the fact that the surface to bulk ratio is higher for the thinner films (Figures 5.59 and 5.60).

- The experiments indicate that the increase in system absorption with increasing Ag thickness was at least partially due to the increase in optical intensity which is a result of the photothermal effect.
- A disadvantage to the use of silver particle films was the lifetime of the characteristic because of the morphologic changes of Ag NPs. More details of its nanostructure are necessary to document this effect.
- This work is only the first step toward the proof-of-concept demonstration of using the flexible thermal generator fibers to improve the signal in sensitive PE detector.

CHAPTER 6

CONCLUSION AND FUTURE DIRECTION

6.1 Introduction

In this project, the synthesis, characterization, thermal properties and applications of nanostructured materials were investigated and discussed. The characteristics of Ag NPs produced by MW technique and the effects of surrounding molecules and irradiation time on nucleation, size distribution, and growth mechanisms were investigated. The PE technique in both back and front PE configuration were applied to determine the variation in thermal diffusivity and thermal effusivity of nanofluids (containing Ag, Al₂O₃ and CuO NPs) as a function of base fluids, particles size, the dispersion/aggregation state of NPs, and particle volume fraction. Finally, the application of the colloidal Ag NPs, based on the highly SPR of the novel metal NPs, was utilized to develop and enhance the PE signal by coating the optical fiber tip with AgNPs, as a TW generator in the OF-TWC technique.

6.2 Conclusion

The preparation of Ag NPs in two different solvents (water and ethylene glycol) in the presence of a PVP solution without any reducing agent was made by MW of radiation as a simpler and greener technique compared to the conventional technique. The fabrication of narrow distribution Ag NPs in water was in the average size between 7 and 17 nm with corresponding standard deviation (σ) of 4.3 and 2.5 nm by varying

irradiation times from 20 to 90 s, respectively. They were very stable in an aqueous solution without any sign of precipitants when left for over six months. The results indicated that by using MW irradiation in comparison with the conventional heating method, it is possible to obtain Ag NPs of regular shape, narrow size distribution and a higher degree of crystallization in a reasonable synthesis time. The presence of Ag NPs in the solution is related to a broad absorbance peak whose maximum occurs at 413 nm. From the result of the Ag NPs fabrication dispersed in solution, the Ag ions interaction with ethylene glycol was much stronger than with water. Therefore, the availability of Ag ions was mostly for the growth of Ag NPs. However, further increase of NPs creation with higher irradiation led to the decrease of Ag NPs size probably because of a large number of nuclei. This result and the narrow distribution indicate that the higher dielectric loss, boiling points and molecular weight of ethylene glycol compared to water may have an important influence on the high crystallinity degree and the growth of Ag NPs.

The OF-TWC is a sensitive technique to measure thermal properties of nanofluids in small volume. The results indicated that, the thermal diffusivity and thermal conductivity of the Ag/Clay nanofluids increases with the volume fraction of Ag NPs in clay suspension. The thermal diffusivity of Ag/clay nanofluid of 0.5 vol% immediately after dispersion with probe sonication is in the highest value, $(1.571 \pm 0.011) \times 10^{-3} \text{ cm}^2/\text{s}$, and decreases around 7.3% in 3 h after dispersion $(1.456 \pm 0.007) \times 10^{-3} \text{ cm}^2/\text{s}$ and it returns closest to its base fluid value over time. This decrement may be due to the increase in agglomeration because the bigger particle gives smaller thermal diffusivity value (Okeke *et al.*, 2012).

Nanofluids can be prepared also by directly dispersed nanopowders in the base fluid but this method may result in a large degree of NPs agglomeration. To reduce the NPs agglomeration, an ultrasonic dispersion technique and fragmentation processes using laser irradiation were tried out in low concentration to produce stable nanofluids. Following this, the OF-TWC was used to obtain the influence of ultrasonic irradiation modes (either bath- or probe-sonication) such as cluster size of Al_2O_3 nanofluids in low concentration on the thermal diffusivity. The ultrasonic bath proved to be almost ineffective in size reduction, most of the Al_2O_3 particles are spherical and are connected to each other to form a porous ranging in size from 1 μm to larger and the probe sonication effectively reduced the particle size to below 100 nm. This shows that oxide NPs in water are agglomerated and some hard aggregates could not be broken into individual NPs under these operating conditions or even at very high energy input (Nguyen, 2011). The results show that the thermal diffusivity of sample prepared by probe sonication ($1.609 \times 10^{-3} \text{ cm}^2/\text{s}$) is higher than that of sample prepared bath sonication ($1.498 \times 10^{-3} \text{ cm}^2/\text{s}$) and deionized water ($1.445 \times 10^{-3} \text{ cm}^2/\text{s}$). This is because the particle surface (the heat transfer area) becomes larger due to higher NPs dispersion in water using probe sonication.

Fragmentation of colloidal Al_2O_3 and CuO NPs by cw laser was investigated to study their morphology, size, size distribution and thermal diffusivity. The result indicated that the standard deviations, σ , in particle diameters were 16.6, 10.1, and 2.8% for before and after 20, 90 min irradiation time, respectively. σ less than 10% in diameter were the most uniform size, thus confirming the stability of the sample prepared under 90 min irradiation times, due to the absorption of the laser energy by the NPs and leading to the fragmentation of particles. The UV-Visible absorption

spectra of Al₂O₃ nanofluids was found to increase exponentially with the increase of laser irradiation, and the slope of spectral curve increased with the increased irradiation time, which may be due to the increase of quantity of Al₂O₃ NPs assembled within the fluid, hence the more stable the suspension, as proved by the Nanophox results. The result of σ 's in the particle diameters of CuO nanofluid were 41.1, 26.8, and 10.1% and of Al₂O₃ were 16.6, 10.1, and 2.8% for before, 20, 90 min irradiation, respectively. Historically, most oxide particles with $\sigma < 10\%$ in diameter were referred to as stability in nanofluids. Clearly, the TEM result showed several small particles produced by the fragmentation process and broke up these agglomerations but, the shape of the NPs remained the same although the mean size was slightly reduced. Consequently, for both the nanofluids (Al₂O₃ and CuO), the laser irradiation time mostly reduces distribution of the particles, rather than their size. This was likely due to irradiation time which produced a large number of agglomerated particles to the fragmentation of smaller NPs.

The thermal diffusivity of Al₂O₃ and CuO nanofluid increased with increasing irradiation times due to gradually dispersion of these NPs in water. It is defined as an aging effect in that the thermal diffusivity gradually increased around 3–6% after laser irradiation. The aging effect is due to a diminished effect of the laser irradiation on fragmentation of NPs and increasing the total number of particles in the solution, and then increases the nanoscale mixing effects, such as Brownian motion (Jonggan *et al.*, 2007). Therefore, may help to enhance the thermal diffusivity of nanofluids.

A metalized PVDF sensor was used as an optically opaque sensor and in a thermally

thick regime for both sensor and sample, instead of a very thick sensor in the conventional Front-PE configuration. From the frequency dependence measurements, the normalized amplitude and phase signal were independently analyzed to obtain the thermal effusivity of the sensor. The differential normalized amplitude measured with water as a substrate was analyzed to determine the sensor thermal diffusivity. The PVDF thermal diffusivity and thermal effusivity agree with literature values. Then, from the known thermal parameters of the sensor, the thermal effusivity of a standard liquid sample, glycerol, and other liquids were obtained by a similar procedure. The proposed Front-PE technique was applied to measure thermal effusivity by utilizing its phase signal of nanofluid that contained Al₂O₃ and CuO NPs dispersed in different solvents, water, ethylene glycol, and olive oil. Thermal effusivity was more precise in the nanofluid with low thermal diffusivity of solvent. The thermal effusivity of the various liquids, mixing with NPs reduces as compared to the pure fluids. By combining the amplitude and phase of the PE signal expressions, one can get both the thermal diffusivity α and effusivity e of the PVDF sensor or thermal effusivity of nanofluid sample. The thermal diffusivity of PE was obtained from the slope of this curve, $\text{slope}_{(\phi, f^{1/2})} = L_p (\pi/\alpha)^{1/2}$ and ϕ was obtained by using Equation 3.36b. The thermal diffusivity of PVDF sensor, $(0.578 \pm 0.01) \times 10^{-3} \text{ cm}^2 \text{ s}^{-1}$, differs only by 1.7% with value described in the literature. Its thermal effusivity calculated by using Equation 3.36a is $565.2 \pm 28.3 \text{ ws}^{1/2} \text{ cm}^{-2} \text{ K}^{-1}$. The thermal effusivity of Ag NPs dispersed in water or ethylene-glycol at a given frequency, was obtained when the thermal diffusivity and thermal effusivity of the sensor are known. The variations in thermal effusivity of Ag dispersed in water between 0.1339–0.1531 $\text{ws}^{1/2} \text{ cm}^{-2} \text{ K}^{-1}$ and Ag dispersed in ethylene-glycol between 0.0766–0.0815 $\text{ws}^{1/2} \text{ cm}^{-2} \text{ K}^{-1}$. It is clear

that, the thermal effusivity of Ag nanofluids decreases with increasing MW irradiation time due to the production of more NPs in the solution. The amplitude of Front-PE technique in thermally very thick regime was modified to propose as an alternative for thermal effusivity measurement of nanofluid, by taking the signal ratio in two different situations: one with water as a reference, and the other with liquid sample. The thermal effusivity of the Ag NPs dispersed in water or ethylene glycol at different MW irradiation times was investigated. The nanofluid thermal effusivity for Ag NPs in water and for that in ethylene glycol at different MW irradiation times shows that its value decreases as the irradiated time increases. This behavior of the experimental data also has been shown in Al_2O_3 nanofluid, the thermal effusivity obtained from the combination of the phase and the amplitude of the PE signal and PE configuration in thermally very thick regime are in good agreement and also agree with the corresponding values reported in the literature such as, water and ethylene glycol. However, a better accuracy and reproducibility of the measurement is observed when the information is taken from the PE configuration in thermally very thick regime.

The Ag NPs-coated optical fiber shows a significant higher PE signal than that of the Ag bulk in Ag paint. The increase in system absorption with increasing Ag thickness was at least partially due to the increase in optical intensity due to the photothermal effect. Conceptually, the significant enhancement of PE signal could be explained by SPR, which suggests that the absorption might play an important role to lead the enhancement in the PE signal as well. This indicates Ag NPs-coated optical fibers gradually melt and connect together to form into conductive Ag film and form continuous smooth Ag film, which can be attributed to improved PE signal. To complete the analysis, the method was tested on air sample as a reference sample to verify its accuracy. It was then applied to the study of thermal diffusivity of air with

both thickness of Ag NPs coated and also Ag paint coated. The thermal diffusivity of the air was measured by performing a frequency scan from the OF-TWRC device with Ag NPs. The results are $\alpha_{\text{air}} = 0.222 \pm 0.003$ and $0.227 \pm 0.01 \text{ cm}^2 \cdot \text{s}^{-1}$, responses to Ag NPs-coated optical fiber film low density and Ag NPs film high density, respectively, are in very good agreement with them and further indicate the superior sensitivity, accuracy, and resolution potential of the responses of the Ag NPs-coated optical fiber approach.

6.3 Suggestions for Future Work

The present work can be considered to compose of two major parts i.e. development of a measurement technique and the application of the technique to study thermal diffusivity and thermal effusivity of nanofluids sample.

The following aspects can be considered in any future work:

- With the PE techniques, it is possible to measure other interesting effect of nanofluid samples on the thermal properties of samples such as different types of nanofluids, different shapes of particles and different temperature of nanofluids.
- The first step toward the proof-of-concept demonstration of using the flexible thermal generator fibers was utilized to improve the signal in sensitive PE detectors. A disadvantage of the use of Ag particle films was that the lifetime of the characteristic because morphologic changes of Ag particles. More details of its nanostructure is necessary to document this

effect. Various key parameters relate to and enable the optimization of the TW generator fabrication process, such as the size of NPs, the concentration of Ag NPs, the AgNP coating time and the Ag NPs coating temperature.

- Lastly, the demonstration here shows a proof of concept to act as both TWgenerator materials and improve PE signal, by applying the thin coating of Ag NPs onto optical fibers. It should be noted that this technique is not limited to use in PE technique, the Ag NPs-coated optical fibers can be also applied to improve the energy efficiency in industrial process.

REFERENCES

- Acharya S, Singh K. (2011) Microwave-Assisted Chemical Reduction Routes for Direct Synthesis of (fct) L10 Phase of Fe-Pt. *Journal of Microwave Power and Electromagnetic Energy*; 45: 63-69
- Agrawal, V. V., Kulkarni, G. U., and Rao, C. N. R. (2008). Surfactant-promoted formation of fractal and dendritic nanostructures of gold and silver at the organic–aqueous interface. *Journal of Colloid and Interface Science*, 318(2), 501-506.
- Ahmad, M. B., Tay, M. Y., Shameli, K., Hussein, M. Z., and Lim, J. J. (2011) Green Synthesis and Characterization of Silver/Chitosan/Polyethylene Glycol Nanocomposites without any Reducing Agent. *Int. J. Mol. Sci.*, 12(8), 4872-4884
- Akman, E., Oztoprak, B. G., Gunes, M., Kacar, E., & Demir, A. (2011). Effect of femtosecond Ti:Sapphire laser wavelengths on plasmonic behaviour and size evolution of silver nanoparticles. *Photonics and Nanostructures - Fundamentals and Applications*, 9(3), 276-286.
- Almond, D.P., Patel, P.M., (1996). *Photothermal Science and Techniques*, Chapman & Hall, London.
- Azmi, B. Z., Liaw, H. S., & Abbas, Z. (2005). Thermal-wave interferometry of gas-liquid applied to a thermal-wave resonator cavity technique. *Review of Scientific Instruments*, 76(7), 074901-074905.
- Azmi, Z., Liaw, H., Zulkifly, A., Wan Mahmood, Y., Jumiah., H. (2006) Measurement of thermal parameter using non-contact photopyroelectric method. *ScienceAsia*, 32 (1). pp. 47-52
- Azmi, B. Z., Noroozi, M., Rizwan, Z., Sulaiman, Z. A., Wahab, Z. A., & Moxsin, M. M. (2008). Simple TWRC technique by using optical fiber. *Infrared Physics & Technology*, 51(3), 270-275.
- Balderas-Lopez, J. A., & Mandelis, A. (2003). Self-consistent photothermal techniques: Application for measuring thermal diffusivity in vegetable oils. *Review of Scientific Instruments*, 74(1), 700-702.

- Balderas-Lopez, J. A., & Mandelis, A. (2001). Simple, accurate, and precise measurements of thermal diffusivity in liquids using a thermal-wave cavity. *Review of Scientific Instruments*, 72(6), 2649-2652.
- Balderas-Lopez, J. A., Mandelis, A., & Garcia, J. A. (2000). Thermal-wave resonator cavity design and measurements of the thermal diffusivity of liquids. *Review of Scientific Instruments*, 71(7), 2933-2937.
- Balderas-López, J. A., & Mandelis, A. (2003). New Photopyroelectric Technique for Precise Measurements of the Thermal Effusivity of Transparent Liquids. *International Journal of Thermophysics*, 24(2), 463-471
- Baruwati, B., Polshettiwar, V., & Varma, R. S. (2009). Glutathione promoted expeditious green synthesis of silver nanoparticles in water using microwaves. *Green Chemistry*, 11(7), 926-930.
- Badr, Y., & Mahmoud, M. A. (2005). Size-dependent surface-enhanced Raman scattering of sodium benzoate on Silver nanoparticles. *Journal of Molecular Structure*, 749(1–3), 187-192.
- Bennett, J. C. A., & Patty, R. R. (1982). TW interferometry: a potential application of the photoacoustic effect. *Appl. Opt.*, 21(1), 49-54.
- Bhattacharya, P., Nara, S., Vijayan, P., Tang, T., Lai, W., Phelan, P. E., et al. (2006). Characterization of the temperature oscillation technique to measure the thermal conductivity of fluids. *International Journal of Heat and Mass Transfer*, 49(17–18), 2950-2956.
- Bilecka, I., Elser, P., Niederberger, M. (2009). Kinetic and Thermodynamic Aspects in the Microwave-Assisted Synthesis of ZnO Nanoparticles in Benzyl Alcohol. *ACS Nano*, 3(2), 467-477.
- Bosbach, J., Martin, D., Stietz, F., Wenzel, T. (1999). Laser-based method for fabricating monodisperse metallic nanoparticles, *Applied Physics Letters*, 74(18), 2605 - 2607
- Caerels, J., Glorieux, C., Thoen, J. (1998). Absolute values of specific heat capacity and thermal conductivity of liquids from different modes of operation of a simple photopyroelectric setup. *Review of Scientific Instruments*, 69(6), 2452-2458.

- Cheng, Y.-T., Uang, R.-H., Chiou, K.-C. (2011). Effect of PVP-coated silver nanoparticles using laser direct patterning process by photothermal effect. *Microelectronic Engineering*, 88(6), 929-934
- Cheng, Y.-T., Uang, R.-H., Wang, Y.-M., Chiou, K.-C., Lee, T.-M. (2009). Laser annealing of gold nanoparticles thin film using photothermal effect. *Microelectronic Engineering*, 86(4-6), 865-867.
- Chirtoc, M., Mihilescu, G. (1989). Theory of the photopyroelectric method for investigation of optical and thermal materials properties. *Physical Review B*, 40(14), 9606-9617.
- Chirtoc, M., Bentefour, E. H., Glorieux, C., Thoen, J. (2001). Development of the front-detection photopyroelectric (FPPE) configuration for thermophysical study of glass-forming liquids. *Thermochimica Acta*, 377(1-2), 105-112.
- Choi, S.U.S., Eastman, J.A. (1995). Enhancing thermal conductivity of fluids with nanoparticles. *osti.gov*, International mechanical engineering congress and exhibition, San Francisco, CA (United States), 12-17 Nov 1995
- Coufal, H. (1984). Photothermal spectroscopy using a pyroelectric thin film detector. *Applied Physics Letters*, 44(1), 59-61.
- Coufal, H. and Mandelis, A. (1991). Pyroelectric sensors for the photothermal analysis of condensed phases. *Taylor & Francis*, 118(1), 379-409
- Dadarlat, D., Gibkes, J., Bicanic, D., Pasca, A. (1996). Photopyroelectric (PPE) measurement of thermal parameters in food products. *Journal of Food Engineering*, 30(1-2), 155-162.
- Dădârlat, D., Neamtu, C. (2006). Detection of molecular associations in liquids by photopyroelectric measurements of thermal effusivity. *Measurement Science and Technology*, 17(12), 3250.
- Dadarlat, D & Neamtu, C. (2009). High Performance Photopyroelectric Calorimetry of Liquids. *Acta chimica slovenica*, 56(1), 225-236.
- Dadarlat, D., Neamtu, C., Streza, M., Turcu, R., Craciunescu, I., Bica, D., et al. (2008). High accuracy photopyroelectric investigation of dynamic thermal parameters of Fe₃O₄ and CoFe₂O₄ magnetic nanofluids. *Journal of Nanoparticle Research*, 10(8), 1329-1336.

- Dadgostar, N., Ferdous, S., Henneke, D. (2010). Colloidal synthesis of copper nanoparticles in a two-phase liquid–liquid system. *Materials Letters*, 64(1), 45-48.
- Darroudi, M., Ahmad, M. B., Zamiri, R., Abdullah, A. H., Ibrahim, N. A., Shameli, K., et al. (2011). Preparation and characterization of gelatine mediated silver nanoparticles by laser ablation. *Journal of Alloys and Compounds*, 509(4), 1301-1304.
- De Albuquerque, J. E., Balogh, D. T., Faria, R. M. (2007). Quantitative depth profile study of polyaniline films by photothermal spectroscopies. *Applied Physics A*, 86(3), 395-401
- Delenclos, S., Chirtoc, M., Sahraoui, A. H., Kolinsky, C., Buisine, J. M. (2002). Assessment of calibration procedures for accurate determination of thermal parameters of liquids and their temperature dependence using the photopyroelectric method. *Review of Scientific Instruments*, 73(7), 2773-2780.
- Dobryszycski, J., & Bialozor, S. (2001). On some organic inhibitors of zinc corrosion in alkaline media. *Corrosion Science*, 43(7), 1309-1319.
- Durán, N., Marcato, P., Alves, O., Silva, J. S., Souza, G. H., Rodrigues, F., et al. (2010). Ecosystem protection by effluent bioremediation: silver nanoparticles impregnation in a textile fabrics process. *Journal of Nanoparticle Research*, 12(1), 285-292.
- Eastman, J. A., Choi, S. U. S., Li, S., Yu, W., & Thompson, L. J. (2001). Anomalously increased effective thermal conductivities of ethylene glycol-based nanofluids containing copper nanoparticles. *Applied Physics Letters*, 78(6), 718-720.
- Esquef, I. A., Siqueira, A. P. L., da Silva, M. G., Vargas, H., Miranda, L. C. M. (2006). Photothermal Gas Analyzer for Simultaneous Measurements of Thermal Diffusivity and Thermal Effusivity. *Analytical Chemistry*, 78(14), 5218-5221.
- Evans, W., Prasher, R., Fish, J., Meakin, P., Phelan, P., Keblinski, P. (2008). Effect of aggregation and interfacial thermal resistance on thermal conductivity of nanocomposites and colloidal nanofluids. *International Journal of Heat and Mass Transfer*, 51(5–6), 1431-1438.

- Fan, M., Yuan, P., Chen, T., He, H., Yuan, A., Chen, K., et al. (2010). Synthesis, characterization and size control of zerovalent iron nanoparticles anchored on montmorillonite. *Chinese Science Bulletin*, 55(11), 1092-1099.
- George, N. A., Vallabhan, C. P. G., Nampoore, V. P. N., George, A. K., Radhakrishnan, P. (2001). Use of an open photoacoustic cell for the thermal characterisation of liquid crystals. *Applied Physics B*, 73(2), 145-149.
- Gilbert, K. E. H., Lehman, J. H., Dillon, A. C., Blackburn, J. L. (2006). Toward rapid and inexpensive identification of bulk carbon nanotubes. *Applied Physics Letters*, 88(14), 143122-143123.
- Gonella, F., Mattei, G., Mazzoldi, P., Cattaruzza, E., Arnold, G. W., Battaglin, G., et al. (1996). Interaction of high power laser light with silver nanocluster composite glasses. *Applied Physics Letters*, 69(20), 3101-3103.
- Govorov, A. O., Richardson, H. H. (2007). Generating heat with metal nanoparticles. *Nano Today*, 2(1), 30-38.
- Graebner, J. E., Jin, S., Kammlott, G. W., Herb, J. A., & Gardinier, C. F. (1992). Unusually high thermal conductivity in diamond films. *Applied Physics Letters*, 60(13), 1576-1578.
- Gutiérrez-Juárez, G., Ivanov, R., Pichardo-Molina, J. P., Vargas-Luna, M., Alvarado-Gil, J. J., & Camacho, A. (2008). Metrological Aspects of Auto-normalized Front Photopyroelectric Method to Measure Thermal Effusivity in Liquids. *International Journal of Thermophysics*, 29(6), 2102-2115.
- Hassen, M. A., Davis, R. H. (1989). Effects of particle interactions on the determination of size distributions by sedimentation. *Powder Technology*, 58(4), 285-289.
- Hashimoto, S., Werner, D., Uwada, T. (2012). Studies on the interaction of pulsed lasers with plasmonic gold nanoparticles toward light manipulation, heat management, and nanofabrication. *Journal of Photochemistry and Photobiology C: Photochemistry Reviews*, 13(1), 28-54.
- Heimlich, M. S., Henke, L., Debono, R. F., Krull, U. J. (1995). Photopyroelectric spectroscopy incorporating surface plasmon amplification for the development of chemical sensors using selective surfaces of nanometer thickness. *Ferroelectrics*, 165(1), 39-53.
- Hidehiro, K., Motoyuki, I. (2010). Surface modification and characterization for dispersion stability of inorganic nanometer-scaled particles in liquid media. *Science and Technology of Advanced Materials*, 11(4), 044304.

Hodak, J. H., Henglein, A., Giersig, M., Hartland, G. V. (2000). Laser-Induced Inter-Diffusion in AuAg Core–Shell Nanoparticles. *The Journal of Physical Chemistry B*, 104(49), 11708-11718.

Holman, J. P. (1990). Heat Transfer, 7th ed. McGraw-Hill, New York.

Honda, M., Saito, Y., Smith, N. I., Fujita, K., Kawata, S. (2011). Nanoscale heating of laser irradiated single gold nanoparticles in liquid. *Opt. Express*, 19(13), 12375-12383.

Hong, J., Kim, S. H., and Kim, D. (2007). Effect of laser irradiation on thermal conductivity of ZnO nanofluids. *Journal of Physics: Conference Series*, 59(1), 301.

Huang, H., Yang, Y. (2008). Preparation of silver nanoparticles in inorganic clay suspensions. *Compos Sci Technol*, 68, 2948–2953.

Inasawa, S., Sugiyama, M., Yamaguchi, Y. (2005). Laser-Induced Shape Transformation of Gold Nanoparticles below the Melting Point: The Effect of Surface Melting, *J. Phys. Chem. B*, 109 (8), 3104–3111

Jia, J., Yu, J. C., Zhu, X.-M., Chan, K. M., Wang, Y.-X. J. (2012). Ultra-fast method to synthesize mesoporous magnetite nanoclusters as highly sensitive magnetic resonance probe. *Journal of Colloid and Interface Science*, 379(1), 1-7.

Jiang, X., Mayers, B., Herricks, T., & Xia, Y. (2003). Direct Synthesis of Se@CdSe Nanocables and CdSe Nanotubes by Reacting Cadmium Salts with Se Nanowires. *Advanced Materials*, 15(20), 1740-1743.

Jiménez-Pérez, J. L., Cruz-Orea, A., Sánchez-Ramírez, J. F., Sánchez-Sinencio, F., Martínez-Pérez, L., López Muñoz, G. A. (2009). Thermal Characterization of Nanofluids with Different Solvents. *International Journal of Thermophysics*, 30(4), 1227-1233.

Kamat, P. (2002). Photoinduced transformations in semiconductor–metal nanocomposite assemblies. *Pure Appl. Chem.*, 74(9), 1693–1706

- Kappe, C. O., & Dallinger, D. (2009). Controlled microwave heating in modern organic synthesis: highlights from the 2004–2008 literature. *Molecular Diversity*, 13(2), 71-193.
- Kappe, C. O. (2004). Controlled Microwave Heating in Modern Organic Synthesis. *Angewandte Chemie. International Edition*, 43(46), 6250-6284.
- Kappe, C. O., Dallinger, D. (2009). Controlled microwave heating in modern organic synthesis: highlights from the 2004–2008 literature. *Molecular diversity*, 13(2), 71-193.
- Kebllinski, P., Prasher, R., Eapen, J. (2008). Thermal conductance of nanofluids: is the controversy over. *Journal of Nanoparticle Research*, 10(7), 1089-1097.
- Kharadea, R. R., Patil, K.R., Patil, P.S., Bhosalea, P.N. (2012). Novel microwave assisted sol–gel synthesis (MW-SGS) and electrochromic performance of petal like h-WO₃ thin films. *Materials Research Bulletin*, 47(7), 1787–1793
- Kulkarni, D. P., Das, D. K., & Vajjha, R. S. (2009). Application of nanofluids in heating buildings and reducing pollution. *Applied Energy*, 86(12), 2566-2573.
- Kumar, S. A., Meenakshi, K. S., Narashimhan, B. R. V., Srikanth, S., & Arthanareeswaran, G. (2009). Synthesis and characterization of copper nanofluid by a novel one-step method. *Materials Chemistry and Physics*, 113(1), 57-62.
- Kusum, H. H., Saidin, M. K., Ibrahim, Z. (2009). Optical Properties of Ti:Al₂O₃ Single Crystal. *J. Fiz. UTM*. 4, 42-49
- Kwan, C.H., Matvienko, A., Mandelis, A. (2007). Optimally accurate thermal-wave cavity photopyroelectric measurements of pressure-dependent thermophysical properties of air: Theory and experiments. *Review of Scientific Instruments*, 78(10), 104902-104910.
- Lapotko, D. (2009). Pulsed photothermal heating of the media during bubble generation around gold nanoparticles. *International Journal of Heat and Mass Transfer*, 52(5–6), 1540-1543.

Lide, D.R., ed. *Handbook of Chemistry and Physics*. 76th Edition ed. 1995-1997, CRC Press: New York.

Lima, J. A. P., Marín, E., Correa, O., Silva, M. G. d., Cardoso, S. L., Gatts, C. (2000). Measurement of the thermal properties of liquids using a TW interferometer. *Measurement Science and Technology*, 11(10), 1522.

Lima, J. A. P., Marín, E., Massunaga, M. S. O., Correa, O., Cardoso, S. L., Vargas, H., et al. (2001). Measurement of the thermal properties of liquid mixtures using a TW interferometer. *Applied Physics B*, 73(2), 151-155.

Link, S., El-Sayed, M. A. (1999). Size and Temperature Dependence of the Plasmon Absorption of Colloidal Gold Nanoparticles. *The Journal of Physical Chemistry B*, 103(21), 4212-4217.

Link, S., El-Sayed, M. A. (2000). Shape and size dependence of radiative, non-radiative and photothermal properties of gold nanocrystals. *International Reviews in Physical Chemistry*, 19(3), 409-453.

Liu, Z., Yuan, Y., Khan, S., Abdolvand, A., Whitehead, D., Schmidt, M. (2009). Generation of metal-oxide nanoparticles using continuous-wave fibre laser ablation in liquid. *Journal of Micromechanics and Microengineering*, 19(5), 054008.

Liu, H., Sadygov, R. G., Yates, J. R. (2004). A Model for Random Sampling and Estimation of Relative Protein Abundance in Shotgun Proteomics. *Analytical Chemistry*, 76(14), 4193-4201.

Longuemart, S., Quiroz, A. G., Dadarlat, D., Sahraoui, A. H., Kolinsky, C., Buisine, J. M. (2002). An application of the front photopyroelectric technique for measuring the thermal effusivity of some foods. *Instrumentation Science & Technology*, 30(2), 157-165.

Longuemart, S., Sahraoui, A. H., Dadarlat, D., Daoudi, A., Laux, V., & Buisine, J. M. (2003). Investigations of the thermal parameters of ferroelectric liquid crystals using the pyroelectric effect in the S C * phase. *Europhysics Letters (EPL)*, 63(3), 453.

- Luo, C., Zhang, Y., Zeng, X., Zeng, Y., Wang, Y. (2005). The role of poly(ethylene glycol) in the formation of silver nanoparticles. *Journal of Colloid and Interface Science*, 288(2), 444-448.
- Mafuné, F., Kohno, J.-y., Takeda, Y., & Kondow, T. (2001). Dissociation and Aggregation of Gold Nanoparticles under Laser Irradiation. *The Journal of Physical Chemistry B*, 105(38), 9050-9056.
- Mandelis, A. (1984). Frequency-domain photopyroelectric spectroscopy of condensed phases (PPES): A new, simple and powerful spectroscopic technique. *Chemical Physics Letters*, 108(4), 388-392.
- Mandelis, A., Vanniasinkam, J., Budhudu, S., Othonos, A., & Kokta, M. (1993). Absolute nonradiative energy-conversion-efficiency spectra in $\text{Ti}^{3+}:\text{Al}_2\text{O}_3$ crystals measured by noncontact quadrature photopyroelectric spectroscopy. *Physical Review B*, 48(10), 6808-6821.
- Marinelli, M., Mercuri, F., Zammit, U., Pizzoferrato, R., Scudieri, F., Dadarlat, D. (1994). Photopyroelectric study of the thermal parameters of antiferromagnets at the Neel temperature. *J. Phys. IV France*, 04(C7), C7-261-C267-266.
- Masuda, H., Ebata, A., Teramae, K., Hishinuma, N. (1993). Alteration of thermal conductivity and viscosity of liquid by dispersing ultra-fine particles [dispersion of Al_2O_3 , SiO_2 and TiO_2 ultra-fine particles]. *Netsu Bussei*, 4, 227-233
- Matvienko, A., Mandelis, A. (2006). Quantitative one-dimensional thermal-wave cavity measurements of fluid thermophysical properties through equivalence studies with three-dimensional geometries. *Review of Scientific Instruments*, 77(6), 064906-064909.
- Matvienko, A., Mandelis, A. (2008). Theoretical analysis of PPE measurements in liquids using a thermal-wave cavity. *The European Physical Journal Special Topics*, 153(1), 127-129.
- Menon, P. C., Rajesh, R. N., Glorieux, C. (2009). High accuracy, self-calibrating photopyroelectric device for the absolute determination of thermal conductivity and thermal effusivity of liquids. *Review of Scientific Instruments*, 80(5), 054904-054909.

- Mohamed, M. B., AbouZeid, K. M., Abdelsayed, V. A. (2010) Growth mechanism of anisotropic gold nanoparticles via microwave synthesis: formation of dioleamide by gold nanocatalysis. *ACS Nano.*, 4, 2766–2772
- Murshed, S. M. S., Leong, K. C., Yang, C. (2006). Determination of the effective thermal diffusivity of nanofluids by the double hot-wire technique. *Journal of Physics D: Applied Physics*, 39(24), 5316.
- Mohamed, S. H., & Raaif, M. (2010). Effects of thickness and rf plasma oxidizing on structural and optical properties of SiO_xNy thin films. *Surface and Coatings Technology*, 205(2), 525-532.
- Murshed, S. M. S., Leong, K. C., Yang, C. (2008). Thermophysical and electrokinetic properties of nanofluids – A critical review. *Applied Thermal Engineering*, 28(17–18), 2109-2125.
- Murugan, A. V., Sonawane, R.S., Kale, B.B., Apte, S.K., Kulkarni, A. V. (2001). Microwave–solvothral synthesis of nanocrystalline cadmium sulfide. *Materials Chemistry and Physics*, 71(1), 98–102
- Naoki, T. (2008). Metal Nanoparticle Catalysts Dekker Encyclopedia of Nanoscience and Nanotechnology, *Second Edition - Six Volume Set (Print Version)* (pp. 2052-2063): CRC Press.
- Nedyalkov, N. N., Imamova, S. E., Atanasov, P. A., Toshkova, R. A., Gardeva, E. G., Yossifova, L. S. (2011). Interaction of gold nanoparticles with nanosecond laser pulses: Nanoparticle heating. *Applied Surface Science*, 257(12), 5456-5459.
- Neamtu, D.D., Neamtu, C. High performance photopyroelectric calorimetry of liquids. *Acta Chim. Slov.* 2009, 56, 225–236.
- Nguyen, V. S., Rouxel, D., Hadji, R., Vincent, B., Fort, Y. (2011). Effect of ultrasonication and dispersion stability on the cluster size of alumina nanoscale particles in aqueous solutions. *Ultrasonics Sonochemistry*, 18(1), 382-388.
- Okeke, G., Hammond, R., Antony, S., J. (2012). Analysis of Structural and Surface Properties of TiO₂ Nanoparticles in Water and Vacuum Using Molecular Dynamics Modeling and Simulations. *Journal of Nanofluids*, 1, 21–27

- Patakfalvi, R., Oszko, A., & Dekany, I. (2003). Synthesis and characterization of silver nanoparticle/kaolinite composites. *Colloids and Surfaces A: Physicochemical and Engineering Aspects*, 220(1), 45-54.
- Patel, K., Kapoor, S., Dave, D. P., & Mukherjee, T. (2005). Synthesis of nanosized silver colloids by microwave dielectric heating. *Journal of Chemical Sciences*, 117(1), 53-60.
- Park, K., Seo, D., & Lee, J. (2008). Conductivity of silver paste prepared from nanoparticles. *Colloids and Surfaces A: Physicochemical and Engineering Aspects*, 313–314(0), 351-354.
- Petryayeva, E., & Krull, U. J. (2011). Localized surface plasmon resonance: Nanostructures, bioassays and biosensing—A review. *Analytica Chimica Acta*, 706(1), 8-24.
- Pyatenko, A., Yamaguchi, M., & Suzuki, M. (2007). Synthesis of Spherical Silver Nanoparticles with Controllable Sizes in Aqueous Solutions. *The Journal of Physical Chemistry C*, 111(22), 7910-7917.
- Raghupathi, R. K., Koodali, R. T., Manna, A. C. (2011). Size-Dependent Bacterial Growth Inhibition and Mechanism of Antibacterial Activity of Zinc Oxide Nanoparticles, *American Chemical Society* , 27, 4020–4028
- Ravikumar, S., Gokulakrishnan, R., Selvanathan, K., Selvam, S. (2011). Antibacterial activity of metal oxide nanoparticles against ophthalmic pathogens, *International Standard Serial*, 3(5), 122 - 127
- Resta, V., Siegel, J., Bonse, J., Gonzalo, J., Afonso, C. N., Piscopiello, E., et al. (2006). Sharpening the shape distribution of gold nanoparticles by laser irradiation. *Journal of Applied Physics*, 100(8), 084311-084311-084316.
- Raffi, M., Hussain, F., Bhatti, T.M., Akhter, J.I. (2008). Antibacterial Characterization of Silver Nanoparticles against. *J. Mater. Sci. Technol.*, 24(2), 192-196
- Richard C. Murdock, Laura Braydich-Stolle, Amanda M. Schrand, John J. Schlager, and Saber M. Hussain, (2008) Characterization of Nanomaterial Dispersion in Solution Prior to In Vitro Exposure Using Dynamic Light Scattering Technique, *Toxicological Sciences* 101(2), 239–253

- Robinson, I., Volk, M., Tung, L. D., Caruntu, G., Kay, N., & Thanh, N. T. K. (2009). Synthesis of Co Nanoparticles by Pulsed Laser Irradiation of Cobalt Carbonyl in Organic Solution. *The Journal of Physical Chemistry C*, 113(22), 9497-9501.
- Rogach, A. L., Nagesha, D., Ostrander, J. W., Giersig, M., & Kotov, N. A. (2000). "Raisin Bun"-Type Composite Spheres of Silica and Semiconductor Nanocrystals. *Chemistry of Materials*, 12(9), 2676-2685.
- Ryu, J. H., Koo, S.-M., Chang, D. S., Yoon, J.-W., Lim, C. S., Shim, K. B. (2006). Microwave-assisted synthesis of PbWO₄ nano-powders via a citrate complex precursor and its photoluminescence. *Ceramics International*, 32(6), 647-652.
- Sadrolhosseini, A. R., Moksini, M. M., Nang, H. L. L., Noroozi, M., Yunus, W. M. M., & Zakaria, A. (2011). Physical Properties of Normal Grade Biodiesel and Winter Grade Biodiesel. *International Journal of Molecular Sciences*, 12(4), 2100-2111.
- Sahraoui, A. H., Longuemart, S., Dadarlat, D., Delenclos, S., Kolinsky, C., Buisine, J. M. (2002). The application of the photopyroelectric method for measuring the thermal parameters of pyroelectric materials. *Review of Scientific Instruments*, 73(7), 2766-2772
- Sahraoui, A. H., Longuemart, S., Dadarlat, D., Delenclos, S., Kolinsky, C., Buisine, J. M. (2003). Analysis of the photopyroelectric signal for investigating thermal parameters of pyroelectric materials. *Review of Scientific Instruments*, 74(1), 618-620.
- Saetveit, N. J., Bajic, S. J., Baldwin, D. P., Houk, R. S. (2008). Influence of particle size on fractionation with nanosecond and femtosecond laser ablation in brass by online differential mobility analysis and inductively coupled plasma mass spectrometry. *Journal of Analytical Atomic Spectrometry*, 23(1), 54-61.
- Samyn, P., Schoukens, G., Abbeele, H., Vonck, L., Stanssens, D. (2011). Application of polymer nanoparticle coating for tuning the hydrophobicity of cellulosic substrates. *Journal of Coatings Technology and Research*, 8(3), 363-373.

- Sato, K., Li, J.-G., Kamiya, H., & Ishigaki, T. (2008). Ultrasonic Dispersion of TiO₂ Nanoparticles in Aqueous Suspension. *Journal of the American Ceramic Society*, 91(8), 2481-2487.
- Sha, B., Gao, W., Wang, S., Xu, F., & Lu, T. (2011). Cytotoxicity of titanium dioxide nanoparticles differs in four liver cells from human and rat. *Composites Part B: Engineering*, 42(8), 2136-2144.
- Sharma, N. (2012). Performances of different metals in optical fibre-based surface plasmon resonance sensor. *Pramana*, 78(3), 417-427.
- Shen, J., and Mandelis, A., (1995). Thermal-wave resonator cavity. *Rev Sci Instrum.* 66, 4999-5005
- Shen, J., Mandelis, A., Aloysius, B. D. (1996). Thermal-wave resonant-cavity measurements of the thermal diffusivity of air: A comparison between cavity-length and modulation-frequency scans. 17(6), *Int. J. Thermophys.* 1241-1254
- Shen, J., Mandelis, A., and Helen Tsai, (1997). Signal generation mechanisms, intracavity-gas thermal-diffusivity temperature dependence, and absolute infrared emissivity measurements in a thermal-wave resonant cavity. *Rev. Sci. Instrum.* 69: 197-203
- Szymańska-Chargot, M., Gruszecka, A., Smolira, A., Bederski, K., Głuch, K., Cytawa, J. (2009). Formation of nanoparticles and nanorods via UV irradiation of AgNO₃ solutions. *Journal of Alloys and Compounds*, 486(1–2), 66-69.
- Sreeram, K. J., Nidhin, M., & Nair, B. U. (2008). Microwave assisted template synthesis of silver nanoparticles. *Bulletin of Materials Science*, 31(7), 937-942.
- Streza, M., Dadarlat, D., Socaciu, C., Bele, C., Dulf, F., Simon, V. (2009). Photopyroelectric Detection of Vegetable Oils' Adulteration. *Food Biophysics*, 4(3), 147-150.
- Son, Y., Yeo, J., Moon, H., Lim, T. W., Hong, S., Nam, K. H., et al. (2011). Nanoscale Electronics: Digital Fabrication by Direct Femtosecond Laser Processing of Metal Nanoparticles. *Advanced Materials*, 23(28), 3176-3181.

- Taylor, R., Phelan, P., Otonicar, T., Adrian, R., Prasher, R. (2011). Nanofluid optical property characterization: towards efficient direct absorption solar collectors. *Nanoscale Research Letters*, 6(1), 225.
- Touloukian, Y. S., Powell, R. W., Ho, C. Y., and Nicolau M. C. (eds.) (1973). *Thermophysical Properties of Matter*, 10 (Plenum Press, New York), 437.
- Tripathi, U. N., Soni, A., Ganesan, V., & Okram, G. S. (2012). Influence of polyvinylpyrrolidone on particle size of Ni nanoparticles preparation. *AIP Conference Proceedings*, 1447(1), 437-438.
- Trisaksri, V., Wongwises, S. (2007). Critical review of heat transfer characteristics of nanofluids. *Renewable and Sustainable Energy Reviews*, 11(3), 512-523.
- Tsuji, T., Iryo, K., Watanabe, N., & Tsuji, M. (2002). Preparation of silver nanoparticles by laser ablation in solution: influence of laser wavelength on particle size. *Applied Surface Science*, 202(1-2), 80-85.
- Thomas, S., Isaac, J., Philip, J. (1995). Thermal diffusivity of solids by photoacoustic cell rotation and phase lag measurement. *Review of scientific instruments*, 66(7) 3907 - 3908
- Tu, M.H., Sun, T, Grattan, K.T.V. (2012). Optimization of gold-nanoparticle-based optical fibre surface plasmon resonance (SPR)-based sensors. *Sensors and Actuators B*, 164 43– 53
- Wang, C., Mandelis, A. (1999). Measurement of thermal diffusivity of air using photopyroelectric interferometry. *Review of Scientific Instruments*, 70(5), 2372-2378.
- Wang, X.-Q., Mujumdar, A. S. (2007). Heat transfer characteristics of nanofluids: a review. *International Journal of Thermal Sciences*, 46(1), 1-19.
- Wang, P., Liu, M., Gao, G., Zhang, S., Shi, H., Li, Z., Zhang, L., and Fang, Y. (2012). From gold nanorods to nanodumbbells: a different way to tailor surface plasmon resonances by a chemical route. *J. Mater. Chem.*, 22, 24006-24011

- Watanabe, H. (1996). Accurate and simultaneous measurement of the thermal conductivity and thermal diffusivity of liquids using the transient hot-wire method. *Metrologia*, 33(2), 101.
- Wei, H., Eilers, H. (2009). From silver nanoparticles to thin films: Evolution of microstructure and electrical conduction on glass substrates. *Journal of Physics and Chemistry of Solids*, 70(2), 459-465.
- Wei, Y., and Xie, H. (2012). A Review on Nanofluids: Preparation, Stability Mechanisms, and Applications. *Journal of Nanomaterials*, 2012, 17 pages
- Yin, Y., and Alivisatos, P. (2004). Colloidal nanocrystal synthesis and the organic–inorganic interface. *Nature*, 437, 664-670
- Yang, B., & Han, Z. H. (2006). Temperature-dependent thermal conductivity of nanorod-based nanofluids. *Applied Physics Letters*, 89(8), 083111-083113.
- Yi-Ting, C., Rouh-Huey, U., & Kuo-Chan, C. (2010, 20-22 Oct. 2010). A fine line/space fabrication process on flexible polyimide film using laser direct writing method by photothermal effect of silver nanoparticles. *Microsystems Packaging Assembly and Circuits Technology Conference (IMPACT)*, 2010
- Yu, W., & Xie, H. (2012). A review on nanofluids: preparation, stability mechanisms, and applications. *J. Nanomaterials*, 2012, 1-17.
- Xiang-Qi, W., and Mujumdar, A.S. (2008) a review on nanofluids - part II: experiments and applications, *Brazilian Journal of Chemical Engineering*, 25(4) 631 - 648
- Xie, H., and Chen, L., (2011). Review on the Preparation and Thermal Performances of Carbon Nanotube Contained Nanofluids. *J. Chem. Eng. Data*, 56 (4), 1030–1041
- Xuan, Y., Li, Q.(2000). Heat transfer enhancement of nanofluids. *International Journal of Heat and Fluid Flow*, 21(1), 58–64
- Zhang, X., Gu, H., and Fujii, M. (2006). Experimental Study on the Effective Thermal Conductivity and Thermal Diffusivity of Nanofluids. *Int. J Thermophys* , 27, 569-580.

Zheng, M., Gu, M., Jin, Y., & Jin, G. (2001). Optical properties of silver-dispersed PVP thin film. *Materials Research Bulletin*, 36(5–6), 853-859.

Zhu, D., Li, X., Wang, N., Wang, X., Gao, J., & Li, H. (2009). Dispersion behavior and thermal conductivity characteristics of Al₂O₃–H₂O nanofluids. *Current Applied Physics*, 9(1), 131-139.

Zhu, H.-t., Lin, Y.-s., & Yin, Y.-s. (2004). A novel one-step chemical method for preparation of copper nanofluids. *Journal of Colloid and Interface Science*, 277(1), 100-103.

Zhu, J., Palchik, O., Chen, S., Gedanken, A. (2000). Microwave Assisted Preparation of CdSe, PbSe, and Cu_{2-x}Se Nanoparticles. *J. Phys. Chem. B*, 104 (31), 7344–7347

BIODATA OF STUDENT

Monir Noroozi was born in Tehran. She got her Diploma in Mathematics & Physics from Payaam High School. In 1988 she received her Bachelor of Science (B.Sc) in Applied Physics from Azzahra University in Tehran.

In December 2004, she joined Faculty of Science, Universiti Putra Malaysia as a Master student to embark on research in the field of Photoacoustic and Photothermal Phenomena under the supervision of Professor Dr. Azmi Bin Zakaria. She received her Master of Science (M.Sc) in 2007. She was immediately accepted for PhD in the field of Applied Optics and Nanomaterial in Faculty of Science, University Putra Malaysia.

LIST OF PUBLICATIONS

Publications

Journals:

- Noroozi, M.,** Zakaria, A., Moxsin, M. M., Wahab, Z. A., & Abedini, A. (2012). Green Formation of Spherical and Dendritic Silver Nanostructures under Microwave Irradiation without Reducing Agent. *International Journal of Molecular Sciences*, 13(7), 8086-8096.
- Noroozi, M.,** Zakaria, A., Moxsin, M. M., & Wahab, Z. A. (2012). An Investigation on the Thermal Effusivity of Nanofluids Containing Al₂O₃ and CuO Nanoparticles. *International Journal of Molecular Sciences*, 13(8), 10350-10358.
- Noroozi, M.,** Zakaria, A., Shahril Husin, M., Moxsin, M. M., & Wahab, Z. A. (2012). Investigating Thermal Parameters of PVDF Sensor in the Front Pyroelectric Configuration. *International Journal of Thermophysics (IJOT)*
- Noroozi, M.,** Azmi, B. Z., & Moxsin, M. M. (2010). The reliability of optical fiber-TWRC technique in liquids thermal diffusivity measurement. *Infrared Physics & Technology*, 53(3), 193-196.
- Azmi, B.Z., **Noroozi, M.,** Sulaiman, Z.A., Wahab, Z.A., and Moxsin, M.M. (2010). TW interferometry of gas-liquid using optical fibre TW resonator cavity.technique, *Journal of Physics Conference Series*, 214(1), 012066
- Noroozi, M.,** Zakaria, A., Moxsin, M. M., & Wahab, Z. A. (2009). Thermal Diffusivity Measurement of Liquid Through thermal Diffusion Length Measurement, *Solid St. Sci. and Technol.* 17(1), 44-49.
- Abedini, A., Saion, E., Larki, F., Zakaria, A., **Noroozi, M.,** & Soltani, N. (2012). Room Temperature Radiolytic Synthesized Cu@CuAlO₂-Al₂O₃ Nanoparticles, *International Journal of Molecular Sciences*, 13(9), 11941-11953.

Conferences/Reports/posters/lectures:

Azmi, B.Z., **Noroozi, M.**, Sulaiman, Z.A., Wahab, Z.A., and Moxsin, M.M. TW interferometry of gas-liquid using OF-TWRC technique Presented at ICPPP15, July 19-24th, 2009.

Noroozi, M., Zakaria, A., Moxsin, M. M., & Wahab, Z. A. Comparison between TW Wavelength Measurement and TW Signal Fitting Schemes in OF-TWRC Technique Presented at Fundamental Science Congress (FSC), organised by Faculty of Science, June 17-18th, 2009

Noroozi, M., Zakaria, A., Moxsin, M. M., & Wahab, Z. A . Measuring Thermal Parameter By Thermal Diffusion Length Measurement Using OF-TWRC Technique presented at The 24th Regional Conference on Solid State Science & Technology 2008 (RCSST 2008).

Azmi, B. Z , **Noroozi, M.**, Moxsin, M. M., & Wahab, Z. A. Measurement Of Thermal Diffusivity of Various Liquid by Using Optical Fiber TWRC Technique, poster presented at Pameran Reka Cipta Penyelidikan dan Inovasi (PRPI 2008), organized by Research Management Centre (UPM), July 29-31st, 2008.

Azmi, B. Z, **Noroozi, M.**, Moxsin, M. M., & Wahab, Z. A. Measuring Liquid Thermal Diffusivity by Using Optical Fiber TWRC Technique, poster presented at Malaysia Technology Expo (MTE2008), organized by Malaysian Association of Research Scientists, Feb. 21-23rd, 2008.

Noroozi, M., Zakaria, A., Moxsin, M. M., & Wahab, Z. A. Enhancement thermal diffusivity of clay suspension with Ag nanoparticles, Fundamental Science Congress, (FSC) Kompleks Mahasiswa, UPM, May 18-19, 2010, PP23